



Universidade do Minho
Escola de Engenharia

Rui Pedro Leitão da Silva Rocha

Microlenses for Optical Microsystems

Rui Pedro Leitão da Silva Rocha · Microlenses for Optical Microsystems

UMinho | 2013

Agosto de 2013



Universidade do Minho
Escola de Engenharia

Rui Pedro Leitão da Silva Rocha

Microlenses for Optical Microsystems

Tese de Doutoramento
Programa Doutoral em Líderes para as Indústrias Tecnológicas

Trabalho efectuado sob a orientação do
Professor Doutor José Higinó Gomes Correia
Doutor João Paulo Pereira do Carmo

Agosto de 2013

DECLARAÇÃO

Nome

Rui Pedro Leitão da Silva Rocha

Endereço electrónico

Rui.Pedro.Rocha@gmail.com

Telefone

964488144

Número do Bilhete de Identidade

10743807

Título dissertação /tese X

Microlenses for Optical Microsystems

Orientadores

Professor Doutor José Higinio Gomes Correia

Doutor João Paulo Pereira do Carmo

Ano de conclusão: 2013

Designação do Mestrado ou do Ramo de Conhecimento do Doutoramento:

Programa Doutoral em Líderes para as Indústrias Tecnológicas

É AUTORIZADA A REPRODUÇÃO INTEGRAL DESTA TESE/TRABALHO APENAS PARA EFEITOS DE INVESTIGAÇÃO, MEDIANTE DECLARAÇÃO ESCRITA DO INTERESSADO, QUE A TAL SE COMPROMETE;

Universidade do Minho, 01/08/2013

Assinatura: _____

“Buy the ticket, take the ride”

Hunter S. Thompson (1937-2005)

Acknowledgements

This is probably the most unfair part of the thesis. There are always so many people we meet, books we read, music we listen to, trips we experience, highs that do not last eternally, lows we endure and doubts that hold us back throughout our lifetime and maybe, just maybe, all of them contribute, even if unconsciously, to shape us to be who we are and what we do with our lives. Honestly speaking, pursuing a PhD degree is something I did not see coming even in my wildest dreams... but then again, life has more imagination than we carry in our dreams. Nevertheless, and taking the risk of letting somebody out of the memory lane, here I am writing the acknowledgements in my thesis.

First of all, I would like to thank my supervisor Professor José Higinio Correia, who I know for many years now, the scientific orientations, suggestions, random *sui generis* discussions and the final revision of the thesis. It has been a real challenge to be a part of his energetic research group.

To my co-supervisor, Doctor João Paulo Carmo, I have to be grateful for all the discussions related to the thesis and also the more ambitious ones about “what if” possibilities.

A very special thanks to Professor Michael Belsley for sharing his expertise, know-how, availability, sympathy and, why not, also his optical laboratories and equipment.

My experience in the MIT Portugal EDAM-LTI Program has been amazing and surreal in many ways. First of all, I want to thank the people I came across, and had the privilege to work with and call my friends; Alexandra Sepúlveda, Cláudio “CEO” Santos, Georgios Koronis, “Grande” Pedro Duarte, Ricardo “Teddy Bear” Sá and his sidekick Eduarda Silva. Also, I would like to express my gratitude to Professor Olga Carneiro for her availability and for trying to make sure everything was normally flowing. To Mário Meira for helping me out every time I needed. Last, but definitely not least, to my friend Professor Alexandre Silva for being who he is.

Now, more specifically concerning my thesis, there are quite a few people I need to publicly acknowledge for their direct contribution on the developed work and many of them I am also lucky to call my friends therefore I am omitting academic titles. All of them, without exception, contributed very much to the successful closure of this thesis. They are Alexandre Peixoto, Ana Lima, Carlos Torres, Débora Ferreira, Graça Minas,

João Ribeiro, Luís Rocha, Manuel Oliveira, Manuel Silva, Marino Maciel, Miguel Gomes, Paulo Sousa, Rui Gomes, Rui Sousa and Vânia Pinto.

An extra recognition, because they are worth it but for completely different reasons, to my colleagues and friends, for all the hangouts and laughter, Beatriz Gonçalves and Pedro Anacleto.

My last **thank you** goes to two very special people in my life, my baby sister Ana, and my little piglet Catarina “*Oinc-Oinc*”. Thank you for reading, revising, giving an outside perspective and critically reviewing the text and format of the document. Thank you for all the help and care.

Finally, I would like to thank, especially, to all the adults that did not forget they too were once children.

The author, Rui Pedro Leitão da Silva Rocha, was supported by the Portuguese Foundation for Science and Technology (SFRH/BD/33733/2009). The author would also like to acknowledge the MIT Portugal Program for supporting this work.

Abstract

Lenses have been used by mankind for thousands of years for innumerable different reasons and applications. More recently, lenses in the micro scale dimension, so called microlenses (MLs), have been designed and fabricated using semiconductor technology. These new lenses are used for collimation, focusing or imaging and are an appealing alternative for applications where miniaturization and alignment simplicity are important requirements. Moreover, they also opened a large number of new applications for optical structures and, at the same time, reducing the mechanical and electrical complexity of the existing systems.

In this context, the presented thesis has as main purposes, the design and development of a process that allows the fabrication of different sized plano-convex MLs with minor intervention on the process parameters. The MLs were fabricated using a photoresist, the AZ4562, through classical photolithography and the thermal reflow process. Another achievement was the fabrication of MLs directly on the surface of a silicon die containing complementary metal–oxide–semiconductor (CMOS) photodiodes (PDs) for quantifying the differences in their photocurrents generation capacity.

The MLs' optimum fabrication process was achieved when a 128k dots per inch (dpi) super high-resolution chrome on soda lime glass 3×3-0.060" photomask was employed. This photomask allows the design pattern to be transferred into the photoresist with very high precision. Nevertheless, for actually obtaining the desired lens profile, it is necessary to apply a thermal treatment to the fabricated microstructures. When the photoresist is submitted to a temperature higher than its glass transition temperature, it softens allowing the shape change to occur. For MLs, the major external force acting during this process is the surface tension.

The fabricated MLs were structurally characterized using a profilometer and scanning electron microscope (SEM) images. For measuring the focal length, an opto-mechanical alignment system was assembled and a difference of just 4% was found between the measured and the theoretical values.

An additional improvement was achieved by introducing a rehydration step in the fabrication process. The prebake stage used during the fabrication serves for evaporating the solvent off the photoresist but also, all of its water content. As a result, it was demonstrated that the AZ4562 needs rehydration in order to obtain excellent results by preventing structural damages in the MLs which are crucial for achieving efficient optical

properties. The main advantage of this new optimized process is the further improvement of well-established standard microfabrication processes, *i.e.*, photolithography combined with photoresist thermal reflow.

Then, three approaches for integrating the MLs with the photodetecting substrate were tested. The first was using a polydimethylsiloxane (PDMS) intermediate layer for controlling the thickness between the MLs and the photodetecting substrate for allowing different focal lengths to be used depending on the application. The second one is setting the MLs' focal length within the photodetectors' depletion region using a 150 μm thin glass substrate for demonstrating that the current generation is enhanced for the same active area. Finally, the third approach consists on a setup composed by a MLs array fabricated directly on top of the PDs and in this approach, two solutions are presented. One is the fabrication of a ML on a square PD with the side measuring 24 μm . This setup enables the capture of light that would otherwise fall outside the photodiodes' active area resulting in an overall photocurrent generation gain. The other is the fabrication of a MLs array using the same photomask but on a square PD with the side measuring 240 μm for determining the level of photocurrent generation. Moreover, two light sources (red and white lights) were used for evaluating the light acquisition enhancement capacity. From the results that were obtained under different integration solutions, the direct fabrication of MLs on PDs was the one with the better results concerning photocurrent generation by improving it by more than 14% and 2% for red and white lights, respectively. The red light has the ideal penetration depth in silicon for achieving the most prominent enhancement in photocurrent generation presented in this thesis.

The MLs that were designed and fabricated, as well as their integration solutions with a photosensitive substrate, show interesting potential in applying them on industry standard fabrication processes for optical microsystems, from light-acquisition enhancement applications to image sensors.

Keywords: Microlenses, thermal reflow, rehydration, photodiodes, current generation.

Resumo

Desde há milhares de anos que a Humanidade tem usado lentes por inúmeras razões e para diferentes aplicações. Mais recentemente, têm sido desenvolvidas e fabricadas lentes de microdimensões, também designadas de microlentes (MLs), utilizando a tecnologia dos semicondutores. Este novo tipo de lentes é normalmente utilizado para colimar, focar ou criar imagens, e é uma alternativa apelativa para aplicações onde a miniaturização e simplicidade de alinhamento são requisitos importantes. Além disso, elas também deram origem a um conjunto de novas aplicações para estruturas óticas reduzindo, ao mesmo tempo, as complexidades mecânicas e elétricas dos sistemas existentes.

Nesta perspetiva, a presente tese tem como principais objetivos o desenho e desenvolvimento de um processo que permita o fabrico de MLs plano-convexas de diferentes tamanhos com intervenção mínima nos parâmetros do processo. As MLs foram fabricadas utilizando um polímero fotosensível (PF), o AZ4562, através de fotolitografia e refluxo térmico. Outro objetivo foi o fabrico de MLs diretamente na superfície de um *die* de silício, que contém fotodíodos (FDs) em tecnologia *complementary metal-oxide semiconductor* (CMOS), para quantificar as diferenças na sua capacidade de gerar fotocorrente (FC).

O processo de fabrico ótimo de MLs foi alcançado quando uma fotomáscara (FM) de crómio de super alta-resolução de 128k *dots per inch* (dpi) foi usada. Esta FM permite que o desenho-padrão seja transferido para o PF com elevada precisão. No entanto, para se obter o perfil de lente, é necessário aplicar um tratamento térmico à microestrutura fabricada. Quando o PF é submetido a uma temperatura mais alta do que a sua temperatura de transição vítrea, este amolece permitindo assim que a sua forma se altere. No caso das MLs, a principal força responsável para que essa mudança ocorra durante este processo térmico é a tensão superficial.

As MLs fabricadas, foram estruturalmente caracterizadas usando um perfilómetro e imagens de *scanning electron microscope* (SEM). Para medir a distância focal (f), foi concebido um sistema de alinhamento opto-mecânico e verificou-se que existe uma pequena diferença de 4% entre o valor medido e o calculado.

Foi conseguida ainda uma melhoria adicional com a introdução de uma fase de reidratação no processo de fabrico. A fase de *prebake* utilizada no fabrico serve para evaporar os solventes do PF mas, todavia, retira também todo o seu conteúdo de água. Por

isso, foi demonstrado que o AZ4562 necessita de ser reidratado para se conseguir excelentes resultados prevenindo danos estruturais nas MLs que é fundamental para a obtenção de propriedades óticas eficientes. A maior vantagem neste novo processo otimizado é a melhoria conseguida nos processos de microfabricação *standard* estabelecidos, *i.e.*, fotolitografia combinada com o refluxo térmico do PF.

Em seguida, foram testadas três formas para integrar as MLs num substrato fotossensível. A primeira consistiu em utilizar uma camada intermédia de polidimetilssiloxano (PDMS) para controlar a espessura entre as MLs e o substrato fotodetector e assim, permitir a utilização de diferentes f dependendo da aplicação. A segunda foi colocar f dentro da região de depleção do FD usando um substrato de vidro com 150 μm de espessura demonstrando que a geração de FC é aumentada para a área ativa. Por último, a terceira abordagem foi o desenvolvimento de um *setup* composto por um *array* de MLs fabricado diretamente sobre os FDs e duas soluções são apresentadas. Uma delas é o fabrico de uma ML num FD quadrado com 24 μm de lado. Este *setup* permite a captura de luz que não iria incidir na área ativa do FD resultando num aumento de geração de FC. O outro é o fabrico de um *array* de MLs usando a mesma FM, mas num FD quadrado com 240 μm de lado, para determinar o nível de geração de FC. Nestes testes, recorreu-se a duas fontes de luz (vermelha e branca) para avaliar a capacidade de aumentar a aquisição de luz. Relativamente à geração de FC, o melhor dos resultados obtidos nas várias soluções de integração propostas, foi conseguido com o fabrico direto de MLs nos FDs com aumentos superiores a 14% e 2% para as luzes vermelha e branca, respetivamente. A luz vermelha tem a penetração ideal no silício para atingir os resultados mais proeminentes no que concerne aos ganhos obtidos na geração de FC apresentado nesta tese.

As MLs que foram desenhadas e fabricadas, bem como as soluções propostas de integração num substrato fotossensível, demonstram um potencial interesse de aplicação em processos industriais de fabrico *standard* para microsistemas óticos, desde aplicações de aumento de aquisição de luz, até sensores de imagens.

Palavras-chave: Microlentes, refluxo térmico, reidratação, fotodíodos, geração de corrente.

Contents

1	Introduction.....	1
1.1	Lenses: an historic perspective.....	1
1.2	Lenses.....	4
1.2.1	Spherical lenses.....	4
1.2.2	Plano-convex microlenses	6
1.3	State-of-the-art in microlenses	7
1.4	Motivation and Objectives	13
1.5	Microsystem integration overview.....	15
1.6	Organization of the thesis.....	16
	References.....	17
2	Light and lenses theory	21
2.1	Light	21
2.1.1	Photons.....	22
2.1.2	Maxwell equations	23
2.1.3	Transverse waves	25
2.1.4	Polarization	27
2.2	Optical surfaces	28
2.2.1	Reflection and scattering.....	29
2.2.2	Absorption.....	30
2.2.3	Refraction.....	31
2.3	Refraction in spherical surfaces	32
2.3.1	Spherical and chromatic aberration	36
	References.....	37
3	Design and fabrication	39
3.1	Fabrication.....	39

3.1.1	Photoresist AZ4562	42
3.1.2	Thermal reflow.....	45
3.1.3	Finite element method: optical behavior.....	47
3.2	Fabrication process: first method	47
3.2.1	Characterization of the microstructures	52
3.3	Fabrication process: second method	56
3.3.1	Photomask.....	56
3.3.2	Pre-thermal reflow array	61
3.3.3	Post-thermal reflow array	63
3.4	Fabrication process: third method	65
3.4.1	Rehydration.....	66
3.4.2	Fabrication efficiency and reproducibility.....	69
3.5	Results analysis	74
	References.....	75
4	Results and discussion	79
4.1	Photodiodes	80
4.1.1	CMOS photodiodes with a n+/p-substrate junction.....	82
4.1.2	Measuring setup	84
4.2	Focal length characterization	90
4.2.1	Interference patterns.....	95
4.3	Microlenses integration with the photodiodes	96
4.3.1	The first approach: using PDMS as substrate	96
4.3.2	The second approach: using a 150 μm thickness glass slide as substrate..	105
4.3.3	The third approach: using the array of photodiodes as substrate.....	109
4.4	Results analysis	118
4.5	Optical filters simulation.....	120
	References.....	123

5	Conclusions and future work	127
5.1	Results and conclusions	127
5.2	Future work and applications	128
5.2.1	Polydimethylsiloxane as substrate	128
5.2.2	Stereoscopic image sensor	129
	Annex	133
	Journal Publications	133

List of Figures

Figure 1.1 – Illustrations of early works on optics. Top left Roger Bacon [6], top right Leonardo da Vinci [7], bottom left Alhazen [8] and bottom right Witello [9].	2
Figure 1.2 – Illustrations of works on optics from the 17 th century. Top Isaac Newton holding a prism dispersing light, bottom left Leeuwenhoek with one of the first microscopes [10] with a magnification of about 40 times. On the bottom right is the depiction of Galileo with his telescope [11].	3
Figure 1.3 – Illustration of the light deflection according to the Snell’s law.	4
Figure 1.4 – Positive equiconvex converging lens. In converging lenses the center is thicker than the edges meaning that the light converges more as it crosses the material with higher index of refraction than air.	5
Figure 1.5 – Negative equiconcave diverging lens. In diverging lenses the edges are thicker than the center meaning that the light diverges more as it crosses the material with higher index of refraction than air.	5
Figure 1.6 – Geometric differences between spherical and aspherical lenses showing the cause of aberration.	7
Figure 1.7 – In a) is illustrated the MLs’ fabrication process whereas in b) is a SEM image of the fabricated MLs array and in c) a SEM image detailing a single ML [17].	8
Figure 1.8 – In a) is the overall layout of the surface tension self-assembled microlens array before assembly. In b) is a front view SEM image of the array [18].	9
Figure 1.9 – Ink-jet printing fabrication process steps [19] are seen in a). The diameter and height of the microlenses are shown in b) and measure approximately 53 and 18 μm , respectively.	9
Figure 1.10 – The fabrication steps are seen in a) and SEM images of the structures before and after the softening process are seen in b) [20].	10
Figure 1.11 – In a) is shown the photonic crystal’s square lattice of air holes and the cross-section of the structure. In b) is a SEM image of the 2D lens. The radius is 20 μm [21].	11

Figure 1.12 – Cross-section of one CCD image sensor with microlens for light acquisition in a digital camera from Sony Corporation [23].	12
Figure 1.13 – Array of photoresist structures fabricated directly on the photodiodes using classical photolithography before the thermal reflow was applied.	14
Figure 1.14 – Array of microlenses fabricated directly on the surface of the photodiodes.	14
Figure 1.15 – Cross-section illustration of an optical microsystem. On top is the ML for capturing and redirecting the light; in the middle it is represented a three layers dielectric optical filter (TiO ₂ and SiO ₂) for excluding the non-visible spectrum light and on the bottom is the photodetector.	16
Figure 2.1 – Representation of the full electromagnetic spectrum and the approximate wavelength intervals in vacuum for different colors.	22
Figure 2.2 – A plane, linearly polarized EM, wave propagating along the x -axis at light speed c . The electric and magnetic fields are mutually perpendicular and are in-phase. The wave propagates in the direction $E \times B$.	26
Figure 2.3 – General perspective of a single wavelength projected into a plane surface with the resulting interactions: reflection, transmission (with refraction) and absorption. It must be noted that the angles θ_1 and θ_2 are the same in specular reflection.	29
Figure 2.4 - Example of the presence of chromophores and auxochromes in basic blue 9.	31
Figure 2.5 – Illustration of the light deflection according to the Snell’s law.	31
Figure 2.6 – Representation of the most relevant parameters of plano-convex spherical lenses.	32
Figure 2.7 – Refraction caused by a spherical surface.	34
Figure 2.8 – Illustration of the effect that a spherical lens has on refraction.	36
Figure 2.9 – Illustration of the chromatic aberration and how it affects different wavelengths.	37
Figure 3.1 – Illustration of the most important steps of the photolithographic process.	39

Figure 3.2 – Parameters for determining the necessary focal length f for the microlenses arrays.	41
Figure 3.3 – Factors determining the geometry needed for a given focal length f	42
Figure 3.4 – AZ4562’s refractive index wavelength dependency chart.	45
Figure 3.5 – Contact angle between the pre-thermal reflow microfabricated structure and the substrate.	46
Figure 3.6 – FEM simulations showing the light concentration for microlenses measuring 5 and 32 μm for the vertex h and width $2r$, respectively.	47
Figure 3.7 – In-house built spin coater for coating photoresist onto substrates.	50
Figure 3.8 – Hotplate and the computer using <i>Labview</i> software to control the temperature profile with PID control.	50
Figure 3.9 – Mask with arrays containing rectangles measuring 1000 and 100 μm for length and width, respectively. This pattern was printed in an acetate sheet in a commercially available printer for achieving arrays of column-like structures that are later thermally reflowed into microlenses.	51
Figure 3.10 – A UV exposure machine typically used for fabricating PCBs.	51
Figure 3.11 – Development phase using magnetic stirrers. In a) is the <i>Laboratory hot plate magnetic stirrer from Agimixt</i> and in b) the <i>Magnetic stirrer MSH 300</i>	52
Figure 3.12 – The PR array before the thermal reflow viewed from the top.	52
Figure 3.13 – Illustration of how the UV light is transmitted by the array of lamps in the PCB exposure machine.	53
Figure 3.14 – Profilometer <i>Veeco Dektak 150</i>	54
Figure 3.15 – Photoresist profile after the photolithographic process. The maximum measured thickness is 5.514 μm	54
Figure 3.16 – In this picture is seen the PR array after the thermal step from a tilted angle.	55
Figure 3.17 – Photoresist profile after the thermal reflow step. The maximum measured thickness is 5.428 μm	55
Figure 3.18 – Real 30–5 μm pattern mask seen through a <i>Leica M80</i> microscope with 120 \times magnification.	57

Figure 3.19 – In a) the whole picture of the array mask drawing is seen and in b) a detailed zoom-in with the chromium rectangle width (30) and spacing (5) expressed in μm	58
Figure 3.20 – Mask aligner MJB 3 from <i>Karl Suss</i> . In a) and in b) are seen a general view and during photolithography exposure, respectively.....	60
Figure 3.21 - In a) and b) SEM images of a single element of the array and a zoom-out of the array, respectively.	62
Figure 3.22 – Illustration of the cross-section of two pre-thermal reflow elements for calculation purposes.	63
Figure 3.23 – In a) and b) SEM images of a single microlens an overview of the ML array, respectively.	64
Figure 3.24 – Cross-section showing the lens' spherical profile.	65
Figure 3.25 – SEM image of a single element of the array before the thermal reflow and with rehydration.....	68
Figure 3.26 – SEM image of a single element of the array after the thermal reflow and with rehydration.....	68
Figure 3.27 – Reflow temperature profile used in the hotplate.	69
Figure 3.28 – The dimensions that were used for evaluating the reproducibility of the fabrication process for the pre-thermal reflow microstructure. If $W_1=W_2$ than the fabricated microstructure would be a rectangular prism.....	70
Figure 3.29 – Mean and standard deviation values for the 24–5 μm pattern mask.	71
Figure 3.30 – Mean and standard deviation values for the 30–5 μm pattern mask.	72
Figure 3.31 – The dimensions that were used for evaluating the reproducibility of the fabrication process for the post-thermal reflow microstructure (microlens).	73
Figure 3.32 – Post-reflow mean and standard deviation values for the 24–5 μm pattern mask.	73
Figure 3.33 – Post-reflow mean and standard deviation values for the 30–5 μm pattern mask.	74
Figure 4.1 – Visible light penetration depth in silicon [3].....	80
Figure 4.2 – In a) electron-hole pair generation with different wavelengths, $\lambda_1<\lambda_2$. In b) electron-hole pair collection in a <i>p-n</i> junction.	81

Figure 4.3 – Cross-section illustration of an n^+/p -substrate photodiode that is used in all the measurements made with and without MLs on top.....	83
Figure 4.4 – Schematic in a) and optical photograph in b) of the photodiodes array. The value of the photocurrent measured for the 240 μm photodiodes is presented in Figure 4.11.	84
Figure 4.5 – Emitted white light spectrum [10] used for measuring the photocurrent generated by the PDs.....	84
Figure 4.6 – Emitted red light spectrum [11] used for measuring the photocurrent generated by the PDs. The peak is $\lambda_0=632$ nm and the full width half maximum (FWHM) is 17 nm.....	85
Figure 4.7 – Photograph of the setup that was used for characterizing the PDs without and with MLs.	85
Figure 4.8 – Illustration of the schematic used for measuring the PDs with different reverse bias voltages.....	86
Figure 4.9 – Dark current, at room temperature, for the 24 μm square PD measured with the <i>Keithley 6487 Picoammeter Voltage Source</i> at 0 and -4 V reverse bias. These measurements were done without and with a ML.	87
Figure 4.10 – Measured photocurrent for the 24 μm photodiode as a function of both the incident normal red and white light illuminance, in lux, at two values of the reverse bias, 0 and -4 V.	88
Figure 4.11 – Measured photocurrent for a 240 μm photodiode as a function of both the incident normal red and white light illuminance, in lux, at two values of the reverse bias, 0 and -4 V.	88
Figure 4.12 – Transmittance measuring setup.	89
Figure 4.13 – AZ4562 transmittance for white and red lights from 0 to 2000 lux.....	90
Figure 4.14 – Average AZ4562 transmittance for white and red lights.	90
Figure 4.15 – Gaussian beam parameters where $w(z)$ is the beam’s radial width at a given distance, w_0 is the thinnest radial width known as beam waist, z_R is the Rayleigh length being $2w_0$ where the beam area is two times bigger than the beam area in w_0 . In the length between these two values, w_0 and $2w_0$, the beam is considered collimated because its size is approximately constant.....	91

Figure 4.16 – Setup with the opto-mechanical alignment system used for measuring the focal length.	92
Figure 4.17 – The false color image of the spatial distribution of the He-Ne laser beam after being focused by the aspheric lens and then passing through glass substrate that serves as a support for the MLs array. The beam has an ISO $1/e^2$ diameter of 2.55 mm.	92
Figure 4.18 – The image obtained after the beam transformed by one of the spherical microlenses in the array. The ISO $1/e^2$ diameters have been calculated to be 1.17 mm and 2.56 mm for the vertical and horizontal axes respectively.	93
Figure 4.19 – The variation of the beam magnification as the microarray lens is translated near the best focus position. The blue curve is the theoretical fit according to equation (4.4) and yields an effective focal length of $f=49\pm 2$ μm in air for the MLs array.	93
Figure 4.20 – Optical setup used for checking the interference patterns caused by the microlenses in the array. This setup is composed by an array of MLs, by a laser source and by a flat surface to project the spread beams. In a) is signaled where the laser dot (with a 1 mm diameter) impinges on the MLs array and in b) is the display of the pattern after the laser travels through the array of MLs.	95
Figure 4.21 – DIL package with the die containing the array of photodiodes (marked in white) and in black is signaled the cavity to be filled with PDMS.	97
Figure 4.22 – Factors determining how the thickness (th) of the PDMS substrate allows defining what ML (W and h) should be chosen depending on the photodiode's cathode width (D).	97
Figure 4.23 – SEM images of the fabricated AZ4562 microstructures before and after the thermal reflow in a) and b), respectively.	98
Figure 4.24 – Cracks appearing in both the PDMS and AZ4562 during fabrication.	99
Figure 4.25 – Setup for real-time visualization of the interface between PDMS and AZ4562 under a temperature ramp up from 50 to 140 °C. The results are presented in Figure 4.26.	100
Figure 4.26 – Snapshots of the AZ4562–PDMS interface taken with the sample being heated-up at a temperature profile similar to the one used	

during the thermal reflow. The scale in the pictures represents 50 μm.	101
Figure 4.27 – <i>Jasco FT-IR 4100</i> spectrometer [22].	102
Figure 4.28 – FTIR analysis to the PDMS and AZ4562 individually and together at different periods of the fabrication. In red are signaled the two identified changes that occur in the materials’ interface. Only in the PDMS+AZ4562+UV+TR line the absorptions peaks disappear hence suggesting that some kind of degradation is occurring. This chemical phenomenon is yet to be fully identified and characterized.	104
Figure 4.29 – Cross-section illustration of the 150 μm thickness glass slide integration solution. The measured photocurrent is seen in Figure 4.35. It should be noted that, in the visible spectrum, the index of refraction is similar for both the glass and the AZ4562 so the refraction between them is not represented.	105
Figure 4.30 – <i>Automatic Dicing Saw Disco DAD 2H/6T</i> with a zoom-in detail of the dicing saw.	106
Figure 4.31 – Blue stick tape used in the dicer for guaranteeing that the fabricated MLs array does not move during the dicing process. The total area of the array is 2.02×2.01 mm and is signaled with a red circle.	106
Figure 4.32 – <i>MEI 1204W Hybrid Wedge Bonder</i> for performing the wire bonding between the die and PCB.	107
Figure 4.33 – Photograph of the MLs fabricated on the 150 μm thickness glass slide placed on top of array of photodiodes characterized in Figure 4.11. The generated photocurrent using this integration solution is shown in Figure 4.35.	107
Figure 4.34 – Illustration of the proposed integration solution. In a) is the cross- section of the light conversion intersection with the photodiode’s surface. In b) is a zoom-in photograph of the 240 μm photodiode.	108
Figure 4.35 – Measured photocurrent as a function of the linearly increasing illuminance (in lux) for incident normal white light. The PD without the integration of MLs (blue line) generates more photocurrent because more active area is being used. The other photocurrent data (red line) is concerning the PD with the MLs integration solution.	109

Figure 4.36 – Cross-section illustration of the direct fabrication on a photodiode. This setup increments the light acquisition because it converges light that would impinge outside the PD into its active area. The measured photocurrents without and with a ML fabricated directly on the photodiode are seen in Figure 4.39. It should be noted that h_2 is the oxides' thickness.	110
Figure 4.37 – A zoom-in of the 24 μm photodiode within the die. The measured photocurrent results are shown in Figure 4.39.	110
Figure 4.38 – Zoom-in optical microscope photograph of the die placed on the PCB and with the wire bonding already performed. The MLs are fabricated directly on the die's surface.	111
Figure 4.39 – Comparison between the photocurrents measured for different reverse bias voltages under red light, without and with the ML on a 24 μm square PD. The improvement in the light-current generation efficiency of the presented 24–5 μm photomask configuration is shown in Figure 4.40.	112
Figure 4.40 – Efficiency improvement (%) achieved at different illuminance values (red light) and reverse bias voltages by the developed MLs fabrication process on a 24 μm square PD.	112
Figure 4.41 – Comparison between the photocurrents measured for different reverse bias voltages under white light, without and with the ML on a 24 μm square PD. The improvement in the light-current generation efficiency of the presented 24–5 μm photomask configuration is shown in Figure 4.42.	113
Figure 4.42 – Efficiency improvement (%) achieved at different illuminance values (white light) and reverse bias voltages by the developed MLs fabrication process on a 24 μm square PD.	113
Figure 4.43 – Cross-section illustration of the direct fabrication on a 240 μm photodiode. The measured photocurrents without and with a MLs array fabricated directly on the photodiode are seen in Figure 4.45.	114
Figure 4.44 – In a) is an optical microscope photograph of the 24–5 μm MLs array fabricated directly on the photodiodes' surface and in b) is a SEM image of the same microstructure. For the presented case, the	

mask/substrate alignment was done so that the maximum number of MLs would be centered within the PD's active area as illustrated in Figure 4.43.	115
Figure 4.45 – Comparison between the photocurrents measured for different reverse bias voltages under red light, without and with the ML on a 240 μm square PD. The average improvement in the light-current generation efficiency of the presented 24–5 μm photomask configuration is shown in Figure 4.46.	116
Figure 4.46 – Efficiency improvement (%) achieved at different illuminance values (red light) and reverse bias voltages by the developed MLs fabrication process on a 240 μm square PD.	116
Figure 4.47 – Comparison between the photocurrents measured for different reverse bias voltages under white light, without and with the MLs array, on a 240 μm square PD. The improvement in the light-current generation efficiency of the presented 24–5 μm photomask configuration under white light is shown in Figure 4.48.	117
Figure 4.48 – Efficiency improvement (%) achieved at different illuminance values (white light) and reverse bias voltages by the developed MLs fabrication process on a 240 μm square PD. It should be noted that in this configuration, for a reverse bias of -4 V, the system reaches equilibrium regarding the current generation gain provided by the MLs and the losses occurring by absorption, reflectance and scattering.	118
Figure 4.49 – A Fabry–Perot optical filter consisting of alternate high and low refractive index materials.	120
Figure 4.50 – In a) and b) are seen the pre and post-thermal reflow structures, respectively, using a photomask design measuring 24–5 μm. In c) is a cross-section of the AZ4562 fabricated on TiO ₂	121
Figure 4.51 – Simulation results of a three layer optical filter and a SiO ₂ resonant cavity. The data concerning the filter is shown in Table 4.5.	123
Figure 5.1 – Illustration of the stereoscopic image formation concept with a single polychromatic CMOS image sensor (example with one microlens and two photodiodes PD _n left and right). In a) is seen the light	

collecting setup and in b) a zoom-in of the array of MLs separating the left and right optical channels to form the stereoscopic image.129

Figure 5.2 – Design of a complete optical microsystem. The optical filters are composed by just three layers. Because of the chromatic aberration, the MLs allow different wavelengths to impinge onto a specific photodiode. It should be noted that this illustration is not to scale.131

List of Tables

Table 1.1 – Lenses definitions according to their radii variations.	6
Table 1.2 – Summary of the different MLs fabrication techniques and materials used.	13
Table 3.1 – Physical and chemical properties of the AZ4562 [13].	43
Table 3.2 – Typical film thickness as a function of the spin coater speed [13].	43
Table 3.3 – Processing guidelines [13].	48
Table 3.4 – Fabrication Process steps and parameters.	49
Table 3.5 – Relevant characteristics of soda lime glass photomasks [28].	57
Table 3.6 – Second fabrication process steps and parameters values.	59
Table 3.7 – Third fabrication process steps and parameters values.	67
Table 4.1 – Dark current values (in pA) for the 24 and 240 μm square PD for two reverse bias voltages. The measurements were done with and without MLs on top of the photodiodes.	87
Table 4.2 – DIL cavity filling process with PDMS.	96
Table 4.3 – Classification of the chemical functional group identified through FTIR analysis.	103
Table 4.4 – Summary of the results achieved in the enhancement of photocurrent generation efficiency. The values presented below are roundings, to the nearest integer, of the previously demonstrated results.	119
Table 4.5 – Layers’ materials and thicknesses of the simulated optical filter.	122

List of symbols

Symbol	Description	Units
$1/e^2$	Asymptotes of the beam irradiance profile	m
$A(\lambda)$	Photoresist's absorption coefficient	m^{-1}
A_0	Amplitude of the incident light	
\mathbf{B}	Magnetic field	$A.m^{-1}$
$B(\lambda)$	Photoresist's absorption coefficient	m^{-1}
c	Speed of light	$m.s^{-1}$
d	Distance travelled across the photoresist	m
D	Photodiode's cathode width	m
d_k	Optical path	m
E	Energy	J
\mathbf{E}	Electric field	$V.m^{-1}$
E_{gap}	Bandgap energy	eV
E_{ph}	Energy of incident photons	eV
f	Focal length, focal distance	m
f	Wave's frequency	Hz
f	External force acting on the fluid	$N.m^{-3}$
h	Planck's constant	$eV.s$
h	Lens apex	m
h_2	Oxides' thickness	m
h_m	Measured thickness	m
h_r	Real thickness	m
\hat{i}	Unit vector	-
I	Light intensity	$J.s.m^{-1}$
I_0	Incident light intensity	$J.s.m^{-1}$
I_P	Photocurrent	A
\hat{j}	Unit vector	-
k	Extinction coefficient	-
k	Reflected beams	-

\hat{k}	Unit vector	-
m	Mass	kg
n	Index of refraction, refractive index	-
N_1	Photoresist's Cauchy's constants	-
N_2	Photoresist's Cauchy's constants	-
N_2	Nitrogen	-
N_3	Photoresist's Cauchy's constants	-
p	Momentum	kg.m.s ⁻¹
p	Pressure	Pa
P_i	Incident optical power	W
q	Electron charge	C
r	Half of W	m
r	Distance from the photomask	m
R_1	Lens' radius	m
R_2	Lens' radius	m
R_{ph}	Photodiode's responsivity	A.W ⁻¹
T_g	Glass transition temperature	°C
u	Lens' arc length (undulation)	M
v	Wave's velocity	m.s ⁻¹
v_p	Propagation speed in a dielectric material	m.s ⁻¹
V	Fluid's flow speed	m.s ⁻¹
V	Voltage	V
V_1	Volume of trapezoidal prism	m ³
V_{bi}	Built-in electrical field	V
W	Lens's width at the interface with the substrate	m
$w(z)$	Beam's radial width at a given distance	m
w_0	Beam waist	m
Z	Wave's impedance	Ω
Z_0	Wave's impedance in free-space	Ω
z_R	Rayleigh length	m
α	Angle	°
α	Optical absorption coefficient	m ⁻¹
β	Wavenumber	m ⁻¹

β	Angle	°
δ	Angle	°
ε	Electric permittivity	F.m ⁻¹
ε_0	Electric permittivity in free space	F.m ⁻¹
ε_r	Relative permittivity	F.m ⁻¹
ζ	Angle	°
η	Photodiode's quantum efficiency	%
θ	Angle	°
λ	Wavelength	m
λ_0	Wavelength in vacuum	m
λ_g	Wavelength in a medium	m
μ	Magnetic permeability	H.m ⁻¹
μ	Material's viscosity	Pa.s
μ_0	Magnetic permeability in free space	H.m ⁻¹
μ_r	Relative permeability	H.m ⁻¹
μ_{w_j}	Mean	-
ρ	Flow density	kg.m ⁻³
σ_{w_j}	Standard deviation	-
σ	Liquid surface tension	N. m ⁻¹
σ_s	Solid surface tension	N. m ⁻¹
σ_{sl}	Solid and liquid boundary tension	N. m ⁻¹
τ	Wave's period	s

List of terms

Term	Designation
2D	Two dimensional
CCD	Charge-Coupled Device
CMOS	Complementary Metal-Oxide Semiconductor
CVD	Chemical Vapor Deposition
DIL	Dual In-Line
DM	Dielectric Materials
dpi	Dots Per Inch
EM	Electromagnetic
FEM	Finite Element Method
FTIR	Fourier Transform Infrared
FWHM	Full Width Half Maximum
He-Ne	Helium-Neon
InGaAsP	Indium Gallium Arsenide Phosphide
InP	Indium Phosphide
IPA	Isopropyl Alcohol
IR	Infrared
LIGA	Lithographie, Galvanoformung, Abformung
ML	Microlens
NA	Numerical Aperture
<i>n</i> MOS	<i>n</i> -channel Metal-Oxide Semiconductor
OF	Optical Filter
PAC	Photo Active Compound
PCB	Printed Circuit Board
PDMS	Polydimethylsiloxane
PEB	Post Exposure Bake
PGMEA	Methoxy-Propyl Acetate
PID	Proportional-Integral-Derivative
PMMA	Polymethylmethacrylate

<i>p</i> MOS	<i>p</i> -channel Metal-Oxide Semiconductor
PR	Photoresist
PVD	Physical Vapor Deposition
r.p.m	Rotations Per Minute
RF	Radio Frequency
SEM	Scanning Electron Microscope
Si	Silicon
SiO ₂	Silicon Dioxide
SOI	Silicon-On-Insulator
TF	Thin-Film
TiO ₂	Titanium Dioxide
TR	Thermal Reflow
UV	Ultra-Violet
VCSEL	Vertical Cavity Surface Emitting Lasers
VLSI	Very Large Scale Integration

1 Introduction

Lenses have been used for quite some time and, throughout their development history, their applications vary considerably. Lenses are passive optical devices that are used, generally, for refracting and transmitting light. For example, lenses were found to be very useful in applications from concentrating sunlight for producing fire, to spectacles for improving eye sight and on telescopes and microscopes for studying the cosmos and microorganisms, respectively. More recently, though, small lenses with diameter smaller than one millimeter (mm), called microlenses (MLs) are used for a number of applications in the micro/nano-scale. Examples of these applications include imaging, biomedical instruments, lab-on-a-chip systems and a variety of uses in optical communications [1-5].

1.1 Lenses: an historic perspective

There are several examples throughout history about the use of lenses, from burning glasses used in Ancient Egypt, Greece and Rome accompanied by the first attempts to explain the physical phenomena behind the nature of light, such as its propagation, reflection and refraction. It should be noted the contributions and curiosity of philosophers and thinkers in Classical antiquity for the first known theories trying to explain what was observed. After the fall of the Roman Empire until the Medieval Era, there was not much advance in optics, maybe with just the exception of the Arabic culture in the 1000s (namely the work entitled “The Book of Optics” or in Arabic *Kitāb al-Manāẓir*). After the translation from Arabic to Latin of previous works, in Europe, a new momentum appeared in the study and development of innovative mathematical and empirical knowledge concerning optics. Individuals like Robert Grosseteste, Witelo, Roger Bacon and Leonardo da Vinci (some centuries later) were, until the 17th century especially, the intellectual forces that drove optical sciences where real and fast improvements started to happen. In Figure 1.1 is seen a compilation of images representing some of the works of the previously mentioned authors.

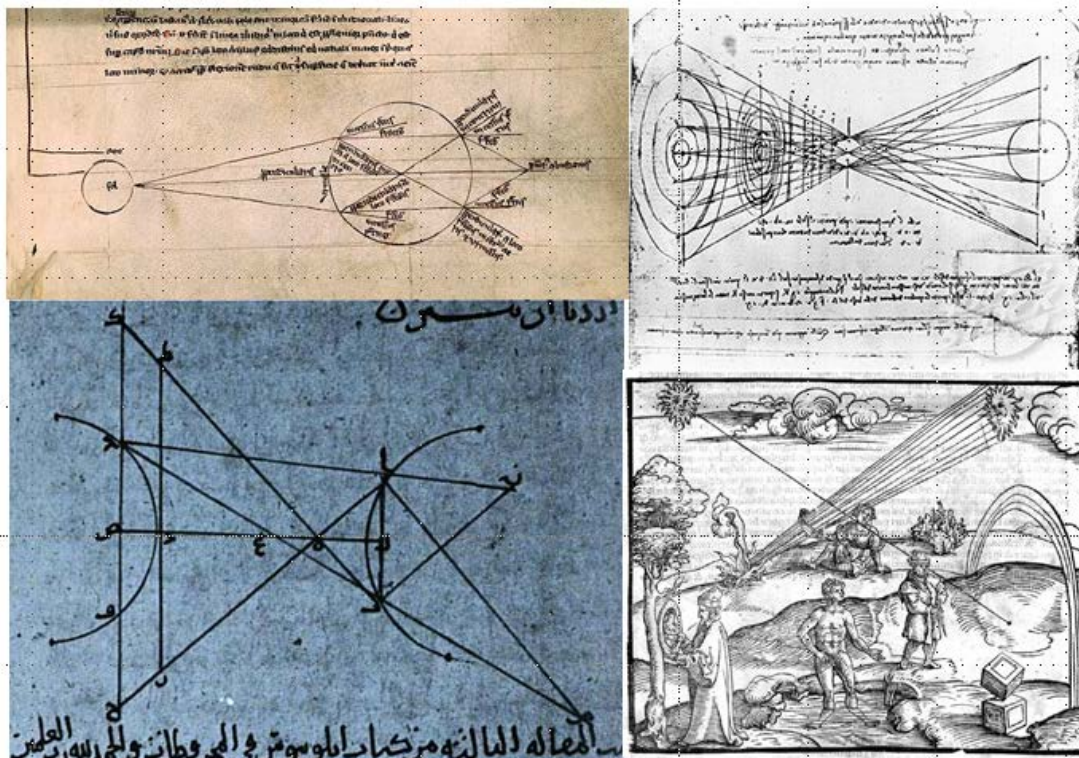


Figure 1.1 – Illustrations of early works on optics. Top left Roger Bacon [6], top right Leonardo da Vinci [7], bottom left Alhazen [8] and bottom right Witello [9].

Many brilliant people helped forging the beginning of what is called Modern Optics from the 17th century upwards. Individuals such as Willebrord Snell, Galileo Galilei, René Descartes, Antonie van Leeuwenhoek, Pierre de Fermat, Johannes Kepler, Isaac Newton, Christiaan Huygens, and so on, made lots of progresses in the development of analytical models, experimental setups and optical devices for understanding and explaining light related phenomena as well as observing microorganisms or far away cosmic bodies. Probably, the most notable examples created during these years were through the progresses made in optical instruments like the telescope and the microscope, for example. As before, in Figure 1.2 is seen a compilation of illustrations representing some of the previously mentioned scientists.



Figure 1.2 – Illustrations of works on optics from the 17th century. Top Isaac Newton holding a prism dispersing light, bottom left Leeuwenhoek with one of the first microscopes [10] with a magnification of about 40 times. On the bottom right is the depiction of Galileo with his telescope [11].

From the 19th century up until the present days, more specific knowledge concerning light propagation and low level physics have allowed new horizons to be seen and new devices to be designed. Scientists like Max Planck, Niels Bohr, Albert Einstein, Albert Michelson and James Maxwell, to name a few, were amongst the main culprits for such advancements. It was during these 200 years that light science evolved considerably and great improvements on lenses' based instruments were achieved enabling optical microscopes with magnifications higher than 1000 \times and telescopes that allow determining the age of celestial bodies in the order of billions of years [9, 12-14]. In the 20th century, technology and the continuous downsizing of devices, permitted the design and fabrication of micro scaled lenses, the so-called microlenses, in different materials and with different techniques.

1.2 Lenses

Basically, lenses are characterized by their curvature on both sides and are positive or negative when the surface is convex or concave towards the impinging light, respectively [12]. In the case of positive lenses, this means that when light crosses the lens, it will be converged into a single point (although this is only achieved by aspherical lenses) located at a distance f , called focal point or focal length. In relation to the negative lenses, the incoming light is diverged when exiting the lens but it seems as it is originating from a point located on the front side of the lens, being also the focal length f but measured in negative units when compared to the f in positive lenses.

1.2.1 Spherical lenses

The effect that these two kinds of lenses have on the light propagation path is also dependent on the Snell's law, illustrated in Figure 1.3 (reflection is not considered) [15]. This equation represents the light deflection due to the refraction which happens when light encounters an interface between two materials with different indexes of refraction n .

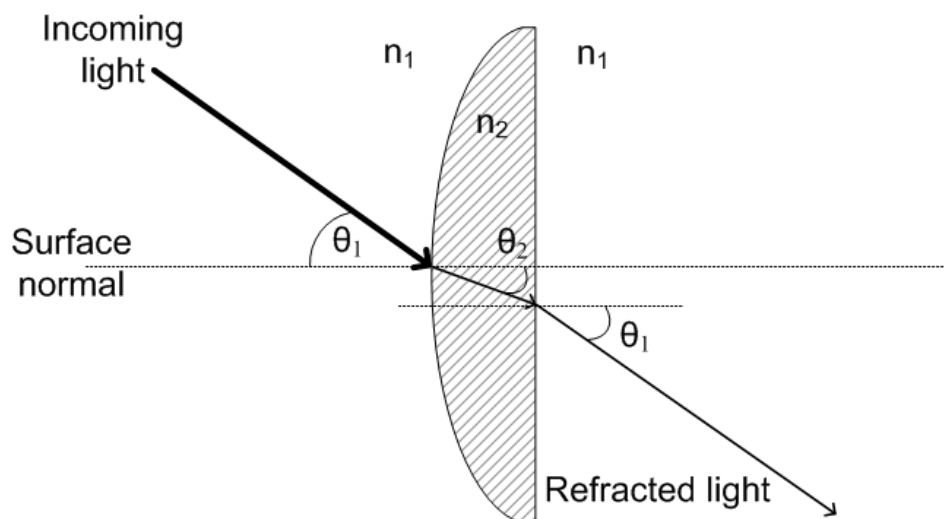


Figure 1.3 – Illustration of the light deflection according to the Snell's law.

$$n_1 \sin \theta_1 = n_2 \sin \theta_2 \quad (1.1)$$

where n_1 and n_2 are the indexes of refraction of two different materials (normally 1 being air and 2 the material of which the lens is made of, *i.e.*, $n_1 < n_2$), θ_1 and θ_2 are the angles

referenced to the surface normal of the incident and refracted (or transmitted) light, respectively.

Figure 1.4 and Figure 1.5 show some of the most important general parameters concerning positive and negative lenses, respectively.

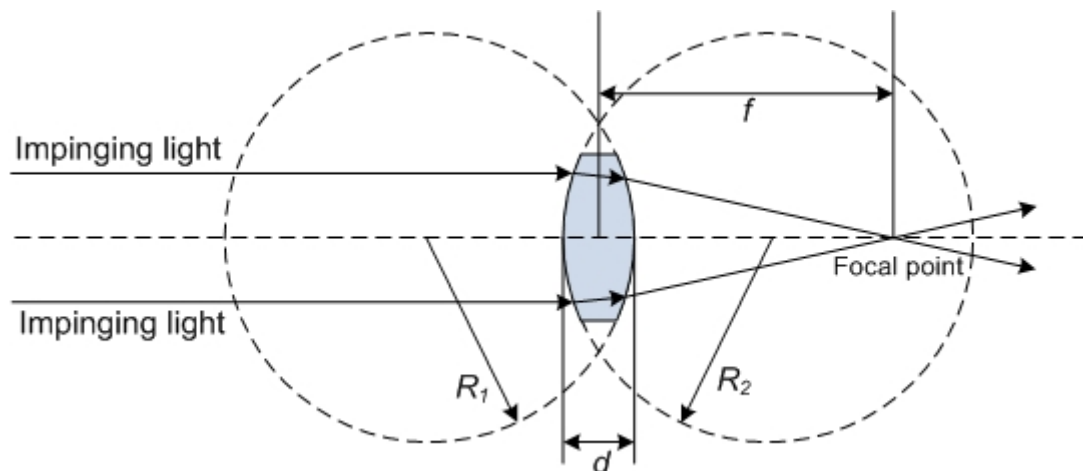


Figure 1.4 – Positive equiconvex converging lens. In converging lenses the center is thicker than the edges meaning that the light converges more as it crosses the material with higher index of refraction than air.

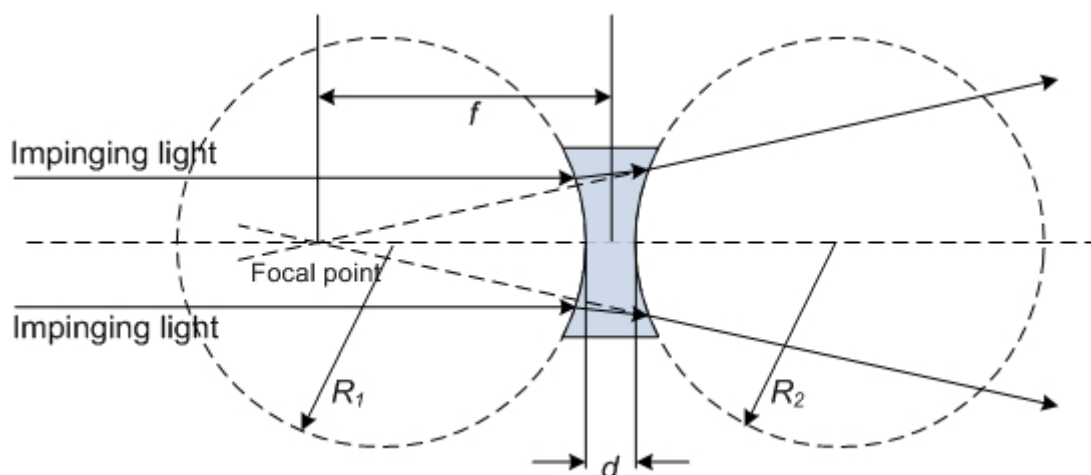


Figure 1.5 – Negative equiconcave diverging lens. In diverging lenses the edges are thicker than the center meaning that the light diverges more as it crosses the material with higher index of refraction than air.

Within the different curvatures that can be attributed to both sides of a lens, in Table 1.1, is represented the main variations in both radii, R_1 and R_2 , presented in the previous pictures [13].

Table 1.1 – Lenses definitions according to their radii variations.

Positive lenses	Negative lenses
Radius $R_1 > 0$ Radius $R_2 > 0$ Positive Meniscus	Radius $R_1 < 0$ Radius $R_2 > 0$ Biconcave
Radius $R_1 > 0$ Radius $R_2 < 0$ Biconvex	Radius $R_1 < 0$ Radius $R_2 < 0$ Negative Meniscus
Radius $R_1 = R_2$ Equiconvex	Radius $R_1 = R_2$ Equiconcave
Radius $R_1 > 0$ Radius $R_2 = \infty$ Plano-convex	Radius $R_1 < 0$ Radius $R_2 = \infty$ Plano-concave

1.2.2 Plano-convex microlenses

Plano-convex MLs were first fabricated in 1988 by Z. Popovic *et al.* [16] and opened a large number of new applications for such optical structures and at the same time reducing the mechanical and electrical complexity of the existing systems. Basically, refractive MLs are used for collimation, focusing or imaging and are an appealing alternative for applications where miniaturization and alignment simplicity are requirements. As illustrated in Figure 1.6, there are two important types of plano-convex microlenses; the spherical and the aspherical. As it can be observed in the figure, the profile of a spheric lens is circular whereas the aspheric lens is not. This means that due to its particular profile, the aspheric lenses are difficult to fabricate with conventional, simple processes [13, 15].

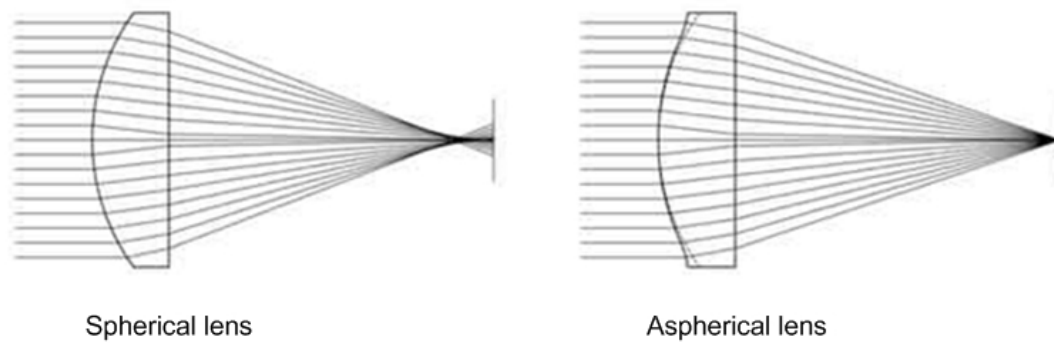


Figure 1.6 – Geometric differences between spherical and aspherical lenses showing the cause of aberration.

The spherical lenses are easier to fabricate than the aspherical ones but present aberration. However, depending on the application, this issue might even be neglected and not have a negative effect on it. Aspheric lenses, unlike their counterparts, are able to focus all the parallel incoming rays of light into the same focal point. This focusing issue can be critical depending on the application.

1.3 State-of-the-art in microlenses

Different techniques and technologies have been applied for the design and fabrication of microlenses. The main objective is to present them rather than to demonstrate all the variances found in the MLs fabrication technologies and materials.

An adaptable and relatively simple method for fabricating different MLs was presented by Y. Hongbin *et al.* [17]. This work shows a way to change the size and focal lengths of MLs by injecting liquid polydimethylsiloxane (PDMS) into the frame. Figure 1.7 shows the fabrication steps, scanning electron microscope (SEM) images of an array and details of a single element of the latter. The PDMS is injected (through a microfluidic network) in such a way that it is possible to control the size of the ML. After filling the cavity and changing the injection pressure thus deforming the cavity membrane, the PDMS is cured thus obtaining the desired profile, shape and size of a solid microlens. This structure presents focal lengths ranging from 1.6 mm to tens of millimeters.

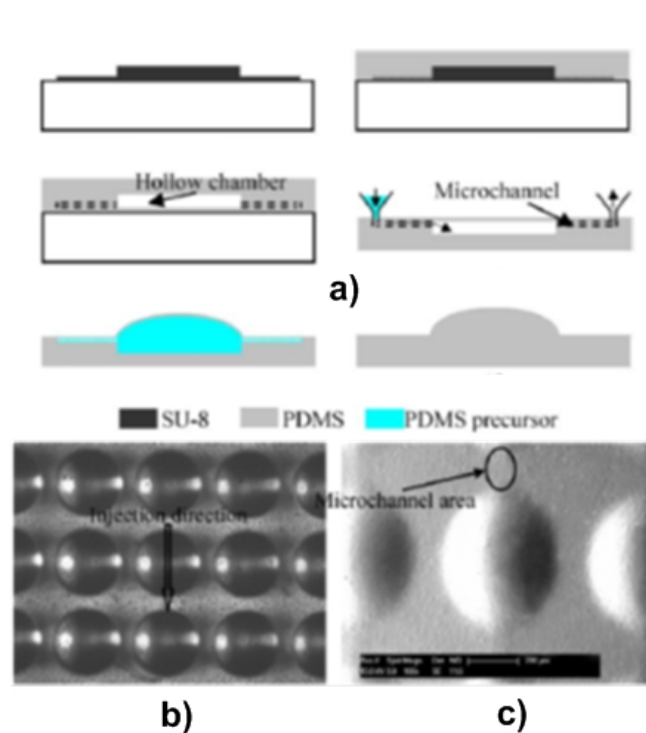


Figure 1.7 – In a) is illustrated the MLs' fabrication process whereas in b) is a SEM image of the fabricated MLs array and in c) a SEM image detailing a single ML [17].

R. Syms [18] demonstrated a new approach in the fabrication of refractive collimating MLs arrays seen in Figure 1.8. When this setup is used the lens mount is formed in the bonded layer of a bonded silicon-on-insulator (SOI) wafer, and rotated out of plane by the surface tension obtained by melting rectangular pads of thick photoresist (PR) bonded. That same photoresist also produces the actual lenses by melting circular pads seen in the following picture. The correct alignment of the mount normal to the substrate is achieved by sequential self-assembly of a supporting silicon frame. The bi-convex spherical lenses (having $f \approx 30 \mu\text{m}$) are arranged in an array of six-elements on an $80 \mu\text{m}$ pitch, and were formed from circular pads of the thick photoresist in dimensions measuring up to $60 \mu\text{m}$ in diameter.

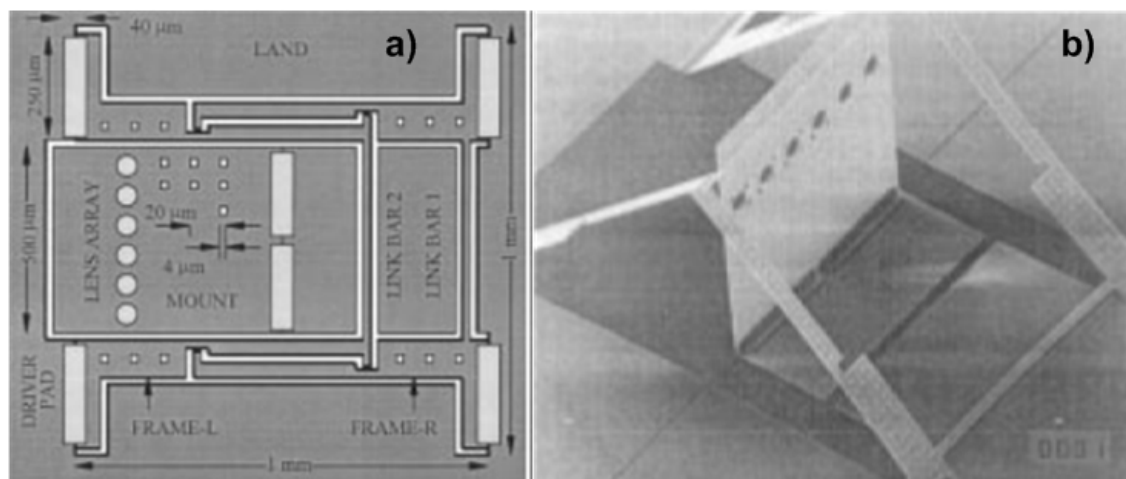


Figure 1.8 – In a) is the overall layout of the surface tension self-assembled microlens array before assembly. In b) is a front view SEM image of the array [18].

Another way to fabricate microlenses was shown by J. Kim *et al.* [19]. In this technique, a direct ink-jet printing of ultra-violet (UV)-curable hybrid polymer is used to fabricate a microlenses array. A pattern of polymer drops is printed on a glass substrate and then cured under UV light. This technique allows the fabrication of periodic arrays of roughly semi-spherical microlenses having a diameter and focal distance of 50 and 48 μm , respectively, seen in Figure 1.9. Moreover, the large numerical aperture (NA) and short focal distance make the ink-jet printing an interesting solution and an alternative to photolithography on applications requiring optical interconnects, pixelated image sensors and large two-dimensional (2D) vertical cavity surface emitting lasers (VCSEL) arrays.

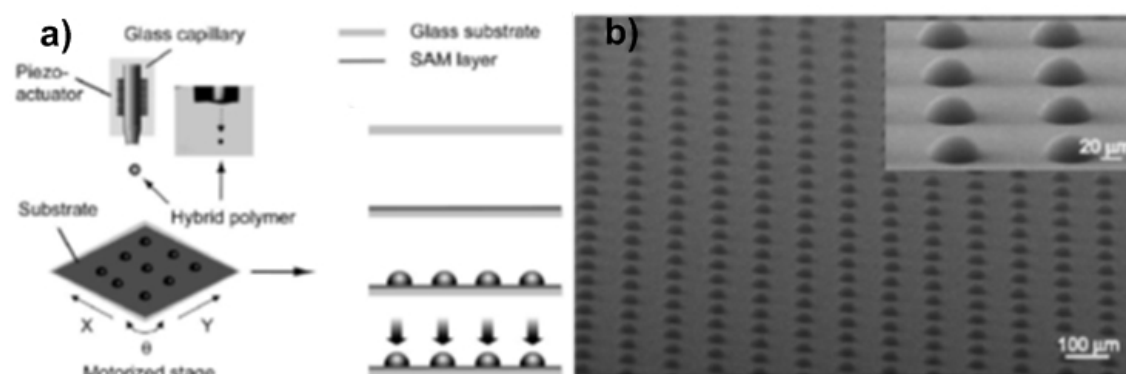


Figure 1.9 – Ink-jet printing fabrication process steps [19] are seen in a). The diameter and height of the microlenses are shown in b) and measure approximately 53 and 18 μm , respectively.

An alternative technique for fabricating MLs arrays is by using a mold [20]. Here, sol-gel glass is used to fabricate the lenses with the help of an SU-8 mold (master) for fabricating the replica in PDMS. In Figure 1.10 are illustrated both the fabrication steps (on the left) and SEM images (on the right) of the material before and after the softening

process. The SU-8 pillars on a silicon wafer produce a replica in a PDMS substrate, making the first mold needed for the fabrication. The replica is then filled with photoresist and the consequent structure obtained is thermally softened turning the upper part of the cylindrical PR into a spherical shape. A new PDMS substrate is then used to build a second, and final mold, where the sol-gel glass gets the lenses shape (measuring $100 \times 100 \mu\text{m}$) after a curing treatment.

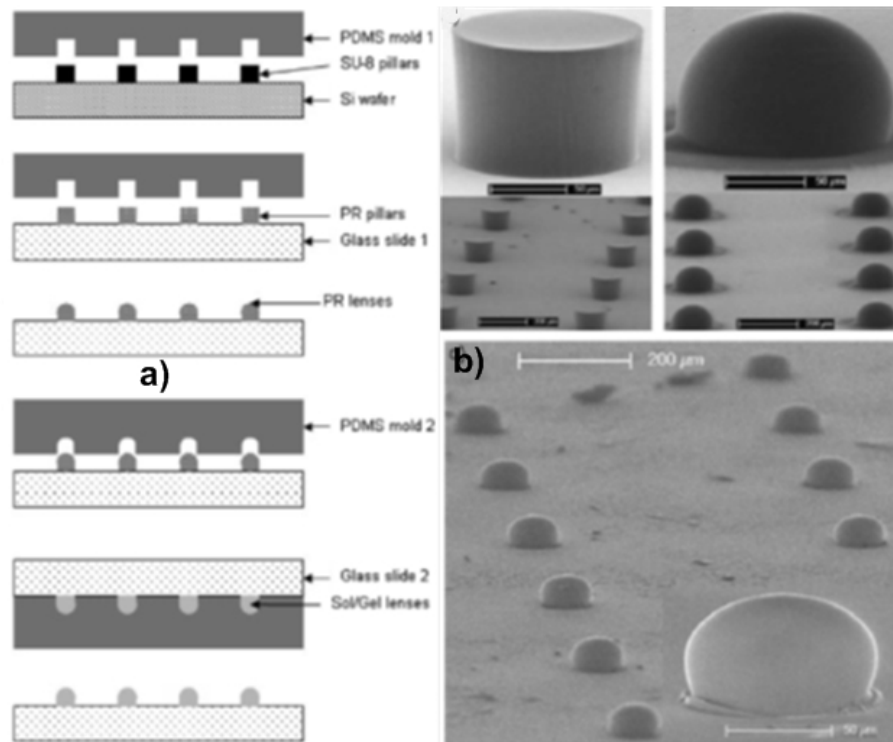


Figure 1.10 – The fabrication steps are seen in a) and SEM images of the structures before and after the softening process are seen in b) [20].

Finally, a technology for fabricating more exotic microlenses was demonstrated in [21] by Casse *et al.* A very short f was achieved in a plano-concave microlens using an indium phosphide (InP) and indium gallium arsenide phosphide (InGaAsP) two-dimensional photonic crystal semiconductor having an index of refraction smaller than one. For a wavelength $\lambda=1500 \text{ nm}$, this microlens' (see Figure 1.11) focal length is in the order of $12 \mu\text{m}$. In this case, the photonic crystal works as an isotropic dielectric medium in which the refraction follows the Snell's law. The air holes were etched in the InP/InGaAsP structure that contains a top 200 nm InP cladding layer, a middle 400 nm InGaAsP layer and a bottom $300 \mu\text{m}$ InP cladding substrate. This refractive negative-index microlens presents an interesting solution for the future optoelectronic devices.

Moreover, even though the radius of the lens is $20\ \mu\text{m}$, its focal point is at $12\ \mu\text{m}$, due to its negative index plano-concave nature.

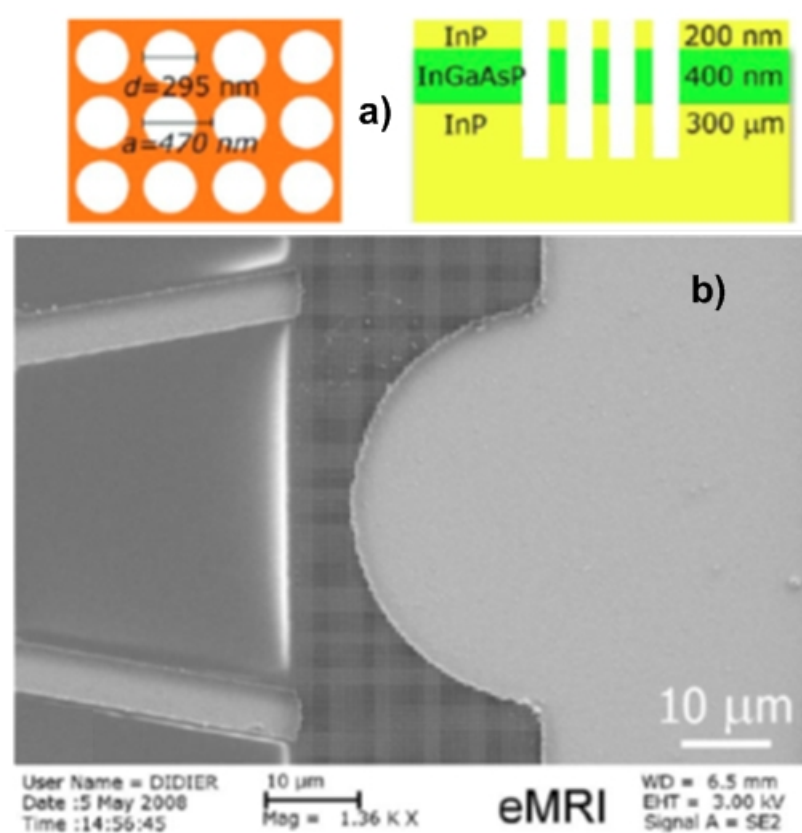


Figure 1.11 – In a) is shown the photonic crystal’s square lattice of air holes and the cross-section of the structure. In b) is a SEM image of the 2D lens. The radius is $20\ \mu\text{m}$ [21].

The interest in light gathering and focusing has several applications in optical devices and end-users electronics as well. All the major companies in the digital cameras market have several products using microlenses for optimizing light acquisition. Below, in Figure 1.12, is one example on how the digital photography industry optimizes the way to collect light for improving the photograph’s image quality. By using more photons from the scene or object being captured, more electron-holes pairs are generated hence improving the sensitivity and, at the same time, obtaining more useful information to be processed digitally. In this particular example, the improvements within the utilization of microlenses on image sensors for compensating the pixel size reduction are illustrated. New low-level architectures demand continuous improvements in light acquisition. This way, the system’s intrinsic losses are reduced for smaller scales than typically done. Photodiodes technology is highly dependent on the optimization of acquiring incident light due to the considerable noise that exists below a given active area. This issue is particularly relevant on images based on complementary metal-oxide semiconductor

(CMOS) technology due to their inherent larger noise when compared with the charge-coupled devices (CCDs) counterparts [22].

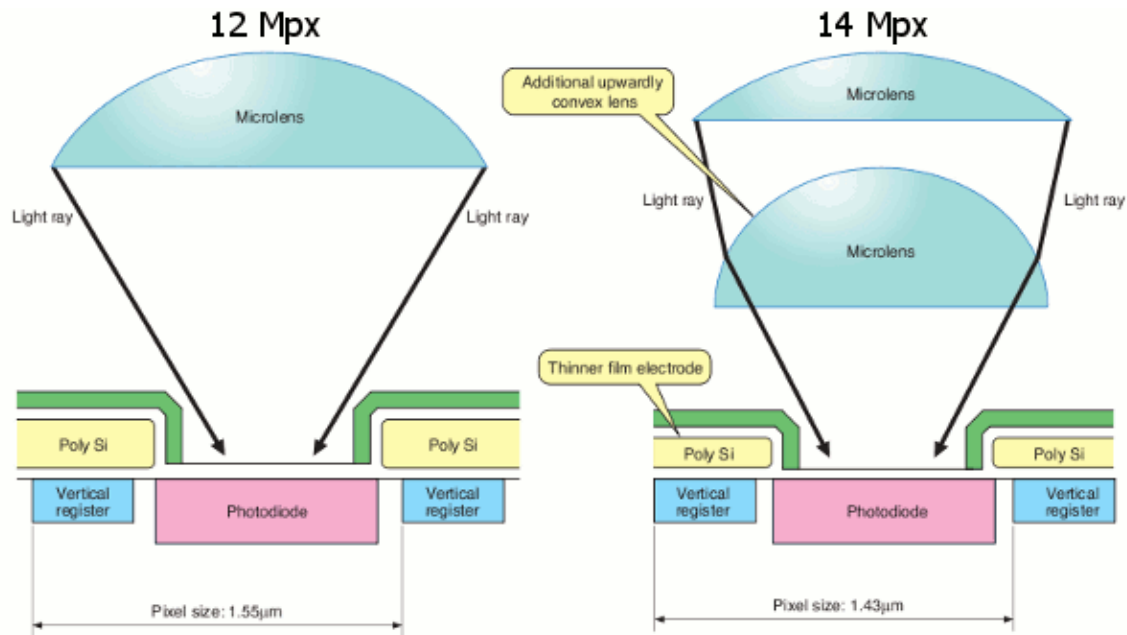


Figure 1.12 – Cross-section of one CCD image sensor with microlens for light acquisition in a digital camera from Sony Corporation [23].

The fabrication techniques and processes have gone through various changes and improvements during the last 20 years. The same can be observed with the materials chosen to fabricate refractive MLs. The two main materials used are glass and polymer-based materials. The current fabrication technologies for the latter include the microjet technique, photoresist reflow, ultraviolet curing, hydrophobic effect, lithographic galvanofarming abformung (LIGA) and the soft replica molding methods [24]. The never stopping improvement in the polymeric based material properties and continuous process technology enhancements justify the focus given to this material for fabricating MLs. There are several techniques used to fabricate MLs and these are summarized in Table 1.2 [24, 25].

Table 1.2 – Summary of the different MLs fabrication techniques and materials used.

Fabrication technique	MLs Material
Ion exchange	Glass
Thermal reflow	Photoresist
Reactive ion etching of thermal reflow lenses	Fused silica
Direct laser writing	Polymer
Deep lithography with protons	Polymethylmethacrylate (PMMA)
Laser ablation	Polycarbonate
Microjet printing	Epoxy polymer
Ultraviolet curing	Polymer
Hydrophobic effect	Polymer
LIGA	PMMA
Soft replica molding	PMMA/SU-8

1.4 Motivation and Objectives

This thesis aims the development of a MLs array fabrication process targeting silicon-based microsystems. The fabrication process has to be compatible with CMOS technology for enjoying all of its imaging advantages while overcoming high optical and electronic crosstalks. Therefore, a process for fabricating arrays of microlenses with high-aspect ratio for enhancing light acquisition was developed. The fabrication is done directly on a substrate with photodetecting capacity for transducing more efficiently photons into photocurrent. In Figure 1.13 and Figure 1.14, respectively, SEM images of the fabricated photoresist array, pre and post thermal reflow, are shown.

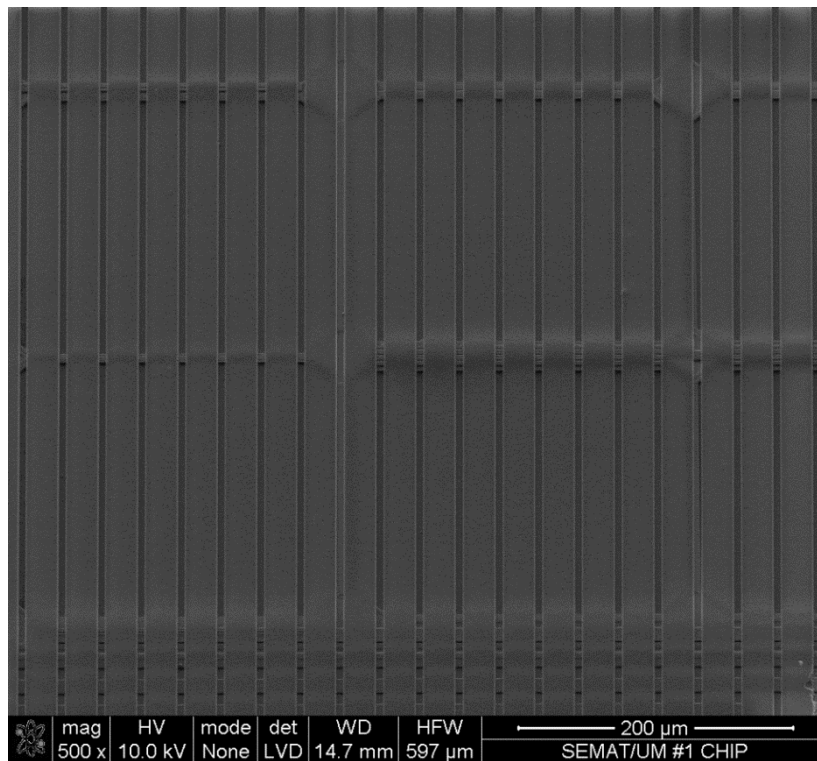


Figure 1.13 – Array of photoresist structures fabricated directly on the photodiodes using classical photolithography before the thermal reflow was applied.

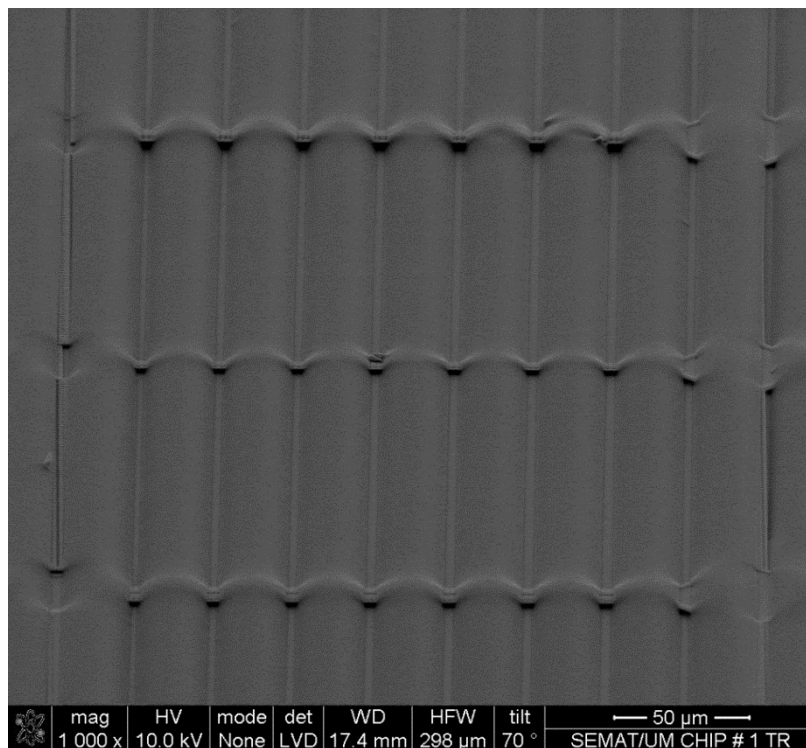


Figure 1.14 – Array of microlenses fabricated directly on the surface of the photodiodes.

This process allows the fabrication of MLs by a reflow process step applied to the photoresist. The reflow process consists in heating the material above its glass transition temperature until it becomes viscous and forms a cylindrical profile due to the surface tension. The purpose is having the fabrication being done directly on top of a photosensor (or on an intermediate substrate) and the main contributions of this microfabrication process are the dimensions, the aspect ratio achieved and the quick reflow time faster than that of the state-of-the-art [26, 27]. A single system architecture that includes the MLs above the sensitive pixels area with CMOS circuits is the final goal. Different approaches were done in the mask design to find out which is the best setup, and number of MLs, on top of photodiodes for maximum light acquisition. The MLs were deposited directly on top of the photodetectors for detecting light at a given range of wavelengths. Moreover, it was also investigated if the microlenses were able to increase the PD's photocurrent generation.

The developed fabrication and integration processes can be seen as a post-processing technique. The main advantage is the compatibility with CMOS technology. The simplicity and reliability achieved in the developed fabrication process (with an accuracy as high as 98%) presented in this thesis include the easy changing of settings, low processing time, its low cost even for small batches and the design changing ability that allows the fabrication of different sized arrays of microlenses.

1.5 Microsystem integration overview

The integration of the MLs developed in this thesis into an optical microsystem for the visible light requires optical filters (OFs) as illustrated in Figure 1.15 for filtering out the unwanted electromagnetic spectrum. The thin-film (TF) deposition of a material in a thin substrate, such as glass or quartz, is a common method to fabricate optical filters.

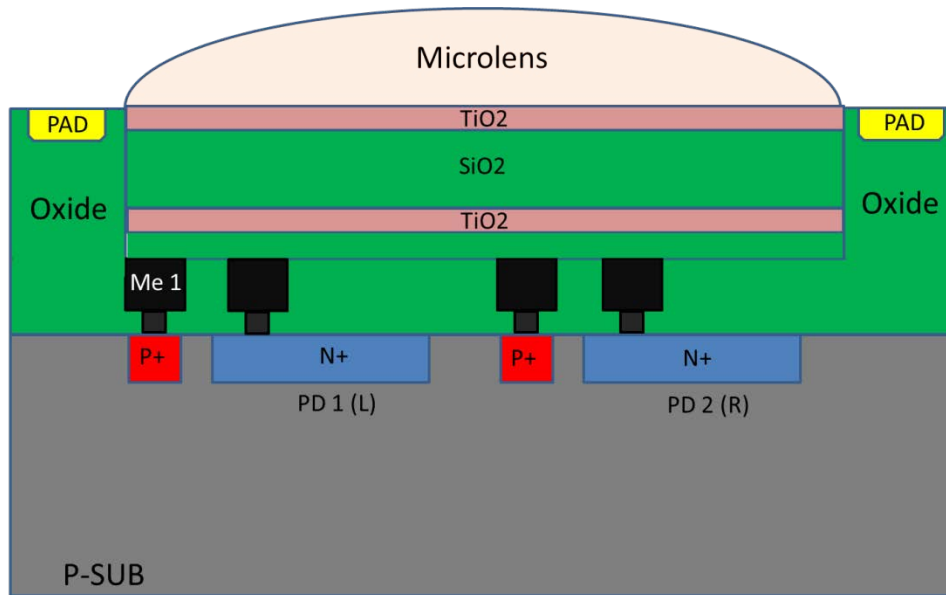


Figure 1.15 – Cross-section illustration of an optical microsystem. On top is the ML for capturing and redirecting the light; in the middle it is represented a three layers dielectric optical filter (TiO_2 and SiO_2) for excluding the non-visible spectrum light and on the bottom is the photodetector.

The fabrication of OFs with a band-pass around a given wavelength is done by successively depositing different dielectric materials (DM) in order to obtain a dielectric multilayer structure able to achieve that characteristic. For each primary color, OFs will be designed to yield a narrow passband around the respective wavelengths. The DMs contained in the OF will be composed of a stack of titanium dioxide (TiO_2) and silicon dioxide (SiO_2) TFs (with refractive indexes $n=2.61$ and $n=1.54$, respectively). SiO_2 is a selected material because the refractive index in the spectral band 480-700 nm is almost constant, *i.e.*, 1.457–1.465. TiO_2 has been selected due to fabrication constraints (the deposition process is well characterized) and silicon compatible. Therefore, the subsequent layers of SiO_2 and TiO_2 will be deposited with the suitable thicknesses. The structures of optical microsystems are assembled together by putting the MLs above the optical filters, which were already fabricated on top of CMOS photodiodes. This integration requires a very precise alignment.

1.6 Organization of the thesis

This chapter introduces the main parameters concerning lenses, what are the main types of lenses and a state-of-the-art about the different techniques and materials used in the design and fabrication of MLs is also presented, as well as the objectives and thesis motivation. Chapter 2 describes the theory associated with the topics concerning lenses

covered during the thesis. Chapter 3 deals with the design and fabrication of the MLs arrays with emphasis given to the learning curve and optimization process of the microfabrication. Chapter 4 presents the results and corresponding discussion focusing on the characterization and measurements done. Finally, conclusions are presented in Chapter 5 as well as some possible improvements and applications for future work.

References

- [1] O. Matoba, E. Tajahuerce and B. Javidi, "Three-dimensional object recognition based on multiple perspectives imaging with microlens arrays," in *LEOS 2001. 14th Annual Meeting of the IEEE Lasers and Electro-Optics Society*, 2001.
- [2] K. Carlson, M. Chidley, K. Sung, M. Descour, A. Gillenwater, M. Follen and R. Richards-Kortum, "In vivo fiber-optic confocal reflectance microscope with an injection-molded plastic miniature objective lens," *Applied Optics*, vol. 44, pp. 1792-1797, 2005.
- [3] C. Nikolas, L. Gang, J. Ki-Hun and L. Luke, "Tunable liquid-filled microlens array integrated with microfluidic network," *Optics Express*, vol. 11, pp. 2370-2378, 2003.
- [4] H. Hamam, "A two-way optical interconnection network using a single mode fiber array," *Optics Communications*, vol. 150, pp. 270-276, 1998.
- [5] S. Van Overmeire, B. Volckaerts, H. Ottevaere, K. Pappaert, G. Desmet and H. Thienpont, "Simulation, fabrication and characterization of microlens oriented fluorescence detection systems for DNA microarrays," in *Proceedings Symposium IEEE/LEOS Benelux Chapter*, Mons, 2005.
- [6] http://fr.wikipedia.org/wiki/Fichier:Optics_from_Roger_Bacon%27s_De_multiplicatone_specierum.jpg. [Accessed 3 February 2013].
- [7] <http://www.superstock.com/stock-photos-images/1895-17920>. [Accessed 3 February 2013].

- [8] <http://rendan.tumblr.com/post/863646102/ibn-al-haytham-fragment-of-a-page-from-the-book>. [Accessed 3 February 2013].
- [9] G. Molesini, "Early advances on rays and refraction: a review through selected illustrations," *Optical Engineering*, vol. 50, no. 12, pp. 121704-1 121704-6, December 2011.
- [10] http://archives.microbeworld.org/microbes/tools_microscopes.aspx. [Accessed 3 February 2013].
- [11] <http://www.studenthandouts.com/01-Web-Pages/01-Picture-Pages/10.01-Scientific-Revolution/Galileo-Galilei/Galileo-Galilei-Showing-the-Doge-of-Venice-How-to-Use-the-Telescope-Giuseppe-Bertini-1858.htm>. [Accessed 3 February 2013].
- [12] Max Born and Emil Wolf, *Principles of optics: Electromagnetic theory of propagation, interference and diffraction of light*, 7th ed., Cambridge: Cambridge University Press, 2002.
- [13] Eugene Hecht, *Optics*, 4th ed., Addison-Wesley, 2002.
- [14] <http://hubblesite.org/newscenter/archive/releases/2002/10>.
- [15] Ian R. Kenyon, *the Light Fantastic: A Modern Introduction to Classical and Quantum Optics*, 2nd ed., Oxford: Oxford University Press, 2011.
- [16] Z. Popovic, R. Sprague and G. Connell, "Technique for monolithic fabrication of microlens arrays," *Applied Optics*, vol. 27, no. 7, pp. 1281-1284, 1998.
- [17] Y. Hongbin, Z. Guangya, C. Siong and L. Feiwen, "Simple Method for Fabricating Solid Microlenses With Different Focal Lengths," *IEEE Photonics Technology Letters*, vol. 20, no. 19, pp. 1624-1626, 1 October 2008.
- [18] R. Syms, "Refractive Collimating Microlens Arrays by Surface Tension Self-Assembly," *IEEE Photonics Technology Letters*, vol. 12, no. 11, pp. 1507-1509, November 2000.
- [19] J. Kim, N. Brauer, V. Fakhfour, D. Boiko, E. Charbon, G. Grutzner and J. Brugger,

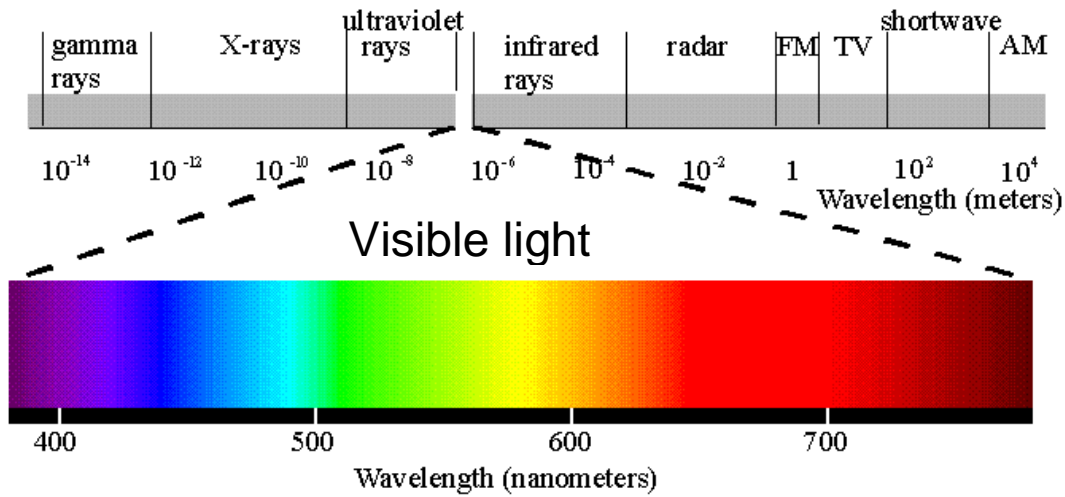
- "Hybrid polymer microlens arrays with high numerical apertures fabricated using simple ink-jet printing technique," *Optical Materials Express*, vol. 1, no. 2, pp. 259-269, 1 June 2011.
- [20] J. Orhan, V. Parashar, A. Sayah and M. Gijs, "Fabrication and Characterization of Three-Dimensional Microlens Arrays in Sol-Gel Glass," *Journal of Microelectromechanical Systems*, vol. 15, no. 5, pp. 1159-1164, October 2006.
- [21] B. Casse, W. Lu, Y. Huang and S. Sridharb, "Nano-optical microlens with ultrashort focal length using negative refraction," *Applied Physics Letters*, vol. 93, no. 5, pp. 053111-053111-3, 7 August 2008.
- [22] Jun Ohta, *Smart CMOS Image Sensors and Applications*, 1st ed., San Francisco: Taylor & Francis, 2008.
- [23] "Sony Corporation," Semiconductor & Component, http://www.sony.net/Products/SC-HP/cx_news/vol60/np_icx681sqw.html. [Accessed 12 February 2013].
- [24] J. Ho, T. Shih, J. Cheng, C. Sung and C. Chen, "A novel method for fabrication of self-aligned double microlens arrays," *Sensors and Actuators A: Physical*, vol. 135, no. 2, p. 465–471, 2007.
- [25] H. Ottevaere, R. Cox, H. Herzig, T. Miyashita, K. Naessens, M. Taghizadeh, R. Völkel, H. Woo and H. Thienpont, "Comparing glass and plastic refractive microlenses fabricated with different technologies," *Journal of Optics A: Pure and Applied Optics*, vol. 8, no. 7, pp. 407-429, 2006.
- [26] V. Lin, H. Wei, H. Hsieh, J. Hsieh and G. Su, "Design and fabrication of long-focal-length microlens arrays for Shack–Hartmann wavefront sensors," *Micro & Nano Letters*, vol. 6, no. 7, p. 523–526, 2011.
- [27] M. Wei, I. Su, M. Jung and K. Huang, "Real-time Observation for the Formation of Microlens Arrays Fabricated Using Thermal Reflow Process," *Tamkang Journal of Science and Engineering*, vol. 7, no. 2, pp. 81-86, 2004.

2 Light and lenses theory

This chapter presents what light conceptually is and how it propagates throughout space. Light is composed of massless particles called photons that exhibit the behavior of both waves and particles. The way light is guided for obtaining the desired result is explained using the lenses' theory and respective optical phenomena, such as reflection and refraction. The attention here is given to spherical lenses, more specifically on plano-convex ones, since this thesis deals with their fabrication process using photolithography and thermal reflow as demonstrated in Chapter 3. Moreover, the purposes of using microlenses are for maximizing the concentration of light in a point in space and converging light that would impinge outside a given photosensitive area.

2.1 Light

Light is an electromagnetic (EM) phenomenon described by the theoretical laws that explain all EM radiation [1]. The full EM radiation range (called electromagnetic spectrum) is illustrated on top of Figure 2.1 from the shortest to the longest wavelengths. From the shortest wavelength to the longest, the spectrum starts with gamma rays and ends with the radio waves. The small part of the EM spectrum addressed in this thesis is the visible light which corresponds to the wavelengths roughly between 380–780 nm [2-4]. In the table of Figure 2.1, colors are differentiated by their wavelength interval. Light is composed by particles called photons that travel in EM waves and carry energy. This energy is related to the wave's frequency meaning that high-frequencies carry more energy.



Color	Wavelengths (nm)
Violet	380–455
Blue	455–492
Green	492–577
Yellow	577–597
Orange	597–622
Red	622–780

Figure 2.1 – Representation of the full electromagnetic spectrum and the approximate wavelength intervals in vacuum for different colors.

2.1.1 Photons

In the sequence of what was previously described in the introduction, the radiated light is considered to be energy and each one of the particles that compose light is called a photon. Photons have the particularity of possessing momentum and energy but no mass, in what is called wave-particle duality. This means that photons behave as both particles and as waves (transverse waves) [3-5]. The relation between the energy E of the photon and its EM wave frequency f , is expressed as the Planck Relation [2], seen in equation (2.1).

$$E = hf \quad (2.1)$$

where h is the Planck's constant ($\approx 4.1356 \times 10^{-15}$ eV.s). The energy of a photon might also be represented as a function of a wavelength λ as demonstrated in the following equation:

$$E = \frac{hc}{\lambda} \quad (2.2)$$

where c is the speed of light ($\approx 300 \times 10^6$ m.s⁻¹). Because the photon's direction of propagation (at speed of light c), and mass m , is the same as the momentum's vector \vec{p} , its magnitude can be demonstrated as follows:

$$p = mv = \frac{E}{c^2}c = \frac{E}{c} = \frac{h}{\lambda} \quad (2.3)$$

2.1.2 Maxwell equations

The wave theory of light was demonstrated by Maxwell in what became the foundations of electromagnetic phenomena and from where the EM waves may be derived. These equations translate the relations that exist between the electric and magnetic fields. These relations are based first on charges and electric currents. Secondly, are based on how a variant magnetic field induces an electric field and *vice-versa*. There are four Maxwell equations that cover the laws of classical electrodynamics [6]. With the proper adaptation to the study of optics, including a non-conducting and free of charge medium, the Maxwell equations, in vectorial form¹, are:

¹

$$\mathbf{E} = (E_x, E_y, E_z) = E_x \hat{i} + E_y \hat{j} + E_z \hat{k}$$

$$\mathbf{B} = (B_x, B_y, B_z) = B_x \hat{i} + B_y \hat{j} + B_z \hat{k}$$

$$\nabla = \left(\frac{\partial}{\partial x}, \frac{\partial}{\partial y}, \frac{\partial}{\partial z} \right)$$

$X = \nabla \cdot \mathbf{A} = \text{div}(\mathbf{A}) \rightarrow \mathbf{A}$ is vector and X is scalar

$\mathbf{X} = \nabla A = \text{grad}(A) \rightarrow A$ is scalar and \mathbf{X} is vector

$\mathbf{X} = \nabla \times \mathbf{A} = \text{curl}(\mathbf{A}) \rightarrow \mathbf{A}$ and \mathbf{X} are vectors

$$\begin{aligned} \nabla|\mathbf{E} = 0 \\ \text{with} \\ \nabla|\mathbf{E} = \frac{\partial E_x}{\partial x} + \frac{\partial E_y}{\partial y} + \frac{\partial E_z}{\partial z} \end{aligned} \tag{2.4}$$

$$\nabla|\mathbf{B} = 0 \tag{2.5}$$

$$\begin{aligned} \nabla \times \mathbf{E} = -\frac{\partial \mathbf{B}}{\partial t} \\ \text{with} \\ \nabla \times \mathbf{E} = \begin{vmatrix} \hat{i} & \hat{j} & \hat{k} \\ \frac{\partial}{\partial x} & \frac{\partial}{\partial y} & \frac{\partial}{\partial z} \\ E_x & E_y & E_z \end{vmatrix} \end{aligned} \tag{2.6}$$

$$\nabla \times \mathbf{B} = \varepsilon_r \varepsilon_0 \mu_r \mu_0 \frac{\partial \mathbf{E}}{\partial t} \tag{2.7}$$

The physical quantities ε_r and μ_r are the relative permittivity (also known as the dielectric constant) and the relative permeability of the medium, respectively. So, the electric permittivity is:

$$\varepsilon = \varepsilon_r \varepsilon_0 \tag{2.8}$$

and the magnetic permeability is:

$$\mu = \mu_r \mu_0 \tag{2.9}$$

where ε_0 and μ_0 are the electric permittivity and magnetic permeability in free-space, respectively.

2.1.3 Transverse waves

As previously stated, EM radiation is a transverse wave, *i.e.*, is a vector measure pointing transverse to the direction of propagation. This type of waves consists on the periodic oscillations that occur perpendicularly to the direction of the energy transfer, *i.e.*, the electric and magnetic fields, \mathbf{E} and \mathbf{B} , respectively. These are the two variables in an EM wave and both are vectorial quantities, which are represented in Figure 2.2 as a transverse wave. The distance between two successive identical points in time, is the wavelength λ . Since this wave is periodic, the wavelength also gives the wave's period τ . The frequency f of the wave is then the number of periodic repetitions per time unit being equal to:

$$f = \frac{1}{\tau} \quad (2.10)$$

Hence, the wave velocity (or phase velocity) is given by:

$$v = f\lambda \quad (2.11)$$

The fields E_y and B_z diverge only by a scalar and have the same time-dependence, so \mathbf{E} and \mathbf{B} are always in-phase. Additionally, $\mathbf{E} = E_y(x,t)\hat{j}$ and $\mathbf{B} = B_z(x,t)\hat{k}$ are mutually perpendicular and their cross-product $\mathbf{E} \times \mathbf{B}$ points in the direction of the x -axis, as seen in the following figure.

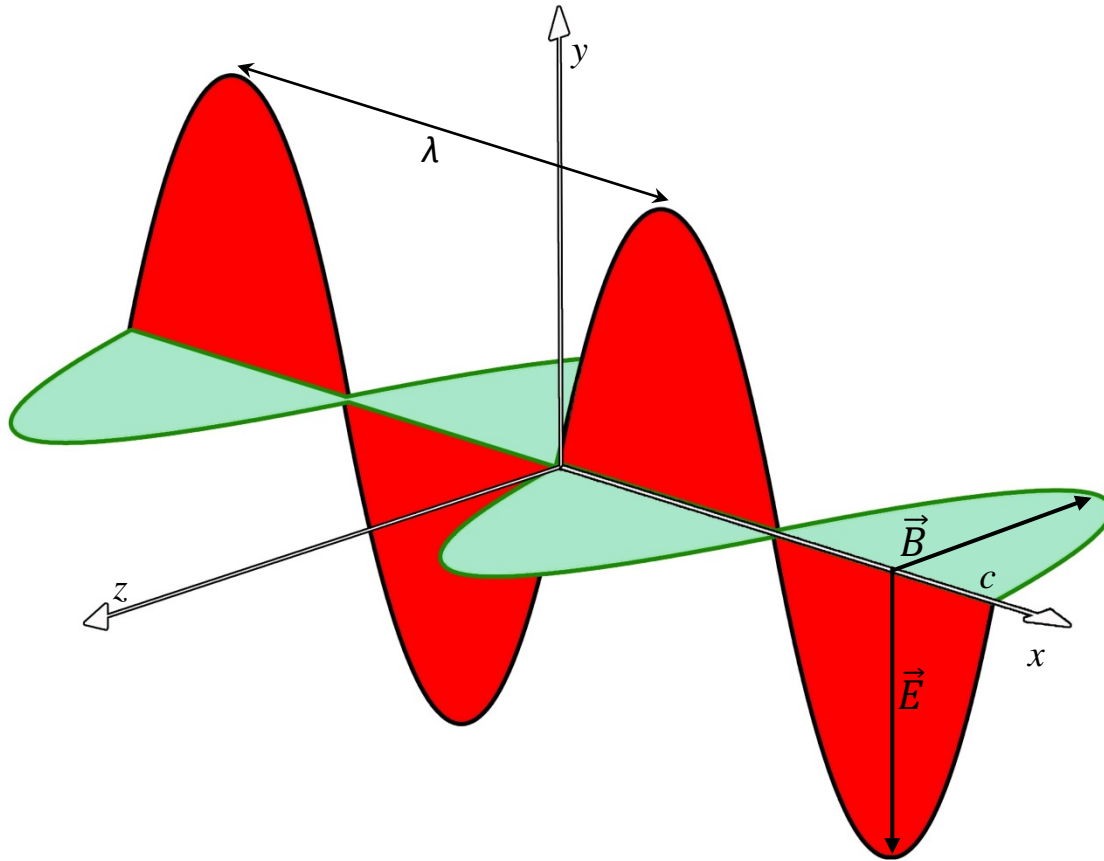


Figure 2.2 – A plane, linearly polarized EM, wave propagating along the x -axis at light speed c . The electric and magnetic fields are mutually perpendicular and are in-phase. The wave propagates in the direction $E \times B$.

Both the electric and magnetic fields are transverse to the direction of propagation and mutually perpendicular. For the case of a plane wave propagating in vacuum, their magnitudes are related to the speed of light c [7]:

$$E = cB \quad (2.12)$$

As the magnitudes E and B have a fixed proportion between them only one of them was represented. Even though these explanations are for free-space propagation, it should be noted that when light is travelling through matter it slows down due to the material's density. The wave impedance Z , in free-space $Z_0 \approx 120\pi \Omega$, is a complex quantity and is given by:

$$Z = \mu \frac{E_y}{B_z} = \sqrt{\frac{\mu}{\epsilon}} \quad (2.13)$$

In a generic dielectric material, the propagation speed v_p is smaller than c and is impedance dependent:

$$v_p = c \frac{Z_o}{Z} \quad (2.14)$$

The impedance's relation is the index of refraction n :

$$n = \frac{Z}{Z_o} = \frac{c}{v_p} \geq 1 \quad (2.15)$$

In the transverse wave, represented in the previous figure, the propagation is being done, at light speed c , along the direction x -axis. So, the two variables, \mathbf{E} and \mathbf{B} , are vectors that may be situated in any direction along the orthogonal plane y, z . According to the first Maxwell's equation it is possible to calculate the intensity of the electric field \mathbf{E} , which is a function of only x and time t . Since \mathbf{E} is independent from y and z , then:

$$\nabla \cdot \mathbf{E} = \frac{\partial E_x}{\partial x} = 0 \quad (2.16)$$

Nonetheless, since E_x is not zero, this means that it is constant at any point in time, which is not correct, so the \mathbf{E} field is said to be exclusively transverse. In order to fully characterize the wave, it is necessary to specify a moment-by-moment direction of \mathbf{E} and this approach deals with the polarization of light. Because each vector remains in a plane as the wave propagates, this wave is said to be linearly polarized [3].

2.1.4 Polarization

The electric field \mathbf{E} was conventionally selected as the referential variable for the purpose of EM waves' polarization. Polarization can be described as the analysis of the vector \mathbf{E} in the plane y, z . In this context, the polarization plane is the one where the light is travelling in (x -axis) and that contains the vector \mathbf{E} . In the presented example, since the \mathbf{E} always stays on the same axis, then the wave is linearly or plane polarized [7]. In Cartesian coordinates, the vector of the electric field is:

$$\mathbf{E} = E_x \hat{i} + E_y \hat{j} + E_z \hat{k} \quad (2.17)$$

where \hat{i} , \hat{j} and \hat{k} are unit vectors in the x , y and z directions, respectively. So, the plane wave $E_y\hat{j}$, in the example shown in Figure 2.2 is:

$$\frac{\partial^2 E_y}{\partial x^2} = \frac{1}{v_p^2} \frac{\partial^2 E_y}{\partial t^2} \quad (2.18)$$

Considering the Helmholtz equation:

$$\nabla^2 E_y + \beta^2 E_y = 0 \quad (2.19)$$

with the wavenumber β being,

$$\beta = \frac{2\pi}{\lambda_g} = n \frac{2\pi}{\lambda_0} \quad (2.20)$$

where λ_g and λ_0 are the wavelengths in the medium and in free-space, respectively. Therefore, for any EM wave in the same propagation conditions, the general solution for the plane wave in Figure 2.2 is:

$$E_y(x, t) = E_0 f(x - ct) \quad (2.21)$$

2.2 Optical surfaces

In the context of this thesis, light is considered as coming from a source in an isotropic homogeneous medium that travels rectilinearly until encountering a surface of a different medium and index of refraction. The interaction between light and a surface will be explained in terms of reflection and scattering, absorption and refraction. Absorption and scattering are considered negligible concerning the actual transmission of light across a solid (in the case of this thesis a microlens), even though they always occur in optical transmission [2]. The general interactions between light and a surface are illustrated in Figure 2.3.

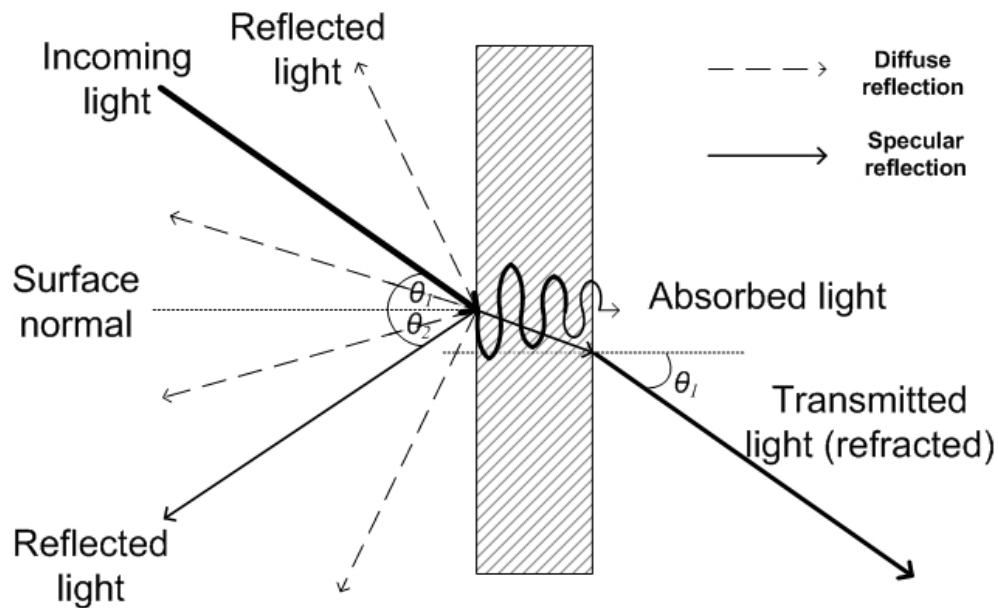


Figure 2.3 – General perspective of a single wavelength projected into a plane surface with the resulting interactions: reflection, transmission (with refraction) and absorption. It must be noted that the angles θ_1 and θ_2 are the same in specular reflection.

2.2.1 Reflection and scattering

In polished surfaces, almost all the light is reflected back in directions that depend, not only on the angle of incidence of light, but also on the geometry of the surface. This type of reflection is called specular and is highly dependent on the polish treatment quality. The reflected angles are demonstrated using the Fresnel's equations, *i.e.*, the angle of incidence equals the angle of reflection, as shown in Figure 2.3.

$$\theta_1 = \theta_2 \quad (2.22)$$

where θ_1 and θ_2 are the angles of incidence and reflection, respectively.

In an unpolished surface, there are many irregularities, *i.e.*, the surface roughness is obviously noticed. The result is that light, in a plane surface, will not reflect back, in a single beam, with the same angle as it came in. This produces many small beams scattering away in a way dependent on the roughness of the impinging point. This is called diffuse reflection. For example, if the surface's roughness dimension is greater than the wavelength being reflected, the diffuse reflection is considerably increased. The portion of light reflected back depends greatly on the material where it is reflecting from [2].

2.2.2 Absorption

When light is reflected off a surface, a portion of it is absorbed. As previously mentioned, the material of the surface and its thickness are what determine the absorption ratio of a given surface. A good example of the effects of EM radiation absorption in a material is the correspondent temperature increase of it. A material is considered opaque when light is not capable of going through it. The opposite of opaque is a material called transparent. For instance, when light impinges on a red opaque object, the wavelengths directly related to that color are reflected hence revealing its color and the remaining wavelengths are absorbed. In a more detailed example, paint is essentially made of three components: binders, pigments (responsible for the color) and solvents. From these components of paint, attention will only be given to the one that defines colors by selectively absorbing the visible wavelengths. Pigments are mainly composed by groups of aromatic rings linked by chromophores (may be azo compounds, carbonyl groups, basic, *etc.* [8]) and are created for absorbing specific wavelengths. The mechanism responsible for providing a color to a pigment is the combination of two molecular components: the chromophores and the auxochromes [8, 9]. Chromophores are the part of the molecule that gives the necessary conjunction to obtain colors. The auxochromes are a group of atoms linked to the chromophores that complement the action of the latter by performing the necessary changes, within the system's total energy, resulting in the final color [10]. An example in basic dye (where chromophores have thiazine group), is seen in Figure 2.4 [11]. Therefore, when a chemical compound absorbs within a specific spectrum, it means that it will display the complementary color.

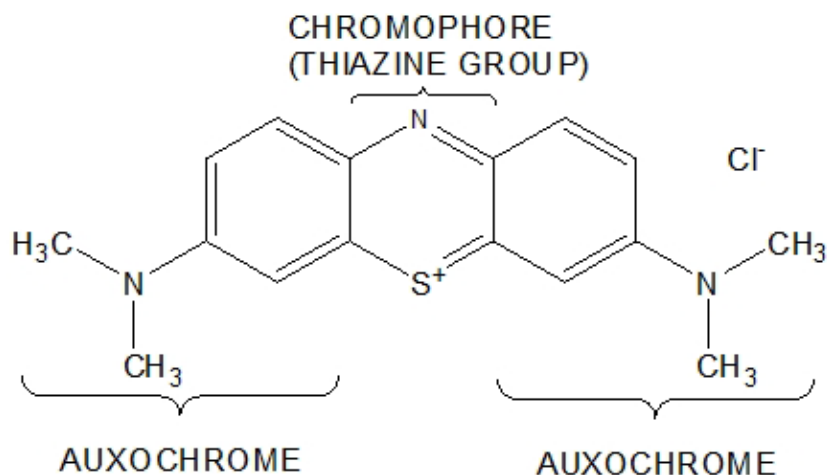


Figure 2.4 - Example of the presence of chromophores and auxochromes in basic blue 9.

2.2.3 Refraction

When light enters a medium with higher index of refraction than air, it changes direction, as depicted in Figure 2.5. This change in direction is commonly described by the Snell's law:

$$n_1 \sin \theta_1 = n_2 \sin \theta_2 \quad (2.23)$$

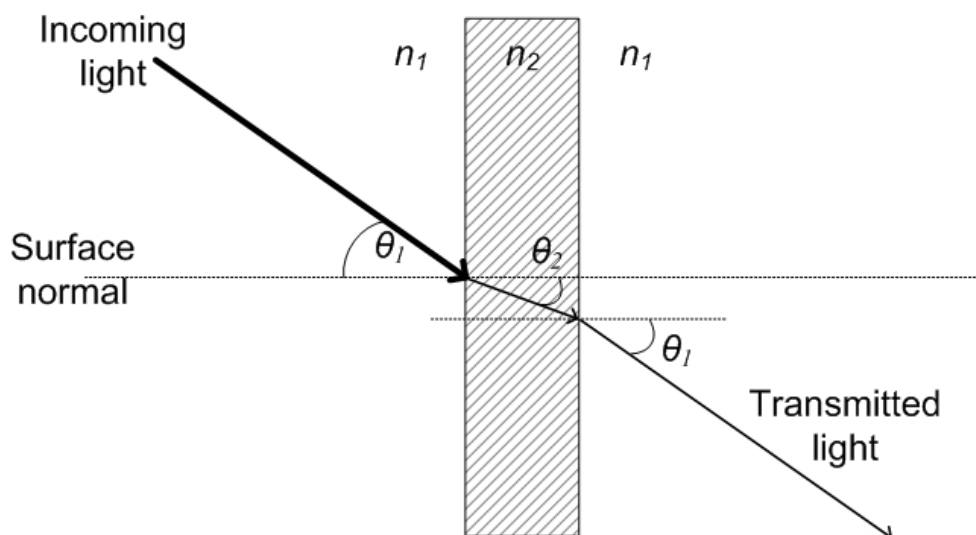


Figure 2.5 – Illustration of the light deflection according to the Snell's law.

This change in direction is caused by the variation of the speed of light when travelling in mediums with different refractive indexes, as shown in equation 2.15. In that equation is presented the absolute index of refraction because the speed of light in free-space, c , is the reference. When dealing with the speed of light in different mediums, it is called relative index of refraction. The reason for using lenses in all their different purposes is basically due to both this light changing speed and refraction capability characteristics. Moreover, normally, the index of refraction of any given material changes with different wavelength values, exemplified by the Newton's prism and known as dispersion. For both reflection and refraction the principle of reversibility of the optical path is applied and the frequency of the wavelength remains the same [2, 3].

2.3 Refraction in spherical surfaces

As introduced in Chapter 1, lenses with spherical surfaces are the ones of interest in the context of this thesis, more specifically, plano-convex lenses. Nevertheless, a plano-convex lens is a particular case of general spherical lenses. The cross-section of a spherical lens is a circular segment, as illustrated in Figure 2.6, where the most relevant parameters are represented.

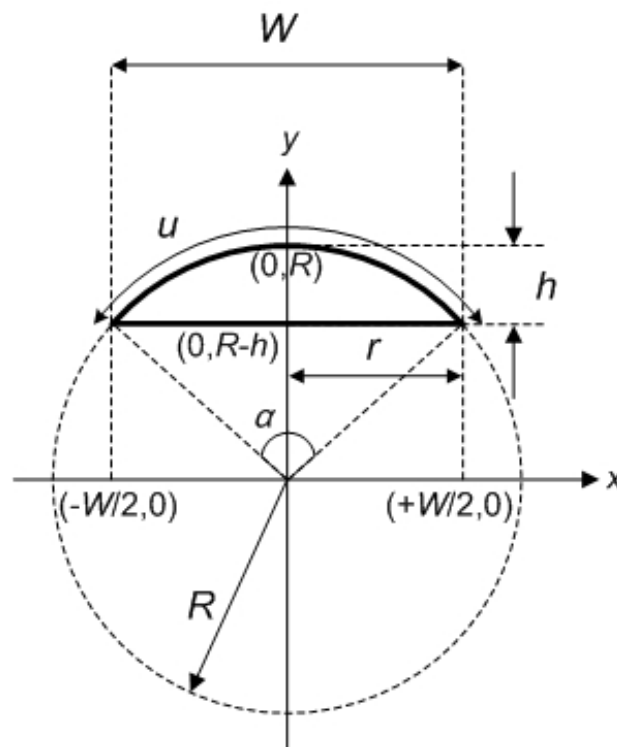


Figure 2.6 – Representation of the most relevant parameters of plano-convex spherical lenses.

The equations that represent these parameters are:

$$R = \frac{r^2 + h^2}{2h} \quad (2.24)$$

$$h = R - \sqrt{R^2 - \frac{W^2}{4}} \quad (2.25)$$

According to the Pythagorean theorem:

$$W = 2\sqrt{2Rh - h^2} \quad (2.26)$$

The length of the undulation (arc length), u , of the lens is:

$$u = \frac{\alpha}{360} 2\pi R \quad (2.27)$$

The angle α , in degrees, that defines the area of the circular sector is:

$$\alpha = 2 \operatorname{arc} \sin \left(\frac{W}{2R} \right) \quad (2.28)$$

The area of the lens is the area of the circular sector minus the area of the triangle going from the coordinates origin to the interface W of the circular segment and is given by:

$$A = \frac{\alpha \pi R^2}{360} - \frac{W(R - h)}{2} \quad (2.29)$$

In a spherical surface, in order to determine the refracting power (bending power or even optical power), consider the example presented in Figure 2.7. How much a ray is refracted into the optical axis (Δx) in a spherical lens depends mostly on its radius R and the location Δy in the arc where the light meets the surface, in this case point F . For

facilitating calculus, and because it is considered a very good estimation, the paraxial approximation is usually done in these cases [2-5]. In the paraxial approximation it is considered that, for an angle δ , both the $\sin(\delta)$ and the $\tan(\delta)$ are assumed $\approx \delta$.

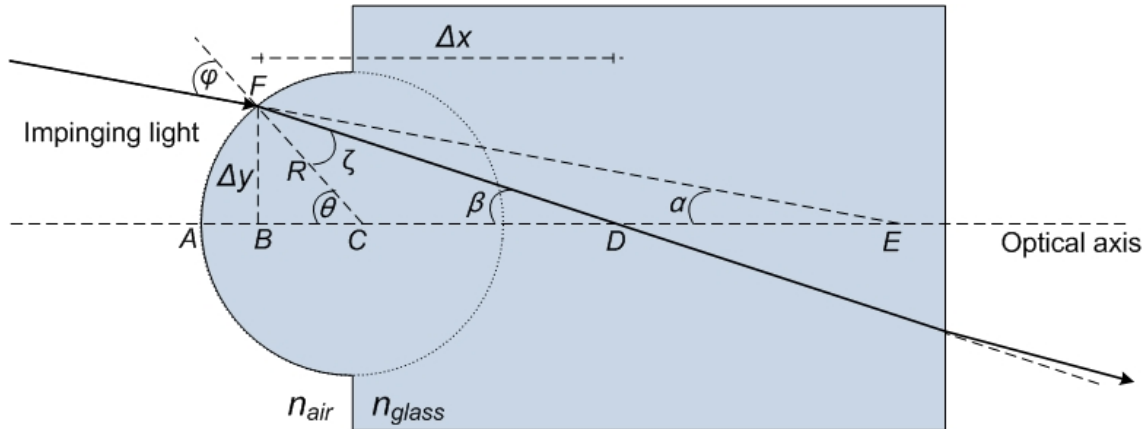


Figure 2.7 – Refraction caused by a spherical surface.

So, for a paraxial approximation applied in this example, the Snell's law becomes:

$$n_{air}\varphi = n_{glass}\zeta \quad (2.30)$$

Now,

$$\alpha = \frac{\Delta y}{AE} \quad (2.31)$$

$$\beta = \frac{\Delta y}{AD} \quad (2.32)$$

$$\theta = \frac{\Delta y}{AC} \quad (2.33)$$

$$\varphi = \theta - \alpha \quad (2.34)$$

$$\zeta = \theta - \beta \quad (2.35)$$

Substituting the angles φ and ζ in equation 2.30:

$$n_{air}(\theta - \alpha) = n_{glass}(\theta - \beta) \quad (2.36)$$

The following equation is obtained:

$$\frac{n_{glass} - n_{air}}{R} = \frac{n_{glass}}{AD} - \frac{n_{air}}{AE} \quad (2.37)$$

So, the measure bending of light (how much light refracts towards the optical axis), or refracting power P , is:

$$P = \frac{n_{glass} - n_{air}}{R} \quad (2.38)$$

If one uses the same assumptions made for equations 2.30–2.38, then, for a generic spherical biconvex lens (one side has radius R_1 and the opposite side has radius R_2), the power P_1 of refraction in the side with radius R_1 is given as follows:

$$P_1 = \frac{n_{glass} - n_{air}}{R_1} \quad (2.39)$$

Analogously, on the side with radius R_2 , the optical power P_2 is:

$$P_2 = \frac{n_{air} - n_{glass}}{R_2} \quad (2.40)$$

The total optical power P_T is the sum of the previous two:

$$P_T = \frac{n_{glass} - n_{air}}{R_1} + \frac{n_{air} - n_{glass}}{R_2} \quad (2.41)$$

By definition, the total optical power is:

$$P_T \equiv \frac{1}{f} \quad (2.42)$$

Therefore, the focal length f , for a glass plano-convex (radius $R_2=\infty$) thin lens in air is:

$$f = \frac{R}{n_{glass} - 1} \quad (2.43)$$

2.3.1 Spherical and chromatic aberration

The spherical aberration is an optical non-ideality resulting from the lens' spherical shape. In the following example, illustrated in Figure 2.8, it is possible to understand the influence that a spherical lens (made of glass, with $n_{glass} > n_{air}$) has on light rays. The ray that coincides with the optical axis propagates along a straight line (being perpendicular to the surface's normal in its contact point thus not being refracted). All the other rays refract towards the axis with the most peripheral ones being more refracted than the ones closer to the axis. This point in the optical axis where light converges to is called the focal point f . In the case of plano-convex lenses with spherical aberration, the focal point is considered to be where the spread of the rays is minimum, also known as the circle of least confusion [3].

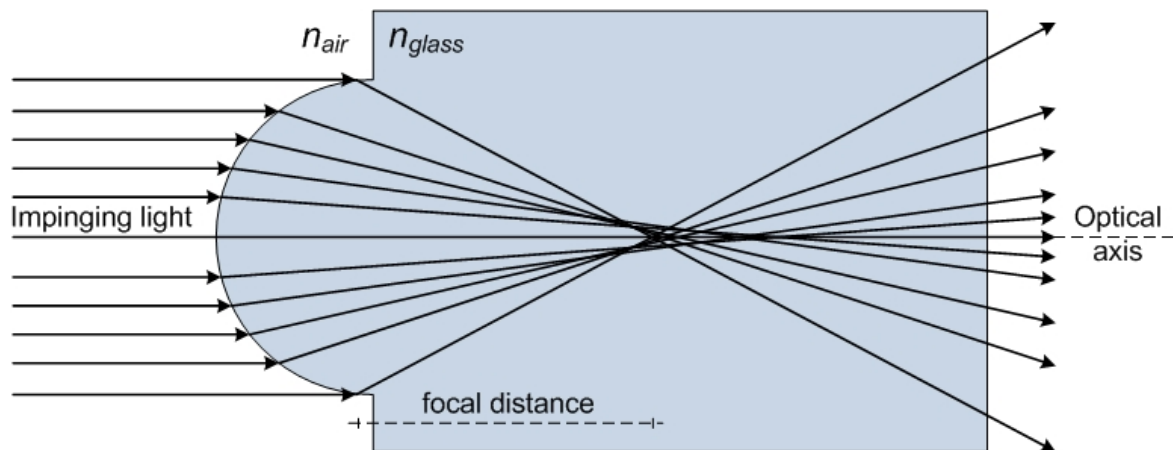


Figure 2.8 – Illustration of the effect that a spherical lens has on refraction.

The spherical aberration causes different focal points to occur along the optical axis. The reason why this happens was already demonstrated in equation 2.38. It should be noted that due to the fact that the refractive index changes for different wavelengths, the latter converge to distinct points in the optical axis. This is called chromatic aberration with shorter wavelengths refracting more than longer ones, as illustrated in Figure 2.9.

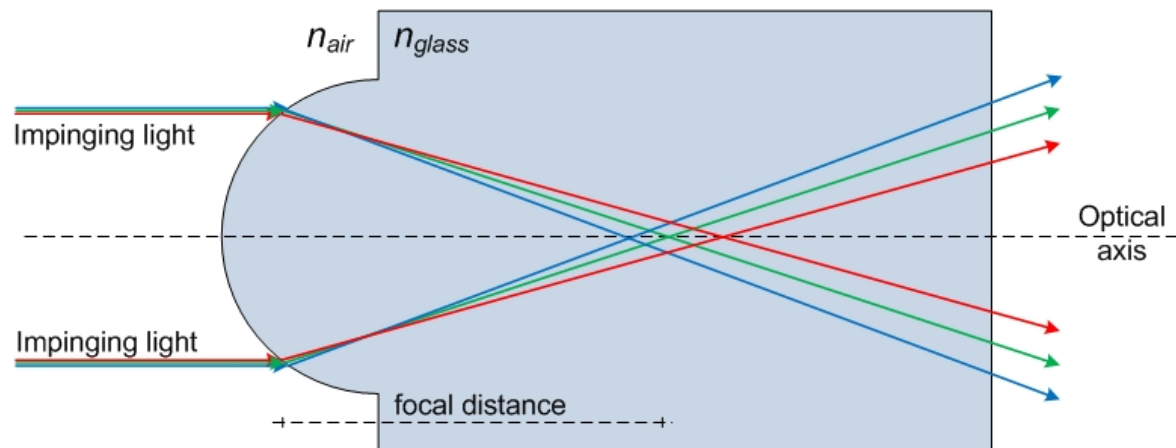


Figure 2.9 – Illustration of the chromatic aberration and how it affects different wavelengths.

References

- [1] J. Correia, Optical Microsystems in Silicon Based on a Fabry-Perot Resonance Cavity: Application for Spectral Analysis of Visible Light, Delft: Delft University Press, 1999.
- [2] M. Freeman and C. Hull, Optics, Eleventh ed., Butterworth-Heinemann, Ed., Edinburgh, 2003.
- [3] I. Kenyon, The Light Fantastic: A Modern Introduction to Classical and Quantum Optics, Second ed., Oxford: Oxford University Press, 2011.
- [4] E. Hecht, Optics, Fourth ed., Pearson Education, 2002.
- [5] M. Born and E. Wolf, Principles of optics: Electromagnetic theory of propagation, interference and diffraction of light, Seventh ed., C. U. Press, Ed., Cambridge, 2002.
- [6] I. Grant and W. Phillips, Electromagnetism, Second ed., J. W. & Sons, Ed., Chichester, 1990.
- [7] F. Smith and T. King, Optics and photonics: An introduction, J. W. & Sons, Ed., Chichester, 2000.
- [8] K. Nassau, The Physics and Chemistry of Color. The Fifteen Causes of Color., J. W. & Sons, 1983.

- [9] Y. Zhang, S. Ghosal, M. Casstevens and R. Burzynski, "Bifunctional chromophore for photorefractive applications," *Applied Physics Letters*, vol. 66, no. 3, pp. 256-258, 1995.
- [10] J. Shore, *Colorants and Auxiliaries: Organic chemistry and application properties*, Second ed., vol. 1, Society of Dyers and Colourists, 2002.
- [11] H. Lachheb, E. Puzenat, A. Houas, M. Ksibi, E. Elaloui, C. Guillard and J. Herrmann, "Photocatalytic degradation of various types of dyes (Alizarin S, Crocein Orange G, Methyl Red, Congo Red, Methylene Blue) in water by UV-irradiated titania," *Applied Catalysis B: Environmental*, vol. 39, no. 1, pp. 75-90, 2002.

3 Design and fabrication

This chapter addresses the design, fabrication, learning curve and optimization of the process, and its parameters, for producing arrays of microlenses (MLs). The learning progression, which includes the familiarization with the photoresist used, the adaptation to the available photolithographic equipment and the thermal reflow (TR) experiments are also described. Moreover, the optimized fabrication process is demonstrated, explained and the results achieved are shown.

3.1 Fabrication

Classical photolithography was employed to fabricate microstructures and thermal reflow was used for obtaining the lens profile in the referred structures [1]. Photolithography, illustrated in Figure 3.1, is the process involving the necessary steps for fabricating arrays of tridimensional microstructures that after the TR process will be turned into arrays of microlenses.

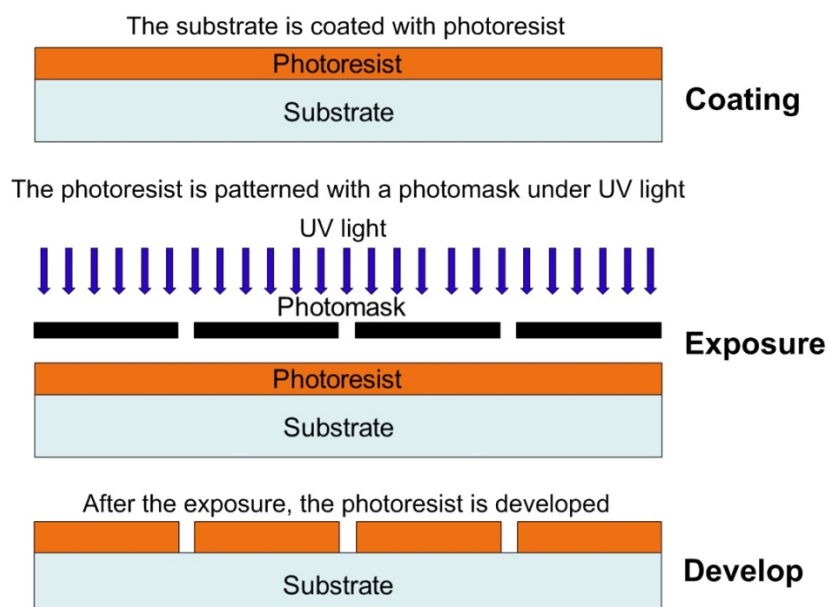


Figure 3.1 – Illustration of the most important steps of the photolithographic process.

Thermal reflow is used mainly for fabricating spherical and parabolic shaped MLs by heating up the photoresist above its glass transition temperature. Once this temperature is reached, the photoresist starts to melt with the surface tension effect causing the

fabricated microstructure to acquire the desired lens profile. The entire process is relatively simple to perform and the thermal reflow is very well controlled without the need for high-technology equipment, guaranteeing good dimensional control and a smooth homogeneous surface. Therefore, the focus in the design of different sized arrays of lenticular plano-convex microlenses is on the thickness of the lens' apex (h) and width of its interface with the substrate (W) (these are the factors more important in determining the focal length f). The learning curve, the optimization and fine tuning of the fabrication process were all performed with the photoresist AZ4562. The actual values of the several process parameters will obviously depend on the desired final size, requirements and applications of the micro-optical device. In the presented case, the purpose is having the fabrication being done directly on top of an image sensor (or on an intermediate substrate) and the main contributions are the different geometric sizes, the aspect ratio achieved and the quick reflow time when compared to other works [2, 3].

Standard microfabrication processes, *i.e.*, photolithography and photoresist thermal reflow, were used to fabricate arrays of lenticular refractive microlenses. By using these technologies, it is possible to fabricate three dimensional microstructures that are reproducible to customize high-quality and cost effective optical microcomponents. Basically, refractive MLs are used for collimation, focusing or imaging and are an appealing alternative for applications where miniaturization and alignment simplicity are requirements. Examples of these applications include imaging [4], biomedical instruments [5], lab-on-a-chip systems [6] and in optical communications [7]. The fabrication processes have been through various changes and improvements along the time, as well as the materials chosen to fabricate refractive MLs. The two main materials used are glass and polymer-based materials and the current fabrication technologies for the latter are the microjet technique, photoresist reflow, ultraviolet curing, hydrophobic effect, LIGA and the soft replica molding methods [8]. The never stopping improvement in the polymeric based material properties and continuous process technology enhancements justify the focus given to this material when fabricating MLs.

As previously stated, one of the main objectives of this thesis is the integration of the MLs fabrication on CMOS technology microdevices. So, several attempts to achieve this goal were done and all of them require a small focal distance ($0 < f \leq 150 \mu\text{m}$ – this interval will be explained in Chapter 4) to maximize the light acquisition into the photodiodes. This constraint, in photolithography, implies the fabrication of plano-convex

microlenses with dimensions corresponding to the following equations' variables also illustrated in Figure 3.2 [9]:

$$R = \frac{r^2 + h^2}{2h} \quad (3.1)$$

$$f = \frac{R}{n - 1} \quad (3.2)$$

$$NA = \frac{W}{2f} \quad (3.3)$$

in (3.1), R is the radius of a single spherical surface, h is the maximum height of the surface undulation and r is half the length of the transversal cut ($2r=W$) and in (3.2) f is the focal length and n is the refractive index of the lens' material for a given wavelength λ . In equation (3.3) is represented the numerical aperture (NA). The NA is the lens' capacity in collecting light over a large incidence angle [10]. The assumption that the lenses were spherical was later confirmed by SEM images.

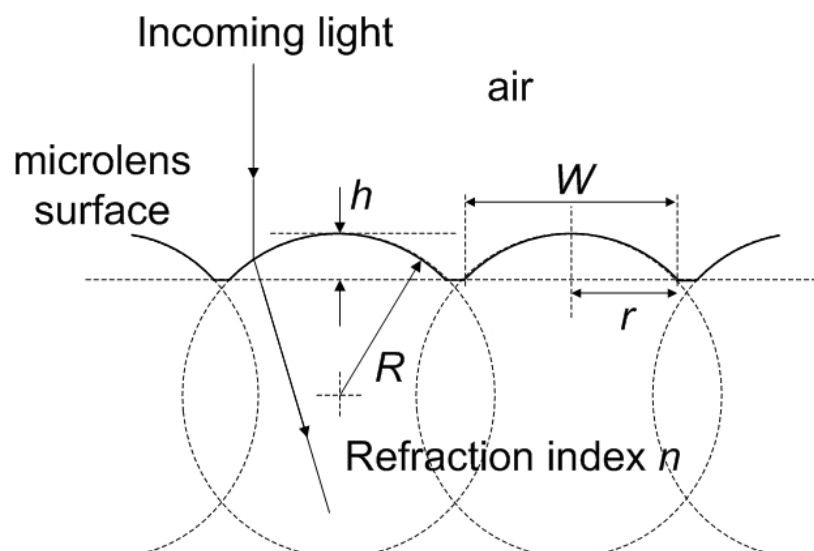


Figure 3.2 – Parameters for determining the necessary focal length f for the microlenses arrays.

Hence, one of the main targets in the design of the MLs is the geometric parameters $\{h, W\}$. Therefore, determining this pair in terms of the coated PR's thickness

h before and after the photolithographic patterning is essential. In Figure 3.3 is seen the trapezoidal shape and geometric edges $\{W_1, W_2\}$ that are obtained after the patterning [11].

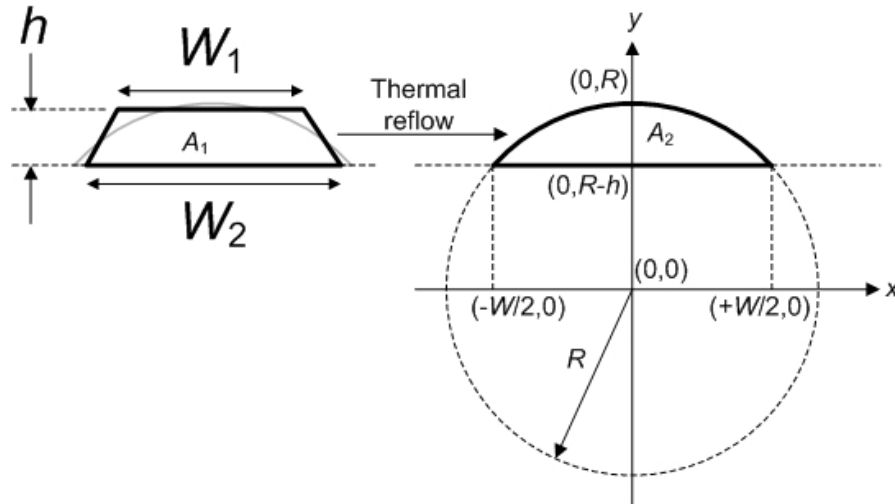


Figure 3.3 – Factors determining the geometry needed for a given focal length f .

The volume V_1 (based on the transversal area) of the material before the thermal reflow is calculated from the cross-sectional area seen in equation (3.4):

$$A_1 = h \left(\frac{W_1 + W_2}{2} \right) \quad (3.4)$$

The radius R is obtained taking into account that the volumes of the material before and after the thermal reflow are the same so the volume $V_1=V_2$ [12]. Therefore, the transversal areas are $A_1=A_2$, with A_2 being:

$$A_2 = \frac{\alpha \pi R^2}{360} - \frac{W(R-h)}{2} \quad (3.5)$$

3.1.1 Photoresist AZ4562

Due to the objectives proposed in this thesis, the selected photoresist is the AZ4562 because of the fabrication requirements. This positive PR is produced by *Clariant* [13], having its physical and chemical properties as well as the film thickness as a function of spin speed seen in Table 3.1 and Table 3.2, respectively. This PR is appropriate for coating thicknesses roughly between 5 and 20 μm without having to increase the exposure energy considerably and still providing enough energy down to the

substrate [14]. Moreover, thermal reflow is achieved at a relatively low temperature ($\approx 110\text{--}130\text{ }^{\circ}\text{C}$) as was discovered during the development of this thesis. It should be noted that in a positive photoresist, the portions exposed to UV light become soluble in the chemical etching, *i.e.*, during development.

Table 3.1 – Physical and chemical properties of the AZ4562 [13].

	AZ4562
Solids content [%]	39.5
Viscosity [cSt@25 °C]	440
Absorptivity [$\frac{1}{\text{g}\times\text{cm}}$]@398 nm	1.01
Solvent	methoxy-propyl acetate (PGMEA)
Maximum water content [%]	0.5
Spectral sensitivity	310–440 nm
Coating characteristic	striation free
Filtration [μm absolute]	0.2
Theoretical glass transition temperature (T_g)	110 °C

Table 3.2 – Typical film thickness as a function of the spin coater speed [13].

Spin speed (r.p.m.)	2000	3000	4000	5000	6000
AZ4562 thickness (μm)	8.77	7.16	6.20	5.55	5.06

Dill Model

A few characteristics of the AZ4562 are important to mention in terms of their optical properties. The UV light intensity I at different depths d across the PR has different chemical reactions on the AZ4562 over time and is described by the Dill Model.

Basically, a positive PR becomes more transparent during exposure and the light intensity I decreases exponentially as follows [15]:

$$I = I_0 e^{-\alpha d} \quad (3.6)$$

where I_0 is the incident intensity. The optical absorption coefficient α , dependent of a given wavelength λ is given by:

$$\alpha = \frac{4\pi k}{\lambda} \quad (3.7)$$

where k is the PR's extinction coefficient and is defined by the Dill Model parameters which describe both the absorption of light in the photoresist and the efficiency of the consequent reaction. The extinction coefficient k is a function of the remaining photo active compound concentration (PAC) and is wavelength dependent. The PAC is normalized to values between 0 and 1 corresponding to completely exposed (bleached) and completely unexposed PR, respectively. For allowing proper microfabrication, the light energy must be absorbed by the PAC which, by exposure, is converted into indene carboxylic acid. This acid is dissolved later using the alkaline developer (refer to Table 3.3). Thus, since during exposure the PAC decreases from 1 towards 0, the extinction coefficient is:

$$k = \lambda \frac{A(\lambda)PAC + B(\lambda)}{4\pi} \quad (3.8)$$

where $A(\lambda)$ and $B(\lambda)$ are the absorption coefficients of the photoresist that becomes bleached and unbleached, respectively, with exposure and are supplied by the manufacturer. These two coefficients are the AZ4562's Dill parameters.

The photoresist's refractive index n for a given wavelength λ is given by the Cauchy's empirical equation:

$$n = N_1 + \frac{N_2}{\lambda^2} + \frac{N_3}{\lambda^4} + \dots \quad (3.9)$$

where N_1 , N_2 and N_3 are the photoresist's constants provided by the supplier [16, 17]. In Figure 3.4 is represented the wavelength dependent refractive index n of the AZ4562 according to the visible light spectrum interval.

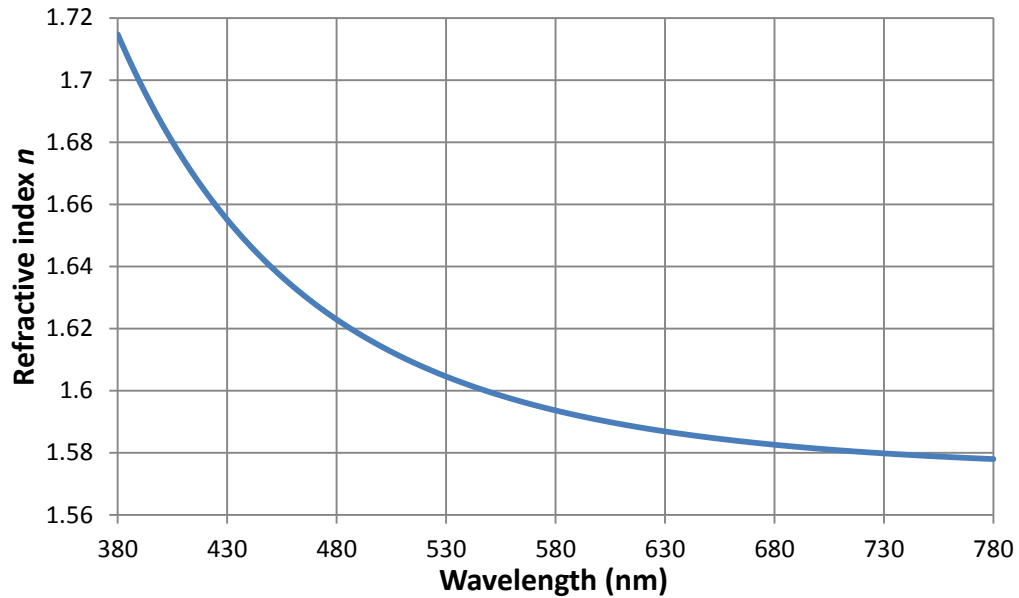


Figure 3.4 – AZ4562's refractive index wavelength dependency chart.

3.1.2 Thermal reflow

For obtaining the desired lens profile, it is necessary to apply a thermal treatment to the fabricated microstructures. When the photoresist is submitted to a temperature higher than its glass transition temperature T_g , it softens allowing the shape transformation to occur. The external forces acting during this process are the surface tension (associated with the contact angle [11]) and gravity, being the latter more significant in lenses with more volume [1, 18, 19]. This type of positive PR has a given softening point that can be used to thermally reflow the fabricated three dimensional microstructures. The AZ4562, being a positive photoresist, has a theoretical softening point around 110 °C [16, 17].

Immediately before the TR is applied, the tensions between the AZ4562 and a solid substrate are represented in Figure 3.5. As soon as the photoresist starts flowing, due to the surface tension, it starts gaining a lens profile until the system reaches equilibrium.

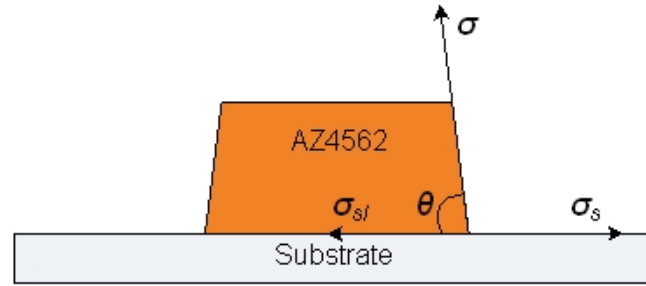


Figure 3.5 – Contact angle between the pre-thermal reflow microfabricated structure and the substrate.

The relation between these acting forces is described by [18, 20]:

$$\sigma_s = \sigma \cos \theta + \sigma_{sl} \quad (3.10)$$

where σ , σ_{sl} and σ_s are liquid surface tension, the solid and liquid boundary tension and the solid surface tension, respectively, and θ is the contact angle before reaching equilibrium. The actual lens profile is highly dependent on these quantities. In these cases, it is assumed that the volume of the microstructure before and after the TR is the same and that the interface with the substrate remains absolutely static.

Reflow speed

Above the material's T_g , its viscosity decreases thus flowing under the influence of the surface tension. In this flowing condition, the AZ4562 obeys the Navier-Stokes equation [21]:

$$\rho \left(\frac{\partial V}{\partial t} + V \cdot \nabla V \right) = -\nabla p + \mu \nabla^2 V + f \quad (3.11)$$

where V is the flow speed, ρ is the flow density, p is the pressure, f is the external force acting on the fluid and μ is the material's viscosity.

Thermal reflow is ideal for fabricating microlenses arrays using positive photoresist. The technique is simple to control, it does not require expensive equipment and guarantees very good results with the lenses showing a very smooth and homogeneous surface as will be demonstrated in section 3.4. The most important parameter is the temperature increase with a ramp profile for guaranteeing a continuous and linear distribution of heat across the substrate.

3.1.3 Finite element method: optical behavior

The ML design started with finite element method (FEM) simulations and in Figure 3.6 it is possible to see the simulation results. The analytical models used to evaluate and define the MLs characteristics are seen in equations (3.1) and (3.2) but with the value of the refractive index already determined using equation (3.9) [22]. The simulated dimensions of the microlens are 5 and 32 μm for the sag and width, respectively, for an impinging wavelength $\lambda=632.8$ nm, similar to a He-Ne (helium-neon) laser, where r is half the line segment of the reflowed photoresist interfacing with the substrate and h is the maximum height (or sag). The light is being irradiated parallel to the surface of the substrate and it is clearly seen that the simulations are in agreement with the theoretical focal length of 49.4 μm (for $n=1.5866$, $R=29$ μm and $h=5$ μm).

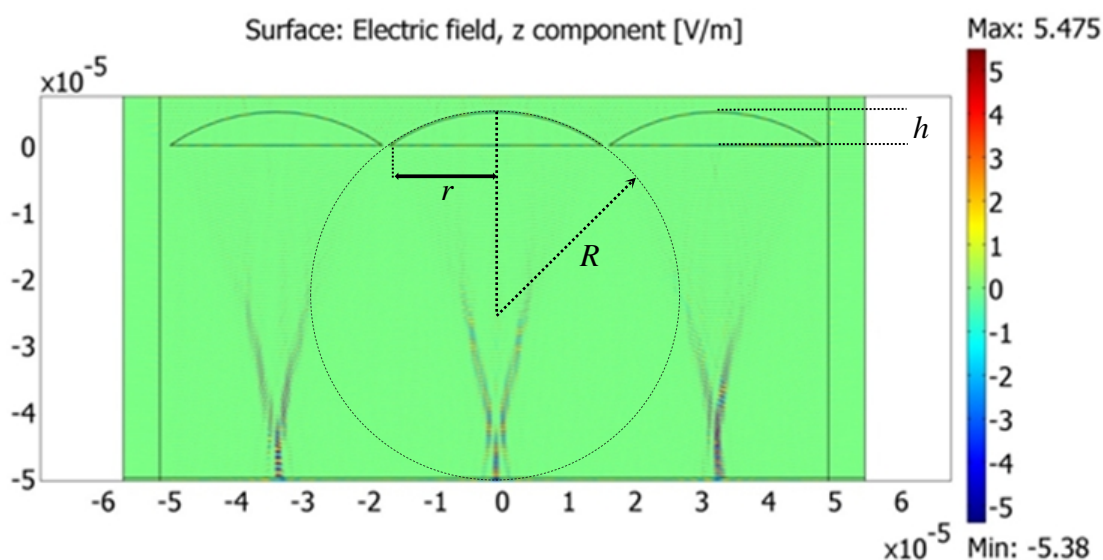


Figure 3.6 – FEM simulations showing the light concentration for microlenses measuring 5 and 32 μm for the vertex h and width $2r$, respectively.

3.2 Fabrication process: first method

Based on the process guidelines provided by the manufacturer seen in Table 3.3, the design of the proposed fabrication process is as follows. First is the process of coating substrates with photoresist, then exposing the PR to UV light using a mask to transfer a pattern into it and finally chemically etching away (development) the photoresist that is not required [23]. Therefore, in order to fabricate the MLs presented in this thesis, classical photolithography processes were used for fabricating three dimensional microstructures.

Table 3.3 – Processing guidelines [13].

Dilution and edge bead removal	AZEBR Solvent
Prebake	100 °C, 50 seconds, hotplate
Exposure	Broadband and monochromatic
PEB (post exposure bake)	Not required
Development	AZ351B, 1:4, 30 seconds/ μm film thickness
Postbake	Not required
Removal	AZ100 Remover

There are several materials available for fabricating microlenses arrays as demonstrated in Table 1.2. The photoresist selected for fabricating MLs allows the transformation from a trapezoidal shape (ideally it should be parallelepipedic) into a spheric one due to the thermal reflow of the raw material. Once the T_g is reached, the photoresist starts to melt with the surface tension effect causing the fabricated microstructure to gain the desired lens profile. The precise form of the microlenses, and hence their focal properties, are determined by the effects of the surface tension [1]. Moreover, the contact angle of the softened resist with the surface of the substrate will strongly influence the shape of the MLs [11]. The fabrication processing steps are summarized in Table 3.4 and the substrate used was a glass microscopic slide measuring $76 \times 26 \times 1$ mm (*length* \times *width* \times *thickness*).

Table 3.4 – Fabrication Process steps and parameters

Process steps	Process parameters
Spin coating	30 seconds@6000 r.p.m.
Prebake (hotplate)	100 seconds@100 °C
Exposure (PCB exposure machine)	2 minutes
Developing	2 minutes using the AZ351B developer in a 1:4 concentration with distilled water
Cleaning	Rinse with distilled water and dry with N ₂ flow
Thermal Reflow (hotplate)	10 hours@180 °C

The fabrication of microlenses array requires several steps. First, it is necessary to deposit the photoresist by means of a spin coater (this in-house assembled equipment is seen in Figure 3.7) in a previously cleaned substrate with isopropyl alcohol (IPA) and dried out with a nitrogen (N₂) flow. Spin coating allows very smooth and homogeneous photoresist films to be achieved, even though it is dependent of some factors such as film thickness, the geometry and surface of the substrate, *etc.* The desired photoresist thickness depends on the spinning time and speed. For achieving the appropriate thickness for the AZ4562 the selected spin velocity is 6000 r.p.m. A high spinning speed also decreases the edge bead appearance in the substrate's corners. Based on the data supplied by the manufacturer, 30 seconds was chosen to achieve a thickness close to 5 μm for obtaining a short focal distance.

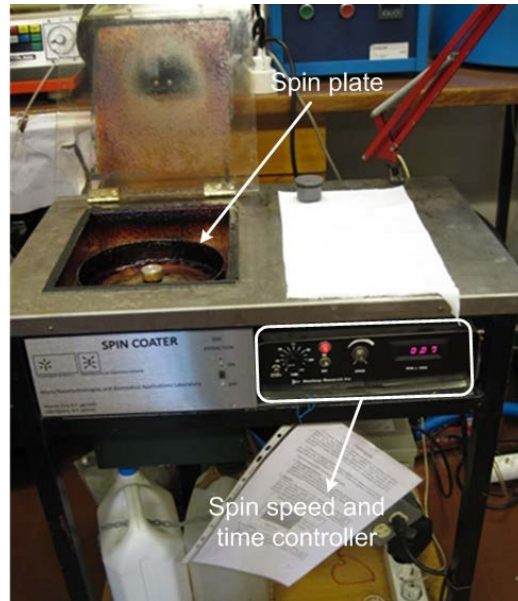


Figure 3.7 – In-house built spin coater for coating photoresist onto substrates.

After the coating, a prebake phase, using a computer controlled hotplate with proportional-integral-derivative (PID) control, at 100 °C for 100 seconds (seen in Figure 3.8) is necessary for evaporating the solvent present in the photoresist. This step is important to clear off the unnecessary components of the AZ4562 needed for obtaining a solid structure, *i.e.*, by extracting these components the state of the material changes from viscous to solid.

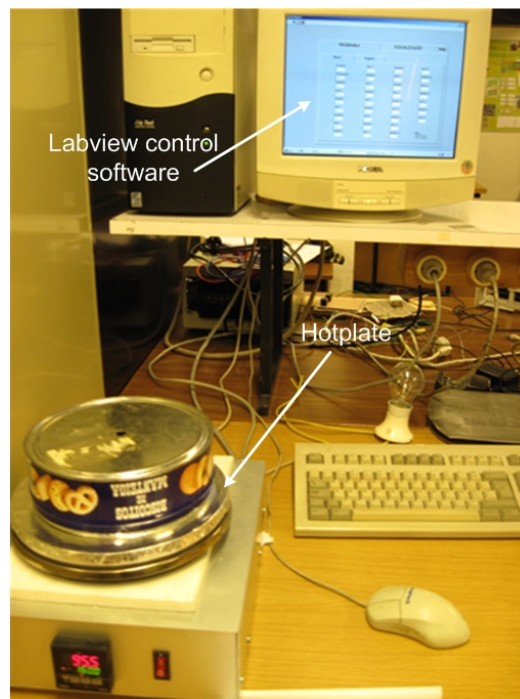


Figure 3.8 – Hotplate and the computer using *Labview* software to control the temperature profile with PID control.

Next, for obtaining the required array-like structure, a mask with the correspondent geometrical design is placed on top of the substrate with the photoresist. This step serves for exposing the PR to UV light thus transferring the pattern in the mask into the AZ4562 and making the unexposed material insoluble. The first pattern that was designed and tested is observed in Figure 3.9.

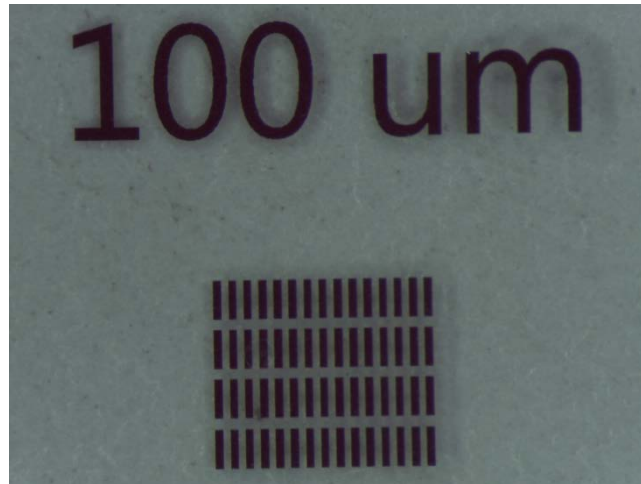


Figure 3.9 – Mask with arrays containing rectangles measuring 1000 and 100 μm for length and width, respectively. This pattern was printed in an acetate sheet in a commercially available printer for achieving arrays of column-like structures that are later thermally reflowed into microlenses.

In these first fabrication trials, for the UV exposure step, a machine for printing printed circuit boards (PCBs) was used, seen in Figure 3.10. For this initial phase in fabricating MLs care was given mostly to understand the photoresist rather than to obtain good and clear microstructures. In the second fabrication phase, once the material was known better, a mask aligner was used for printing the photomask design into the photoresist.

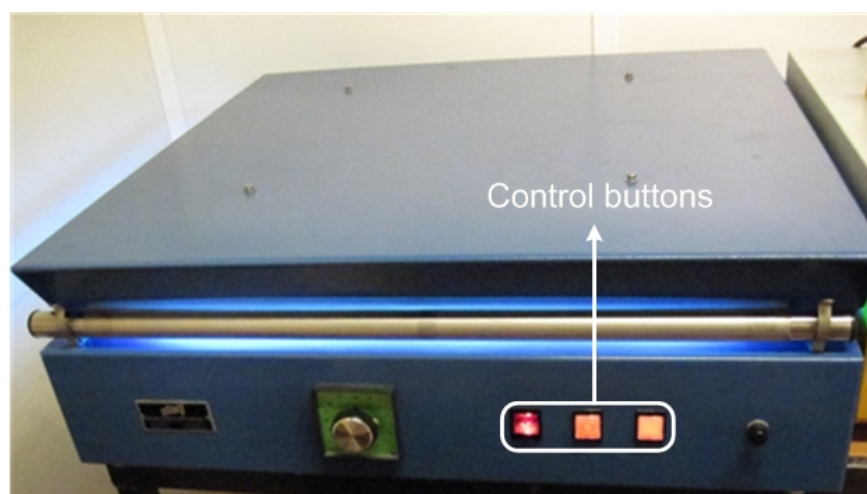


Figure 3.10 – A UV exposure machine typically used for fabricating PCBs.

Finally, during the development phase, using the AZ351B developer, the soluble portions of the exposed photoresist are chemically etched away leaving just the structures that will be thermally reflowed into microlenses. For clearing the exposed AZ4562 the substrate is immersed in the remover bath with magnetic stirrers for two minutes in a 1:4 concentration with distilled water.

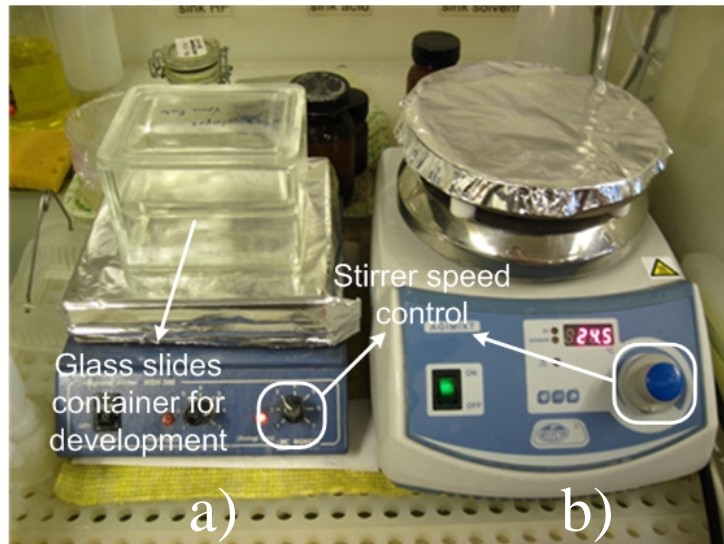


Figure 3.11 – Development phase using magnetic stirrers. In a) is the *Laboratory hot plate magnetic stirrer from Agimixt* and in b) the *Magnetic stirrer MSH 300*.

3.2.1 Characterization of the microstructures

Once the fabrication process is finished, it was required to characterize the fabricated microstructures in order to get a real understanding of what was being done. In Figure 3.12, an optical microscopy photograph showing the PR array before the reflow step is presented [24].

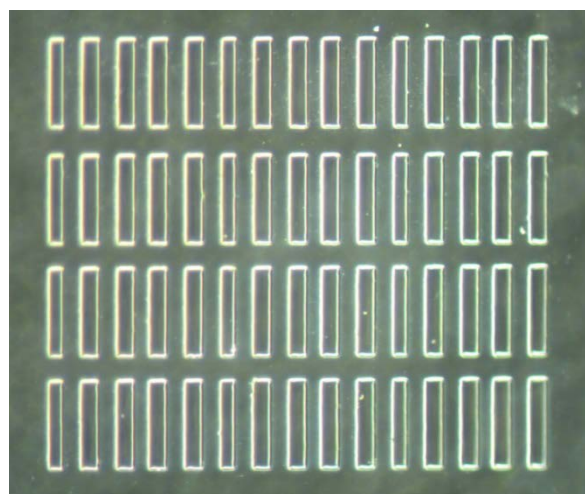


Figure 3.12 – The PR array before the thermal reflow viewed from the top.

It should be noted that mainly due to the printer precision (and ink quality) and the UV source, the structures are not similar along both columns and rows. The main purpose for using a photomask in photolithography is precisely for having complete opaque areas from where the UV light cannot go through. Moreover, the light should fall perpendicular to the surface of the photoresist, guaranteeing a real replication of the photomask pattern. The UV exposure machine used for this process has a row of UV lamps scattering the light in a 180° angle facing the mask (making light to imping on the AZ4562 from many different sides and not just perpendicularly) plus the reflection caused by the metallic stuffing seen in Figure 3.13. Another significant issue is using transparent substrates, in this case glass. This transparency causes light to also travel inside the substrate during UV radiation causing rear-side exposure of the photoresist. So, special attention must be given to over-exposure when using transparent substrates.

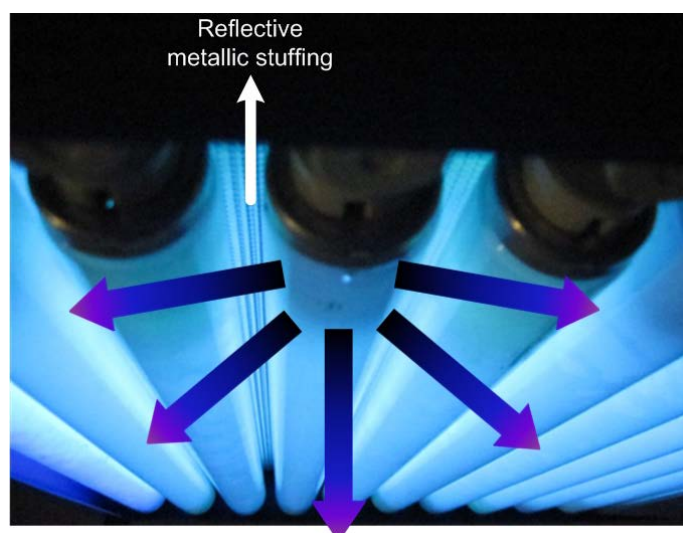


Figure 3.13 – Illustration of how the UV light is transmitted by the array of lamps in the PCB exposure machine.

When a visual confirmation of the fabricated microarrays was achieved, more detailed measurements were required. Therefore, in Figure 3.15 it is possible to see the profile of the PR after the photolithographic process measured with a *Veeco Dektak 150* profilometer (Figure 3.14) [24-26]. This figure presents the typical initial profile seen during the fabrication of microlenses using PR [20, 27]. It is also clear from this measurement that the initial $\approx 100\ \mu\text{m}$ width in the photomask is translated into $\approx 75\ \mu\text{m}$ due to the aforementioned reasons which represents a big loss, dimensionally speaking, from mask to structure sizes.



Figure 3.14 – Profilometer *Veeco Dektak 150*.

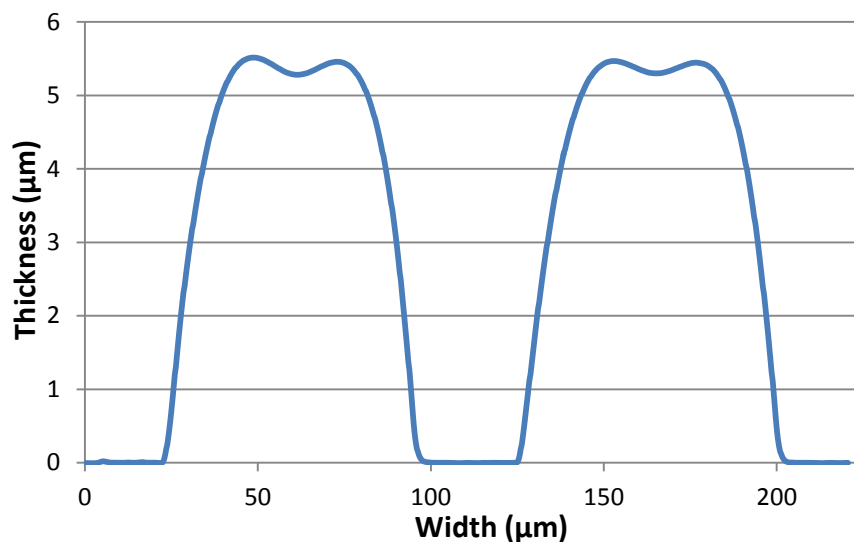


Figure 3.15 – Photoresist profile after the photolithographic process. The maximum measured thickness is 5.514 µm.

Practical use of the thermal reflow technique

Based on the literature [2, 3], the thermal reflow applied in this first fabrication process was done with the substrate coated with the PR array placed in a hotplate at 180 °C during 10 hours and the result is observable in Figure 3.16. The brownish color was found out to be related to the parameters of the thermal reflow. So, after applying a temperature higher than the glass transition temperature T_g of the PR, the viscosity decreases and the consequent flow due to the surface tension occurs.

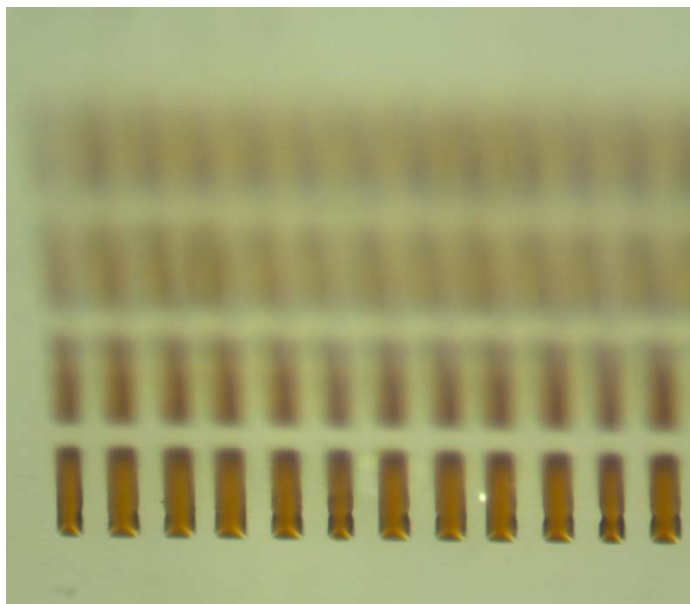


Figure 3.16 – In this picture is seen the PR array after the thermal step from a tilted angle.

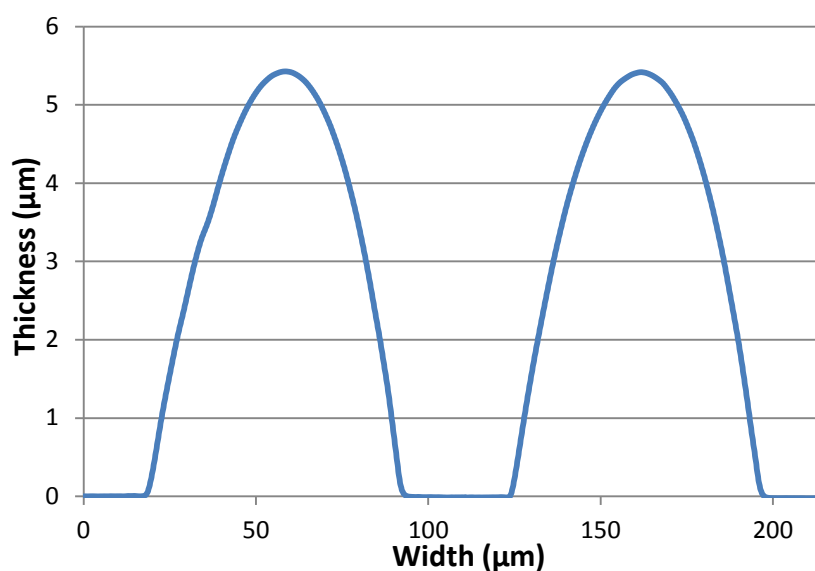


Figure 3.17 – Photoresist profile after the thermal reflow step. The maximum measured thickness is 5.428 μm .

Good-quality lenses are fabricated with relatively crude lithography methods although greater consistency and reliability is achieved only if the process is carried out efficiently. It is possible to fabricate microlenses arrays but the precision achieved using this fabrication process is still far from what should be expected. These structures are the first prototypes built using photolithography and thermal reflow. As demonstrated later, the final size of the microlenses can be further reduced as well as the MLs' optical quality with a more homogeneous, smooth and clear surface using a chromium-on-glass mask and mask aligner for UV exposure. Nevertheless, it is clear from the previous figures that

the TR step permitted obtaining the desired microlens profile to concentrate the light into a focal distance. Moreover, during this fabrication trial, it was realized that the parameters and equipment used were not adequate for the objectives, and their dimensions, proposed in this thesis but nonetheless were very helpful in gaining the necessary know-how and sensitivity in working with these technologies and materials.

3.3 Fabrication process: second method

With the knowledge gained during the first method in the design of the fabrication process, a second one was developed. The two steps more obviously seen in need for improvement were the quality of the photomask and the UV source used, or in other words, the core of any photolithographic process. A new photomask containing 18 different patterns was made. The length of the rectangles in every pattern is the same (4.9 mm) and their widths are 12, 19, 24, 30, 35 and 40 μm . The pitch between adjacent rectangles have three different values; 1.5, 2 and 5 μm . In the example demonstrated in this process, the pattern measures $4900 \times 30 \times 5 \mu\text{m}$ (*length* \times *width* \times *thickness*) permitting the production of an array containing 142 microlenses.

3.3.1 Photomask

Based on the previous experience in mask design within the group of Micro and Nano Technologies and Biomedical Applications, the best technology was found to be in choosing a 128k dpi (dots per inch) super high-resolution chrome on soda lime glass $3 \times 3 - 0.060''$ mask [28] and each one of the 18 patterns covers an area of $5 \times 5 \text{ mm}$. The rectangles are coated with chromium making them opaque to light and the spacing between rectangles is transparent allowing the photoresist under it to be exposed to the UV light later on. In Table 3.5 are shown the most relevant characteristics of these photomasks for the current application.

Table 3.5 – Relevant characteristics of soda lime glass photomasks [28].

Transmittance (375–450 nm)	88%
Thermal coefficient expansion	$\frac{93 \times 10^{-7}}{^{\circ}\text{C}}$
Glass flatness class	5 μm
Chrome optical density@450 nm	3.0
Chrome reflectivity@436 nm	11%

A photograph of the actual mask is shown in Figure 3.18 with the illustration of the mask being seen in Figure 3.19. In narrow structures it is normal to have a smaller effective exposure intensity towards the substrate when compared to wide ones. When the gap between adjacent chrome areas is in the range of the exposure wavelength, it acts as a linear light source having an intensity I with r being the distance from the photomask, equation (3.12). A broad gap acts as parallel light source without a r dependency.

$$I = \frac{1}{r} \quad (3.12)$$

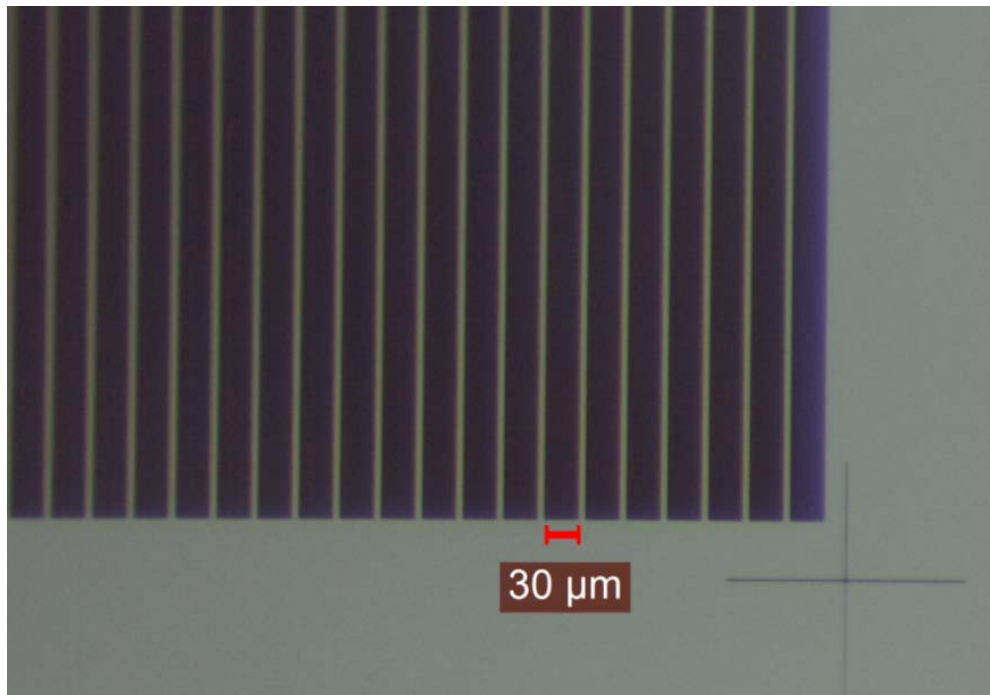


Figure 3.18 – Real 30–5 μm pattern mask seen through a *Leica M80* microscope with 120 \times magnification.

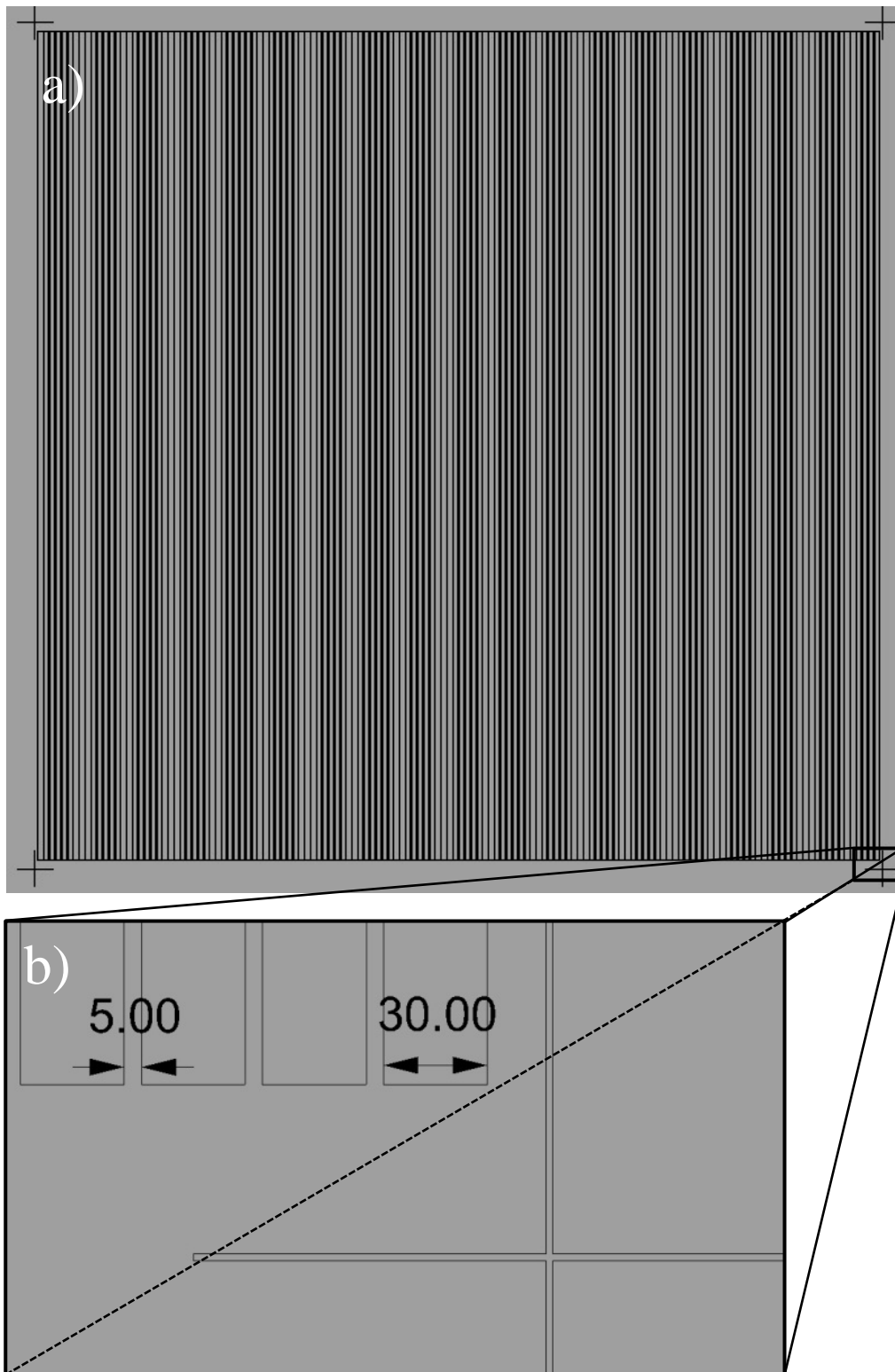


Figure 3.19 – In a) the whole picture of the array mask drawing is seen and in b) a detailed zoom-in with the chromium rectangle width (30) and spacing (5) expressed in μm .

The new values for the fabrication parameters are presented in Table 3.6. The differences are already substantial when compared to the first fabrication process.

Table 3.6 – Second fabrication process steps and parameters values.

Process steps	Process parameters
Spin coating	20 seconds@6000 r.p.m.
Prebake (hotplate)	5 minutes@100 °C
Exposure 365 nm (mask aligner)	30 seconds in contact mode @134 W (394 mJ/cm ²)
Developing	2×(2 minutes and 15 seconds) in AZ400K or AZ351B developers in a 1:4 concentration with distilled water
Cleaning	Rinse with distilled water and dry with N ₂ flow
Thermal Reflow (hotplate or oven)	5 minutes@130 °C

As before, the first step is to spin coat the AZ4562 at 6000 r.p.m. during 20 seconds, in a previously cleaned glass substrate, to achieve a value close to the 5 μm thickness objective. After the coating, the prebake phase, using the same computer controlled hotplate at 100 °C for 5 minutes, is necessary for evaporating the solvent present in the photoresist. If this is not accomplished the trapped solvent may form bubbles and lift the resist film causing adhesion failure. Next, for obtaining the required array-like structure, the photomask with the correspondent geometry is placed on top, in contact mode with the coated photoresist and exposed to UV light (365 nm) using the mask aligner seen in Figure 3.20.

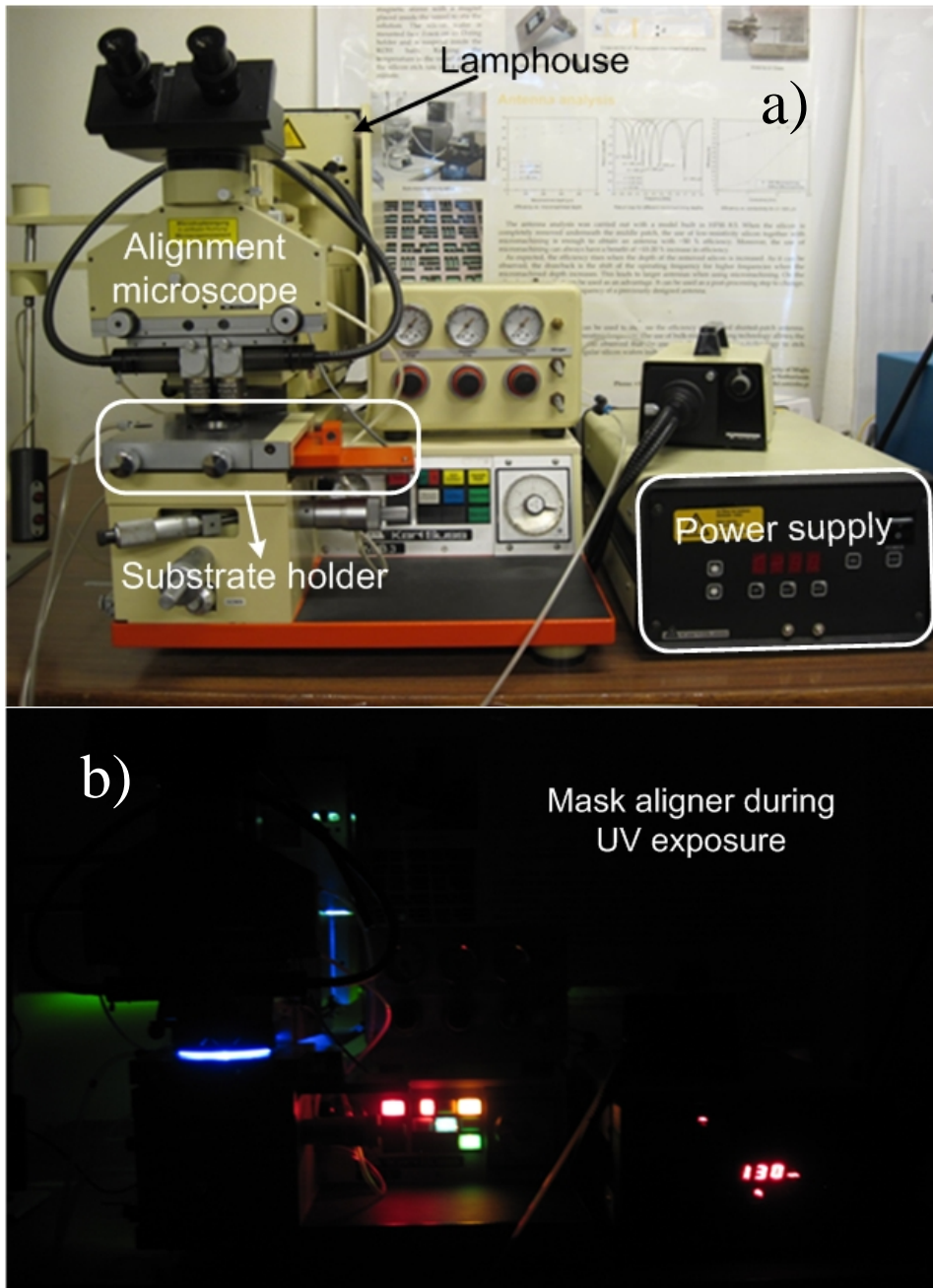


Figure 3.20 – Mask aligner MJB 3 from *Karl Suss*. In a) and in b) are seen a general view and during photolithography exposure, respectively.

The AZ4562 being under a 394 mJ/cm^2 exposure energy makes the unexposed material insoluble. Afterwards, the developing phase is achieved by either the AZ400K or the AZ351B developers in a 1:4 concentration with distilled water. To accomplish it, the substrate with the photoresist patterning is immersed into two developer baths for 2 minutes and 15 seconds each, in a magnetic stirrer plate (several benchmarking tests were performed with both developers but no difference was noticed in all the results). This is required to leave just the unexposed photoresist in the substrate. The photolithographic

process ends with the structures being rinsed with distilled water and dried out with a nitrogen flow. Finally, for obtaining the lenses' profiles, the thermal reflow technique was again applied so the substrate holding the array containing the fabricated structures is placed on a hotplate at 130 °C for 5 minutes. Also, several tests were performed for comparing the thermal reflow step using either a hotplate or an oven. Besides a small working temperature difference, <5 °C, no changes were noticed in the final results. In this second fabrication process, the hotplate was selected more often due to its better ability to evaporate the solvent as it ramps up to the final selected prebake temperature.

3.3.2 Pre-thermal reflow array

By considerably reducing the existing bulk solvent concentration, a better resist profile is achieved as well as a decrease of the developer etch to the unexposed resist. Figure 3.21 shows SEM images of the fabricated microstructure after the photolithographic process. It should be noted that the dimensions of the elements in the array, *i.e.* width and pitch distance, are very close to the mask's dimensions. This considerable improvement in the results is a clear demonstration on how a super high-resolution photomask and a mask aligner are the most responsible for such an increment in the quality of microfabrication achievements. Moreover, these tridimensional microstructures are closer to the ideal parallelepipedic shape that is desired.

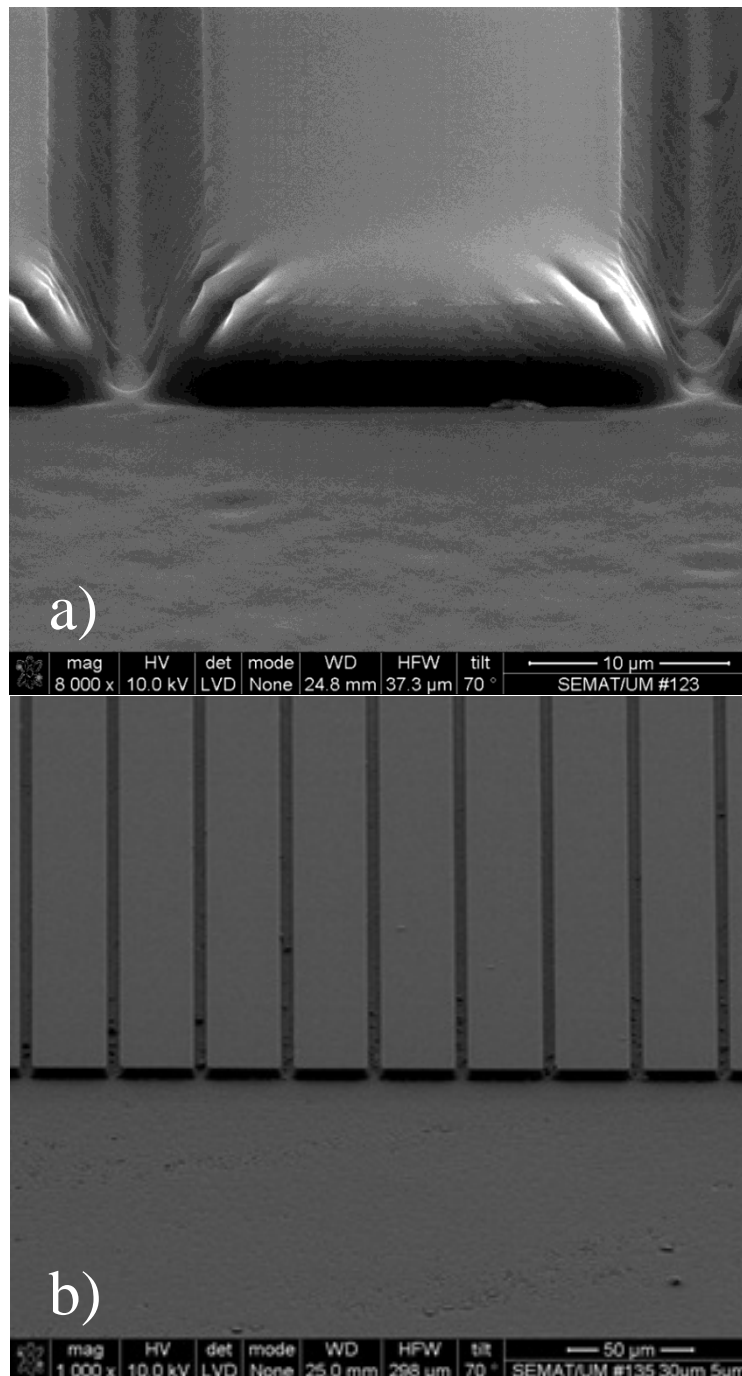


Figure 3.21 - In a) and b) SEM images of a single element of the array and a zoom-out of the array, respectively.

Figure 3.22 illustrates the cross-section of two adjacent elements of the pre-thermal reflow array. From the values obtained in SEM shown in Figure 3.21a) and using equation (3.13), the area and volume of the elements on the array can be easily calculated as well as the angle θ that ideally should be 90° .

$$\theta = \tan^{-1} \left(\frac{Y - X}{2h} \right) + 90^\circ \quad (3.13)$$

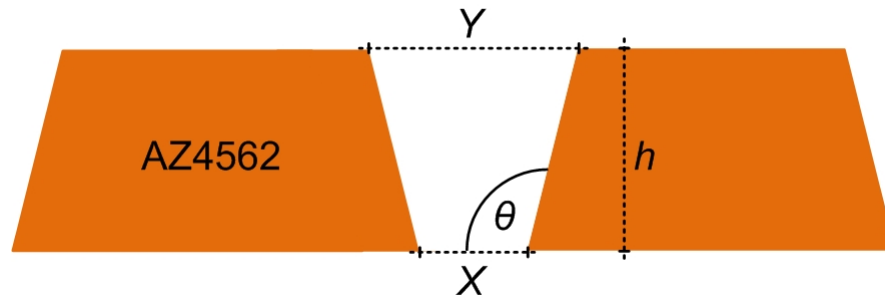


Figure 3.22 – Illustration of the cross-section of two pre-thermal reflow elements for calculation purposes.

Since the measured thickness h_m in Figure 3.21a) was taken with a 70° tilt (β) in the SEM, then, the real thickness h_r is:

$$h_r = \frac{h_m}{\sin\left(\beta \frac{\pi}{180^\circ}\right)} \quad (3.14)$$

This means that the actual photoresist thickness seen in Figure 3.21a) is $5.735 \mu\text{m}$ instead of the $5.39 \mu\text{m}$ shown in 70° view tilt.

3.3.3 Post-thermal reflow array

The AZ4562 has a given softening point that can be used to thermally reflow the fabricated three dimensional structures. In this case, the theoretical softening point is around 110°C [16]. It was realized during this fabrication process that a better reflow condition was achievable with the hotplate being at a temperature close to 130°C during 5 to 10 minutes (depending on the thermal coefficient and thickness of the substrate) when compared to the first fabrication process. After applying the designated temperature, the PR's viscosity decreases and the consequent flow occurs due to surface tension, thus achieving the desired ML profiles. Also, in Figure 3.23a) and b) are represented SEM images of one lens and a part of the entire MLs array, respectively. It is clear from the figures that the thermal reflow process using a hotplate allows obtaining the desired microlens profiles necessary to refract the incident light.

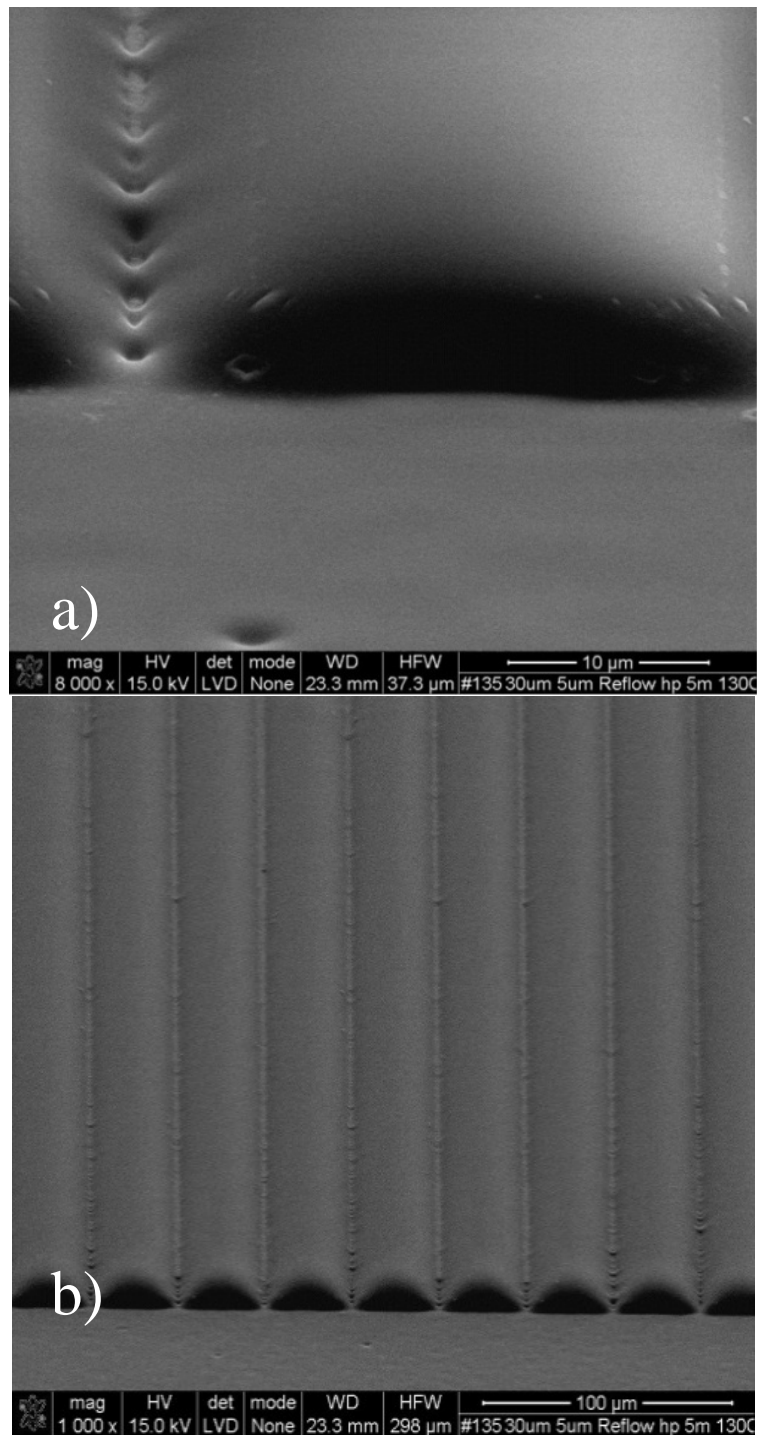


Figure 3.23 – In a) and b) SEM images of a single microlens and an overview of the ML array, respectively.

The lens' profile was confirmed to be spherical through the cross-section SEM image seen in Figure 3.24.

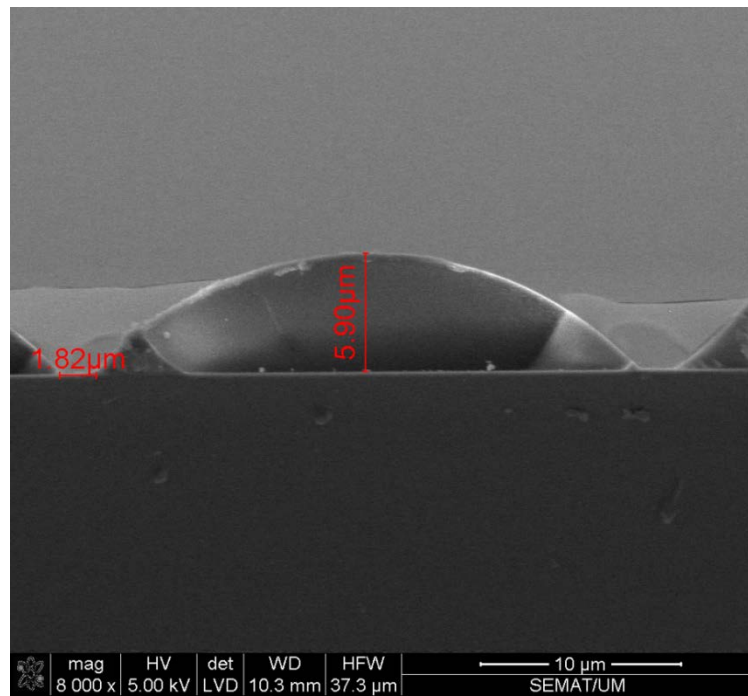


Figure 3.24 – Cross-section showing the lens' spherical profile.

This fabrication process of refractive lenticular microlenses arrays demonstrated results closer to the proposed solution presented in this thesis. Nevertheless, some improvements were identified and will be shown next.

3.4 Fabrication process: third method

This third fabrication process refers to the optimal solution found for this thesis context. At the end of the second fabrication process, it was discovered that the prebake step not only cleared off the solvent but also the photoresist's water content. In this final, optimal fabrication process, a smaller dimensional array with better structural quality was achieved when compared to the previous fabrication method. The MLs were fabricated for a length of (but not restricted to) 4.9 mm and a *width–thickness* (at the apex) product of 24–5 μm.

3.4.1 Rehydration

In this fabrication process, it is shown that the AZ4562 needs rehydration in order to obtain excellent results by preventing structural damages in the MLs which are crucial for achieving efficient optical properties. The biggest advantage of this new optimized process is the further improvement of well-established standard microfabrication processes, *i.e.*, photolithography combined with photoresist thermal reflow. Again, the entire process is relatively simple to perform and, this technique specifically, is very well controlled without needing high-technology equipment guaranteeing good dimensional control and a smooth homogeneous surface. The proposed optimization towards the enhancement of the process, consists in adding the rehydration step, thus preventing the non-uniformity on the surface of polymer based MLs to occur, prejudicing their optical properties [29]. The patterning by UV-photolithography is done in such a way that produces arrays containing MLs of good optical quality in just a few minutes. The fabrication steps are again summarized in Table 3.7. It should be also noted a slight increase in the exposure energy for guaranteeing that only the unexposed photoresist was left in the substrate after the development.

Note that on this fabrication method, particular attention was given to the prebake, used to evaporate the solvents off the AZ4562. If not all the solvent is cleared off, at least most of it should be in order to create a better PR profile as well as a decrease of the developer etch to the unexposed photoresist. Moreover, as said before, the trapped solvent may form bubbles and lift the resist film causing adhesion failure. Nevertheless, the prebake has the drawback of also evaporating the AZ4562 water content, so it is mandatory to rehydrate the PR afterwards.

Table 3.7 – Third fabrication process steps and parameters values.

Process steps	Process parameters
Spin coating	20 seconds@6000 r.p.m.
Prebake (hotplate)	5 minutes@100 °C
Rehydration (40–45 % humidity)	10 minutes
Exposure 365 nm (mask aligner)	40 seconds in contact mode @134 W (526 mJ/cm ²)
Developing	2×(2 minutes and 30 seconds) in AZ400K or AZ351B developers in a 1:4 concentration with distilled water
Cleaning	Rinse with distilled water and dry with N ₂ flow
Thermal Reflow (temperature profile in Figure 3.27)	5 minutes@130–140 °C

The rough edges and wrinkles seen in Figure 3.21a) and Figure 3.23a) are obvious and occur due to the lack of water in the AZ4562, *i.e.*, the photoresist literally dries out. The rehydration step serves mainly to guarantee a sufficient amount of water in the PR during the UV exposure to allow a reasonably high development rate and contrast. It also prevents the development time to increase due to insufficient water and for obtaining good results (as seen in the figures, the lack of water produces visible cracks). For solving this problem of utmost importance, a new fabricating step consisting on letting the samples rest for a period of 10 minutes at room temperature was added. This way, the PR absorbs water from the air humidity, somewhere between 40–45% is enough, which rehydrates the AZ4562 making it smooth and homogeneous. Figure 3.25 and Figure 3.26 show SEM images of the fabricated microstructures following the same fabrication process with just the addition of the rehydration time period.

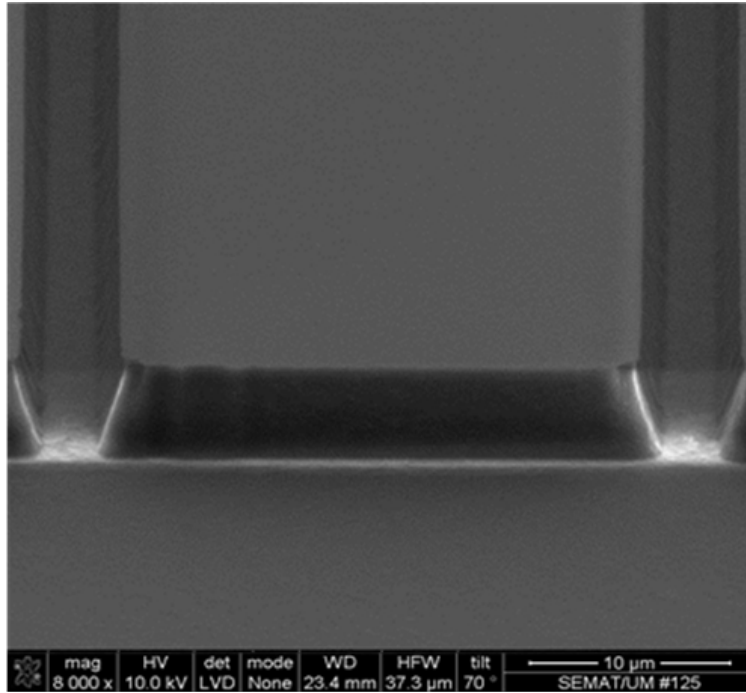


Figure 3.25 – SEM image of a single element of the array before the thermal reflow and with rehydration.

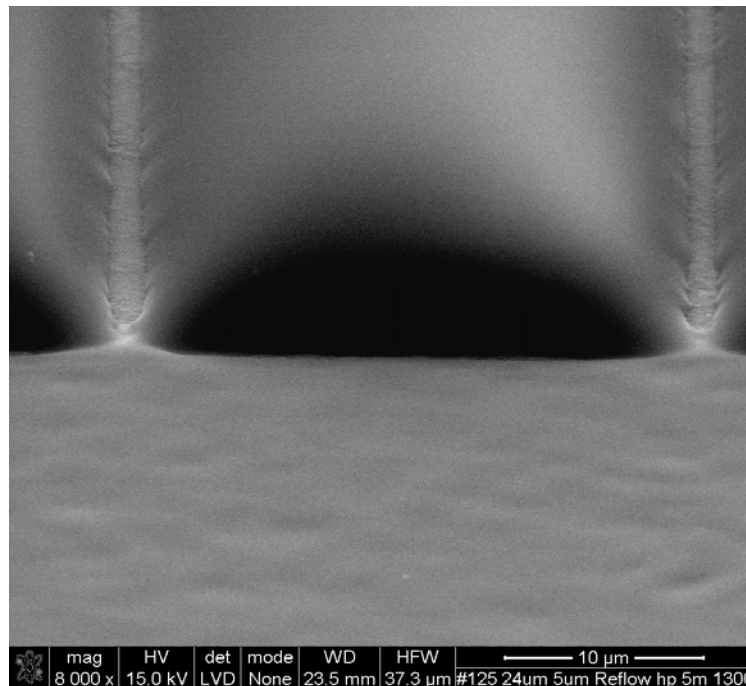


Figure 3.26 – SEM image of a single element of the array after the thermal reflow and with rehydration.

The rehydration facilitates the fabrication of pre-thermal reflow structures with a profile closer to the theoretical parallelepipedic shape rather than a trapezoidal one. Therefore, the rehydration is the key factor for obtaining the very smooth and homogeneous structures seen in the pictures which are essential for good optical quality

microlenses. For obtaining more consistent good results, it was observed that the thermal reflow temperature should be between 130–140 °C, which facilitates the overall smoothness and homogeneity of the surface. A new thermal profile was applied and is illustrated in Figure 3.27. A temperature increase with a ramp profile is the more efficient way to guarantee a successful thermal reflow for fabricating microlenses. This way, the AZ4562 does not have a fast temperature gradient applied to it, which can prejudice the surface tension phenomenon resulting in an unsuccessful fabrication process. Therefore, a continuous and linear distribution of heat across the substrate and the PR is highly desirable. It should be noted that the actual reflow time starts when the temperature reaches 100 °C.

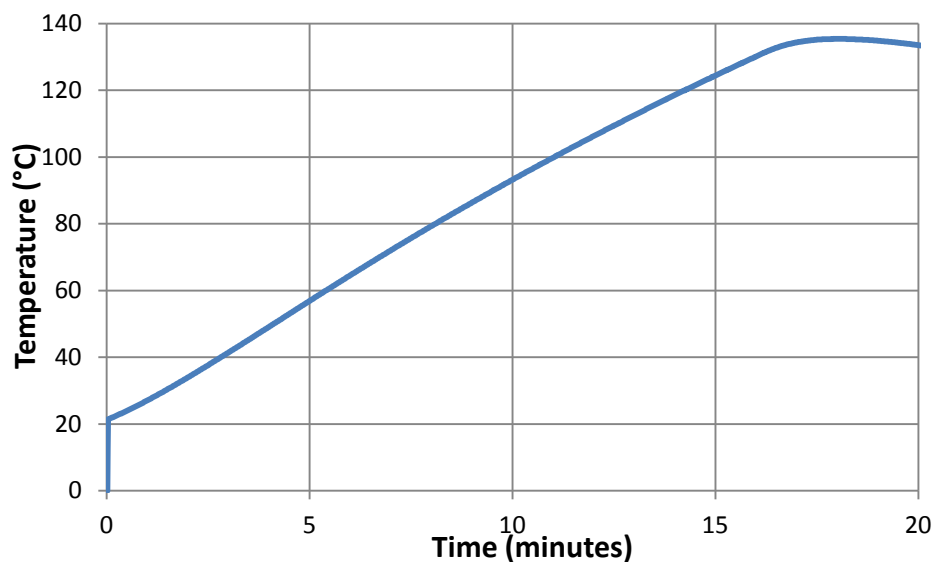


Figure 3.27 – Reflow temperature profile used in the hotplate.

3.4.2 Fabrication efficiency and reproducibility

The way the fabrication process was designed and developed allows great flexibility in terms of easily readapting it for microlenses with different dimensions and guarantees reproducible results.

Pre-thermal reflow structures

In Figure 3.28 is represented a tridimensional microstructure before thermal reflow with the three parameters that were used (W_1 , W_2 and h), for measuring the mean and standard deviation of the fabrication process.

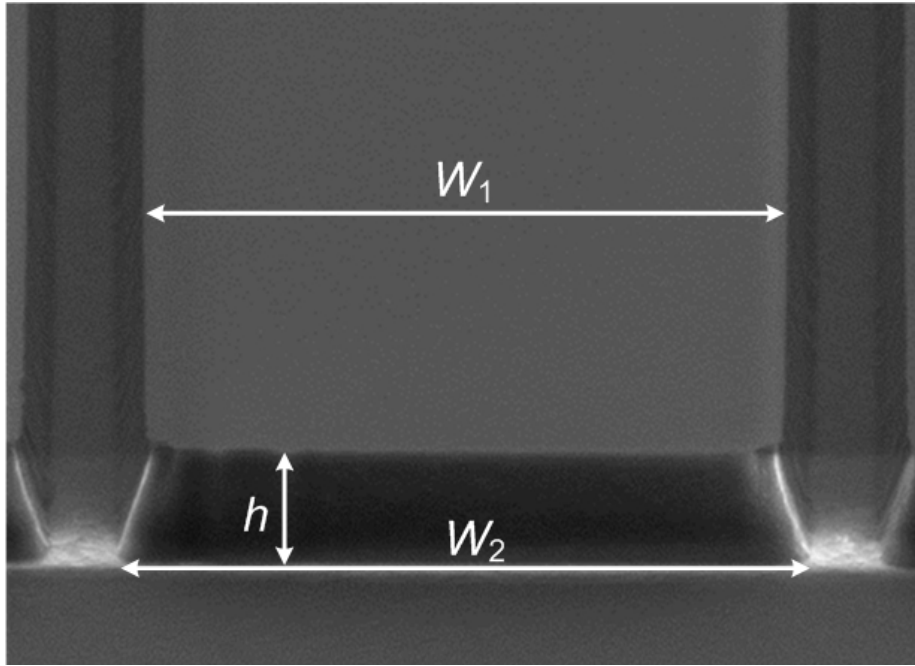


Figure 3.28 – The dimensions that were used for evaluating the reproducibility of the fabrication process for the pre-thermal reflow microstructure. If $W_1=W_2$ than the fabricated microstructure would be a rectangular prism.

The statistical population is composed by 20 randomly selected samples that were measured using SEM. The reproducibility study presented here was done for two mask patterns, with the respective widths being 24 and 30 μm separated by 5 μm . As previously stated, ideally, the fabricated microstructure should be a rectangular prism. Although this solid was not achieved, a close geometric volume with isosceles trapezoidal cross-section was obtained. Figure 3.29 shows the values of the mean and standard deviation for the mask pattern 24–5 μm based on the 20 values measured for dimensions W_1 , W_2 and height h . Therefore, for $n=20$ and $j=1,2$ the mean is:

$$\mu_{w_j} = \frac{1}{n} \sum_{i=1}^n w_{j,i} \quad (3.15)$$

The standard deviation is given by:

$$\sigma_{w_j} = \sqrt{\frac{1}{n} \sum_{i=1}^n (\mu_{w_j} - w_{j,i})^2} \quad (3.16)$$

The mean and standard deviation values for the height h , are given analogously by:

$$\mu_h = \frac{1}{n} \sum_{i=1}^n h_i \quad (3.17)$$

$$\sigma_h = \sqrt{\left[\frac{1}{n} \sum_{i=1}^n (\mu_h - h_i)^2 \right]} \quad (3.18)$$

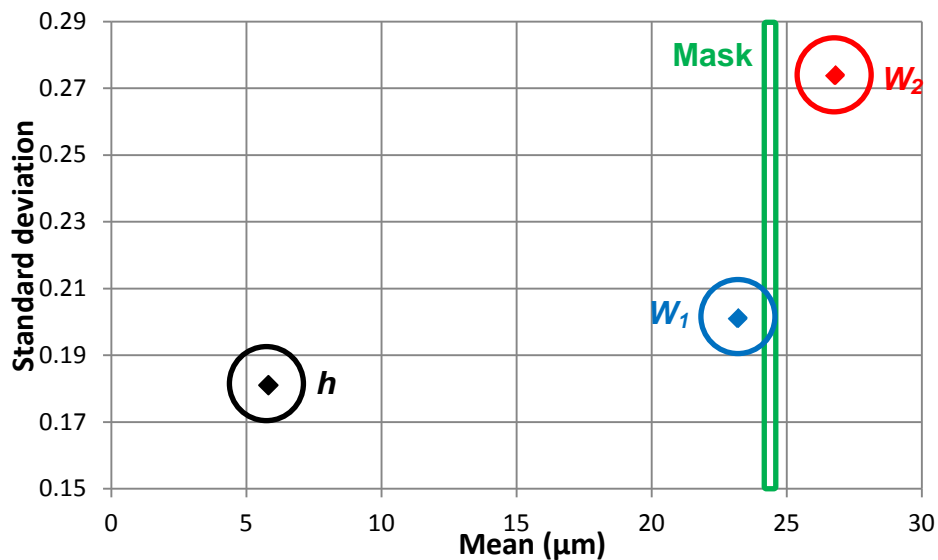


Figure 3.29 – Mean and standard deviation values for the 24–5 μm pattern mask.

Based on the results, for the mask pattern 24–5 μm, the developed fabrication process concerning the measured values *versus* mask dimension, has an accuracy of $W_1=96.6\%$ and $W_2=88.4\%$.

For the mask pattern 30–5 μm, the statistical results for the same conditions as the mask pattern 24–5 μm, are seen in Figure 3.30.

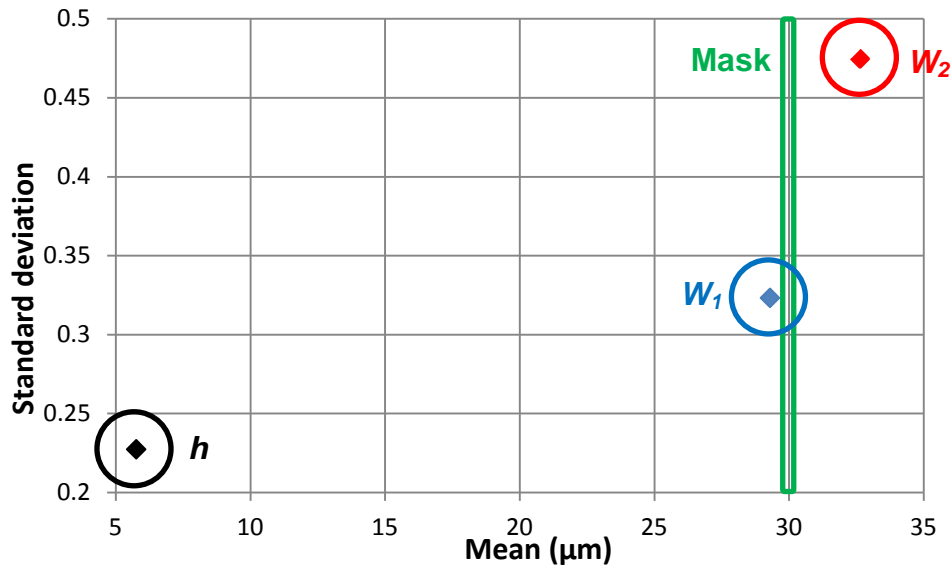


Figure 3.30 – Mean and standard deviation values for the 30–5 μm pattern mask.

Equally as before, based on the results, for the mask pattern 30–5 μm, the developed fabrication process concerning the measured values versus mask dimension, has an accuracy of $W_1=97.6\%$ and $W_2=91.2\%$.

It should be noted that the difference between the measured height h and the manufacturer's process guidelines value (5.06 μm) is mainly due to the different equipment and conditions utilized in both processes. However, this difference is not critical in practical applications because the focal length f is only affected by $\approx 9\%$. Nevertheless, the value of h , is easily readjusted with more spin time, speed or both.

Post-thermal reflow structures (microlenses)

In Figure 3.31 is represented the post-thermal reflow microstructures (microlens) with the two parameters (W and h) that were used for measuring the mean and standard deviation.

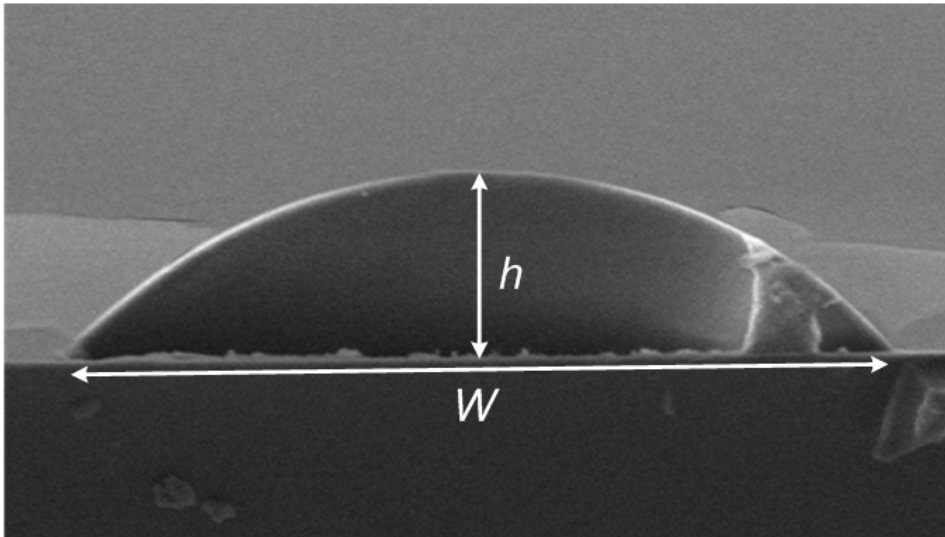


Figure 3.31 – The dimensions that were used for evaluating the reproducibility of the fabrication process for the post-thermal reflow microstructure (microlens).

The same methodology and equations used before were applied in this post-thermal reflow statistical study. The presented values (Figure 3.32 and Figure 3.33) are in accordance with the surface tension flow mechanics.

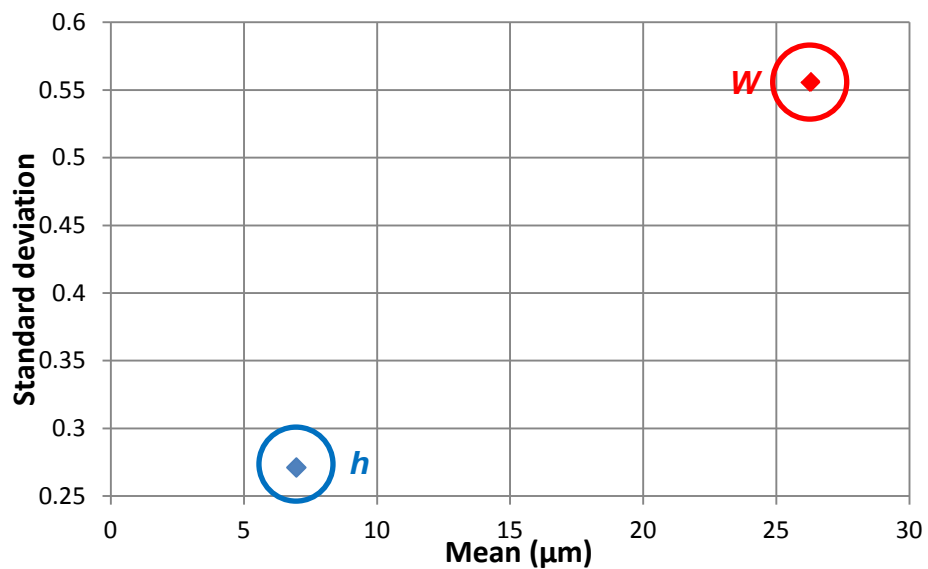


Figure 3.32 – Post-reflow mean and standard deviation values for the 24–5 μm pattern mask.

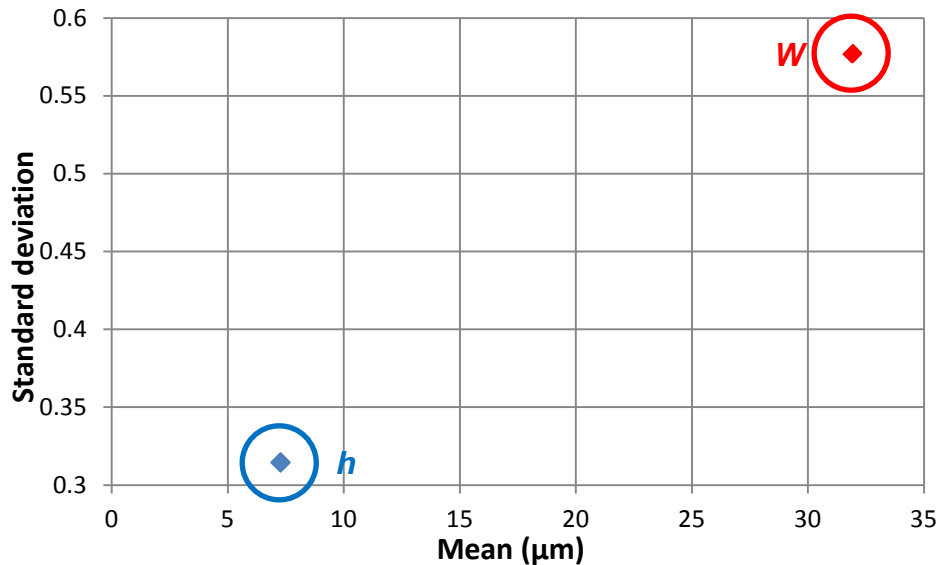


Figure 3.33 – Post-reflow mean and standard deviation values for the 30–5 μm pattern mask.

3.5 Results analysis

The microlenses design started with the FEM simulations to set and evaluate some parameters needed to fulfill the desired objectives. These objectives included the microlenses' purpose of enhancing the light capture on photodetectors. The complete fabrication processes, and correspondent comparison and evolution, were explained and the initial and final structures obtained were measured and characterized using profilometry and SEM images. The several steps that comprise the photolithographic process were explained and justified, and are flexible enough to be changed according to the desired final size, requirements and applications of the micro-optical device. It was also shown that the thermal reflow technique is ideal for obtaining lens profiles in polymer based microstructures due to the surface tension effect. Moreover, the thermal reflow is an easy process to control and the results obtained are very smooth, a requirement for microlenses with good quality. The developed fabrication process has great flexibility in terms of resizing the lenses as will be shown in Chapter 4. The direct fabrication of arrays of MLs on top of image sensors, such as CMOS electronics, as already presented in Chapter 1, opens new approaches and applications for optical microsystems by promoting the easy integration of passive and active elements in micro-optical systems.

References

- [1] A. Schilling, R. Merz, C. Ossmann and H. Herzig, "Surface profiles of reflow microlenses under the influence of surface tension and gravity," *Optical Engineering*, vol. 39, no. 8, pp. 2171-2176, 2000.
- [2] V. Lin, H.-C. Wei, H.-T. Hsieh, J.-L. Hsieh and G.-D.J. Su, "Design and fabrication of long-focal-length microlens arrays for Shack–Hartmann wavefront sensors," *Micro & Nano Letters*, vol. 6, no. 7, p. 523–526, 2011.
- [3] M. Wei, I. Su, M. Jung and K. Huang, "Real-time Observation for the Formation of Microlens Arrays Fabricated Using Thermal Reflow Process," *Tamkang Journal of Science and Engineering*, vol. 7, no. 2, pp. 81-86, 2004.
- [4] O. Matoba, E. Tajahuerce, B. Javidi, "Three-dimensional object recognition based on multiple perspectives imaging with microlens arrays," in *LEOS 2001. 14th Annual Meeting of the IEEE Lasers and Electro-Optics Society. Part vol.2*, pp.495-6, Piscataway, New Jersey, USA, 2001.
- [5] K. Carlson, M. Chidley, K. B. Sung, M. Descour, A. Gillenwater, M. Follen, R. Richards-Kortum, "In vivo fiber-optic confocal reflectance microscope with an injection-molded plastic miniature objective lens," *Applied Optics*, vol. 44, no. 10, pp. 1792-1797, 2005.
- [6] N. Chronis, G. Liu, K. Jeong and L. Lee, "Tunable liquid-filled microlens array integrated with microfluidic network," *Optics Express*, vol. 11, no. 19, pp. 2370-2378, 2003.
- [7] H. Hamam, "A two-way optical interconnection network using a single mode fiber array," *Optics Communications*, vol. 150, no. 1-6, pp. 270-276, 1998.
- [8] J. Ho, T. Shih, J. Cheng, C. Sung and C. Chen, "A novel method for fabrication of self-aligned double microlens arrays," *Sensors and Actuators A: Physical*, vol. 135, no. 2, p. 465–471, 2007.
- [9] S. Sinzinger and J. Jahns, *Microoptics*, Second ed., Weinheim: Wiley-VCH, 2003.

- [10] F. Smith and T. King, *Optics and photonics: An introduction*, J. W. & Sons, Ed., Chichester, 2000.
- [11] R. Rocha, J. Carmo and J. Correia, "Fabrication Methodology of Microlenses for Stereoscopic Imagers Using Standard CMOS Process," *ECS Transactions: Electrochemical Society*, vol. 49, no. 1, pp. 323-330, 2012.
- [12] C. Lin, H. Yang and C. Chao, "Hexagonal microlens array modeling and fabrication using a thermal reflow process," *Journal of Micromechanics and Microengineering*, vol. 13, no. 5, pp. 775-781, 2003.
- [13] <http://www.clariant.com>, C. GmbH.
- [14] <http://www.microchemicals.com/products.html>.
- [15] E. Hecht, *Optics*, Fourth ed., Pearson Education, 2002.
- [16] <http://www.microchemicals.eu>, M. GmbH.
- [17] R. Rocha, J. Carmo, J. Gomes and J. Correia, "Fabrication of AZ4562 refractive microlenses array for light enhancement on optical microsystems," in *Proceedings of MME 2012*, Ilmenau, Germany, 9-12 September 2012.
- [18] J. Lee, K. Kim, M. Jung, H. Kang, J. Kim, J. Hong and H. Oh, "Modeling for Resist Reflow of an Elongated Contact Hole," *Journal of the Korean Physical Society*, vol. 49, no. 2, pp. 646-650, August 2006.
- [19] J. Tsai and Y. Hsu, "Profile of Microlens Fabricated by the Thermal Reflow Process," *IEEE Transactions on Magnetics*, vol. 47, no. 3, pp. 598- 601, March 2011.
- [20] F. O'Neill and J. Sheridan, "Photoresist reflow method of microlens production: part I. Background and experiments," *Optik*, vol. 113, p. 391-404, 2002.
- [21] T. Osswald, L. Turng and P. Gramann, *Injection Molding Handbook*, Second ed., Munich: Hanser, 2008.

- [22] R. Rocha, J. Carmo, J. Gomes, M. Belsley and J. Correia, "Microlenses array made with AZ4562 photoresist for stereoscopic acquisition," *Procedia Engineering, Elsevier Science*, vol. 47, pp. 619-622, 2012.
- [23] I. Kenyon, *The Light Fantastic: A Modern Introduction to Classical and Quantum Optics*, 2nd ed., Oxford: Oxford University Press, 2011.
- [24] J. Carmo, M. Silva, R. Rocha, J. Ribeiro, L. Goncalves and J. Correia, "Stereoscopic image sensor in CMOS technology," *Procedia Engineering, Elsevier Science*, vol. 25, pp. 1277-1280, 2011.
- [25] R. Rocha, J. Carmo and J. Correia, "Microlenses for stereoscopic image formation," in *BIODEVICES 2012 - International Conference on Biomedical Electronics and Devices*, Vilamoura, Portugal, 1-4 February 2012.
- [26] R. Rocha, J. Carmo, M. Silva and J. Correia, "Polichromatic image sensor with microlenses for stereoscopic acquisition," in *Annual Seminar on Automation, Industrial Electronics and Instrumentation (SAAEI'12)*, Guimarães, Portugal, 11-13 July 2012.
- [27] A. Emadi, H. Wu, S. Grabarnik, G. de Graaf and R. Wolffenbuttel, "Vertically tapered layers for optical applications fabricated using resist reflow," *Journal of Micromechanics and Microengineering*, vol. 19, no. 7, 2009.
- [28] <http://www.jdphoto.co.uk/index.htm?sub-plots.html>.
- [29] H. Ottevaere, R. Cox, H. Herzig, T. Miyashita, K. Naessens, M. Taghizadeh, R. Völkel, H. Woo and H. Thienpont, "Comparing glass and plastic refractive microlenses fabricated with different technologies," *Journal of Optics A: Pure and Applied Optics*, vol. 8, no. 7, pp. 407-429, 2006.

4 Results and discussion

This chapter describes the results obtained concerning both the focal length characterization and the different approaches for integrating the MLs with the photodetecting substrate. Three approaches are considered: the first is to control the thickness between the MLs and the photodetecting substrate for allowing different focal lengths to be used depending on the application. The second one is setting the MLs' focal length within the photodetectors' depletion region for demonstrating that the current generation is enhanced for the same active area. Finally, the third application consists on a setup composed by a MLs array fabricated directly on top of the photodiodes (PDs) and in this approach, two solutions are presented. One is the fabrication of a ML using a photomask design measuring 24–5 μm (explained in section 3.4) on a square PD with the side measuring 24 μm . This setup enables the capture of light that would otherwise fall outside the photodiodes' active area resulting in an overall photocurrent generation gain. The other is the fabrication of a MLs array using the same photomask but on a square PD with the side measuring 240 μm for determining the level of photocurrent generation. Moreover, two light sources (red and white lights) were used for evaluating the light acquisition enhancement capacity. The three integration experiments that were done are listed below:

- polydimethylsiloxane (PDMS) was used as substrate enabling the thickness control of the layer between MLs and photodiodes;
- the middle layer between the MLs array and photodiodes being a 150 μm thin glass substrate for testing MLs with different dimensions and longer focal length f than previously done;
- direct fabrication of MLs on top of the photodiode substrate.

Moreover, the choice made concerning the photodiodes in complementary metal–oxide semiconductor (CMOS) technology is also justified.

4.1 Photodiodes

CMOS technology is extensively used in the fabrication of microelectronics. The main reasons for using this technology are the low-energy consumption, the same process and simultaneous steps for easy integration of both the n MOS and p MOS transistors in the same die and the comparative smaller required area (when compared with other processes such as the bipolar [1]) in the silicon wafer for fabricating a single transistor. The latter enables the integration of many transistors per area unit in what is known as very large scale integration (VLSI), allowing different functions to be achieved within the same die, such as signal acquisition, read-out and processing. Therefore, photosensitive structures, *i.e.*, photodiodes, are easily fabricated in CMOS technology and their use is appropriate for the context presented in this thesis. A photodiode uses the photoelectric effect for converting light (incident photons) into electric current (generation of electron-hole pairs), also called photocurrent. An interesting property is that the longer the wavelength, the smaller its energy is thus the deeper it penetrates into silicon [2] (see Figure 4.1).

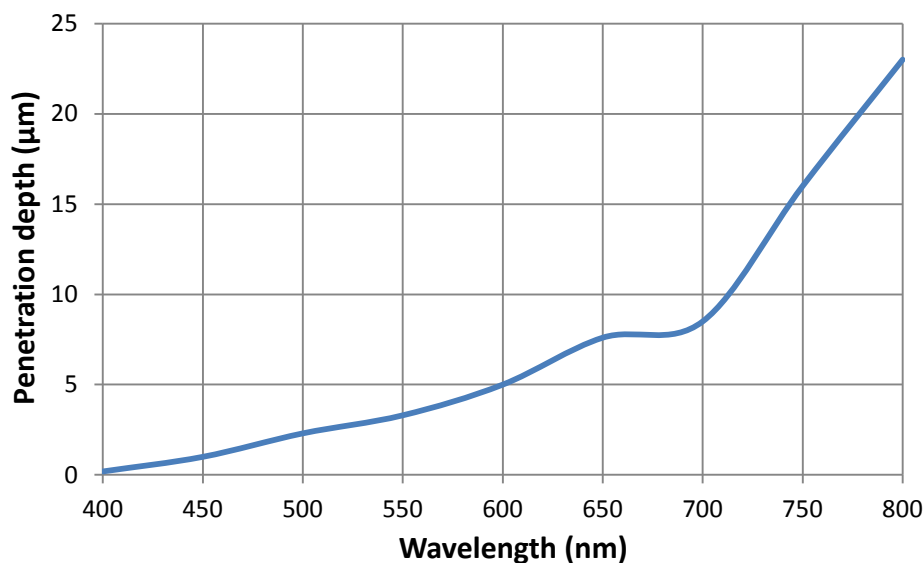


Figure 4.1 – Visible light penetration depth in silicon [3].

For the particular case of silicon, this conversion occurs when the energy of incident photons (E_{ph}) is greater than the bandgap energy, $E_{gap} \approx 1.1$ eV [4], and as demonstrated in equation (2.1), $E_{ph} = h \cdot f \geq E_{gap}$. Once this happens, an electron-hole pair is created, see concept in Figure 4.2. Due to the existence of a built-in electrical field (V_{bi}) in the p - n junction, the majority of the collected pairs comes from the depletion region. The

p and n type semiconductors are differentiated for having more holes and electrons working as carriers, respectively and for this reason they are called majority carriers [5]. This means that doping silicon (a chemical element from group IV which has four covalent electrons) with elements from group III, with more holes than electrons, a p type semiconductor is created. On the other hand, doping silicon with elements from group V, then, an n type semiconductor is produced. The neutral zone around the junction between these two types of semiconductors is called the depletion region [6]. This happens because the junction of two semiconductors, of n and p type, creates an electric field around them which makes the electrons-holes move out of it in opposite ways being then depleted of moving charges. The majority of the pairs that are generated outside the depletion region are recombined before overcoming the depletion boundary.

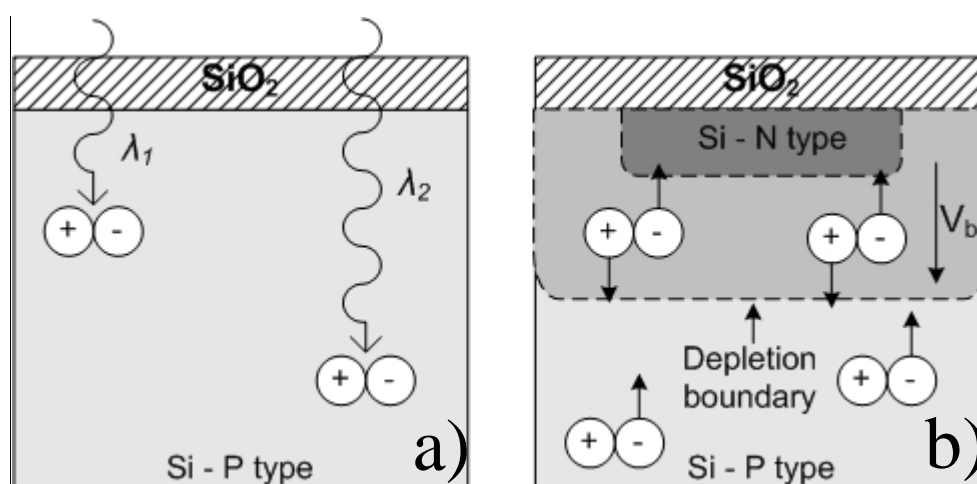


Figure 4.2 – In a) electron-hole pair generation with different wavelengths, $\lambda_1 < \lambda_2$. In b) electron-hole pair collection in a p - n junction.

Incident photons are absorbed by electrons in the valence band (electron donor) thus being excited to the conduction band (electron acceptor) and whose absence in the valence band corresponds to a hole which in turn, behaves like a positive charge in terms of effective motion. Many of the electrons in the conduction band recombine with the holes left in the valence band. For actually obtaining an electric current, it is necessary to remove the electrons before they naturally recombine. This is achieved using a p - n junction which is reversely biased thus originating a region without moving charges, *i.e.*, the depletion region. The direction of the existing electric field in this region forces the charges out of it. The electrons excited by the photons inside, or close to, the depletion region are drawn to the n -type region before they are recombined to the p -type region.

This is the process responsible for creating a photocurrent I_P which is proportional to the incident light intensity and is represented by [7]:

$$I_P = \frac{q\eta\lambda P_i}{hc} \quad (4.1)$$

where q is the electron charge, η is the photodiode's quantum efficiency, λ is the impinging wavelength, P_i is the incident optical power, h is the Planck's constant ($\approx 4.1356 \times 10^{-15}$ eV.s) and c is the speed of light ($\approx 300 \times 10^6$ m.s⁻¹). In other words, η is the probability of collecting electron-hole pairs created by the impinging photons before they can recombine.

$$\eta = \frac{\text{Electrons generation rate}}{\text{Photons incidence rate}} \quad (4.2)$$

In this sequence of ideas, photodiodes can be characterized by their quantum efficiency (the ability to absorb light being measured in %) and responsivity (which relates the generated current I_p with the incident optical power P_i and is measured in A/W). Therefore, the photodiode's responsivity R_{ph} is derived from equation (4.1) and is given by:

$$R_{ph} = \frac{I_p}{P_i} = \frac{q\eta\lambda}{hc} \quad (4.3)$$

4.1.1 CMOS photodiodes with a n+/p-substrate junction

The photodiodes, cross-section illustration seen in Figure 4.3, used as substrate are based on the type n^+/p -substrate junction photodiode fabricated in a standard CMOS process. These PDs were chosen due to the fact that they are a good option for visible light detection and also present good quantum efficiency for the visible spectrum [8]. Moreover, the selected PDs yield high fill-factor, since a deep n -well is not required for every pixel. The *On-semiconductor* 2-metal/1-poly 0.7 μm CMOS process was selected for fabricating the array [9]. In this process, the junction depth of the photodiodes is fully defined and cannot be changed. However, the spectral responsivity (*i.e.*, sensitivity) can

be improved by a suitable arrangement of dielectric layers on top of the photodiode surface. Basically, there are three major dielectric layers above the $p-n$ junction that implement the photodetector. The first oxide and second oxide are composed of silicon dioxide (SiO_2). The top protecting layer (overlayer) is made of both SiO_2 and silicon nitride (Si_3N_4). The *On-semiconductor* foundry allows the removing of the overlayer without providing any metal layer. For achieving this task, the regions of the layout must contain big polygons drawn with the overlayer mask (the mask used for defining the bonding pads locations) without polygons of *Metal 2* beneath.

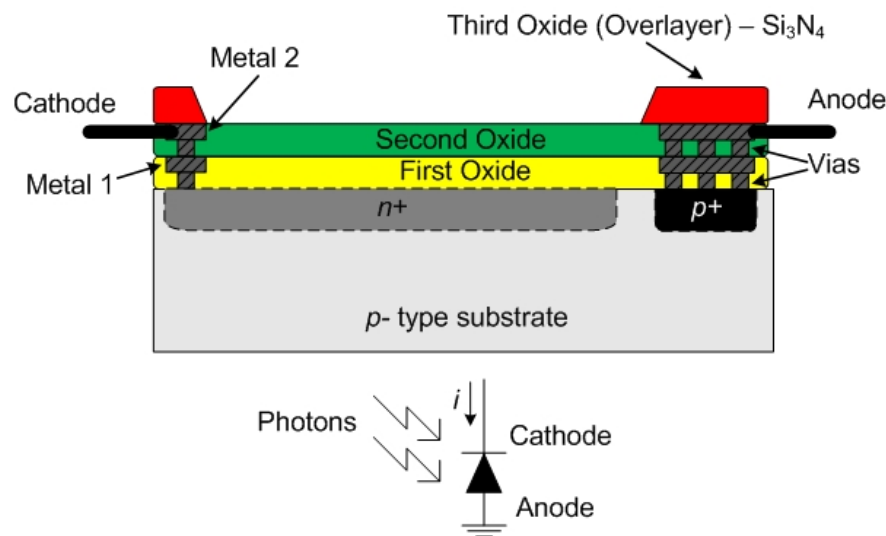


Figure 4.3 – Cross-section illustration of an n^+/p -substrate photodiode that is used in all the measurements made with and without MLs on top.

Therefore, an array of 16 photodiodes is used as the photodetecting element for light-current conversion. Figure 4.4 shows both a schematic drawing and a photograph of the fabricated CMOS microdevice, in a) and b) respectively, with the photodetectors array being composed by a matrix of 8×8 photodiodes. The square PDs side measures $240 \mu\text{m}$ and its measured photocurrent is presented in Figure 4.11 at different reverse bias values. Moreover, for different testing purposes, this die also contains single square PDs with sides measuring 5, 10, 24 (also shown in Figure 4.10), 50 and $120 \mu\text{m}$ which are visible on the die's right flank. It should be noted that some dies in dual in-line (DIL) packages were also supplied by the foundry and were used in the PDMS integration approach.

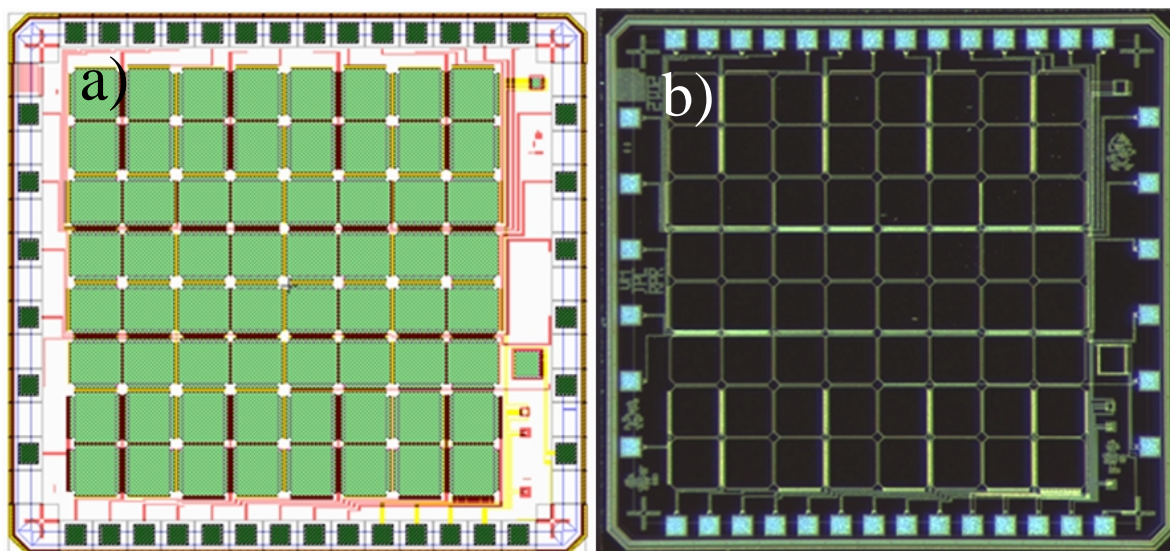


Figure 4.4 – Schematic in a) and optical photograph in b) of the photodiodes array. The value of the photocurrent measured for the $240\ \mu\text{m}$ photodiodes is presented in Figure 4.11.

4.1.2 Measuring setup

Two different light sources, white and red lights in Figure 4.5 and Figure 4.6, respectively, were used for measuring the photocurrents generated by different size photodiodes without and with MLs on top of them. This comparison serves for determining and quantifying the ability of the array of MLs for improving the PD's light-current conversion for the visible spectrum.

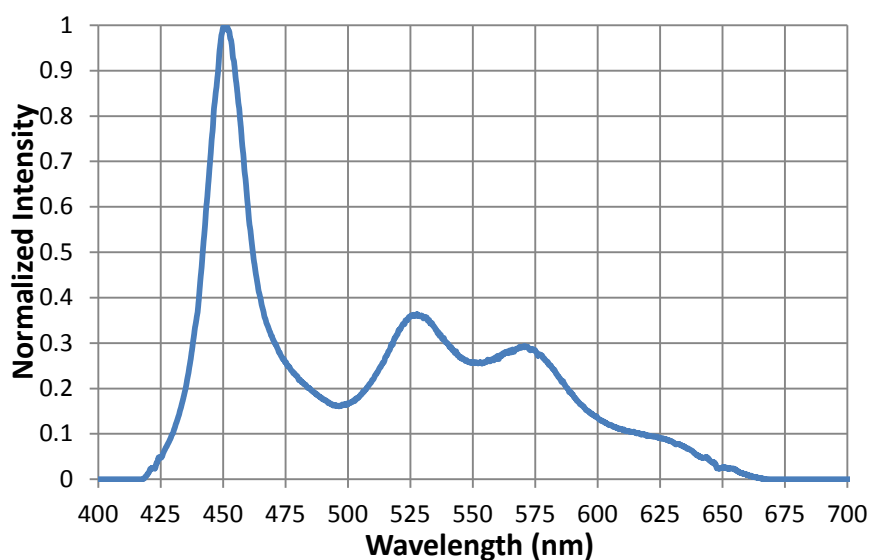


Figure 4.5 – Emitted white light spectrum [10] used for measuring the photocurrent generated by the PDs.

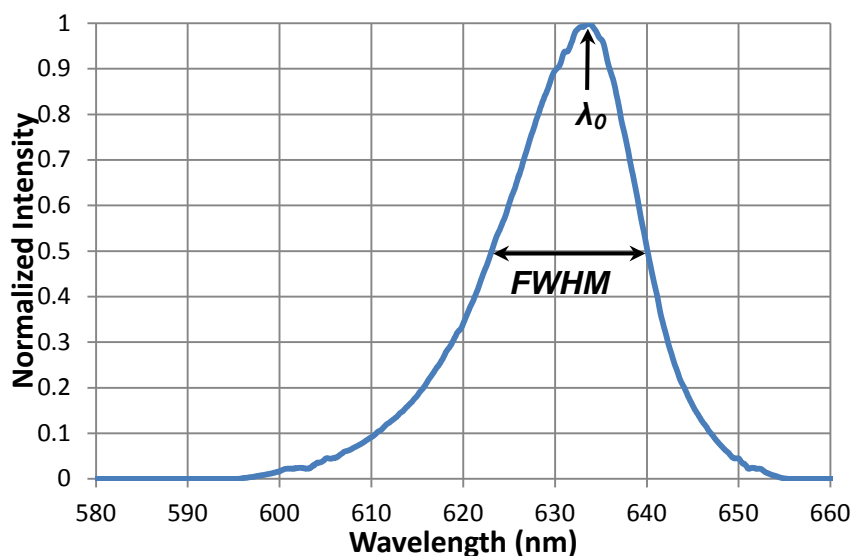


Figure 4.6 – Emitted red light spectrum [11] used for measuring the photocurrent generated by the PDs. The peak is $\lambda_0=632$ nm and the full width half maximum (FWHM) is 17 nm.

First of all, it was necessary to measure the photodiodes' intrinsic dark current for determining an important noise inherent in this type of CMOS devices. Figure 4.7 shows the experimental setup that was used for characterizing the PDs without and with an array of MLs fabricated on their surface. This setup is composed by a dark chamber, two light sources, a collimating lens for obtaining a parallel light beam, a luxmeter with a resolution of 0.1 lux (*CET CT 1330B High Accuracy Lux Digital Light Meter*) for measuring and calibrating the impinging light's optical power, a metallic positioning/aligning mechanical support and by the integrated microdevice (PDs without and with MLs). The distance between the collimating lens and the die is 33 cm.

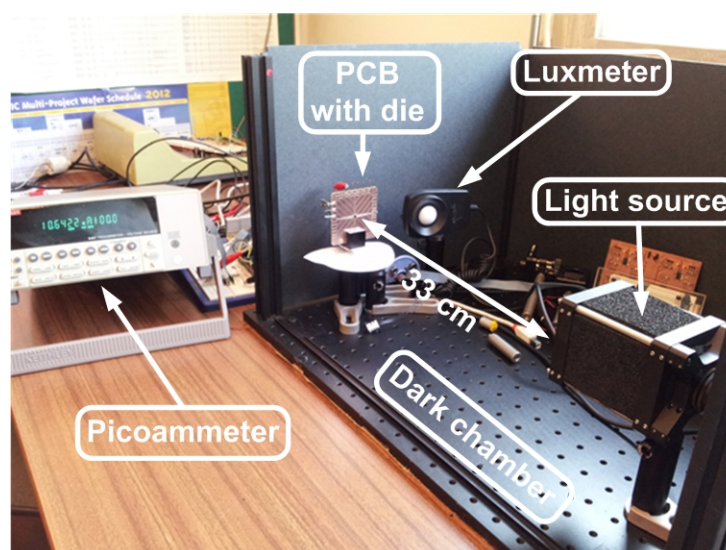


Figure 4.7 – Photograph of the setup that was used for characterizing the PDs without and with MLs.

The photocurrents were measured using a *Keithley 6487 Picoammeter Voltage Source* [12] with the setup schematic illustrated in Figure 4.8. This precision device allows measuring the photocurrent with a resolution of 10^{-14} A while being able to apply an electric potential difference to the measured photodiode for obtaining different reverse bias voltages. The reference for all the measurements presented in this thesis is the illuminance that is impinging on the luxmeter regardless of which light source was used. The illuminance is described as being the total luminous flux impinging on a surface per area unit. Moreover, the PDs were subjected to a linear increment of the illuminance from 0 to 2000 lux.

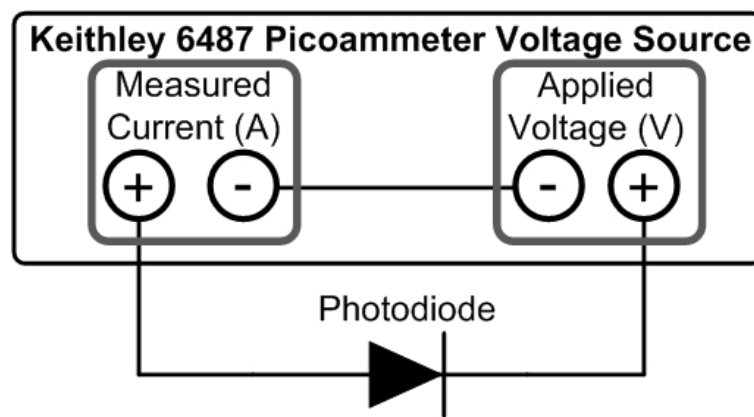


Figure 4.8 – Illustration of the schematic used for measuring the PDs with different reverse bias voltages.

Dark current measurements

The dark chamber is ideal for measuring the dark current and also prevents interferences from the environmental light to impinge into the photodetectors for the light-current conversion measurements. The dark current is the limiting factor in a photodiode that can be measured directly and one of the most relevant parameters [13]. This current is defined as the residual current that flows in a photodiode when there is no light impinging on it. The dark current is temperature dependent and not constant along the time, so, in Figure 4.9, is illustrated the typical dark current variation values. In this figure are represented the measurements for the 24 μm square PD without and with a ML on top of it at different values of the reverse bias voltages (0 and -4 V).

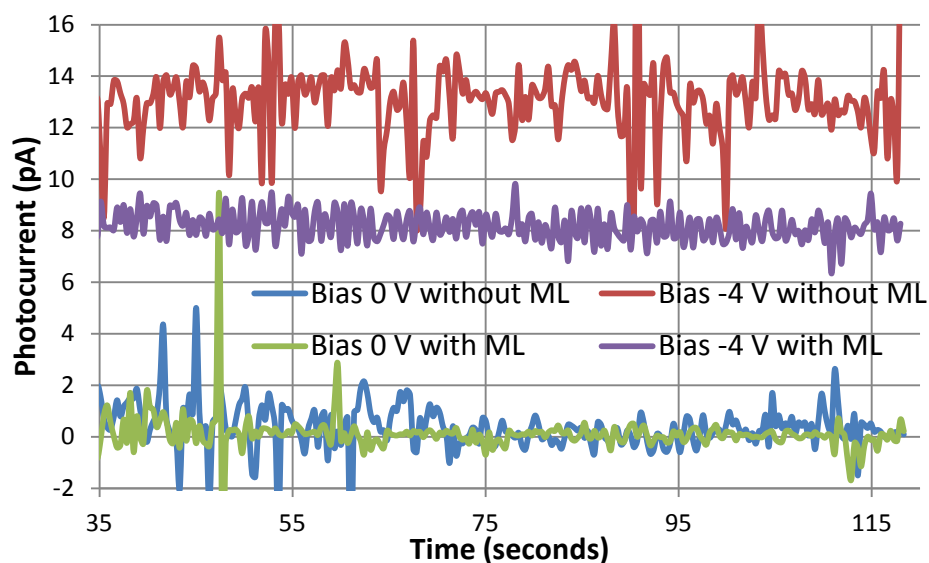


Figure 4.9 – Dark current, at room temperature, for the 24 μm square PD measured with the *Keithley 6487 Picoammeter Voltage Source* at 0 and -4 V reverse bias. These measurements were done without and with a ML.

Moreover, in Table 4.1, the photocurrent values (in pA) obtained for a different solution in fabricating MLs directly on the PD's surface (under the same measurement conditions as in the previous example) are shown. As demonstrated in section 4.3.3, this solution is a setup consisting of an array of eight 24–5 μm MLs fabricated on a 240 μm square PD. Therefore, the dark current values for the 240 μm square PD without and with a MLs array are presented in the following table. It should be noted that, with MLs, not only the dark current values decrease but also the chart lines have less pronounced variations.

Table 4.1 – Dark current values (in pA) for the 24 and 240 μm square PD for two reverse bias voltages. The measurements were done with and without MLs on top of the photodiodes.

	Without MLs		With MLs	
	Bias 0 V	Bias -4 V	Bias 0 V	Bias -4 V
24 μm square PD	0.685	13.426	0.442	8.67
240 μm square PD	1.06	21.5	0.907	18.4

Photodiodes measurements

The photocurrents measured for the 24 μm and 240 μm photodiodes are shown in Figure 4.10 and Figure 4.11, respectively. These measurements were done without MLs

on top of the PDs and under the linear increment of the two light sources' illuminance (from 0 to 2000 lux) for two values of reverse bias voltage, 0 and -4 V. The data displayed in Figure 4.9 and Table 4.1 demonstrate that, in this measuring setup, the order of magnitude of the dark current is very small when compared to the measured photocurrent so it can be considered negligible.

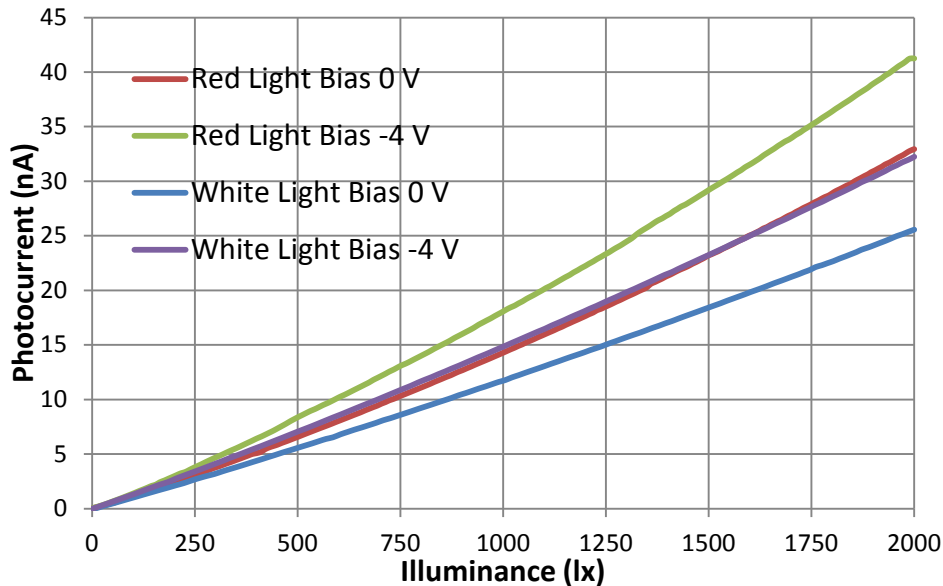


Figure 4.10 – Measured photocurrent for the 24 μm photodiode as a function of both the incident normal red and white light illuminance, in lux, at two values of the reverse bias, 0 and -4 V.

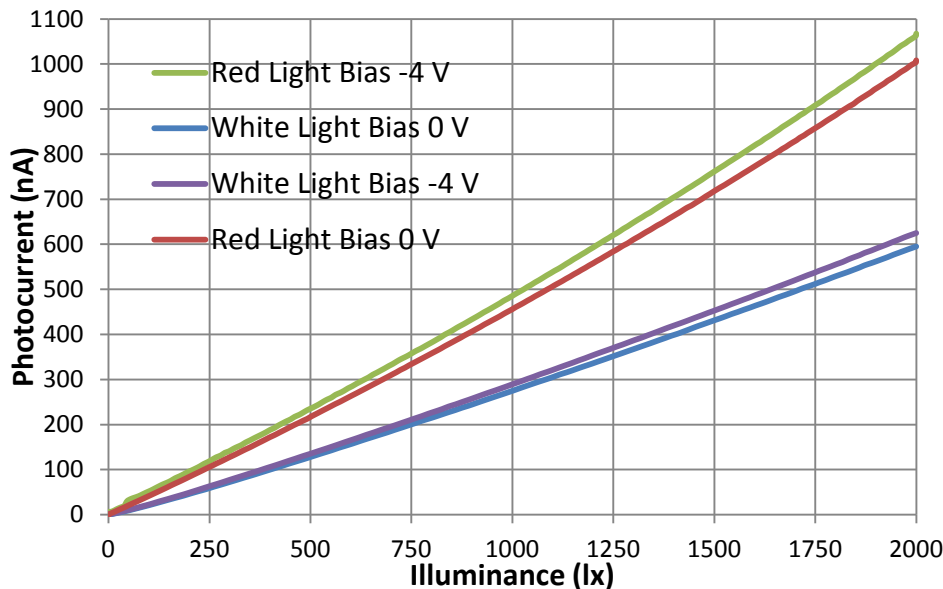


Figure 4.11 – Measured photocurrent for a 240 μm photodiode as a function of both the incident normal red and white light illuminance, in lux, at two values of the reverse bias, 0 and -4 V.

The increment of the reverse bias increases the width of the depletion region thus the PD is able to generate more current. The current generation is even more evident for the red light due to its penetration depth in silicon.

AZ4562 transmittance measurement

In order to determine the losses that the film of AZ4562 produces in light transmission, the setup seen in Figure 4.12 was used. Under the same conditions as the previous results, the photocurrents that a PD is able to generate without and with a film of AZ4562 are investigated. When these results are compared, it is possible to determine how much light is lost as it crosses the AZ4562 film thus measuring the photoresist's transmittance for the two light sources. This quantity is then considered as being the total optical losses in the proposed fabrication and integration solutions. The thickness of photoresist film used in this measurement is the same as the MLs' maximum height h .

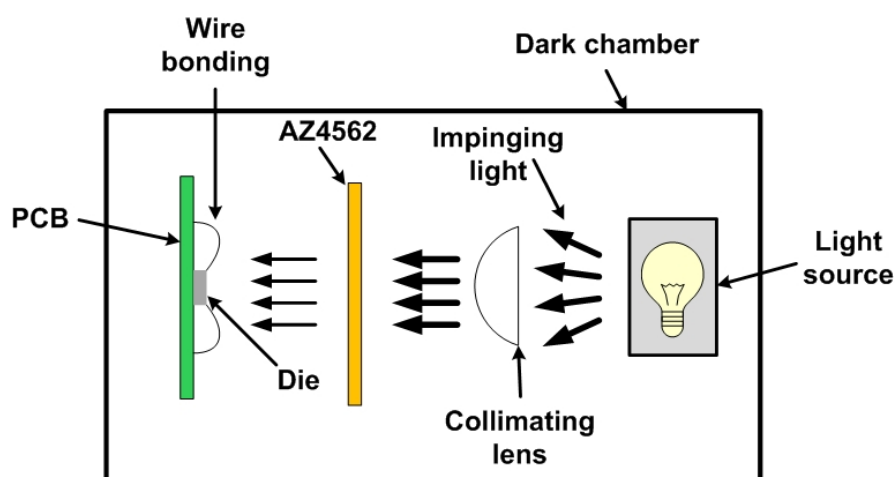


Figure 4.12 – Transmittance measuring setup.

Therefore, Figure 4.13 shows the AZ4562 measured transmittance as the illuminance is linearly incremented for the two light sources used.

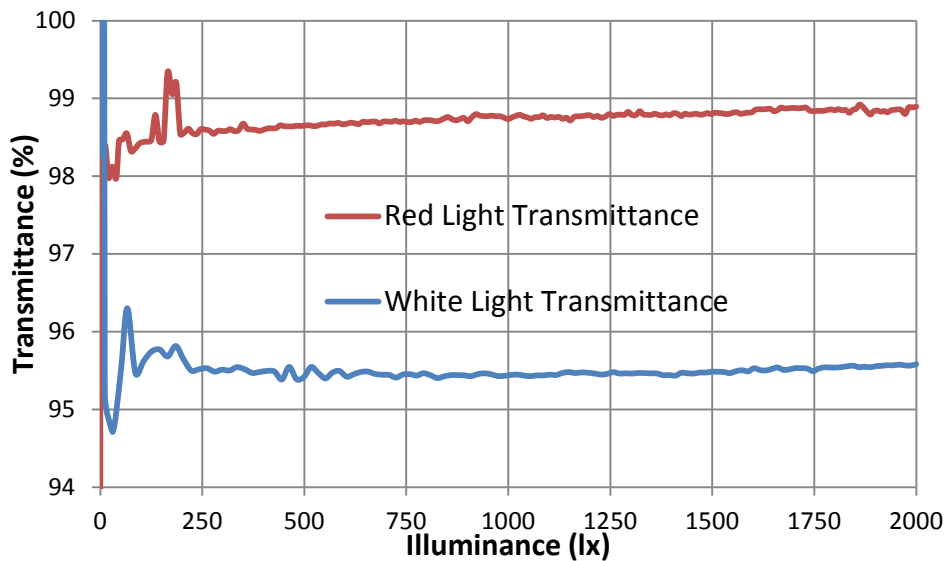


Figure 4.13 – AZ4562 transmittance for white and red lights from 0 to 2000 lux.

Whereas in Figure 4.14 is illustrated the average value of the AZ4562 transmittance for the two light sources.

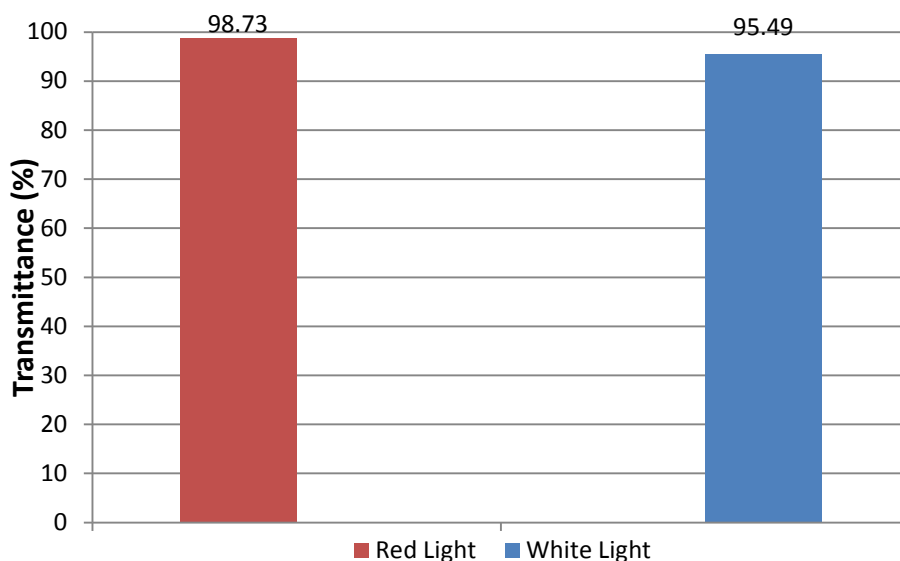


Figure 4.14 – Average AZ4562 transmittance for white and red lights.

4.2 Focal length characterization

An experimental setup was assembled for determining the focal length of one of the fabricated spherical microlenses arrays samples presented in Chapter 3. In simple terms, this setup allows one to monitor the variations in the spatial profile of a tightly focused Gaussian beam as one lens of the microarray is translated near its waist, thus determining the focal length of the microarray lens. Normally, lasers (with $\lambda=632.8$ nm)

are used in optical systems due to their propagating Gaussian beam nature (depicted in Figure 4.15). In this picture is presented the $1/e^2$ asymptotes of the beam irradiance profile [14]. In this mathematical approximation the beam waist radius w_0 is probably the most important parameter [6] being equal to $1/e^2$ of the beam's peak value intensity. It should be noted that this is the representation of a real laser beam whereas an ideal laser beam should be closer to a parallel profile.

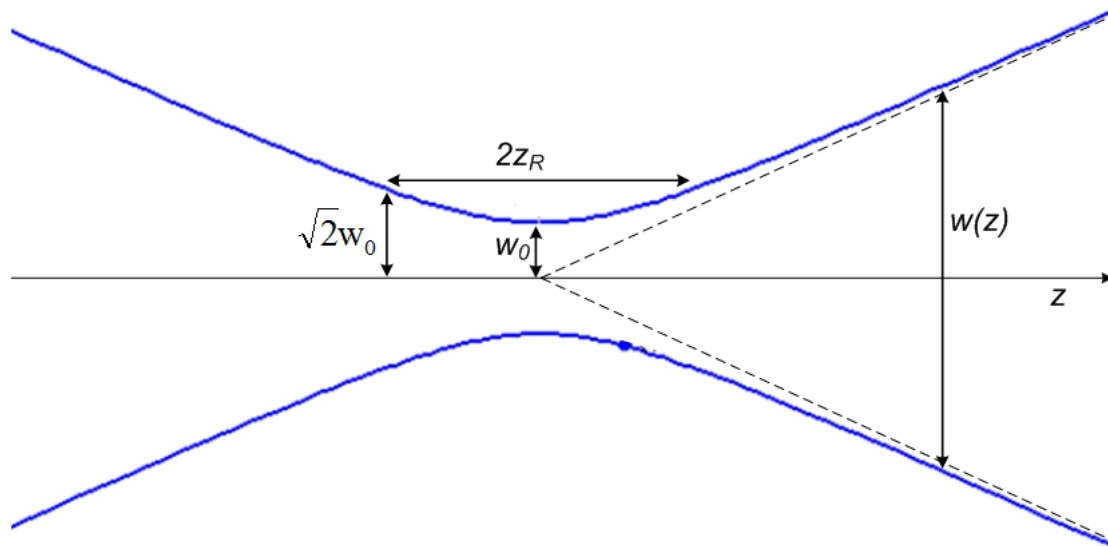


Figure 4.15 – Gaussian beam parameters where $w(z)$ is the beam's radial width at a given distance, w_0 is the thinnest radial width known as beam waist, z_R is the Rayleigh length being $\sqrt{2}w_0$ where the beam area is two times bigger than the beam area in w_0 . In the length between these two values, w_0 and $\sqrt{2}w_0$, the beam is considered collimated because its size is approximately constant.

Therefore, a Gaussian beam from a He-Ne (helium-neon) laser (*Melles Griot model 05LHP171*) was focused to a beam waist with a $1/e^2$ diameter of approximately $4.2 \mu\text{m}$ using an aspheric lens (*New Focus model 5724*) with an effective focal length of 8 mm and a numerical aperture of 0.5. A 14-bit CCD camera, without a glass cover filter designed for laser beam characterization (*DataRay WinCamD*), was then placed with the CCD surface approximately 1.2 cm downstream from the beam waist (narrowest radial size) created by the aspheric lens. The glass slide with the fabricated microarray was then mounted on a micrometer driven $x \times y \times z$ translation stage and placed perpendicular to the beam with the MLs array on the exit side, as shown in the measuring setup displayed in Figure 4.16.

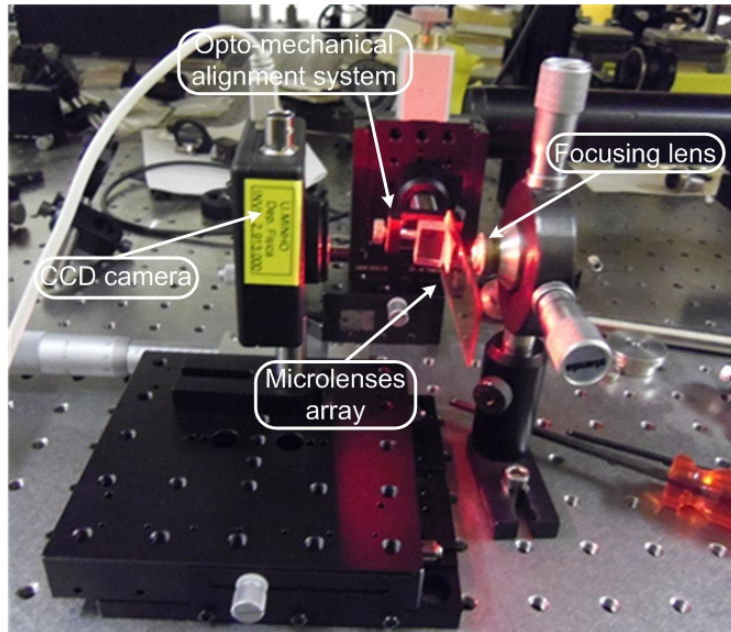


Figure 4.16 – Setup with the opto-mechanical alignment system used for measuring the focal length.

Figure 4.17 shows the beam profile captured by the CCD camera when the slide was positioned so that only the glass substrate was illuminated.

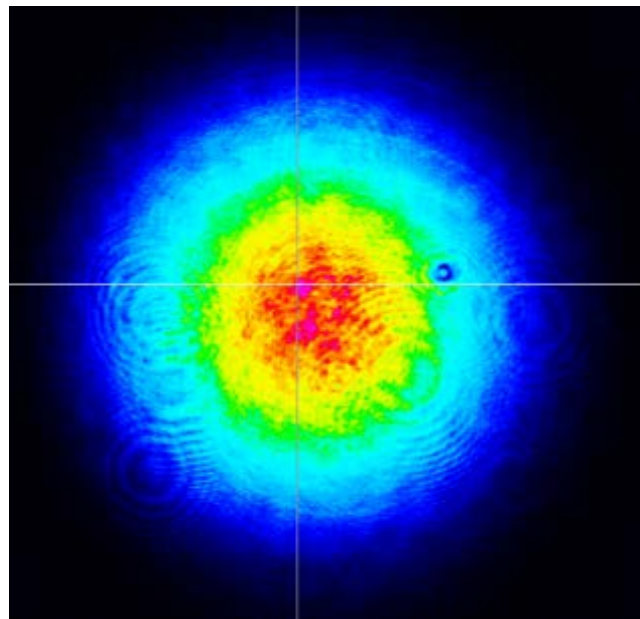


Figure 4.17 – The false color image of the spatial distribution of the He-Ne laser beam after being focused by the aspheric lens and then passing through glass substrate that serves as a support for the MLs array. The beam has an ISO $1/e^2$ diameter of 2.55 mm.

The microarray was then shifted into the beam and translated until a minimum spot size, along the direction of the spherical lens axis (vertical direction), was obtained as shown in Figure 4.18.

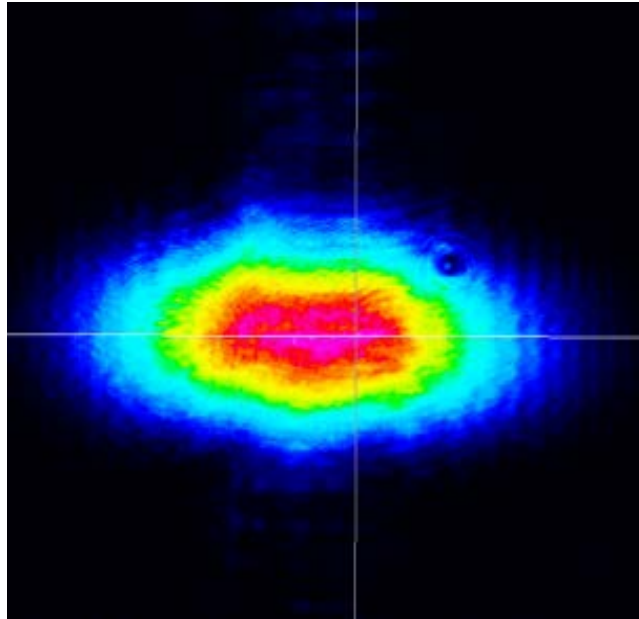


Figure 4.18 – The image obtained after the beam transformed by one of the spherical microlenses in the array. The ISO $1/e^2$ diameters have been calculated to be 1.17 mm and 2.56 mm for the vertical and horizontal axes respectively.

Using the micrometer stage the microarray was then translated about the position of the best focus and the respective diameters along the vertical direction were determined by the *Dataray* beam analysis software. The results are displayed in Figure 4.19. Simultaneously, the beam width along the horizontal axes was also measured and was found to remain nearly constant at 2.56 ± 0.01 mm.

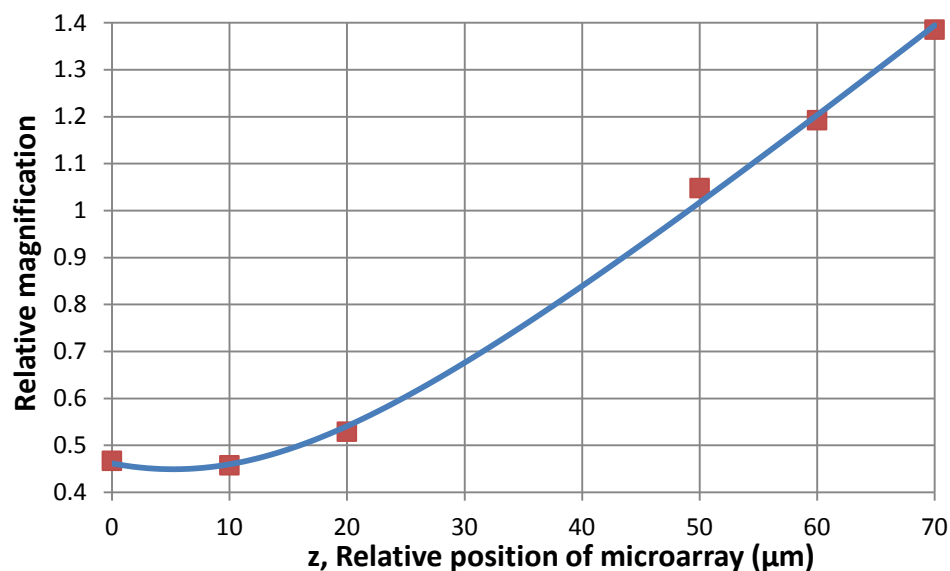


Figure 4.19 – The variation of the beam magnification as the microarray lens is translated near the best focus position. The blue curve is the theoretical fit according to equation (4.4) and yields an effective focal length of $f=49 \pm 2$ μm in air for the MLs array.

The blue curve in Figure 4.19 is a theoretical fit assuming Gaussian beam propagation and treating the microlenses array as a thin lens with an effective focal length f [15]. The predicted variation of the beam $1/e^2$ diameter propagating along the z -axis on the fixed CCD camera as the microarray lens is translated near the point of best focus is given by the following equation [15]:

$$M = \sqrt{\left(1 - \frac{z_0 + z}{f}\right)^2 + \left(\frac{z_R}{f}\right)^2} \quad (4.4)$$

where M is the effective magnification (ratio between the vertical and horizontal beam diameters), f is the effective focal length of the microlens, $z_0 + z$ is the distance between the lens and the beam waist created by the aspheric lens, while the Rayleigh length of the beam focused by the aspheric lens with w_0 the corresponding $1/e^2$ beam radius is given by [16]:

$$z_R = \frac{\pi w_0^2}{\lambda} \quad (4.5)$$

where λ is the laser wavelength and w_0 is the beam waist. This expression is valid in the limit that the distance between the CCD camera plane and the beam waist created by the aspheric lens is much greater than either the Rayleigh length or the effective focal length of the microlenses array. In carry out the measurements the MLs array was started close to one effective focal length behind the initial beam waist (z_0 represents this initial distance) and then translated the microarray through several different positions (*i.e.*, varied z). A nonlinear least squares fit to the data resulted in the following values:

- $f = 49 \pm 2 \mu\text{m}$;
- $z_0 = 44 \pm 4 \mu\text{m}$;
- $z_R = 22 \pm 1 \mu\text{m}$;

This value for the Raleigh distance is consistent with that estimated from the divergence of the He-Ne laser beam after being focused by the aspheric lens. Moreover, the error obtained for the focal length resulted in values that did not exceed 4.1% of the nominal f , which is very good for lenses with dimensions that are in the range of few

dozens of micrometers. This focal length characterization demonstrated that the values obtained in both the FEM simulations and the theoretical assumptions made in the calculations were accurate. This is valid for any different sized spherical microlens and the very small differences that exist can be neglected for the presented applications.

4.2.1 Interference patterns

Figure 4.20 shows the results of some experiments done with one MLs array [17]. The creation of the interference patterns was done by impinging the same laser beam, into the MLs array and observing the diffraction pattern in a perpendicular plane. In Figure 4.20a), signaled with a white arrow, is seen the laser dot (with a 1 mm diameter) impinging on the MLs array with the following corresponding pattern seen in the background. The distance between the array and the plane is 1.6 m and the pitch between the smaller red dots, seen in Figure 4.20b), is 3.5 cm. It can be observed in the picture below that each microlens in the array spreads the laser beam into a specific direction and it is also possible to see the interaction between the spread beams.

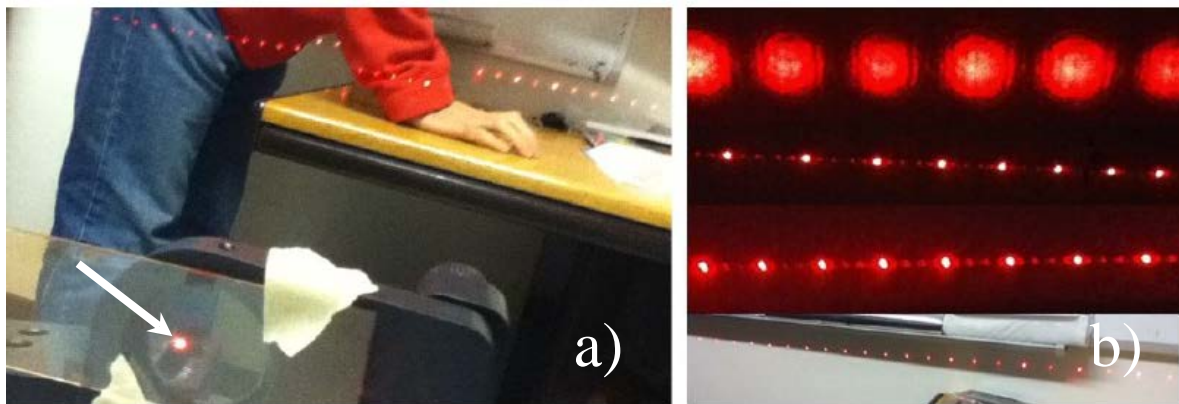


Figure 4.20 – Optical setup used for checking the interference patterns caused by the microlenses in the array. This setup is composed by an array of MLs, by a laser source and by a flat surface to project the spread beams. In a) is signaled where the laser dot (with a 1 mm diameter) impinges on the MLs array and in b) is the display of the pattern after the laser travels through the array of MLs.

4.3 Microlenses integration with the photodiodes

4.3.1 The first approach: using PDMS as substrate

For fabricating MLs arrays on top of photodiodes, and being able to control the layer thickness (*i.e.*, the substrate) between these two parts, a transparent elastomer was chosen, the polydimethylsiloxane (PDMS) *Sylgard 184* from *Dow Corning*. The PDMS is a heat-curable polymer and is supplied as a two-part kit. The kit is composed by the base elastomer (prepolymer) and the curing agent (cross-linker). This fabrication process is as follows (summarized in Table 4.2). The base elastomer and curing agent are manually mixed using a glass stick at a 10:1 weight ratio, respectively. After pouring this mixture into the DIL package's cavity where the die is glued on (see Figure 4.21), it is degassed in a vacuum chamber for a time period between 5 and 10 minutes, in order to remove all air bubbles. The curing process at 85 °C for one hour is required for promoting the cross-linking at a constant curing rate.

Table 4.2 – DIL cavity filling process with PDMS.

Process steps	Process parameters
Base and curing agent mixing	10:1 weight ratio
Pouring mixture into DIL cavity	Fill with micropipette until obtaining the desired thickness
Degassing (vacuum chamber)	5–10 minutes
Curing	1 hour@85 °C

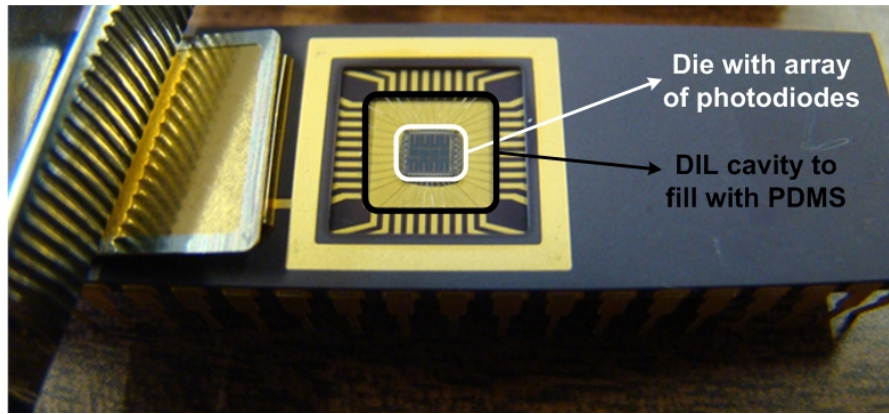


Figure 4.21 – DIL package with the die containing the array of photodiodes (marked in white) and in black is signaled the cavity to be filled with PDMS.

The factors that determine how the PDMS substrate thickness defines what MLs (using the parameters W and h) should be chosen depending on the dimension of the photodiode's cathode width (D) are represented in Figure 4.22.

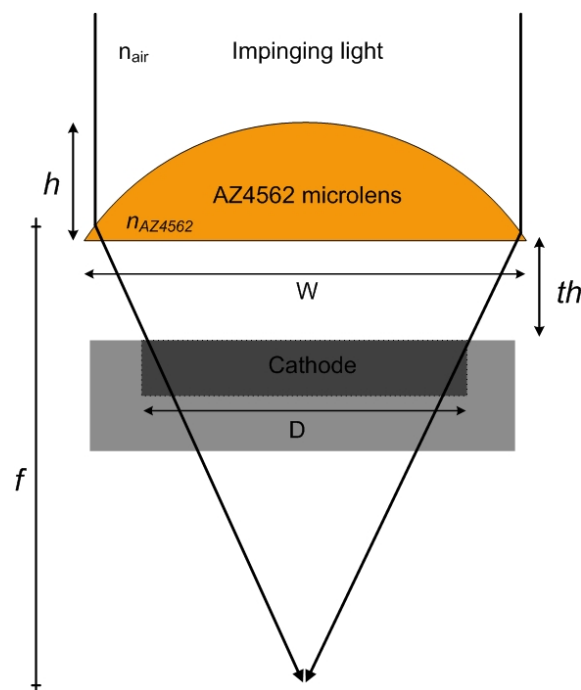


Figure 4.22 – Factors determining how the thickness (th) of the PDMS substrate allows defining what ML (W and h) should be chosen depending on the photodiode's cathode width (D).

The calculation of the PDMS thickness (th) needed for controlling the interception between the light convergence's cone with the surface of the photodiode's active area width (D) can be approximated to:

$$th = f - h - \frac{D}{W}(f - h) \quad (4.6)$$

The ability to control the PDMS thickness increases the flexibility for using different sized MLs depending on the application. This material presents itself as being a good choice for the proposed integration because it has a simple handling process and a working temperature interval (-45 to +200 °C) [18, 19] considerably larger than any of the MLs' fabrication process steps. It should be remembered that the prebake is done at 100 °C and the thermal reflow between 130 and 140 °C. Moreover, PDMS is transparent from 240 to 1100 nm [20], and has a refractive index $n \approx 1.41$. For the thicknesses that are considered it is possible to embed optical components into PDMS with minimal loss due to absorption [21]. In its unprocessed state, PDMS is liquid which facilitates the cavity filling. The curing agent, under temperature, cross-links the prepolymer turning it into a solid and, therefore, a substrate. Several DIL packages were filled with different amounts of PDMS with a micropipette for testing varying substrate thicknesses. For a volume range between 0.1–2.0 μl , the *biopette plus* autoclavable micropipette, has an accuracy of ± 12 to $\pm 1.5\%$ and precision < 6.0 to $< 0.7\%$, respectively. This filling procedure allows the user to control the thickness of the PDMS layer (*i.e.*, microlenses' substrate) so that MLs with different focal lengths can be fabricated on top of it.

The typical geometric volume with isosceles trapezoidal shape was achieved as is demonstrated in Figure 4.23a). Unexpectedly though, when these structures were submitted to the thermal reflow, the two layers, PDMS and AZ4562, merged together as is seen in Figure 4.23b).

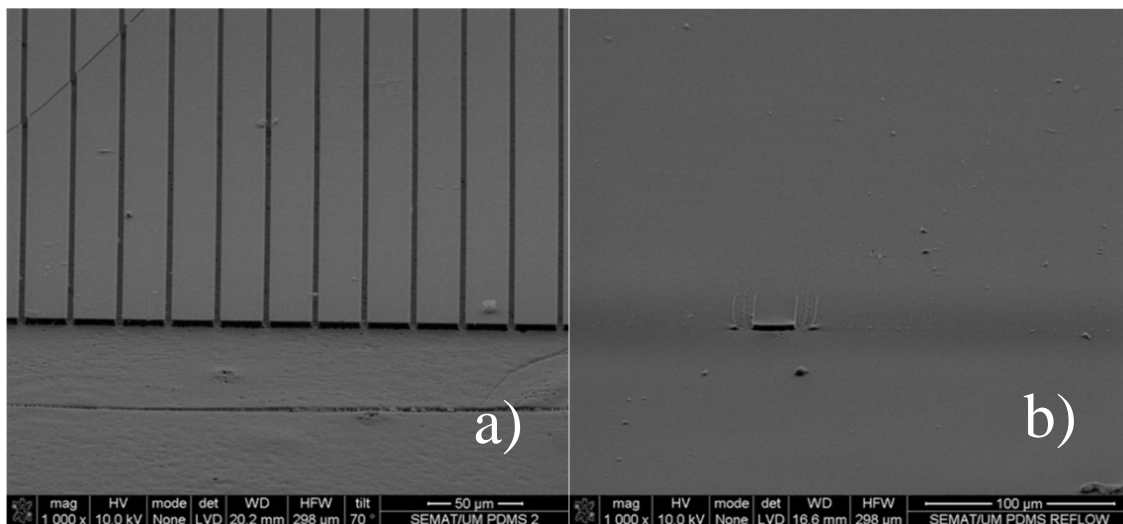


Figure 4.23 – SEM images of the fabricated AZ4562 microstructures before and after the thermal reflow in a) and b), respectively.

Since there were no obvious reasons why this mixture happened, several tests were performed in order to try and identify what could be the cause for this merge to be

happening. Moreover, in Figure 4.23a) cracks are also seen and other regions of the fabricated microstructure present more visible damages as Figure 4.24 clearly demonstrates.

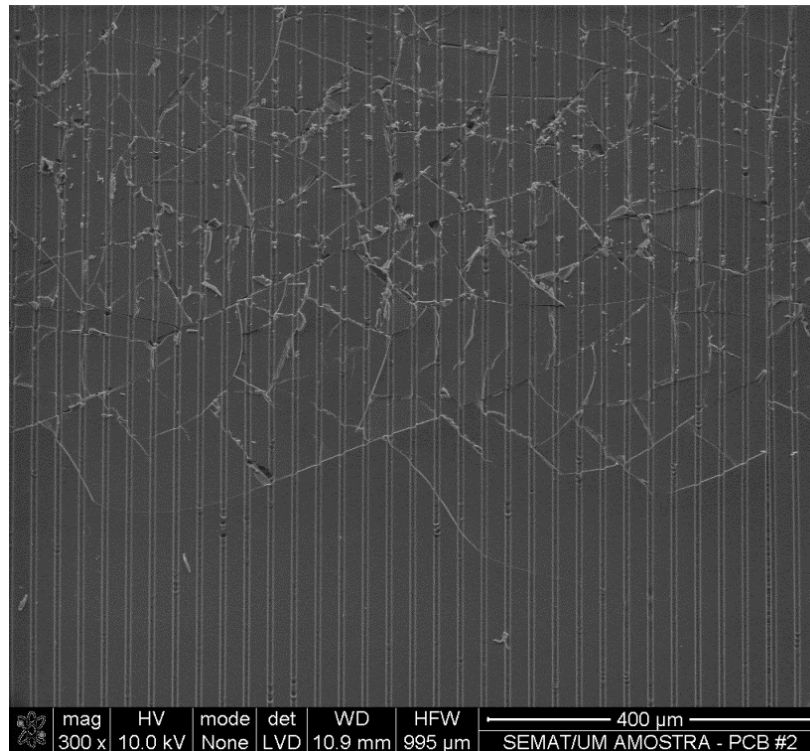


Figure 4.24 – Cracks appearing in both the PDMS and AZ4562 during fabrication.

Interface AZ4562–PDMS analysis

In order to identify, and thus take the necessary steps for preventing these structural damages from occurring in the AZ4562–PDMS interface, two analyses were performed. The first one is the real-time visualization through transmission optical microscopy of what happens in the materials' interface when subjected to the temperature gradient used in the thermal reflow. The measuring setup is seen in Figure 4.25.

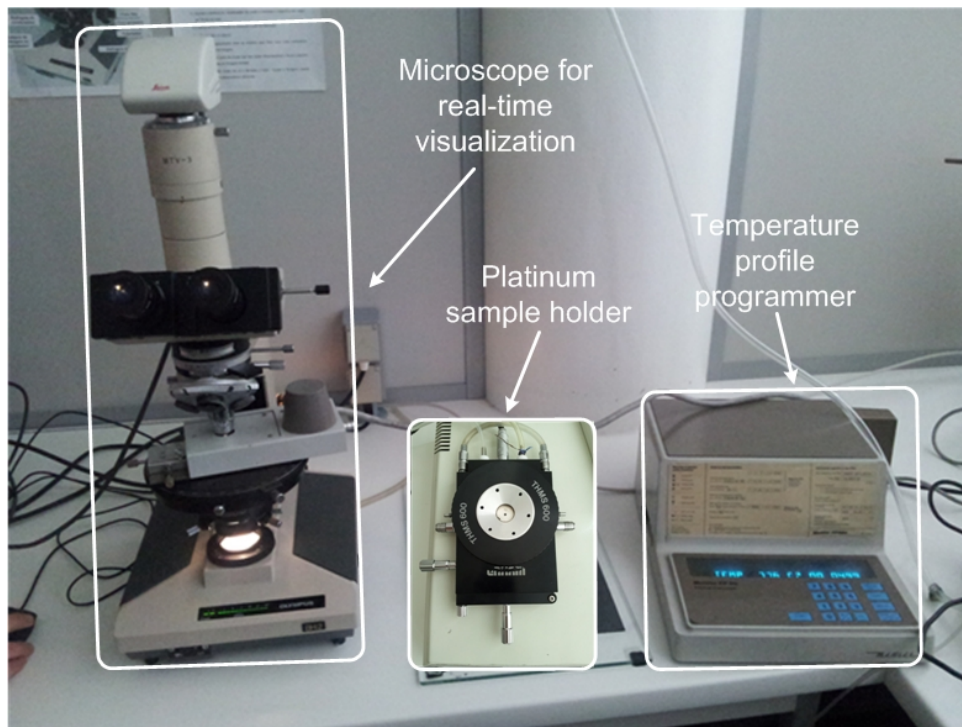


Figure 4.25 – Setup for real-time visualization of the interface between PDMS and AZ4562 under a temperature ramp up from 50 to 140 °C. The results are presented in Figure 4.26.

Basically, the sample is placed inside a platinum holder that is heated-up with the desired temperature profile. The sample holder is placed under the microscope and different snapshots are taken periodically along the time at increasing temperature values, from 50 to 140 °C, *i.e.*, similar to the thermal reflow temperature profile. The results of this analysis are shown in Figure 4.26 where a cross-section of a layer of AZ4562 coated on a PDMS substrate is seen. No changes in the interface were observed during this test so a different kind of analysis is required.



Figure 4.26 – Snapshots of the AZ4562–PDMS interface taken with the sample being heated-up at a temperature profile similar to the one used during the thermal reflow. The scale in the pictures represents 50 μm .

Since both materials used are polymers, then, a Fourier transform infrared (FTIR) spectroscopy analysis (equipment seen in Figure 4.27) was done. This analysis is for identifying chemical groups and then checking if any chemical phenomenon is occurring

in the materials' interface when subjected to the thermal reflow that could justify this merging.

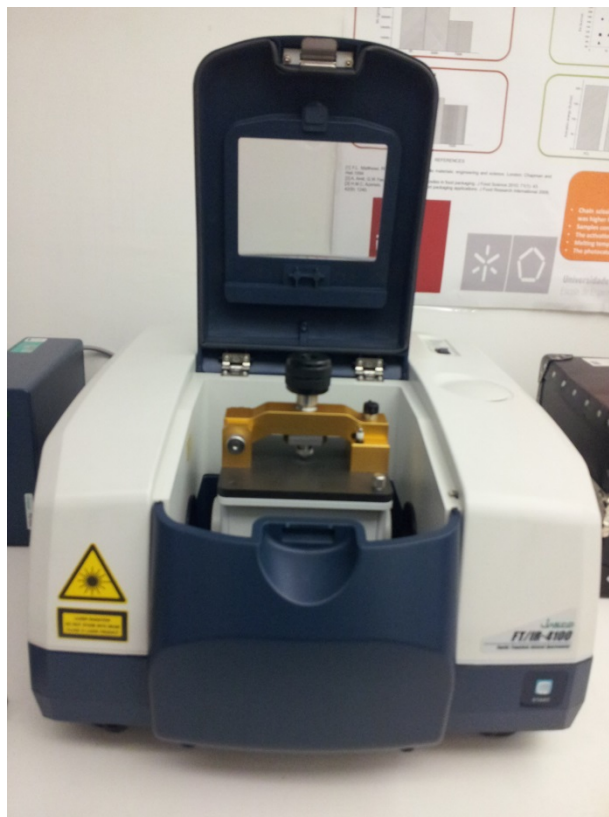


Figure 4.27 – *Jasco FT-IR 4100 spectrometer* [22].

In FTIR spectroscopy a sample containing different molecules is irradiated with infrared (IR) light while the transmitted spectrum is detected by a photosensor. Some of the emitted light might interact with various molecules contained in the sample. When a molecule absorbs a wavelength (in FTIR the wavenumber in cm^{-1} is normally used), it converts its energy into molecular vibration, *i.e.*, stretching or bending [23]. Since different types of molecular bonds absorb IR light of different wavelengths, then, specific chemical functional groups (chemicals compounds) can be identified. As certain groups of atoms absorb different wavelengths' energies they provide information about specific functional groups thus supplying valuable information about molecular properties. Therefore, FTIR data is represented as the measurement of the IR transmittance (%) across a sample and troughs in the chart lines are characterized as being absorptions. FTIR spectroscopy was done to the AZ4562 and PDMS alone and also together at intermediate steps of the fabrication process and the corresponding data is presented in Figure 4.28. These are each material's individual and joined signatures along important fabrication process steps such as UV exposure and thermal reflow. The two significant

changes that occur are signaled with a red circle. Only in the line “PDMS+AZ4562+UV+TR”, is identified that a chemical phenomenon does occur. This line corresponds to the sample containing a layer of AZ4562 on top of the PDMS substrate after UV exposure and thermal reflow. After the UV exposure during photolithography there’s a reduction in the peaks relating to the wavenumber interval 2100–2200 cm^{-1} and around absorption peak 2350 cm^{-1} . But, it is during the thermal reflow that those peaks disappear completely. This means that the chemical components that absorb energy at those frequencies deteriorate hence suggesting that some kind of undesirable degradation phenomenon is occurring in the materials’ interface. According to the literature [23], the wavenumber absorption interval 2100–2200 cm^{-1} is identified as being from the functional group alkyne described in Table 4.3 [24].

Table 4.3 – Classification of the chemical functional group identified through FTIR analysis.

Bond	Type of vibration	Specific type of bond	Appearance
C–C	C≡C Stretch	Terminal alkynes	Weak

The other absorption peaks around 2350 cm^{-1} are not classified yet and information about them in literature is also missing, therefore, this topic requires further research. The PDMS is a very flexible and promising solution for using as substrate in this type of integration. Nevertheless, further investigation should be done for understanding the merging and structural damage phenomena that is occurring between the two polymeric layers.

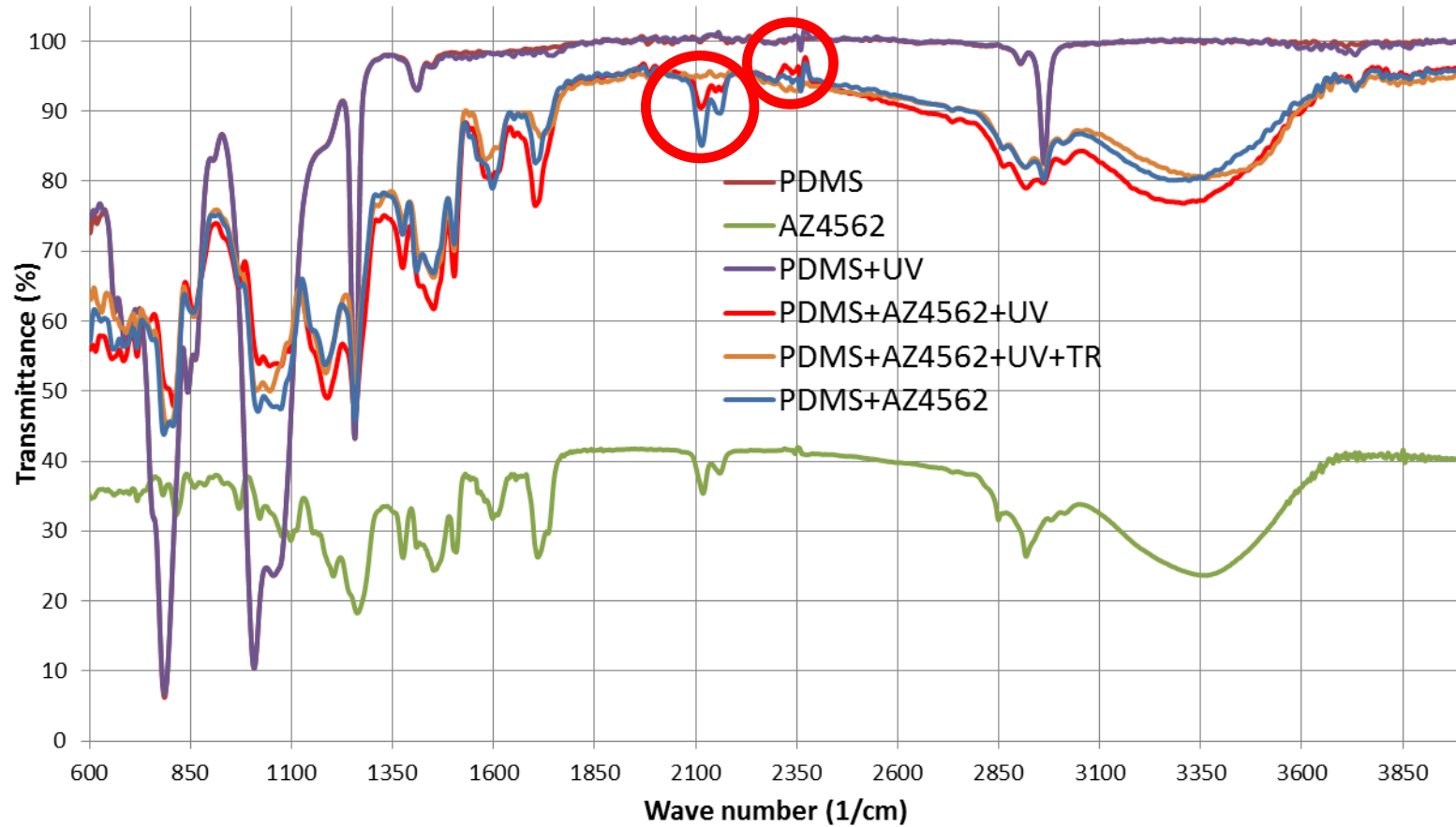


Figure 4.28 – FTIR analysis to the PDMS and AZ4562 individually and together at different periods of the fabrication. In red are signaled the two identified changes that occur in the materials’ interface. Only in the PDMS+AZ4562+UV+TR line the absorptions peaks disappear hence suggesting that some kind of degradation is occurring. This chemical phenomenon is yet to be fully identified and characterized.

4.3.2 The second approach: using a 150 μm thickness glass slide as substrate

A glass slide measuring $24\times 50\times 0.15$ mm (*length* \times *width* \times *thickness*) was used as the substrate for fabricating an array of MLs with $f\approx 170$ μm for demonstrating that they are capable of providing focus. With this procedure, it is shown that it is possible to set the focal length inside the depletion region (or very close to it). This is achieved by using a new photomask design (with the pattern explained in Chapter 3) measuring $73\text{--}5$ μm . It should be noted that, as demonstrated in section 4.2, there is only a small difference of $\approx 4\%$ between the theoretical and measured focal lengths. The MLs serve also to redirect light that would otherwise impinge outside the PD's active area into it. The proposed integration setup is illustrated in Figure 4.29. The photomask used allows the fabrication of three microlenses for each square 240 μm photodiode and the MLs' focal length is designed to be within the depletion region.

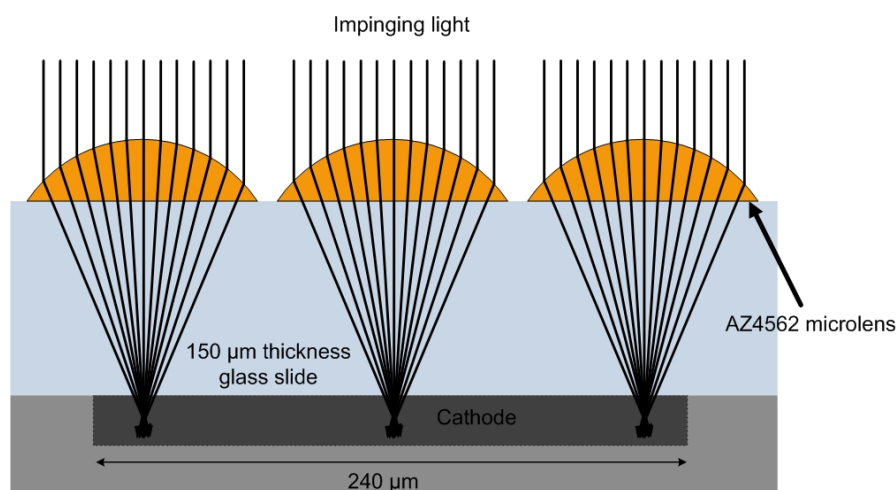


Figure 4.29 – Cross-section illustration of the 150 μm thickness glass slide integration solution. The measured photocurrent is seen in Figure 4.35. It should be noted that, in the visible spectrum, the index of refraction is similar for both the glass and the AZ4562 so the refraction between them is not represented.

A dicer was used to cut out of the glass slide just the area where the array was fabricated on. The dicing machine, shown in Figure 4.30, is an *Automatic Dicing Saw Disco DAD 2H/6T* [25] and the electroformed bond hub blade has a thickness of 200 μm .

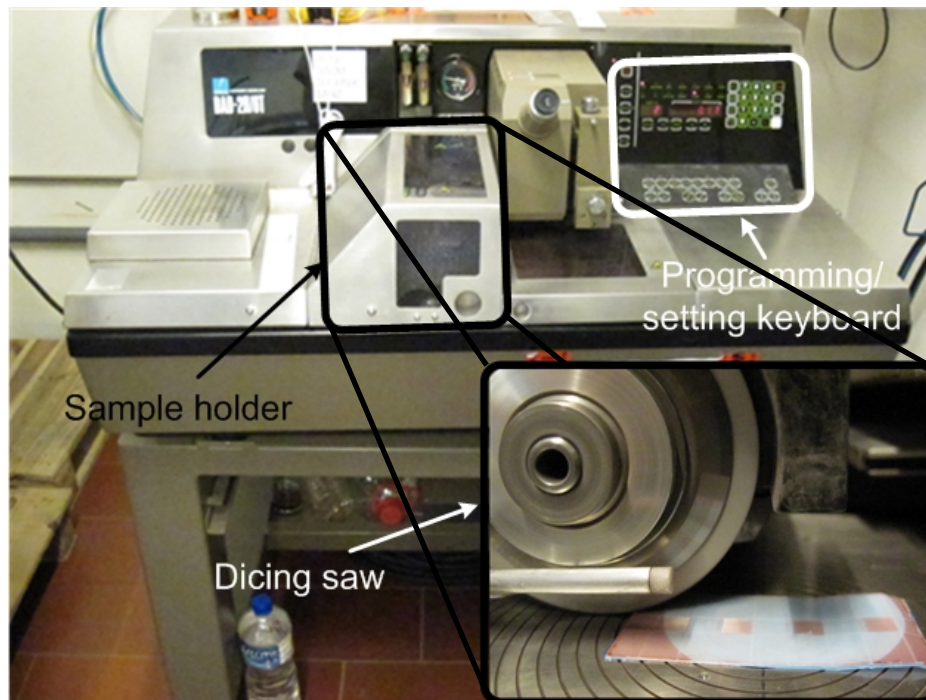


Figure 4.30 – Automatic Dicing Saw Disco DAD 2H/6T with a zoom-in detail of the dicing saw.

The cuts were done along the alignment marks in the mask at a speed of 1 mm.s^{-1} , a precision of $2 \mu\text{m}$ and with the blade rotating at 30.000 r.p.m . The glass slide is placed on a blue sticky tape, seen in Figure 4.31, so that it stays in position during the high-speed rotation of the saw.

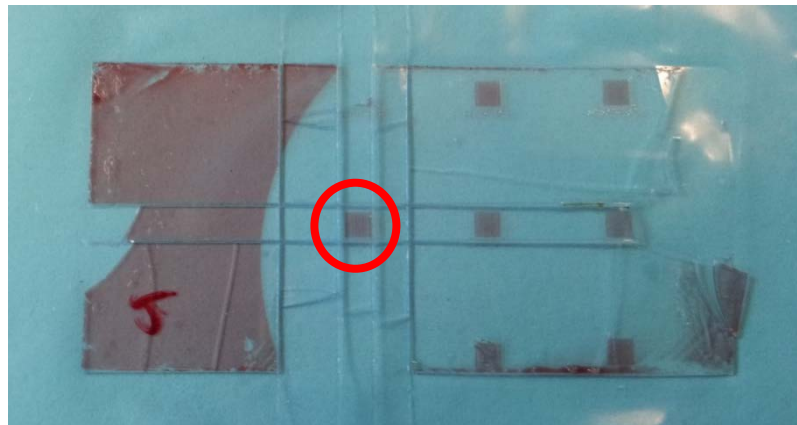


Figure 4.31 – Blue sticky tape used in the dicer for guaranteeing that the fabricated MLs array does not move during the dicing process. The total area of the array is $2.02 \times 2.01 \text{ mm}$ and is signaled with a red circle.

The die is attached to a PCB for performing the electrical connections between these two elements with the purpose of reading the generated photocurrent. Therefore, a *MEI 1204W Hybrid Wedge Bonder* (Figure 4.32) was used for performing the wire bonding between the die's pads and the PCB. The PCB serves as an adaptation board required for connecting to the picoammeter.

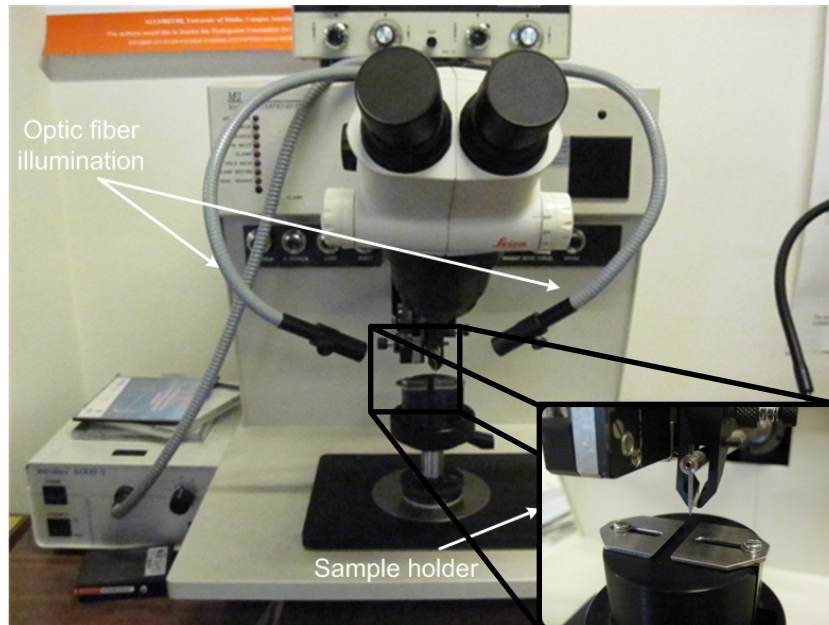


Figure 4.32 – MEI 1204W Hybrid Wedge Bonder for performing the wire bonding between the die and PCB.

Once the die is connected to the PCB, the glass slide with the MLs is mounted on top of the photodiodes array with the final assembly seen in Figure 4.33. The photocurrent of one 240 μm PD without MLs is used for comparison purposes and the measured photocurrent for this setup is seen in Figure 4.35.

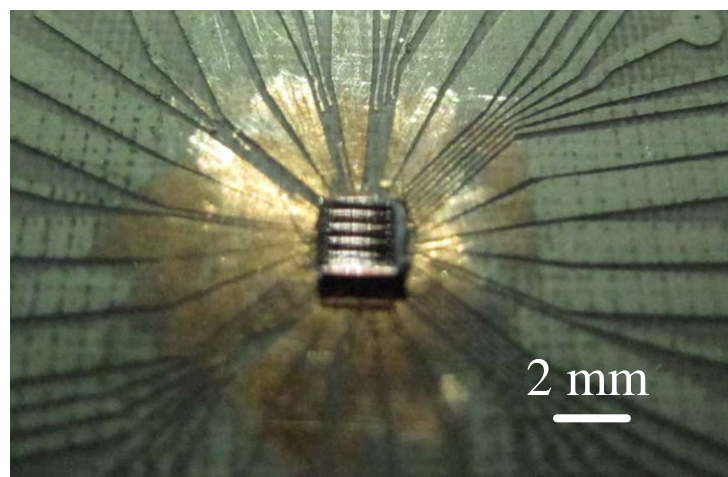


Figure 4.33 – Photograph of the MLs fabricated on the 150 μm thickness glass slide placed on top of array of photodiodes characterized in Figure 4.11. The generated photocurrent using this integration solution is shown in Figure 4.35.

As illustrated in Figure 4.34 the light intersects the photodiode at a cross-section dimension D . The variable D in equation (4.6) can be adapted to this case and is given by:

$$D = W \left(1 - \frac{th}{f - h} \right) \quad (4.7)$$

where W is the ML width at the interface with the substrate, f is the focal length, h is the ML's apex and th is the thickness of the glass slide. In Figure 4.34, the photodiode's active area is marked inside a white square.

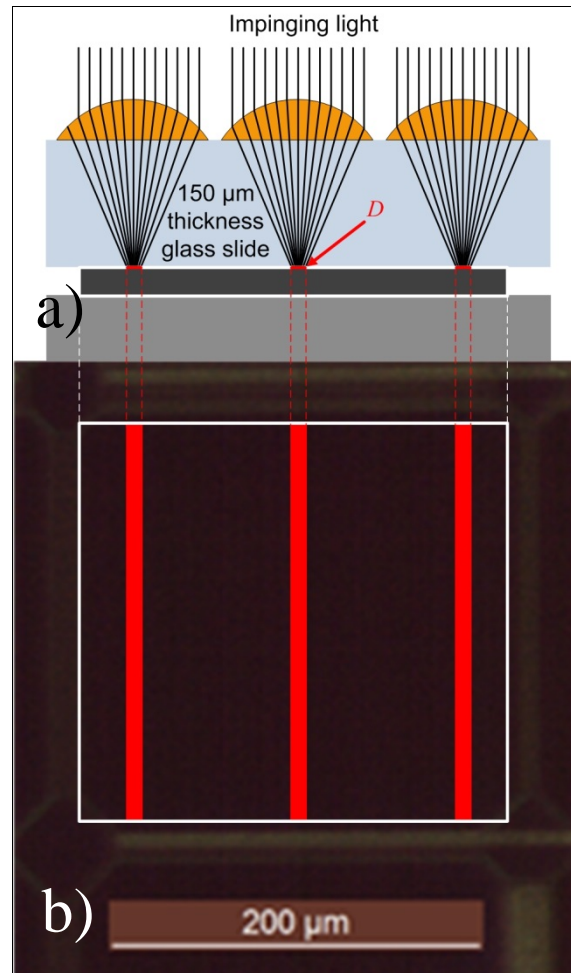


Figure 4.34 – Illustration of the proposed integration solution. In a) is the cross-section of the light conversion intersection with the photodiode's surface. In b) is a zoom-in photograph of the 240 μm photodiode.

Figure 4.35 shows the measured current of one 240 μm PD with MLs converging light into its depletion region compared to the photocurrent generated without any MLs. These measurements were done for white light and without reverse bias and just these are represented for easy understanding of the information. This solution, as expected, generates less photocurrent due to the MLs focus on the PDs depletion region, whereas without MLs, all the PD's active area is being used for light-current generation. Moreover, for specific applications, it is possible to set the light focus on an exact location by just changing the light's angle of incidence.

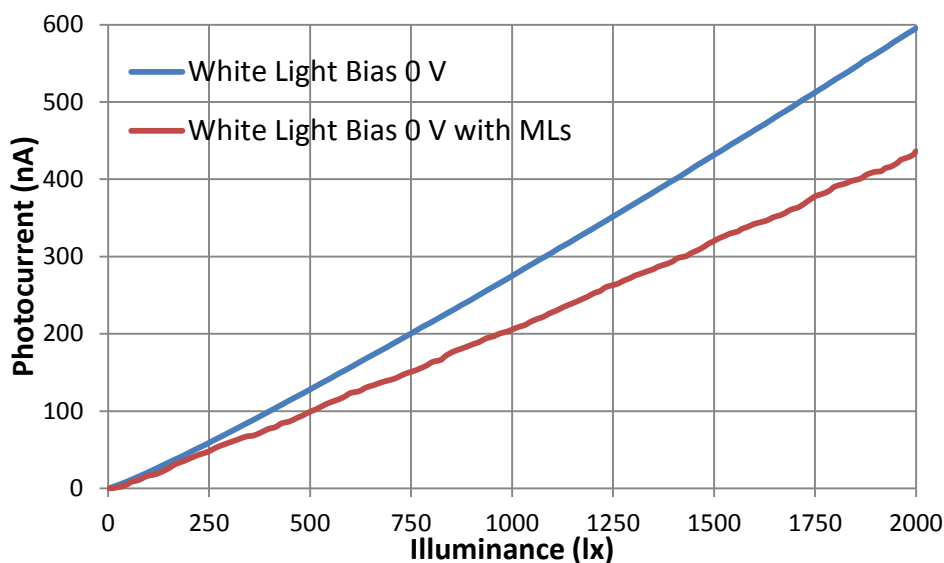


Figure 4.35 – Measured photocurrent as a function of the linearly increasing illuminance (in lux) for incident normal white light. The PD without the integration of MLs (blue line) generates more photocurrent because more active area is being used. The other photocurrent data (red line) is concerning the PD with the MLs integration solution.

4.3.3 The third approach: using the array of photodiodes as substrate

For better capturing the light that would otherwise fall outside the photodiode's active area it is necessary to fabricate the MLs array directly on the substrate. This approach has two purposes. The first one is to test the concept shown in Figure 4.36, *i.e.*, demonstrating how a ML centered on a PD with smaller width can enhance the light acquisition property of the CMOS microdevice. The second one is for applying the same concept on the 240 μm PD (meaning that an array of MLs is used) and check if it can also generate more current.

Photomask pattern 24–5 μm on a 24 μm PD

As shown in Figure 4.4, the die is mainly occupied with an 8×8 photodiodes array where each has an active area measuring 240×240 μm^2 (*length*×*width*) but smaller square PDs were also fabricated for different testing purposes. For determining the possible enhancement in light acquisition using MLs in a PD's entire area, the concept demonstrated in Figure 4.36 was tested. Therefore, using a photomask design measuring 24–5 μm , an array of MLs is fabricated directly on top of the photodiodes. The die containing the array of photodiodes is glued (using a double sided duct tape) to a glass

slide measuring $76 \times 26 \times 1$ mm (*length* \times *width* \times *thickness*) for facilitating the fabrication process.

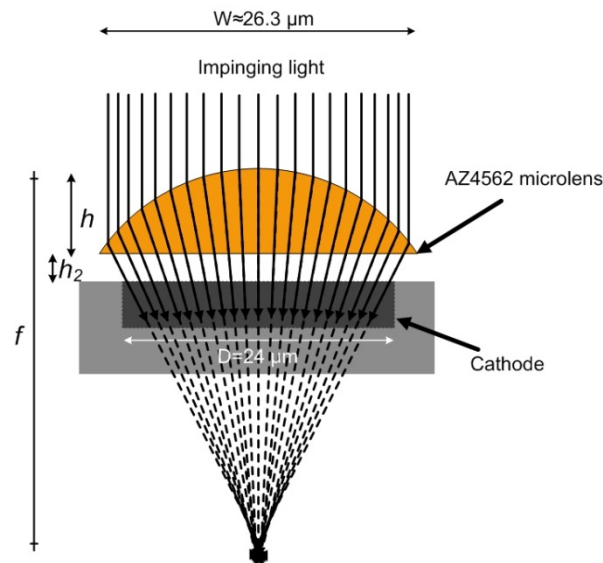


Figure 4.36 – Cross-section illustration of the direct fabrication on a photodiode. This setup increments the light acquisition because it converges light that would impinge outside the PD into its active area. The measured photocurrents without and with a ML fabricated directly on the photodiode are seen in Figure 4.39. It should be noted that h_2 is the oxides' thickness.

So, using the die as substrate, a $24\text{--}5$ μm ML is aligned and fabricated directly on top of the PD. The mask/substrate alignment was done so that the ML apex h was centered on the 24 μm PD. A zoom-in optical photograph of the ML centered on the PD (signaled with a red circle) is demonstrated in Figure 4.37.

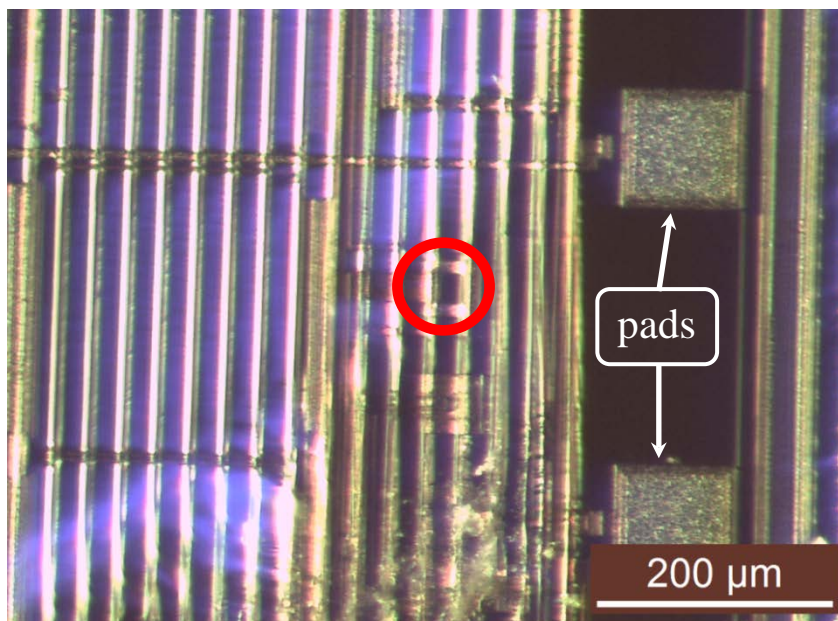


Figure 4.37 – A zoom-in of the 24 μm photodiode within the die. The measured photocurrent results are shown in Figure 4.39.

Figure 4.38 shows a zoom-in optical microscope photograph of the die glued on the PCB, and with the wire bonding already performed, for measuring purposes using the picoammeter.

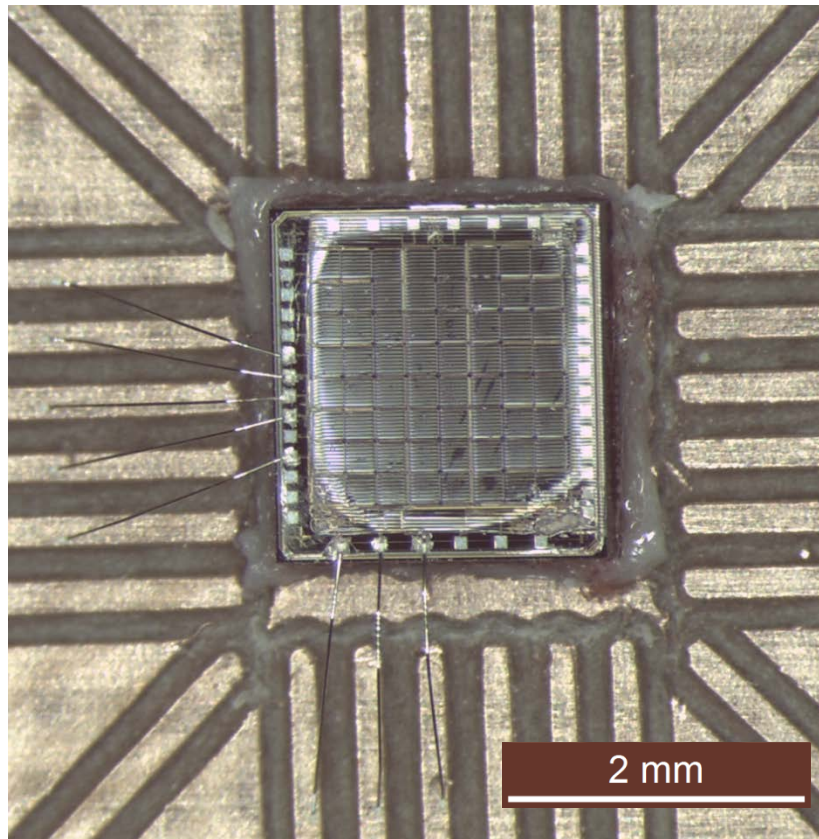


Figure 4.38 – Zoom-in optical microscope photograph of the die placed on the PCB and with the wire bonding already performed. The MLs are fabricated directly on the die's surface.

Figure 4.39 displays the results for the 24 μm PD without and with a ML fabricated directly on top of it using the 24–5 μm photomask configuration under the red light source. With ML, the gain in current generation efficiency is almost the same across the linear increment of the red light illuminance with either a reverse bias voltage of 0 or -4 V. These results demonstrate that, for red light, the ML is able to increase the PD's photocurrent generation efficiency at an approximately constant rate $\approx 13.5\%$. The integration of a properly designed ML, and its fabrication process, is able to surpass the intrinsic losses that occur due to absorption, reflectance and scattering within different materials and their interfaces.

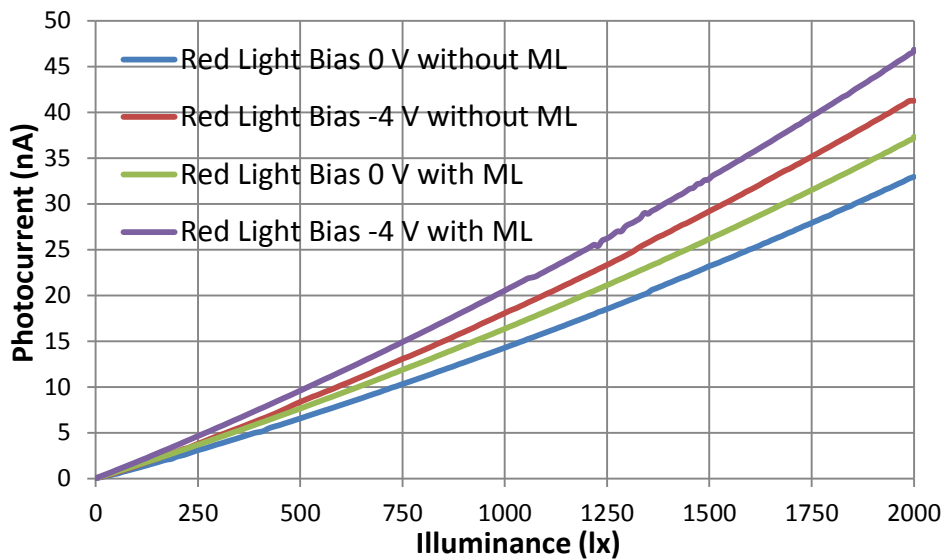


Figure 4.39 – Comparison between the photocurrents measured for different reverse bias voltages under red light, without and with the ML on a 24 μm square PD. The improvement in the light-current generation efficiency of the presented 24–5 μm photomask configuration is shown in Figure 4.40.

The obtained efficiency in light-current conversion (%) for red light with the integration of a ML is demonstrated in Figure 4.40. This improvement remains almost constant across the illuminance linear increment (from 0 to 2000 lx) and also at different reverse bias voltages.

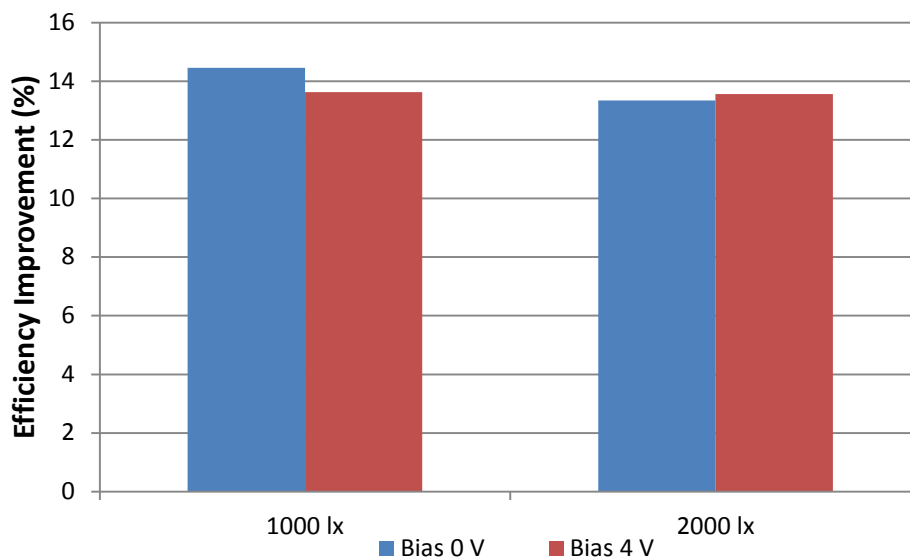


Figure 4.40 – Efficiency improvement (%) achieved at different illuminance values (red light) and reverse bias voltages by the developed MLs fabrication process on a 24 μm square PD.

Figure 4.41 shows the results for the 24 μm PD without and with a ML fabricated directly on top of it using the 24–5 μm photomask configuration under the white light

source. These values demonstrate that, for white light, the ML is able to increase the PD's photocurrent generation efficiency at an approximately constant rate $\approx 1.6\%$.

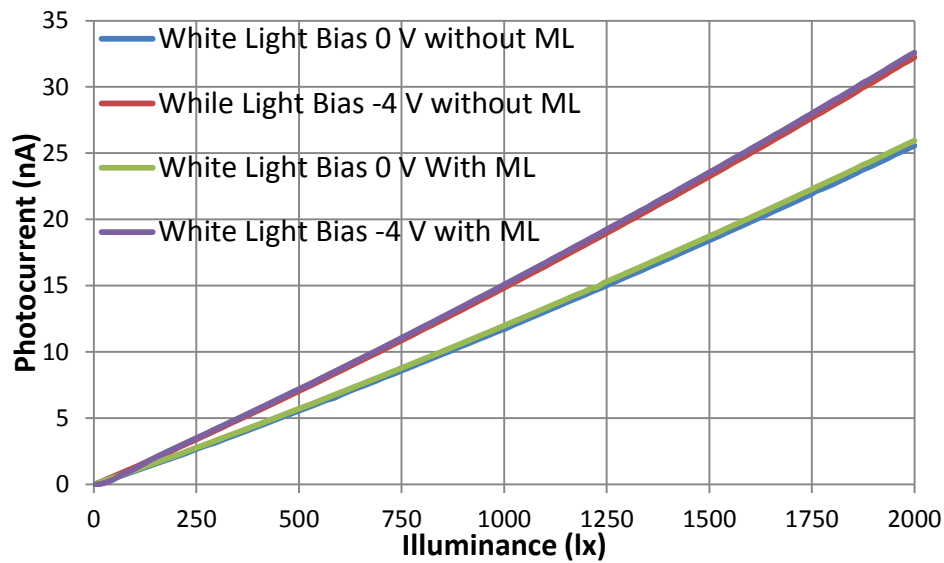


Figure 4.41 – Comparison between the photocurrents measured for different reverse bias voltages under white light, without and with the ML on a $24 \mu\text{m}$ square PD. The improvement in the light-current generation efficiency of the presented $24\text{--}5 \mu\text{m}$ photomask configuration is shown in Figure 4.42.

The obtained efficiency in light-current conversion (%) for white light with the integration of a ML is considerably lower than for red light as seen in Figure 4.42. With ML, the gain in current generation efficiency is most evident for a reverse bias of 0 V.

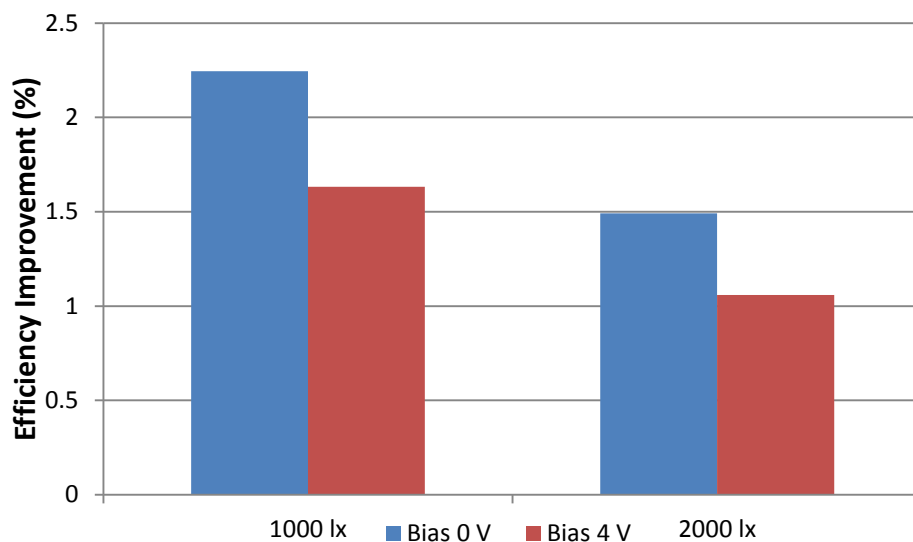


Figure 4.42 – Efficiency improvement (%) achieved at different illuminance values (white light) and reverse bias voltages by the developed MLs fabrication process on a $24 \mu\text{m}$ square PD.

These results illustrate that, for white light, the ML is unable to increase the PD's photocurrent generation efficiency at a level as high as for red light. As seen in Figure 4.5, the white light spectrum contains a range of wavelengths that have different penetration depths in silicon, most of them outside the PD's depletion region. Therefore, when impinging on a photodiode, white light is less capable of generating photocurrent than red light is.

Photomask pattern 24–5 μm on a 240 μm PD

The second test is to apply the same MLs array on a 240 μm thus verifying if there is also an increase in the photocurrent generation process. In this setup, eight 24–5 μm MLs are converging light into the 240 μm PD as illustrated in Figure 4.43.

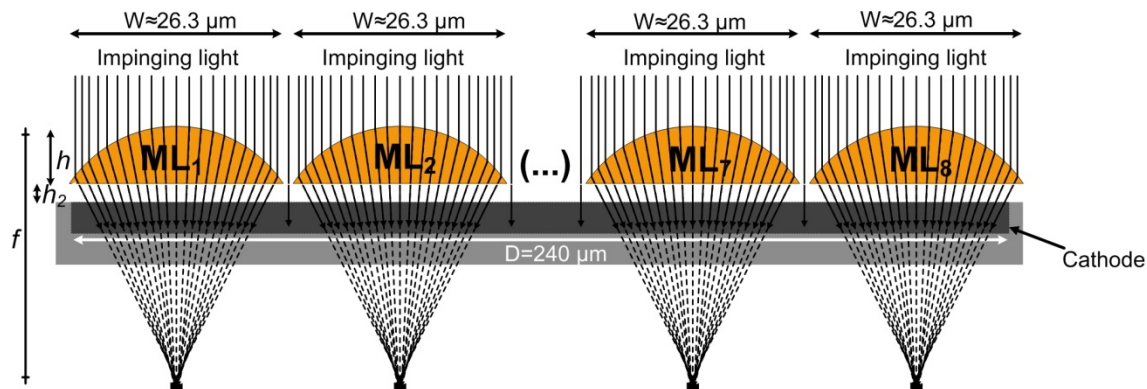


Figure 4.43 – Cross-section illustration of the direct fabrication on a 240 μm photodiode. The measured photocurrents without and with a MLs array fabricated directly on the photodiode are seen in Figure 4.45.

Again, using the die as substrate, a 24–5 μm MLs array is fabricated directly on top of the 240 μm PD. The mask/substrate alignment was done so that the maximum number of MLs would be centered within the PD's active area. In Figure 4.44 is shown an optical microscope photograph and a SEM image of the MLs array successfully fabricated directly on the photodiodes thus confirming the fabrication consistency.

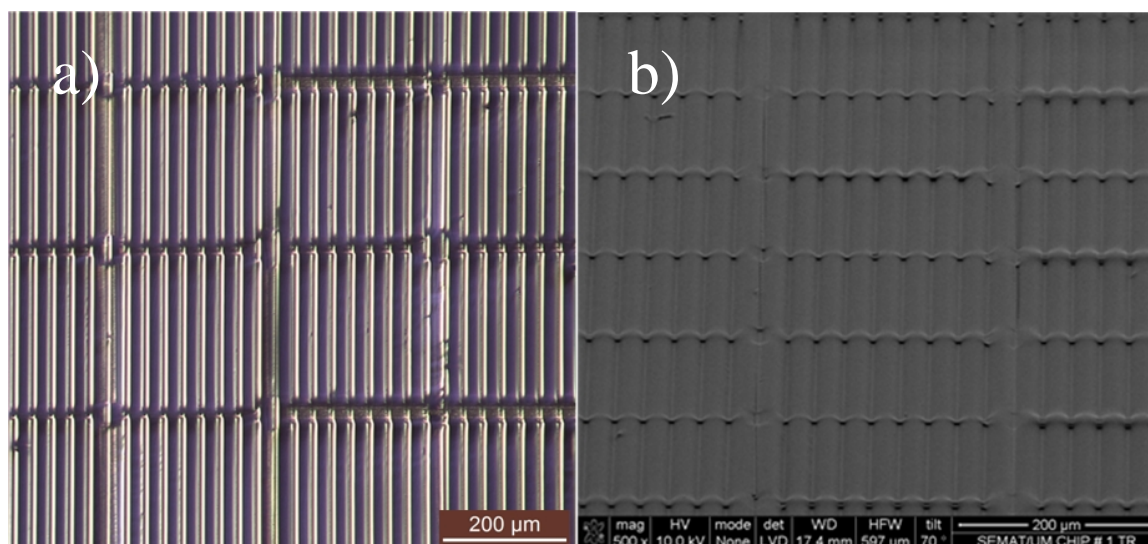


Figure 4.44 – In a) is an optical microscope photograph of the 24–5 μm MLs array fabricated directly on the photodiodes' surface and in b) is a SEM image of the same microstructure. For the presented case, the mask/substrate alignment was done so that the maximum number of MLs would be centered within the PD's active area as illustrated in Figure 4.43.

Figure 4.45 presents the results for the 240 μm PD without and with a MLs array fabricated directly on top of it using the 24–5 μm photomask configuration under red light. With MLs, as it happened in the first demonstration², the gain in current generation efficiency is also almost constant across the linear increment of the red light illuminance with either a reverse bias voltage of 0 or -4 V. The MLs array is able to increase the PD's photocurrent generation efficiency at a rate approximately $\approx 4.4\%$. In this case, the gain in current generation efficiency is smaller than in the previously demonstrated solution. The integration of an array of MLs increases the light transmission losses but the solution is still able to surpass, to a less significant extent, the current generation of the 240 μm PD without MLs.

² Photomask pattern 24–5 μm on a 24 μm PD

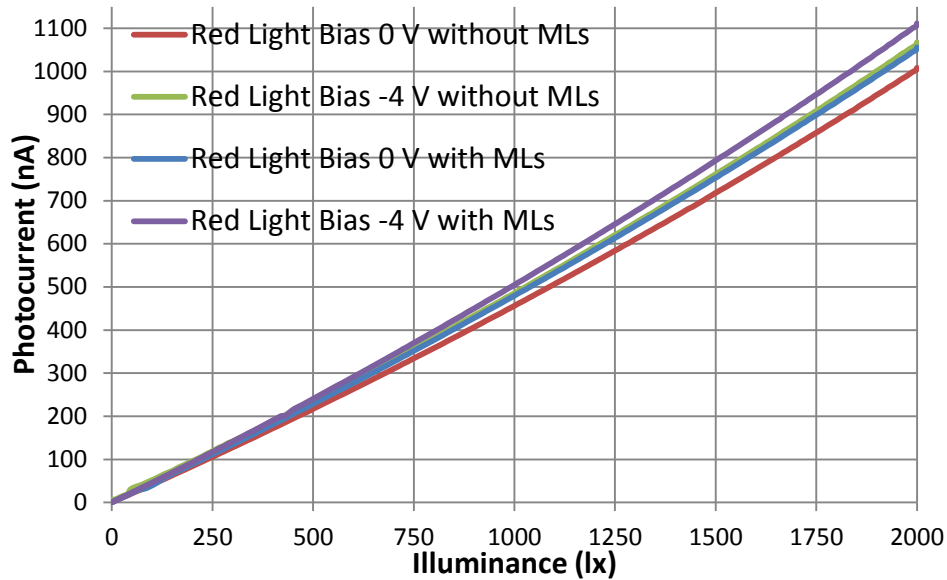


Figure 4.45 – Comparison between the photocurrents measured for different reverse bias voltages under red light, without and with the ML on a 240 μm square PD. The average improvement in the light-current generation efficiency of the presented 24–5 μm photomask configuration is shown in Figure 4.46.

The obtained efficiency in light-current conversion (%) for red light with the integration of a MLs array is seen in Figure 4.46. This improvement remains almost constant across the illuminance’s linear increment (from 0 to 2000 lx) and also at different reverse bias voltages, 0 and -4 V.



Figure 4.46 – Efficiency improvement (%) achieved at different illuminance values (red light) and reverse bias voltages by the developed MLs fabrication process on a 240 μm square PD.

Figure 4.47 shows the results for the 240 μm PD without and with a MLs array fabricated directly on top of it using the 24–5 μm photomask configuration under white

light. With MLs, the gain in current generation efficiency is most evident for a reverse bias of 0 V (seen in Figure 4.48).

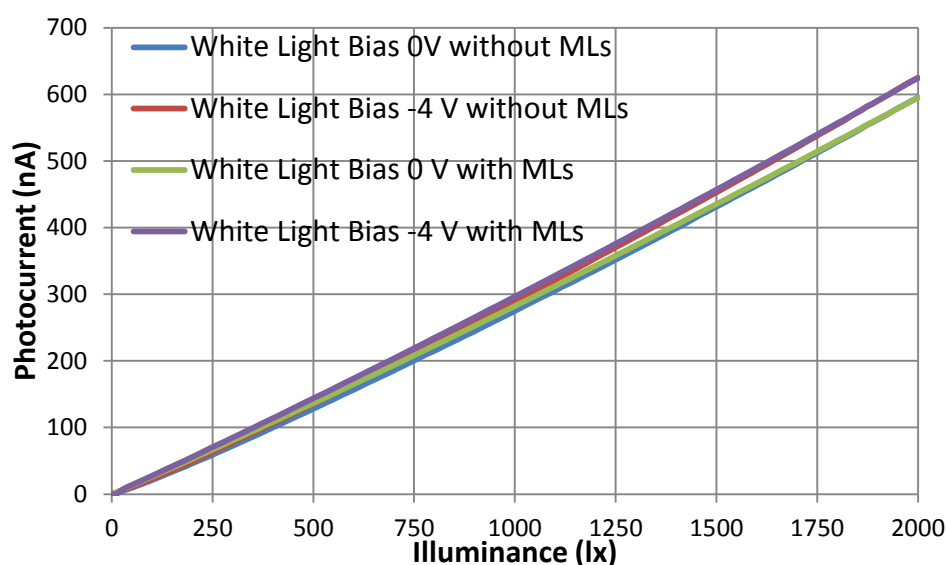


Figure 4.47 – Comparison between the photocurrents measured for different reverse bias voltages under white light, without and with the MLs array, on a 240 μm square PD. The improvement in the light-current generation efficiency of the presented 24–5 μm photomask configuration under white light is shown in Figure 4.48.

The obtained efficiency in light-current conversion (%) for white light with the integration of a MLs array is demonstrated in Figure 4.48. For an illuminance of 1000 lux, with a reverse bias voltage of either 0 or -4 V, the PD presents a gain in current generation efficiency of $\approx 2.5\%$.

However, at an illuminance of 2000 lux, the MLs array is unable to enhance the PD's capacity for improving the current generation. In this case, basically, the presence of MLs has a negligible effect in generating more current than without MLs. When the array of MLs is fabricated on the PD, there is a loss in its ability to generate photocurrent of -0.04 and -0.12 %, for a reverse bias voltage of 0 and -4 V, respectively. It is for this case that the light-current generation gain provided by the integration of MLs reaches equilibrium with the system's optical losses. So, for an array with more than eight 24–5 μm MLs under white light, the 240 μm PD starts to generate less current than without MLs due to the fact that the amount of optical losses is greater than the improvements obtained in light acquisition.

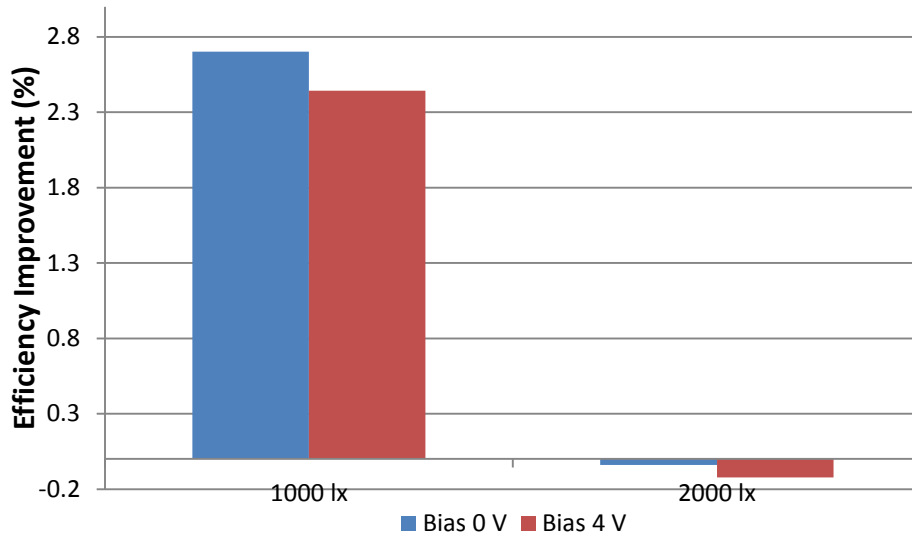


Figure 4.48 – Efficiency improvement (%) achieved at different illuminance values (white light) and reverse bias voltages by the developed MLs fabrication process on a 240 μm square PD. It should be noted that in this configuration, for a reverse bias of -4 V, the system reaches equilibrium regarding the current generation gain provided by the MLs and the losses occurring by absorption, reflectance and scattering.

4.4 Results analysis

The goal for determining if the developed process was capable of enhancing the light capture onto photodiodes was demonstrated and successfully achieved, with the results summarized in Table 4.4. This table shows the enhancement (in %) of the PDs' ability to generate more photocurrent when MLs are fabricated directly on their surface under white and red lights and for reverse bias voltages of 0 and -4 V. It should be noted that the values presented are roundings, to the nearest integer, of the results that were measured and presented in section 4.3.3.

Table 4.4 – Summary of the results achieved in the enhancement of photocurrent generation efficiency. The values presented below are roundings, to the nearest integer, of the previously demonstrated results.

		Efficiency Improvement (%)			
		White light		Red light	
		Bias 0 V	Bias -4 V	Bias 0 V	Bias -4 V
One ML on a 24 μm PD	1000 lx	2	2	14	14
	2000 lx	1	1	13	14
MLs array on a 240 μm PD	1000 lx	3	2	5	4
	2000 lx	0	0	5	4

The consistent fabrication and integration processes and the results comparisons and benchmarkings that were shown, validate the use of MLs for current generation improvement. This enhancement is mainly obtained by collecting more light into the photodiode's active area. Due to its penetration depth in silicon, the red light presented the best results in light-current generation efficiency. This light source emits the wavelengths that penetrate within, or very close to, the PD's depletion region. Moreover, when using a white light source, there is also an enhancement of light acquisition by the optical microsystem but with more modest results. The light that is emitted from the white source contains wavelengths that do not contribute as efficiently as the red light source for the electron-hole pair generation. This happens because their penetration depths are out of the PD's depletion region range, either by excess or deficit (as illustrated in Figure 4.1). From the presented solutions, the one that reached equilibrium (*i.e.*, the quantity optical losses occurring during light transmission is similar to the light acquisition enhancement provided by the MLs) was for the 240 μm square PD with an array of eight 24–5 μm MLs under white light illuminance. Due to the losses added by each individual ML, an array with more than eight 24–5 μm elements, results in the decrease of the 240 μm square PD's ability for generating photocurrent.

4.5 Optical filters simulation

In order to achieve a full optical microsystem on the same device, optical filters (OF) for filtering out the non-visible light spectrum are also necessary. The example depicted in Figure 4.49 helps to illustrate the mechanism that explains this type of wavelength filtering, *i.e.*, Fabry–Perot interferometry. Just three OFs are needed for covering the entire visible spectrum and each one of the three peaks concerns one color, *i.e.*, blue, green and red (refer to Figure 4.51).

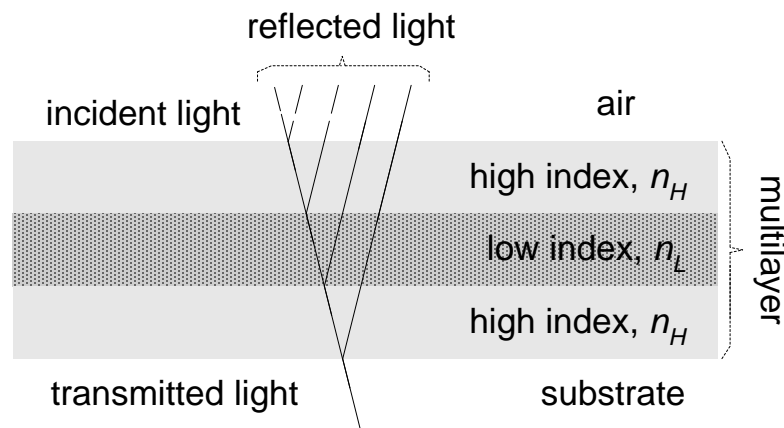


Figure 4.49 – A Fabry–Perot optical filter consisting of alternate high and low refractive index materials.

In this example, the reflected light is the combination of four k reflected beams with four different phases and amplitudes, where each component k contains its own optical path d_k . The same applies to the transmitted light, which can be simplified as being the difference between the incident and the reflected light. If A_0 is the amplitude of the incident light, then each k reflected component is [26]:

$$k = A_0 A_k e^{-j\beta_k d_k} \quad (4.8)$$

with,

$$|A_k| < 1 \text{ and } \beta_k = \frac{2\pi}{\lambda_k} \quad (4.9)$$

where A_k is the amplitude of the reflected light and β_k is the wavenumber.

This makes both the reflected and the transmitted light wavelength λ dependent. This interferometer-based mechanism is what explains the optical filtering with respect to the wavelength.

Therefore, optical filters can be fabricated using a thin-film multi-layer structure, deposited by physical vapor deposition (PVD) or chemical vapor deposition (CVD) [27]. The technology for fabricating the OFs must allow their integration with the microelectronics, *i.e.*, PDs and respective readout electronics. This can be achieved with dielectric materials compatible with silicon such as silicon dioxide (SiO_2) and titanium dioxide (TiO_2). It must be observed that the thickness of the central layer (with low refractive index) is not the same for the three filters as seen in Table 4.5, and that is what defines which color is transmitted. The central layer is composed by SiO_2 , being the material from the two with smallest refractive index, and for this reason is denominated by L . The top and bottom layers are composed by TiO_2 (the highest refractive index, *e.g.*, the H material). In Figure 4.50 are presented SEM images of a MLs array (using a photomask design measuring 24–5 μm) already fabricated on a TiO_2 surface demonstrating the feasibility of this process.

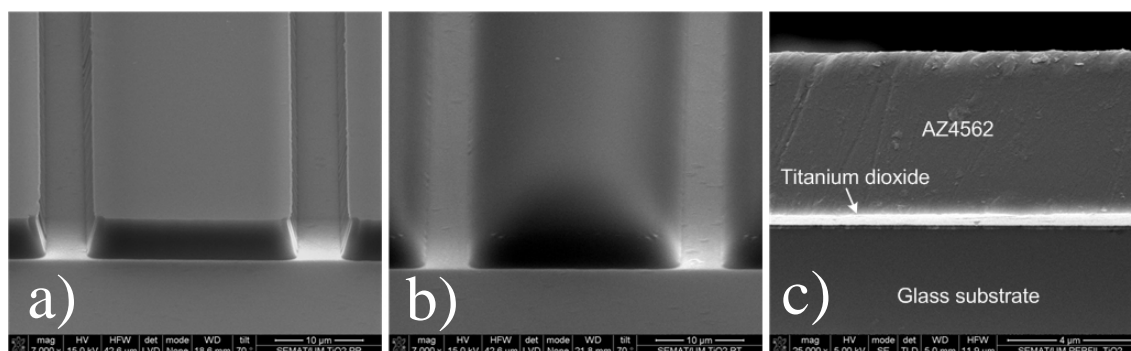


Figure 4.50 – In a) and b) are seen the pre and post-thermal reflow structures, respectively, using a photomask design measuring 24–5 μm . In c) is a cross-section of the AZ4562 fabricated on TiO_2 .

These dielectric materials not only present low light absorption but also have the advantage of being deposited using the same reactive radio frequency (RF) sputtering deposition technique and, additionally, it is very difficult to remove them from the silicon substrate. Finally, the TiO_2 and the SiO_2 were selected also because all depositions can be done without opening the deposition chamber, thus avoiding air contamination and temperature gradients, and the deposition process is well characterized. For the proposed OF, a narrow FWHM is not required due to the fact that the visible light spectrum consists on an interval of approximately 400 nm. This large wavelength range has the advantage of reducing the number of dielectric layers composing the optical filters.

Through simulation, a first approach was already developed concerning the design of an OF for the visible light spectrum. These preliminary results were obtained with just three alternating dielectric layers of TiO₂ and SiO₂ with the resonant cavity being SiO₂ in a Fabry–Perot filter configuration (see Table 4.5).

Table 4.5 – Layers’ materials and thicknesses of the simulated optical filter.

Layer (nm)	Blue	Green	Red
TiO₂	45	45	45
SiO₂	157	197	240
TiO₂	45	45	45
λ_0	455	528	606
FWHM	87	134	187

Moreover, the simulation already presents promising results because the superposition of the three optical filters reasonably covers the visible spectrum. The refractive indexes for TiO₂ and SiO₂ are $n=2.61$ and $n=1.54$, respectively, being approximately constant across the visible spectrum. It should be noted that the fabrication of dielectric layers is fairly complex because these layers are very thin (thicknesses in the nm range) and even small variations might negatively influence the filter’s performance [13, 28]. The thickness of the SiO₂ middle layer is what defines the central wavelength λ_i , $i \in \{\text{red, green, blue}\}$, whereas the top and bottom layers (TiO₂) are mainly responsible for defining the bandwidth. When such an optical filter is implemented in the system, the unwanted wavelengths in the electromagnetic spectrum are filtered out as illustrated in Figure 4.51. The simulations were done using *TFCalc*TM 3.5 for thin-films calculations.

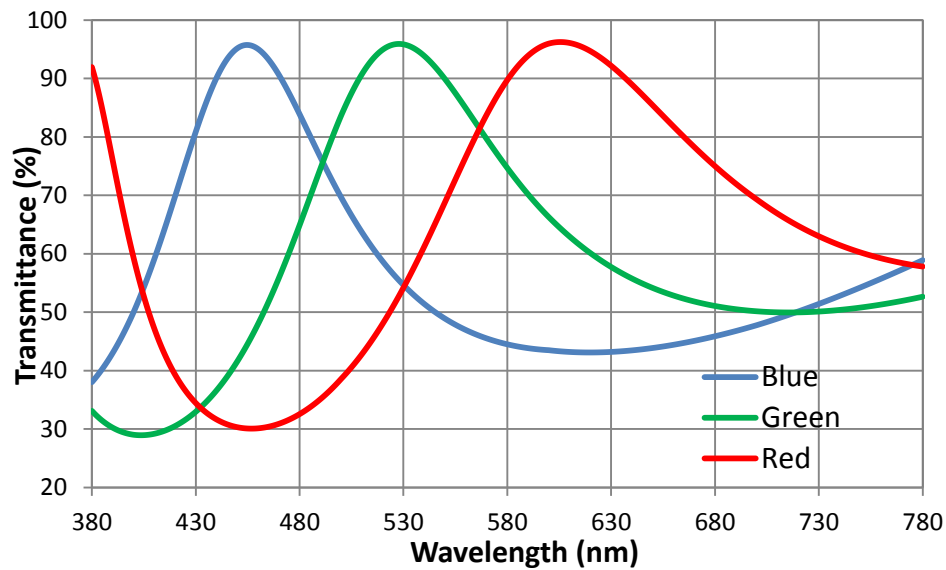


Figure 4.51 – Simulation results of a three layer optical filter and a SiO₂ resonant cavity. The data concerning the filter is shown in Table 4.5.

References

- [1] D. Monteiro, CMOS-based integrated wavefront sensor, Delft: Delft University Press, 2002.
- [2] X. Wang, Noise in Sub-Micron CMOS Image Sensors, Delft: Delft University Press, 2008.
- [3] [Online]. Available: <http://learn.hamamatsu.com/articles/quantumefficiency.html>.
- [4] I. Kenyon, The Light Fantastic: A Modern Introduction to Classical and Quantum Optics, Second ed., Oxford: Oxford University Press, 2011.
- [5] J. Millman and A. Grabel, Microelectronics, Second ed., McGraw-Hill International Editions, 1987.
- [6] F. Smith and T. King, Optics and photonics: An introduction, J. W. & Sons, Ed., Chichester, 2000.
- [7] B. Fowler, CMOS area image sensors with pixel level A/D conversion, Stanford: Stanford University, 1995.

- [8] A. Moini, Vision Chips, Kluwer Academic Publishers, 2000.
- [9] O. Semiconductor. <http://www.onsemi.com/PowerSolutions/content.do?id=16697>.
- [10] <http://www.thorlabs.com/thorproduct.cfm?partnumber=MCWHL2>.
- [11] <http://www.thorlabs.com/thorproduct.cfm?partnumber=M625L3>.
- [12] <http://www.keithley.com/products/dcac/voltagesource/application/?mn=6487>.
- [13] J. Correia, Optical Microsystems in Silicon Based on a Fabry-Perot Resonance Cavity: Application for Spectral Analysis of Visible Light, Delft: Delft University Press, 1999.
- [14] M. Serkan and H. Kirkici, "Reshaping of a Divergent Elliptical Gaussian Laser Beam Into a Circular, Collimated, and Uniform Beam With Aspherical Lens Design," *IEEE Sensors Journal*, vol. 9, no. 1, pp. 36-44, January 2009.
- [15] P. Milonni and J. Eberly, Laser Physics, J. W. & Sons, Ed., Hoboken, 2010.
- [16] C. Nelson and J. Crist, "Predicting laser beam characteristics," *Laser Technik Journal*, vol. 9, no. 1, pp. 36-39, 2012.
- [17] R. Rocha, J. Carmo, J. Gomes, M. Belsley and J. Correia, "Microlenses array made with AZ4562 photoresist for stereoscopic acquisition," *Procedia Engineering, Elsevier Science*, vol. 47, pp. 619-622, 2012.
- [18] <http://www.dowcorning.com/applications/search/default.aspx?r=131en>.
- [19] A. Sepúlveda, R. de Villoria, J. Viana, A. Pontes, B. Wardle and L. Rocha, "Full elastic constitutive relation of non-isotropic aligned-CNT/PDMS flexible nanocomposites," *Nanoscale*, vol. 5, no. 11, p. 4847–4854, 2013.
- [20] J. McDonald and G. Whitesides, "Poly(dimethylsiloxane) as a material for fabricating microfluidic devices," *Accounts of Chemical Research*, vol. 35, no. 7, p. 491–499, 2002.

- [21] Y. Fainman, L. Lee, D. Psaltis and C. Yang, *Optofluidics: Fundamentals, Devices and Applications*, McGraw Hill Professional, 2009.
- [22] <http://www.jascoinc.com/products/spectroscopy/ft-ir-spectrometers>.
- [23] R. Silverstein, G. Bassler AND T. Morrill, *Spectrometric identification of organic compounds*, Fifth ed., New York: Wiley, 1991.
- [24] S. Pine, *Organic Chemistry*, Fifth ed., New York: McGraw-Hill, 1987.
- [25] <http://www.disco.co.jp/eg/index.html>.
- [26] M. Maciel, M. Silva, R. Rocha, J. Carmo, J. Gomes and J. Correia, "Optical filters for stereoscopic image sensors," in *SBMicro 2013, Chip in Curitiba, 28th Symposium on Microelectronics Technology and Devices*, Curitiba, Brazil, 2-6 September, 2013.
- [27] J. Carmo, R. Rocha, M. Bartek, G. Graaf, R. Wolffenbuttel and J. Correia, "A review of visible-range Fabry–Perot microspectrometers in silicon for the industry," *Journal of Optics & Lasers Technology: Elseviser Science*, vol. 44, no. 7, pp. 2312-2320, October 2012.
- [28] H. Macleod, *Thin-Film Optical Filters*, Third ed., Bristol: Institute of Physics Publishing, 2001.

5 Conclusions and future work

This final chapter presents the last conclusions concerning the work developed. The future work and further improvements that can be still made are also presented and discussed. The fabrication process was designed and developed for fabricating different sized arrays of microlenses. The fabrication parameters are easily adapted and changed for obtaining MLs with different focal lengths while maintaining the entire process steps unchanged. Nevertheless, the different solutions for integrating the MLs with the substrate composed by photodiodes, fabricated in standard CMOS technology, remain valid. The direct fabrication of such an array of MLs on photodiodes resulted in the enhancement of their intrinsic capacity to generate a photocurrent. The work developed in this thesis opens new approaches and applications for optical microsystems, namely on image sensors.

5.1 Results and conclusions

Therefore, the main achievements reached with this thesis are:

- the development of a fabrication process using photolithography and thermal reflow for obtaining arrays of microlenses;
- the fabrication parameters can be adapted for fabricating different sized MLs;
- the MLs fabrication process accuracy can be as high as 98%;
- the MLs present a small difference of $\approx 4\%$ between the theoretical and measured focal lengths;
- three different approaches for integrating MLs on photodiodes were presented, *i.e.*, PDMS as fabrication substrate, a 150 μm thick glass substrate and direct fabrication on the PD's surface;
- the direct fabrication of MLs on the PDs presented very interesting results concerning the enhancement of light for improving the photocurrent generation efficiency.

The PDMS as fabrication substrate requires further research but it looks promising for future applications. The 150 μm thick glass substrate enables to direct the ML's focus

into the PD's depletion region. Moreover, the focus can be set into a specific spot by controlling the angle of incidence of light. For the developed integration, the direct fabrication of MLs on PDs has shown to increase the photocurrent generation by more than 14% and 2% for red and white lights, respectively. The red light has the ideal penetration depth in silicon for achieving the most prominent enhancement in photocurrent generation presented in this thesis. For the best results achieved in this thesis, the mask alignment was done in such a way that the apex h of a single 24–5 μm element in the MLs' array is centered on top of 24 μm square PD. This was accomplished because the MLs array was purposely designed and integrated for converging light that would impinge out of the PD's active area. On the other hand, from the work developed, it was also realized that the MLs ability for enhancing the photocurrent generation ceases for the 240 μm square PD with an array of eight 24–5 μm MLs under white light illuminance. This occurs because white light has a penetration depth in silicon that is mainly outside the PD's depletion region range, either by excess or deficit. Moreover, it is also due to the fact that the amount of optical losses that an eight element array introduces in the system surpasses the light acquisition benefits introduced by the MLs.

5.2 Future work and applications

5.2.1 Polydimethylsiloxane as substrate

The PDMS solution should be further investigated for understanding why the cracks are appearing, as well as to know the reasons behind the merging between this polymer and the AZ4562. Further structural and chemical analysis should be done and a more detailed chemical characterization of both materials alone, and combined, is mandatory. This integration process seems very promising by enabling to control this layer's thickness, and therefore, allowing different size MLs to be fabricated over the same substrate. The flexibility to adapt the fabrication of MLs over different size PDs increases the possibilities for achieving different setups and solutions.

5.2.2 Stereoscopic image sensor

A new die with at least, for example, an array of 256×256 (512×512 or 1024×1024), $24 \mu\text{m}$ square photodiodes (or even smaller) should be fabricated. It has been demonstrated that the maximum efficiency achieved for improving the photocurrent generation is obtained when a similarity between the sizes of both the MLs and the PDs exists. The MLs widths at the interface with the substrate are limited by the AZ4562's maximum attainable working thickness h (from 5 to $20 \mu\text{m}$). Moreover, a considerable increment in the number of PD's within the array will also allow the creation of an image on the sensor thus opening the possibility for new applications. This new die should also permit the development of a stereoscopic image formation optical microsystem, with the working principle illustrated in Figure 5.1.

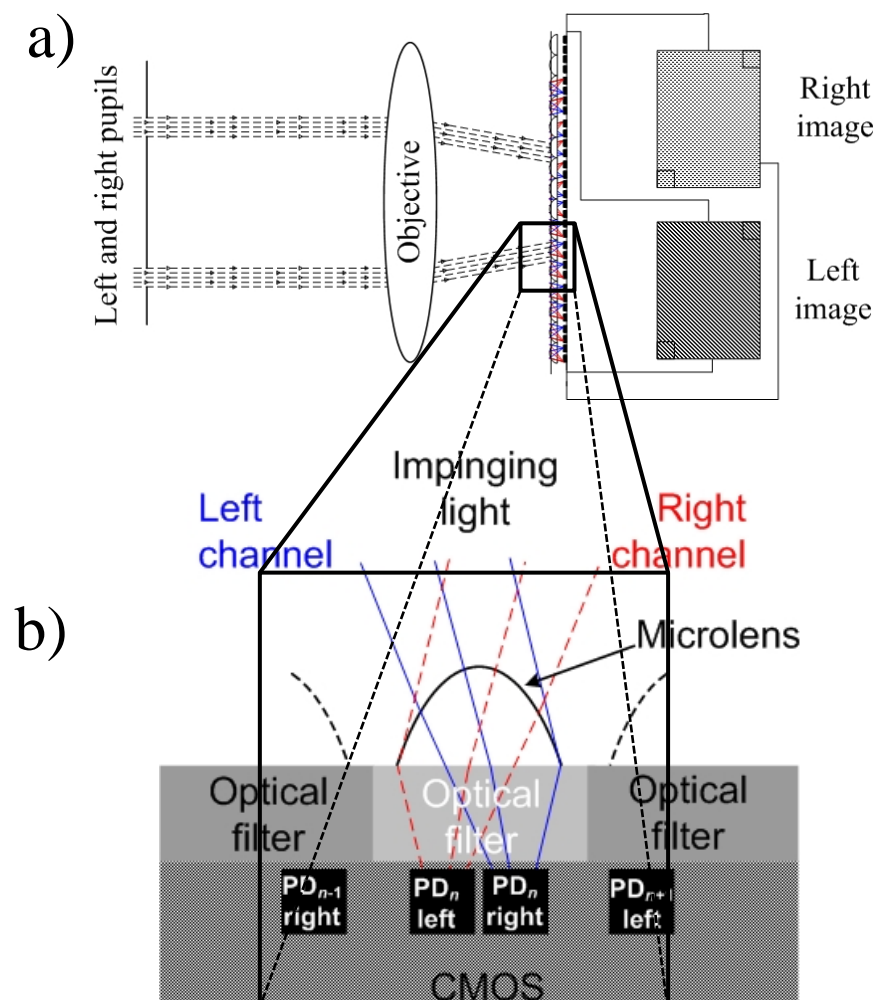


Figure 5.1 – Illustration of the stereoscopic image formation concept with a single polychromatic CMOS image sensor (example with one microlens and two photodiodes PD_n left and right). In a) is seen the light collecting setup and in b) a zoom-in of the array of MLs separating the left and right optical channels to form the stereoscopic image.

This setup is composed by a telecentric image objective and two pupils (two entrance apertures just like the human eyes) from where both the left and right images (that originate the tridimensional effect) pass through before being focused into the photodetectors by an objective lens. This lens focuses the two incident beams in the direction of an array of microlenses like the ones developed in this thesis. Then, different wavelengths are concentrated onto specific PDs, where the left and right images are separated by focusing each side onto the appropriate sensor column under the microlens. The chromatic aberration phenomenon demonstrated in Chapter 2, has the effect of enabling the concentration of different wavelengths to be directed for specific photodiodes under the same ML. The CMOS sensor then provides left and right interleaved images that will be de-interleaved in a personal computer. The photodiodes define a small sensitive area where the light is converted into photocurrent and later amplified and used by a display device. With the proper readout electronics the data impinging on each row of PDs can be digitally processed for creating a stereoscopic image.

Optical filters fabrication

The optical filters' design and simulation presented in section 4.5 shows results that are adequate to the purpose of filtering and transmitting to the PDs just the visible light. This OF uses the Fabry–Perot configuration with the top and bottom layers composed of TiO_2 and the resonant cavity is made of SiO_2 . Moreover, an array of MLs using a photomask design measuring $24\text{--}5\ \mu\text{m}$ was already fabricated on a TiO_2 surface demonstrating the feasibility of this process. Nevertheless, it is still necessary to fabricate the optical filters, directly on the photodiode's surface, using thin-films deposition techniques and then characterize them.

Therefore, in Figure 5.2 is represented the cross-section of how a full optical microsystem might be. In this illustration, there are two PDs for providing stereoscopic image. On the die's surface, optical filters are fabricated using thin-films deposition techniques and the MLs array is then fabricated on top of all these layers.

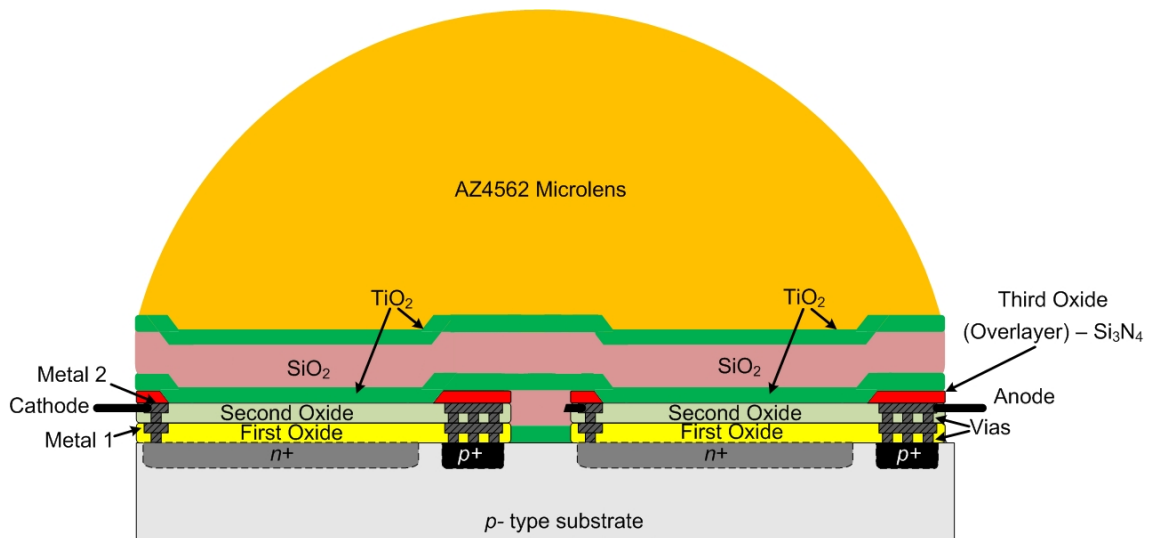


Figure 5.2 – Design of a complete optical microsystem. The optical filters are composed by just three layers. Because of the chromatic aberration, the MLs allow different wavelengths to impinge onto a specific photodiode. It should be noted that this illustration is not to scale.

Annex
Journal Publications

1. R. P. Rocha, J. P. Carmo and J. H. Correia, "Fabrication Methodology of Microlenses for Stereoscopic Imagers Using Standard CMOS Process", ECS Transactions: Electrochemical Society, Vol. 49, No. 1, pp. 323-330, ISSN 1938-6737, 2012.

2. João Paulo Carmo, Rui Pedro Rocha, Marian Bartek, Ger de Graaf, Reinoud F. Wolffenbuttel and J. H. Correia, "A review of visible-range Fabry–Perot microspectrometers in silicon for the industry", Journal of Optics & Lasers Technology: Elsevier Science, Vol. 44, No. 7, pp. 2312-2320, October 2012.

3. J. P. Carmo, A. F. Silva, R. P. Rocha and J. H. Correia, "Application of Fiber Bragg Gratings to Wearable Garments", IEEE Sensors Journal, Vol. 12, No. 1, pp. 261-266, January 2012.

Fabrication Methodology of microlenses for stereoscopic imagers using standard CMOS process

R. P. Rocha, J. P. Carmo, and J. H. Correia

Department of Industrial Electronics, University of Minho, Campus de Azurém, 4800-058 Guimarães, PORTUGAL, {rrocha,jcarmo,higino.correia}@dei.uminho.pt

This paper presents the fabrication technology of microlenses maintaining a high reproducibility of their characteristics with low cost. The objective of microlenses is to be integrated into imagers in CMOS technology to allow stereoscopic vision. The fabricated microlenses form cylindrical arrays to be placed above the optical filters and photodetectors, in order to potentiate stereoscopic vision and at the same time maximizing the color fidelity. An array of optical filters centered at the primary colors will enable a multicolor usage. The AZ4562 material was the photoresist selected for fabricating the microlenses. The cylindrical shape is obtained by reflowing the photoresist using the hot-plate technique.

Introduction

The available image sensors are not ready for stereoscopic acquisition. The stereoscopic vision as well as the high resolution enhances the quality of the images. The traditional solutions for acquiring tridimensional images are based on two or three monoscopic cameras, which must be perfectly synchronized with the penalty of losing the tridimensional effect or the emergence of artifacts in the images [1]. Moreover, it is very common the use of both depth sensors and monoscopic image sensors for doing the conversion between the bidimensional to the tridimensional domain [1].

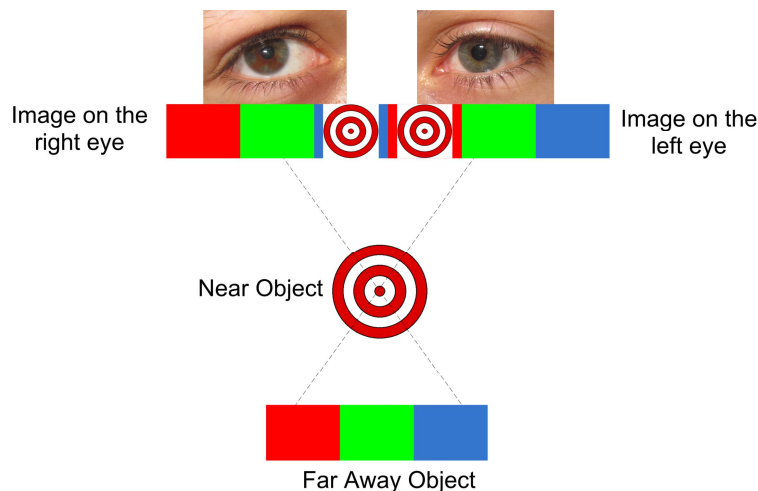


Figure 1. Illustration of the parallax effect for inducing sensation of depth in the brain [1].

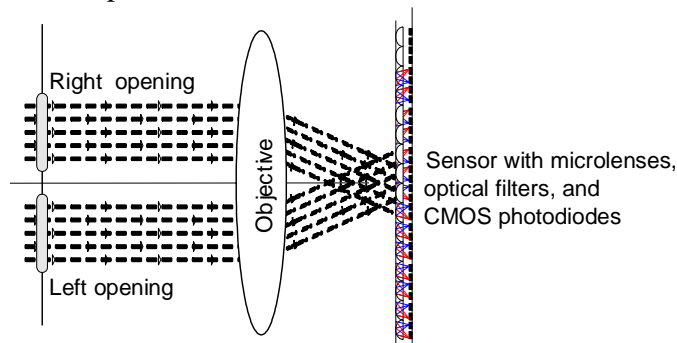
The stereoscopic vision uses the parallax effect to cheat the brain for making it gain depth perception (which is also known as stereopsis), and thus the name “stereoscopy”. This

means that a stereoscopy with bad quality consequently induces perceptual ambiguity to the viewer [2]. This happens because the human brain is much more sensitive and less tolerant to bad stereoscopic images than to monocular images. Thus, a conscious of double vision can be caused by a multiplicity of factors, but all due to differences between the right and left images. The nature of such differences can be due to differences in brightness, differences in contrast, changes in reflection angle, differences in colors, and so on. Additionally, and according to the media experts, (even better) tridimensional image sequences can take few milliseconds to allow the brain and eyes to naturally adapt, to get the scene and adjust to it. The stereoscopic image sensor concept presented in this paper is composed by two entrance apertures (as it happens inside the human eyes) from where the left and right channels (the two images to be converted to the tridimensional domain) are passing before being focused by an objective lens into the sensitive area of the CMOS microdevice. The objective lens focuses the two incident beams (two viewpoints) in the direction of the microlens, where the light is concentrated in a small area (i.e., into the sensitive area of the CMOS photodiodes). After the passage by the optical filters, the individual rays of left and right viewpoints are steered towards the respective CMOS photodiodes. These two viewpoints are separated by focussing each side on the appropriate sensor column under the microlens and optical filters.

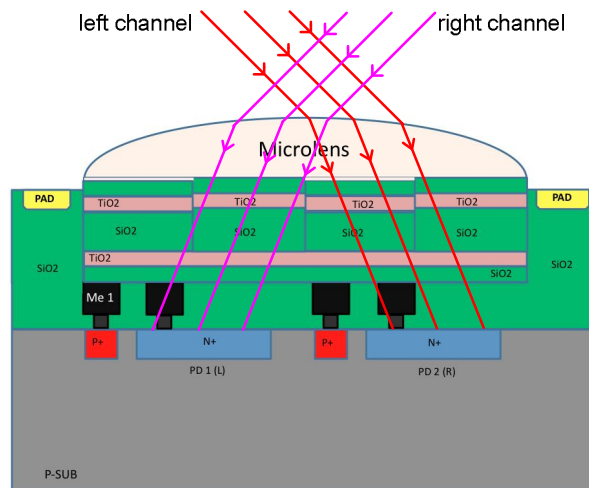
The fabrication of such a microdevice can be done using a cheap process because it allows the production of both the photodetectors and the read-out electronics within a reasonable cost. Finally, since the aforementioned process is very well characterized and known, the time to manufacture the first working prototype is expected to be short. This paper presents the design and fabrication technology of the microlenses for providing stereoscopic vision in a test-chip designed in the $0.7\ \mu\text{m}$ CMOS process from on-semiconductor foundry.

Image sensor architecture and stereoscopic image formation

As showed in the Figure 2, the image sensor is composed by two pupils (two entrance apertures just like the human eyes) from where the left and right channels (the two points of view that will originate the tridimensional effect) pass through before being focused by an objective lens. This lens focuses the two incident beams in the direction of the microlens, where the light is concentrated in a small sensitive area where the photodiodes are placed. After passing through the optical filters, the wavelengths coming from both the entrance apertures are directed towards the respective CMOS photodiodes. The two points of view are separated by focusing each side onto the appropriate sensor column under the microlens and optical filters.



(a)



(b)

Figure 2. (a) Illustration of the stereoscopic image formation, and (b) illustration of the concept associated to the microlenses array for stereoscopic acquisition with a single polychromatic CMOS image sensor (example with one lens and two photodiodes).

Microlenses array

Design

There is available a huge number of materials for fabricating microlens such as the SU-8/2, AZ9260 and AZ4562, for example. These polymers allow the microlens fabrication by thermally reflowing the raw material, whose processing steps of the reflow process are presented in the Figure 3. This permits the production of arrays containing a million or more microlens of good optical quality in just a few minutes and with high degree of reproducibility of their characteristics [3].

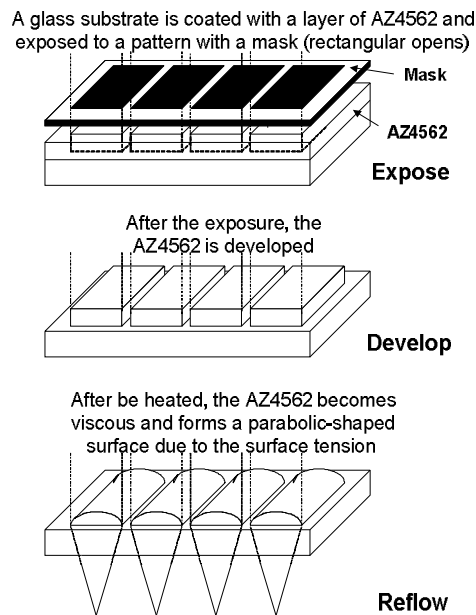


Figure 3. Microlenses array fabrication steps.

There are few geometrical parameters to take in account before fabricating the microlenses. The Figure 4(a) shows the several geometrical parameters of a plano-convex lens: n is the refractive index n of the lens material (e.g., the AZ4562), R [m] is the radius of a single spherical surface, h [m] is the height of the surface undulation, W [m] is the length of the transversal cut. The focal length f [m] of the lens is straightforward to obtain: $f=(n-1)R$. Therefore, the major task is to obtain the radius R in terms of this set of geometric parameters $\{h, W\}$. The next question that arises, is how to get $\{h, W\}$ in terms of the thickness th [m] of deposited AZ4562 as well as in terms of the resulted shape after doing the patterning. The Figure 4(b) shows the trapezoidal shape and geometric edges $\{W_1, W_2\}$ that is possible to obtain after the patterning task. The volumes (in this case, the transversal areas) of the material before $A_1=th \times (W_1+W_2)/2$ [m²] and after A_2 [m²] the reflow must be equal. R is obtained keeping in account that $A_1=A_2$ where:

$$A_2 = \int_{-\frac{W}{2}}^{+\frac{W}{2}} (R^2 - x^2)^{\frac{1}{2}} dx - W \cdot (R - h) \quad (1)$$

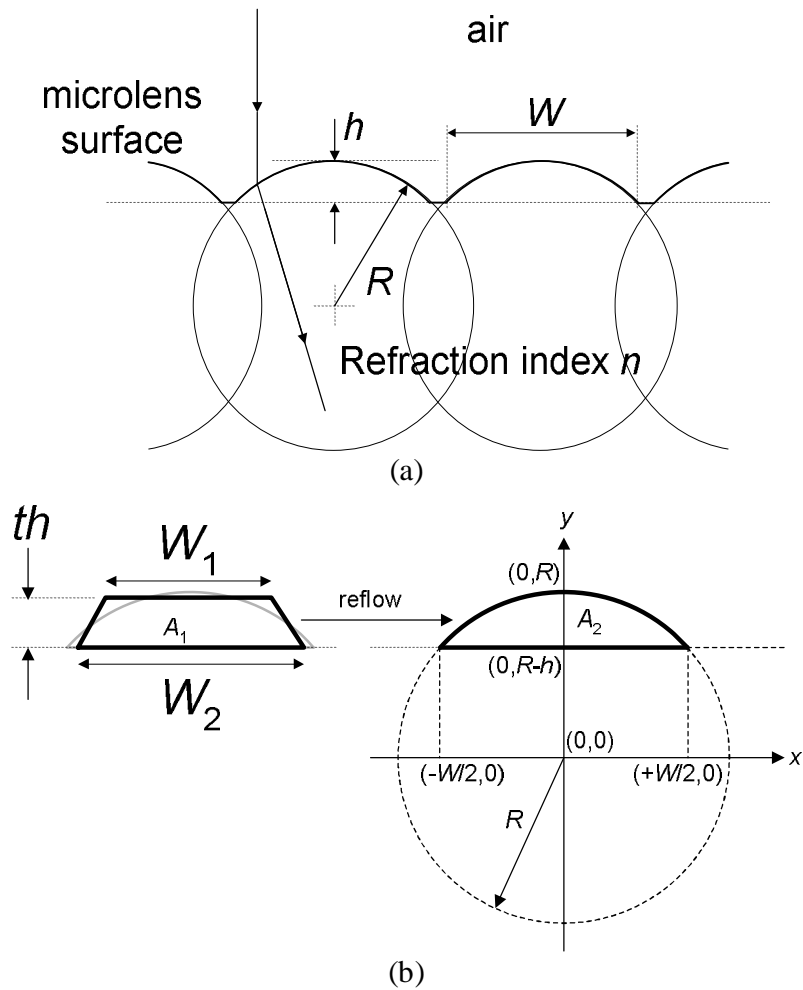


Figure 4. Factors determining the focal length of microlens and concept illustration.

The Figure 5 shows (with the help of a selected sample) the concept to estimate the values of R , as well as the respective focal length f . For this selected sample $R \approx 21 \mu\text{m}$, which combined with $n_{\text{AZ4562}} \approx 1.5936$ for $\lambda = 580 \text{ nm}$ (green) gives $f \approx 33.5 \mu\text{m}$. Good-quality lenses are fabricated with relatively crude lithography although greater consistency and reliability is achieved only if the process is carried out efficiently. The precise form of the microlens, and hence their focal properties are determined by the effects of surface tension. In particular the contact angle of the softened resist with the surface of the substrate will strongly influence the shape of the microlens.

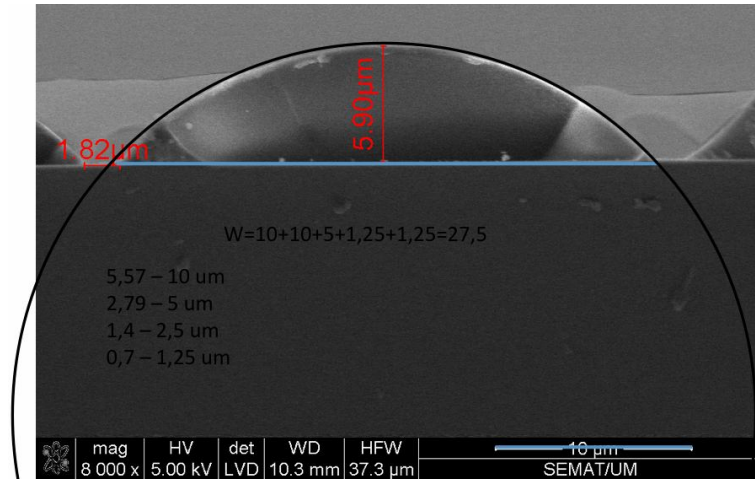


Figure 5. Factors determining the focal length of microlens and concept illustration.

Fabrication

The fabrication process illustrated in the Figure 3 allows the production of an array containing 142 microlenses. The rectangles that compose the mask array measure 4.9 mm in length, width of $30 \mu\text{m}$ and $5 \mu\text{m}$ spacing between adjacent rectangles. This setup allows the fabrication of good optical quality in just a few minutes and with high degree of reproducibility of their characteristics. To the author's knowledge, this is the first time that such a geometry with the presented dimensions and aspect ratio, is used to fabricate an array of microlenses. Different sized arrays were de-signed and printed into a 128 kdpi mask with each array covering an area of 5 mm^2 . The rectangles are coated with chromium making them opaque to light and the spacing between rectangles is transparent allowing the photoresist under it to be exposed to the UV light later on. The fabrication process of the microlenses array requires several steps and process parameters summarized in Table 1. First, it is necessary to spin coat the AZ4562 at 6000 rpm during 20 seconds, in a previously cleaned substrate, to achieve the desired $5 \mu\text{m}$ thickness.

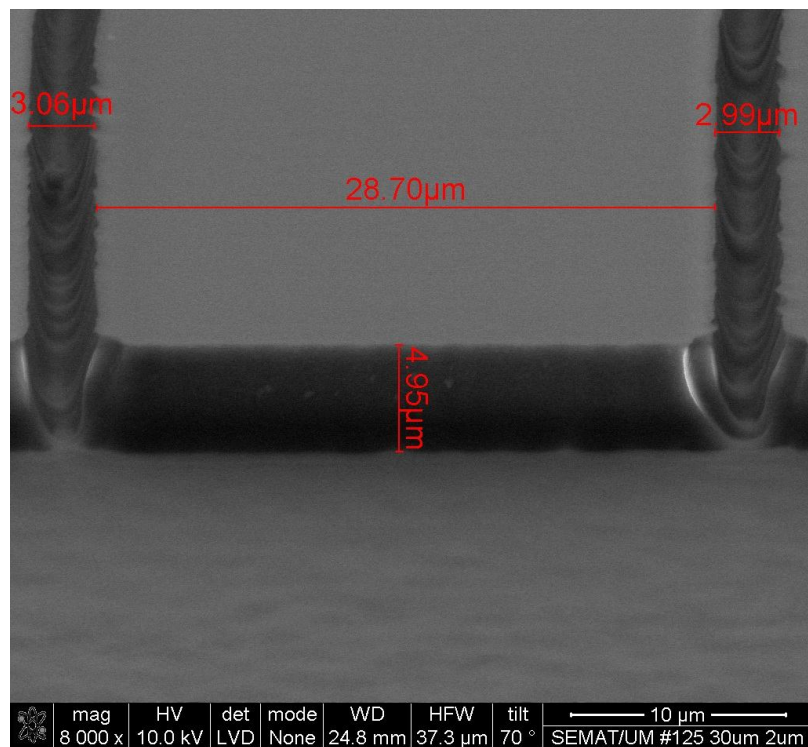
TABLE I. Fabrication Process steps and parameters.

Process steps	Process parameters
Spin coating	20 seconds @ 6000 RPM
Prebake (hotplate)	5 minutes @ 100 °C
Exposure (mask aligner)	30 seconds in contact mode @ 134 W
Developing	AZ400K or AZ351B developers in a 1:4 concentration with distilled water (2×2minutes and 15 seconds)
Cleaning	Rinse with distilled water and dry with N_2 flow
Thermal Reflow (hotplate)	5 minutes @ 130 °C

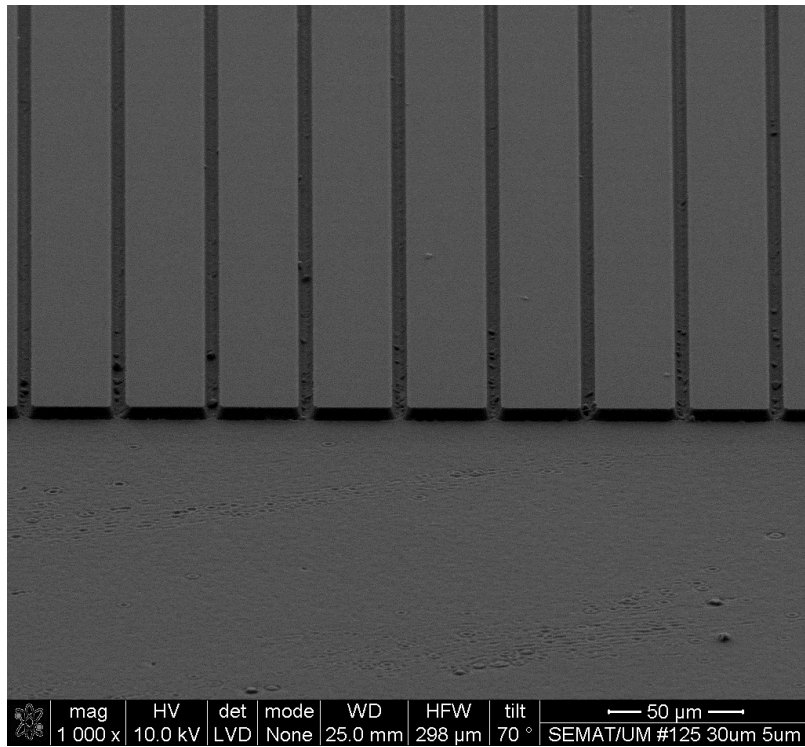
After the coating, a prebake phase, using a computer controlled hot-plate at 100 °C for 5 minutes, is necessary to evaporate the solvents present in the photoresist. Next, to obtain the required array-like structure, the mask with the correspondent geometry is placed on top, directly contacting with the coated photoresist and exposed to UV light using a mask aligner. The AZ being under a 134 W exposure during 30 seconds makes the unexposed material insoluble. Afterwards, the developing phase is achieved by either the AZ400K or the AZ351B developers in a 1:4 concentration with distilled water. To accomplish it, the substrate is immersed into two developer baths for 2 minutes and 15 seconds each, in a magnetic stirrer plate. This is required to leave just the unexposed photoresist in the substrate. The photolithographic process ends with the parallelepiped structures being rinsed with distilled water and dried out with a nitrogen flow. Finally, to obtain the lens profiles, the thermal reflow technique is applied so the substrate with the array containing the fabricated structures is placed on a hotplate at 130 °C for 5 minutes.

Results

The Figures 6 and 7 show two photographs of the photoresists array before and after the reflow step, respectively. The parts (a) and (b) of correspond to a single element of the array and an overview of the array, respectively. These structures refer a sample prototype built using photolithography with a chromium-on-glass mask. It is clear from the previous figures that the thermal reflow process permitted obtaining the desired microlens profile to concentrate the light into specific directions.

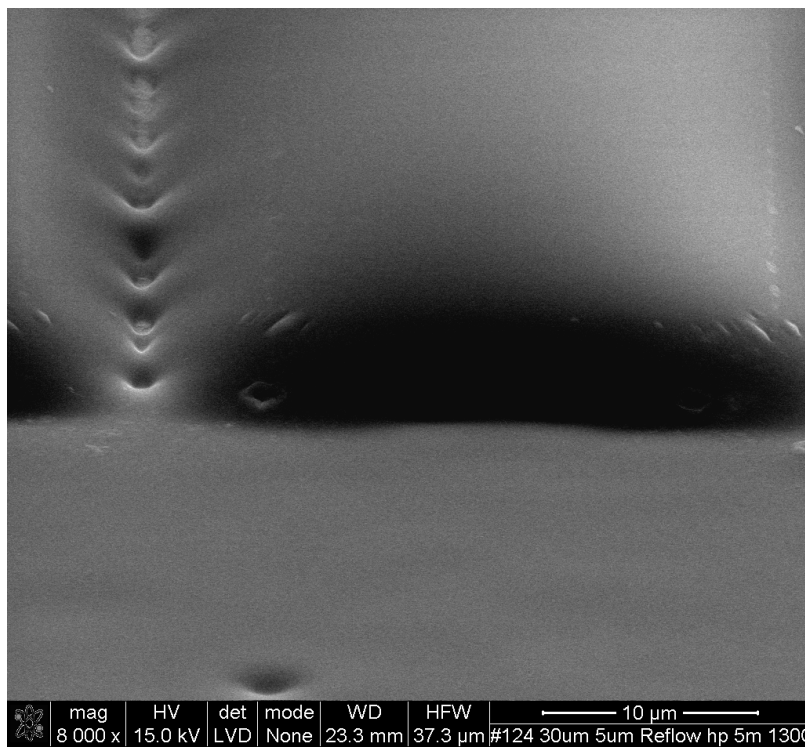


(a)

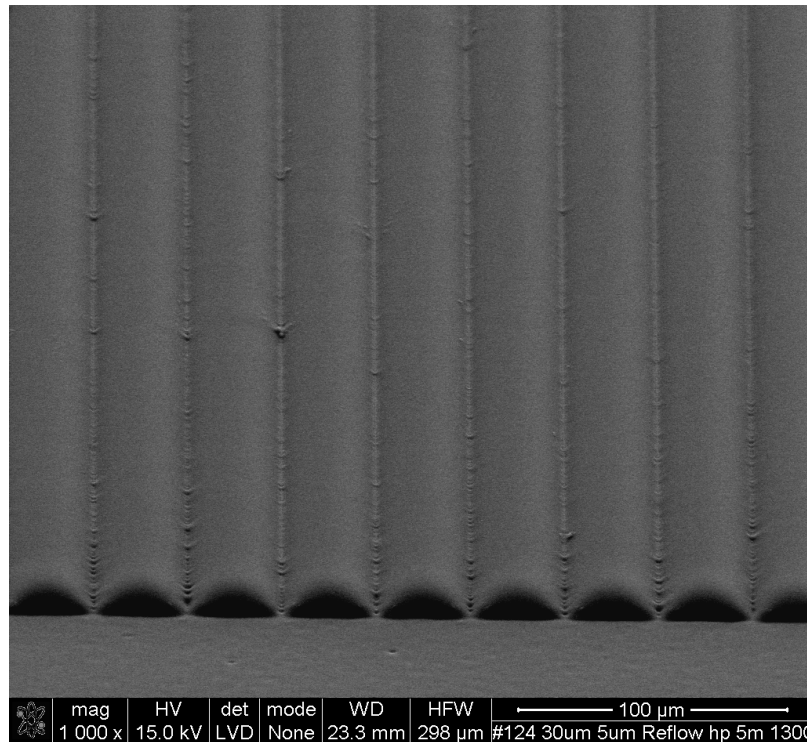


(b)

Figure 6. SEM images (a) of a single element and (b) an overview of the array. These photographs were taken from an array of microlenses before doing the thermal reflow.



(a)



(b)

Figure 7. SEM images (a) of a single element and (b) an overview of the array. These photographs were taken from an array of microlenses after doing the thermal reflow.

Conclusions

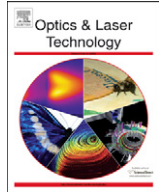
This paper presented a microlenses fabrication process for integration on a stereoscopic image sensor in CMOS technology for use in biomedical devices. The microlenses design started with the FEM simulations to set some parameters needed to fulfill the desired objectives. Each photodetector measures a specific wavelength with is diffracted by the microlenses. The complete fabrication process was explained and the initial and final structures obtained were physically characterized. It was shown that the reflow step is what determines the actual microlenses profile. The several steps that comprise the photolithographic fabrication process were done with a chromium-on-glass mask and a mask aligner as the UV light source.

Acknowledgments

This work and Rui Pedro Rocha were fully supported by the Portuguese Foundation for Science and Technology under the project FCT/PTDC/EEA-ELC/109936/2009 and the financial grant SFRH/BD/33733/2009, respectively. The authors also acknowledge to Dr.-Ing Christian Koch from MicroChemicals GmbH for the technical support.

References

1. I. Andorko, P. Corcoran, P. Bigioi, in Proceedings of OPTIM 2010, Brasov, Romania, 20-22 May 2010, 920-925.
2. S. Zeki, *Consciousness and Cognition*, **13**, 173-196.
3. H. Takahashi, et al, *IEEE Journal of Solid State Circuits*, **39**(12), 2417-2424.



Review

A review of visible-range Fabry–Perot microspectrometers in silicon for the industry

João Paulo Carmo^{a,*}, Rui Pedro Rocha^a, Marian Bartek^b, Ger de Graaf^b, Reinoud F. Wolffenbuttel^b, José Higinio Correia^a

^a University of Minho, Department of Industrial Electronics, 4800-058 Guimarães, Portugal

^b Delft University of Technology, Faculty of EEMCS, Department ME/EI, Mekelweg 4, 2628CD Delft, The Netherlands

ARTICLE INFO

Article history:

Received 30 December 2011

Received in revised form

23 March 2012

Accepted 26 March 2012

Available online 12 April 2012

Keywords:

Microspectrometer

Integrated silicon microsystem

Industrial applications

ABSTRACT

This review presents microspectrometers in silicon for the industry for measuring light in the visible range, using the Fabry–Perot interferometric technique. The microspectrometers are devices able to do the analysis of the individual spectral components in a given signal and are extensively used on spectroscopy. The analysis of the interaction between the matter and the radiated energy can found huge applications in the industrial sector. The microspectrometers can be divided on three types, determined by the dispersion element or the used approach and can be found microspectrometers based on prisms, gratings interferometers. Both types of microspectrometers can be used to analyze the spectral content ranging from the ultraviolet (UV, below 390 nm), passing into the visible region of the electromagnetic spectrum (VIS, 390–760 nm) up to the infrared (IR, above 760 nm). The microspectrometers in silicon are versatile microinstruments because silicon-compatible techniques can be used to assembly both the optical components with the readout and control electronics, thus resulting high-volume with high-reproducibility and low-cost batch fabrications. A compensation technique for minimizing the scattered light effects on interferometers was implemented and is also a contribution of this paper. Fabry–Perot microspectrometers for the visible range are discussed in depth for use in industrial applications.

© 2012 Elsevier Ltd. All rights reserved.

Contents

1. Introduction	2312
2. Microspectrometer's taxonomy	2313
3. Grating microspectrometers	2314
4. Interferometric microspectrometers	2314
4.1. Microspectrometer design	2314
4.2. Case study	2315
4.3. Limitations	2317
4.4. Compensation of scattering non-idealities	2318
5. Conclusions	2319
References	2319

1. Introduction

The developments in the microelectronic field observed on last years resulted in an increased well being for the mankind. This is

especially true when looking for almost all aspects of the human life, where it is possible to found microelectronic devices and microstructures whose fabrication were impossible without the currently available fabrication techniques [1–7]. In this context, new industrial applications of Microsystems made possible the development and proliferation of low-power wireless devices with reduced dimensions for data and sensory communications [8], object tagging and components for chain fabrication facilities [9],

* Corresponding author. Tel.: +351 253 510190; fax: +351 253 510189.
E-mail address: jcarmo@dei.uminho.pt (J.P. Carmo).

silicon-compatible microbatteries [10] for micropowering and photonic applications [11–13]. However and despite the huge and fascinating range of applications for microsystems, the most challenging is undeniably those one used to detect and/or manipulate the light. This idea backs to the second century before our age, when Archimedes planned to destroy enemy ships using a solar heat ray with an array of actuators to change the shape of a mirror [14]. The field of photonics is one that offers the possibility to achieve one of the greatest realizations and applications because the light is present in all aspects of the human life and our way of living is impossible without light. A detailed search for microsystems application in the industry allows concluding that the spectroscopy is the field where the use of optical sensors is essential.

Spectroscopy is the science of studying the interaction of light with matter as a function of the wavelength, λ [nm]. The state of electrons in atoms and molecules can be changed due to the interaction between the light and the matter. In this case, the exchanging of energy between them can result in one of the following effects: scattering, emission or absorption of light [15]. The spectrography is a well-established technique in several fields of science (e.g., physics, chemistry and biology) and can be applied in virtually almost applications. The near infrared (NIR) spectroscopy analyses the spectral region located between 700 nm and 2500 nm [16] and can be used for monitoring the quality control of food and beverages [17], as well as for detecting counterfeit medicines [18]. The spectral region located between 1.4 μm and 10 μm is the so-called mid infrared (MIR) range and it can be used in the agriculture for quantitative analysis of soil contents [19] as well as for doing quality control in the food industry by detecting oils and/or fats [20]. The MIR spectroscopy can also be used with success by criminalist investigators for doing forensic analysis of several kinds [21]. It is possible applying spectroscopy methods in the visible range of the electromagnetic spectrum. The visible range is a small part of the entire electromagnetic spectrum located between 390 nm and 760 nm and the only part which can be perceived by the human eye. Many applications require spectral analysis at the visible wavelengths: inspection of product defects in the industry by means of color determination, biochemical analysis (e.g., physiological fluid, human blood, muscle tissue, DNA fibers) [22], light scattering by materials (liquids, plastics, polymers and gels), and so on. It is also possible to use the energy-dispersive X-ray spectroscopy (EDS or EDX) technique for doing the characterization of environmental particles [23], but its use is out-of-the-scope of this paper. A microspectrometer is an instrument that separates the light into its basic spectral components [24] for analysis.

It is commercially available few high-performance multiple-grating spectrometers featuring impressive spectral resolutions, $R = \lambda/\Delta\lambda$, that easily exceeds $R = 10^6$, where $\Delta\lambda$ [nm] is the -3 dB power bandwidth (also known as the full-width half-maximum, FWHM) for a particular settled wavelength, λ [nm], but only very specific applications such as those required by the astronomy require such spectral resolutions [25]. Furthermore, the strong dependence of the quantity R with the resolving power capability makes it the most important indicator of a spectrometer. The spectral resolutions found in microsystems based on assembled MEMS and based on integrated silicon components are typically limited by $R = 100$ and $R = 20$, respectively [26]. Fortunately, the majority of the industrial applications (including the formerly cited) require smaller spectral resolutions that do not exceed few dozens. The main consequence of this is the huge industrial potential of microspectrometers, where its small size and cost more than compensates their R -limitation [27].

This review presents visible-ranged microspectrometers based in the Fabry–Perot interferometric technique for the industry, and is followed by a discussion on the limitations imposed to these

devices. An array-type microspectrometer for the visible is present as a case study. A compensation technique to minimize the effect of the scattered light was implemented and is also a major topic of discussion.

2. Microspectrometer's taxonomy

Since spectrometers work with the optical domain, specific techniques are required for processing the wavelength components of the light beam. A wavelength separator of some kind can be found in a spectrometer and depends from the used dispersion element. This leads to three know types of spectrometers: these one based on prisms, on gratings and on interferometers. The first type requires long optical paths and thus, it is not suitable for fabricating microspectrometers.

Fig. 1 shows simplified schematics of typical grating and interferometric type microspectrometers. In a grating type microspectrometer, the incident passes by an entrance slit and is dispersed by way of a grating [15]. Normally, the diffraction gratings are composed of closely spaced transmitting slits on a

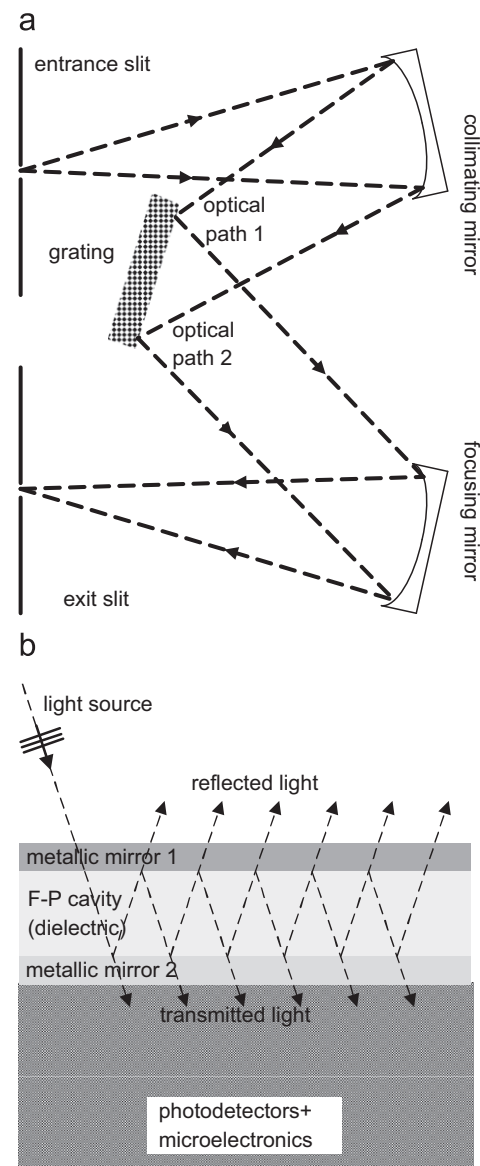


Fig. 1. Simplified schematics illustrating the principle of (a) grating and (b) interferometric (a Fabry–Perot cavity) microspectrometers.

flat surface (also known as transmission gratings) [28] or alternate reflecting and non-reflecting grooves on a flat or curved surface (the reflection gratings) [29]. For the case of microspectrometer based on interferometers, the dispersion of the incident light is done by splitting it on several components and putting them traveling several optical paths. After their recombination, these components interfere constructively only if their path difference is an integer quantity of a selected wavelength. This means that an interferometer is a device that acts as a filter for transmitting certain wavelengths and reflecting (rejecting) the others back to the light source. It exist at least four types of interferometric techniques (e.g., Michelson [30], Mach-Zender [31], Sagnac [32] and Fabry–Perot [33]). The most promising approach for fabricating interferometer type microspectrometers is using Fabry–Perot interferometer (also known as Fabry–Perot etalon) for acting as a dispersion element - see Fig. 1(a). This is true because the interferometer can be mounted on top of microelectronic devices (CMOS and/or bipolar) using IC-compatible fabrication techniques (deposition techniques of both dielectric and metal layers, etching techniques (e.g., bulk micromachining using wet solutions of potassium hydroxide solutions — KOH — and dry micromachining by way of reactive ion etching – RIE) [26].

3. Grating microspectrometers

Grating microspectrometers are generally fabricated using bulk micromachining techniques (either with KOH alkaline solutions or RIE techniques). The roughness resulted on micromachined surfaces make these type of microspectrometers to be very difficult to fabricate and to reproduce their spectral characteristics. Moreover, high-quality gratings are required to match the targeted resolutions and can take two types of shapes: transmission slits [34] and reflective gratings [35] arrays. The need of dedicated processing steps for obtaining diffraction gratings is the main limitation associated to the fabrication of these microspectrometers. It must be noted that these kind of microspectrometers are more suitable for separating the light in the infrared (IR) range and behind (i.e., outside the visible range). In this sequence of ideas, the microspectrometers based on interferometric techniques constitute cheaper and simpler approaches.

4. Interferometric microspectrometers

4.1. Microspectrometer design

Fabry–Perot etalons (FPEs) are structures widely used for separating a specific wavelength from a broad band light source. FPEs are composed by two highly reflective surfaces (e.g., two parallel mirrors) facing each other and a dielectric resonant cavity in-between those with a selected distance d [m]. There are two methods to fabricate such structures. One method is stacking a given number of dielectric layers, which defines the properties of the mirror but having a very complex and hard to control fabrication process due to the number of layers (and their thicknesses) required for defining the full width half maximum (FWHM). The other method uses two plasmonic waveguides in the following interfaces: air/resonance cavity and resonance cavity/photodetector. Because the thickness of the metallic mirrors is in the nanometer range, the light transmission between dielectric mediums is done through the mirrors working as plasmonic waveguides [36]. Simultaneously, these mirrors work as highly reflecting surfaces inside the cavity (e.g., the light resonate due to successive reflections) [37]. The optimum result obtainable when working with FPEs is dependent on the light

source beam and the generic homogeneity and smoothness of the fabricated structure. This type of devices is fabricated by stack-like thin-film deposition techniques inducing even more stray-light in the FPE environment due to the interface surfaces' roughness caused by the fabrication processes. The contact interfaces between layers are critical in quantifying the light scattering phenomenon that decreases the efficiency in the spectral selectivity expected for these resonant cavities.

The spectral selectivity of a FPEs depends directly on the finesse, F_{int} , of the resonator. It is desirable to have the highest possible value of F_{int} in order to increase the resolution. The finesse of parallel mirrors is given by:

$$F_{\text{int}} = \pi \cdot r^{1/2} \times (1-r)^{-1} \quad (1)$$

where r is the reflection coefficient of the mirrors. The most relevant aspects when designing such devices are the ability to fabricate flat mirrors with high reflectivity and at the same time guaranteeing that the two are parallel to each other. The resolution depends on the incidence angle of the light entering the cavity (for a given wavelength) and takes the maximum value when the parallelism of mirrors is perfect. This enhances the number of reflections and at the same time, this increases the number of interferences with the consequent finesse improvement. The spectral information can be obtained simply by varying the variables intrinsically associated with the resonator, whose values are (under ideal conditions) given by:

$$q\lambda = 2nd\cos(\alpha) \quad (2)$$

where q is an integer number that gives the interference order, α [°] or [rad] is the angle of incidence, n is the refractive index inside the cavity and d [m] is the distance between the mirrors. The resonance in the cavity occurs at $2nd = q\lambda_0$. It should be noted that such devices are designed for $q=1$ for application in the visible spectrum. As illustrated in Fig. 2, the distance between the mirrors must be within the 200–390 nm range, for operation in the visible spectrum with $q=1$. The distance between mirrors (for the same wavelength range) decreases when the dielectric material that forms the cavity is replaced by another one with a higher refractive index. This means that using silicon dioxide, the distance between the mirrors must decrease in accordance for

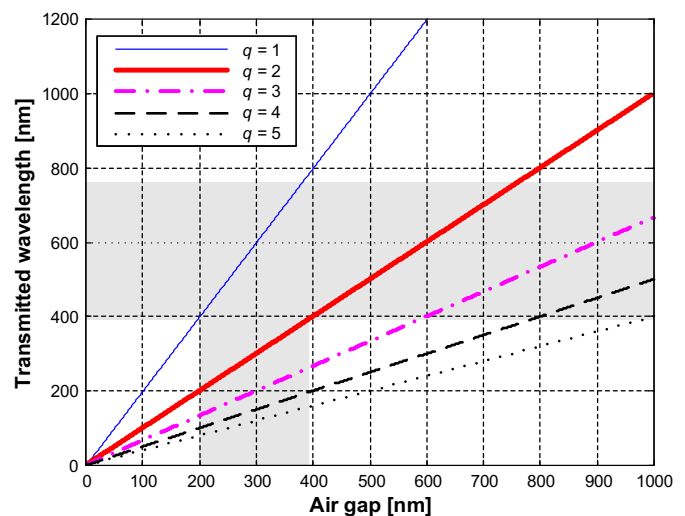


Fig. 2. Transmitted wavelength versus air gap ($n=1$) between mirrors. The visible range is in the horizontal shading. The cavity width must be in the range 200–390 nm ($q=1$) for allowing only one wavelength (vertical shading) in the range 400–780 nm to pass through it.

still covering the visible spectrum. This happens because the refractive index of this material ($n=1.46$) is higher than of the air ($n=1$).

The FPEs design was done in a way to allow their integration with the electronics of control and optoelectronic conversion. In this context, the aluminum (Al) was the selected material for the bottom mirror due to its compatibility with microelectronics processes (either CMOS and/or bipolar) [36,38]. The aluminum could be also a suitable candidate for the top mirror, but unfortunately this material presents higher absorption losses in the visible when compared with silver (Ag) [36,38]. Contrary to what happens in the macroscopic scale, a good protection from environmental exposition must be provided (for example, by sealing the complete microsystem) for avoiding any type of mirror degradation. In this sequence of ideas, it must be noted that to perform the spectral analysis, both the aluminum and silver mirrors cannot be opaque in order to allow the light to enter into the resonating cavity. This semi-transparency state is what will allow the light to enter into the etalon and resonate inside the cavity and reflect back and forth as many times as possible until exiting. The number of reflections and transmissions occurring during the resonating time evaluates the effect of the wavelength's interference until it is completely dissipated. The silicon dioxide (SiO_2) is transparent enough to allow the light to resonate within dielectric cavities and at the same time it is simple to deposit above the bottom mirror. This makes the silicon dioxide a suitable material for fabricating the dielectric cavities. Moreover, the silicon dioxide presents a constant refractive index approximately of 1.46 in the visible region, which is an added advantage for applications working in this particular portion of the electromagnetic spectrum. Since different wavelengths have different penetration depths, it means that shorter wavelengths will have smaller penetration depths. Fig. 3(a) shows this concept. This simplifies the fabrication of matrixes of cavities (each single cavity for a single photodetector) with different thicknesses of silicon dioxide [39]. The summary of the main characteristics (optical, electronic and mechanical) of this microspectrometer can be found in Table 1.

Alternatively and as illustrated in Fig. 3(b), a tapered cavity (above a large number of photodetectors) with a continuously variation in the thickness profile also constitutes an interesting idea for fabricating microspectrometers [40]. Independently of the used fabrication processes, the cavities must resonate within the visible spectrum. The Fabry–Perot interferometer fabricated by Emadi et al. [40] was designed to cover the spectrum between 570 nm and 720 nm. These specifications were achieved by fabricating cavities with its thickness varying linearly between 850 nm and 1000 nm. For this reason, this interferometer was denominated as Linear-Variable Optical Filter (LVOF). Moreover and contrary to what is usual, the mirrors were fabricated using layers made of different dielectric materials with different thicknesses. Each mirror contains five alternate layers of titanium dioxide (TiO_2) and silicon dioxide (e.g., three layers of TiO_2 and two layers of SiO_2 with 67 nm and 112 nm, respectively). The LVOF was tested with the help of a commercial CCD digital camera, by attaching it into the camera's objective and selecting the wavelength of a light source. A monochromator was used for this purpose. Then, a successive number of snapshots were acquired for further analysis, as well as for calibrating the whole system (composed by the LVOF and the camera). This is not a true-silicon microspectrometer. However, this opens good perspectives for future fabrication of complete microspectrometers because the techniques and the materials used for fabricating the LVOFs are compatible with those used by the microelectronics industry (either CMOS or bipolar or both). Table 1 also lists the main characteristics of this approach.

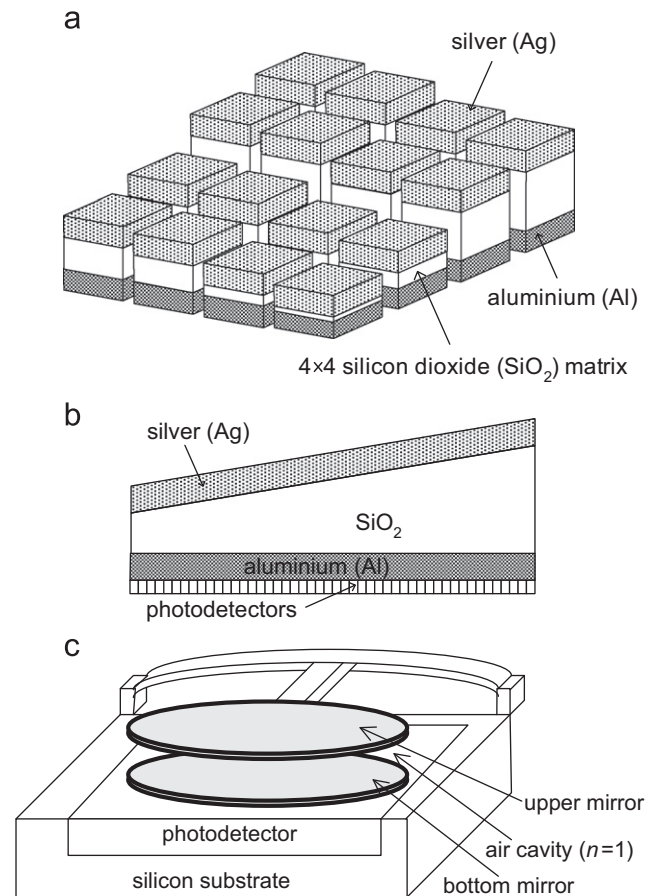


Fig. 3. Approaches for obtaining Fabry–Perot integrated microspectrometers used by (a) Correia et al. [39], (b) Emadi et al. [40], and (c) Chang et al. [41] (for convenience of illustration, only one Fabry–Perot etalon with air cavity is showed).

A previous attempt using the air ($n=1$) as the material within the cavities array was achieved by Chang et al. [41]. This microspectrometer contains 16 photodetectors (forming a 4×4 matrix of photodetectors) made of lateral interdigit PIN diodes, which were fabricated on a High Resistive Silicon (HRS) substrate for providing high isolation between adjacent photodetectors. As illustrated in the artwork of Fig. 3(c), the mirrors are both made of silver with a thickness of 50 nm and presenting a circular shape. The main difference between the mirrors relies in the selected materials for providing mechanical adaptation. The bottom mirrors are supported on a $1 \mu\text{m}$ -thick silicon nitride (SiN) layer, whereas each of the top mirrors are suspended by a 50 nm-thick silicon dioxide pre-buckled bridge. The width of the air cavities are in the range 140 nm and 290 nm for detecting light within the 400–680 nm range. The summary with the main characteristics of this microspectrometer can also be found in Table 1.

4.2. Case study

Fig. 4 illustrates the array with 16 resonators (i.e., the 4×4 Fabry–Perot etalons array) without the upper mirror [39]. This Figure clearly illustrates this concept, whose result is the thinning of silicon dioxide layers into 16 channels with different thicknesses. The white squares in black masks are holes that were drilled in order to allow the plasma etching of the silicon dioxide. The Scanning Electron Microscope (SEM) photograph in Fig. 5(a) shows a cross section of one of the fabricated Fabry–Perot etalons, where it is possible to observe the resonant cavity made of silicon dioxide layer between the top silver

Table 1
Summary of the several approaches for obtaining Fabry–Perot microspectrometers.

	Correia et al. [40]	Emadi et al. [39]	Chang et al. [41]
Chip-area	3.9 × 4.2 mm ²		
FWHM	18 nm	0.2 nm	
Technology	1.6 μm CMOS	LVOF mounted on a CCD Canon EOS 10D digital camera	Lateral interdigit PIN diodes
Wavelength range (nm)	380–500	570–720	400–680
Photodetectors (PDs)	P ⁺ /N-well photodiodes	Individual CCD pixels of the digital camera	Lateral interdigit PIN diodes on a HRS substrate
Number of PDs	16: 4 × 4 matrix	13: 200 pixels within 13 groups of 15 pixels	16: 4 × 4 matrix
Dark current (fA)	30		633
Size of PDs	500 × 500 μm	75 μm: groups of 15 pixels in a 5 μm pitch	< 160 μm
Mirror types	Metallic materials	Dielectric materials	Dielectric metallic mixed materials
Top mirror materials	Silver (Ag)	Alternate layers made of titanium dioxide (TiO ₂) & silicon dioxide (SiO ₂)	Silicon dioxide (SiO ₂) bridge/silver (Ag)
Bottom mirror materials	Aluminum (Al)	Alternate layers made of titanium dioxide (TiO ₂) & silicon dioxide (SiO ₂)	Silicon nitride (SiN)/silver (Ag)
Thickness of Top/Bottom mirrors (nm)	45 nm/20 nm	TiO ₂ /SiO ₂ /TiO ₂ /SiO ₂ /TiO ₂ 67/112/67/112/67 nm total thickness=425 nm	50 nm of SiO ₂ and 50 nm of Ag/1 μm of SiN and 50 nm of Ag
Cavity materials	Silicon dioxide (SiO ₂)	Silicon dioxide (SiO ₂)	Air
Refractive index, <i>n</i> , of cavities	≈ 1.46	≈ 1.46	≈ 1
Thickness range of cavities (nm)	225–300, step=5 nm	850–1000, linear thickness variation	140–290

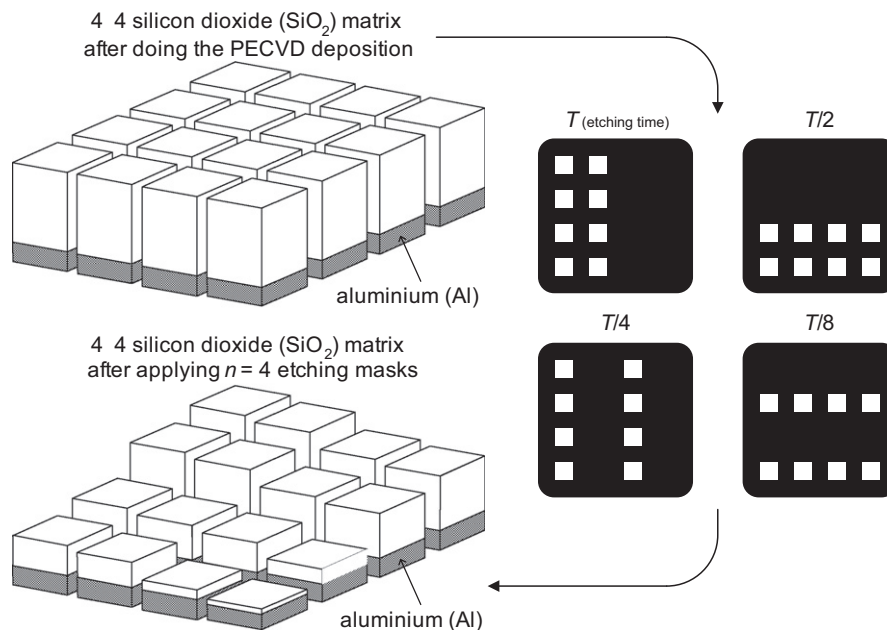


Fig. 4. The principle used to form the etalons matrix. After the deposition of the 4 × 4 silicon dioxide matrix, different etching times are used for each mask. The result is a 4 × 4 silicon dioxide matrix with different thicknesses.

and the bottom aluminum mirrors. The artwork depicted in Fig. 5(b) makes clear how the FPEs were deposited on top of the photodetectors (which were fabricated in a 1.6 μm standard CMOS process).

A thin-film optics software package was used for structural optimization of the 16 FPEs because the thickness of the silver layer is a trade-off between the absorption loss and the full-width half-maximum (FWHM). Contrary to what happens under ideal conditions, the simulations already taken in account the effects introduced by the materials used in the mirrors. In this context, the simulations showed that the most suitable thicknesses of mirrors were, respectively, 45 nm and 20 nm for the silver and aluminum. In terms of technology there are no constraints associated to the silicon dioxide, because this material acts as an adaptation layer, ensuring the further coexistence of silver

with the microelectronics (e.g., the array of 16 photodiodes). As showed in Fig. 5, the thickness of the 16 dielectric cavities was selected to change from 225 nm up to 300 nm and increasing in increments of 5 nm. This makes possible to cover the 400–500 nm wavelength range with an inter-channel shift of about 6 nm.

The performance evaluation of the device was done by measuring the electrical characteristics and the optical response of each individual channel. The measurement setup was mounted as follows: a light beam sourced by a monochromator (model Triax-180 featuring a 1.2 kg mm⁻¹ grating with a spectral dispersion of 3.6 nm mm⁻¹ for achieving a spectral resolution of 0.3 nm at the 546 nm wavelength) was collimated with the help of a lens. Then a slit, a pinhole and focusing lenses allowed the production of an optical beam with a 400 μm of diameter for testing the 16 channels in the matrix. Both the electrical and

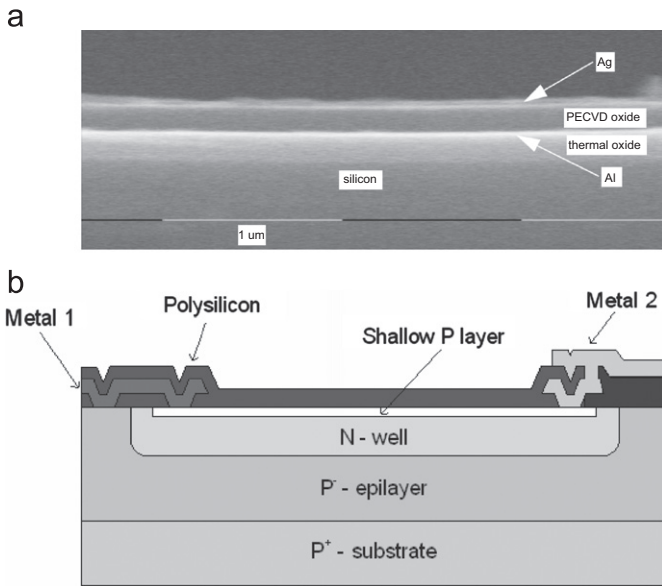


Fig. 5. (a) Cross section SEM photograph of a selected sample of Fabry–Perot cavity, which is composed of a SiO₂ layer (with a thickness of 300 nm) between a top silver and a bottom aluminum mirrors. The roughness of the contacting surfaces between the different layers is clearly visible in the device. (b) Artwork illustrating the cross section of the photodetector design in a 1.6 μm standard CMOS process.

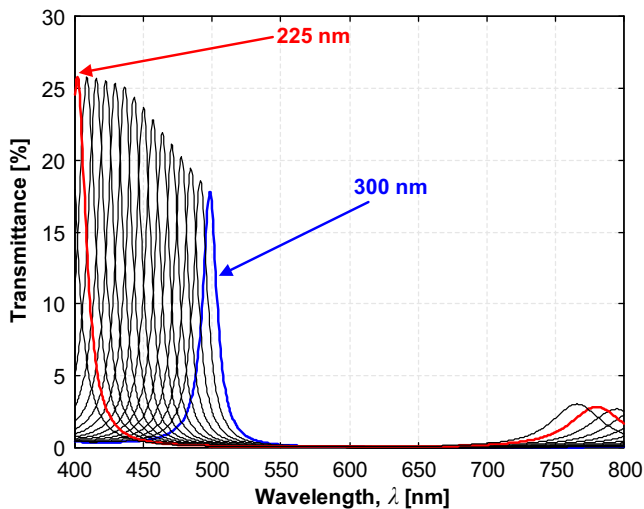


Fig. 6. Simulated transmittance versus the wavelength for a set of 16 Fabry–Perot etalons with mirrors made of silver and aluminum with thicknesses of 45 nm and 20 nm, respectively. The thickness of their dielectric layers made of silicon dioxide is in the 225–300 nm wavelength range and varies in integer steps of 5 nm.

optical characteristics of the 16 channels were measured with the help of a DC source/monitor HP model 4142B (featuring a full-scale ranging from 1 fA up to 1 A with a resolution of 0.1 pA). A commercial photodiode (Hamamatsu model S1336-5BQ) was used for calibrating the measurement system in order to make the measurements the most reliable as possible. To finish, all the measurement hardware was mounted and aligned on top of an optical table with an anti-vibrating system to guarantee the precise focusing of the individual channels. Fig. 7 illustrates the setup for a better understanding.

Fig. 8 shows the spectral responsivity, R [A·W⁻¹], of the 16 channels, which were measured for the 400–800 nm wavelength range with the help of the respective on-chip photodiodes. It can be observed that the ratio between the base line and the

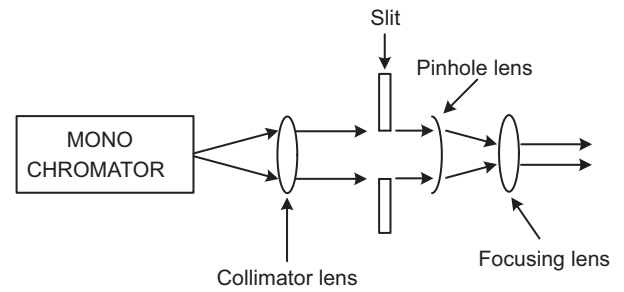


Fig. 7. Focusing light setup for performance evaluation of the device.

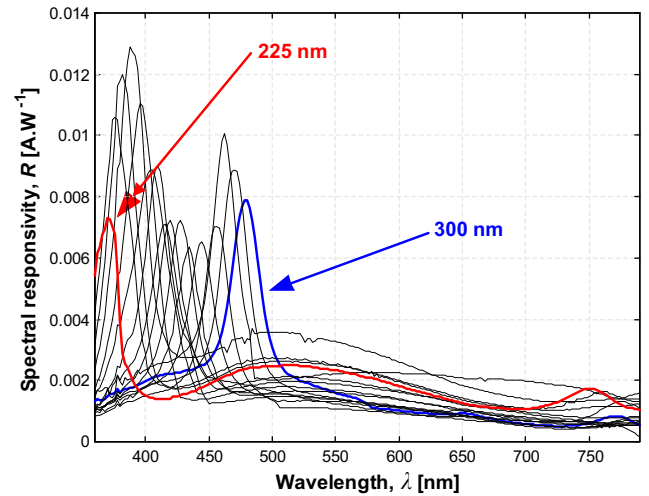


Fig. 8. Measured spectral responsivity of the 16 channels versus the wavelength.

peak maximum ranges from 4 to 7. It can be also observed that the relatively high scattered light, the beam divergence and the roughness surface are the main causes that affected the background signal. As presented in one of the next subsections, a method to compensate the scattered light will help to reduce the effect of the non-idealities of both the incident light beam and the FPEs. The photography of this array-type microspectrometer for the visible range of the electromagnetic spectrum is showed in Fig. 9.

4.3. Limitations

The spectral range can be extended up to about 571 nm (e.g., to more than 480 nm) by using two adjacent dies with 16 channels each (each die with a 4 × 4 matrix) and doing an initial PECVD silicon dioxide deposition with a thickness of 350 nm. Then, an additional fifth etching mask can be applied in the second die for doing a fifth etching step during a time of $T/16$ s. This simple technique is used to form a 32 channels microspectrometer with a higher wavelength range. This technique can be further extended to yield a device with 64 channels ($T/32$) or even with 128 channels ($T/64$).

The major and obvious limitation of array-type microspectrometers is the high waste of the impinged optical power. This happens because the light is projected into the direction of the microspectrometer and then, it is distributed over the array before the dispersion take place. This means that the optical power delivered to each etalon is inversely proportional to the number of channels. The resolution of the fabricated microspectrometer presented in this paper is thus intrinsically limited to $R=16$. This limited performance is due to only the first-mode ($q=1$) be the one allowed for operation in these type of microspectrometers

with the consequence to have a FWHM equal to the finesse, F_{int} , of the FPE (that is limited by the mirror reflectivity) — see Eq. (2). The thickness of thin-films used for fabricating the mirrors limits the designer's action because IC-compatible materials (as it is the case of the aluminum) must be used at least in the bottom mirrors. The fabrication of good aluminum mirrors is a complex and challenging task because high resolutions require mirrors with high reflectances and at the same time, high throughputs are only achieved with low absorptions. This is evident when looking for the thickness increase of aluminum mirrors from 5 nm to 10 nm, whose consequence is an optical transmission reduction from 90% to only 5% and inversely the reflectivity varies from 10% to 85% [42]. These contradictory factors trade between them and difficult the task to get good mirrors in aluminum, especially when the absorption increases rapidly with the thickness of the metallic layer. Therefore, the consequence is achieving a poor signal-to-noise ratio. Practical devices with FPEs made with metallic mirrors typically present throughput peaks at resonance of only 10%. High-performance (high-reflection/low-absorption) mirrors can be fabricated by combining a multiplicity of layers made of dielectric materials [40]. These dielectric mirrors can be easily assembled on top of microelectronic devices (in CMOS or

bipolar technology) using IC-compatible thin-film deposition techniques (chemical vapor deposition, CVD) as well as IC-compatible materials (silicon dioxide, SiO_2 , and titanium dioxide, TiO_2) for the several layers of the mirrors [40,43].

Other problems in microspectrometers are the structural induced and the light source noises. The first one happens due to the non-perfectly matching connecting surfaces resulted from the thin-film deposition process where different materials inherently present non-parallelism and roughness. The light source noise problem happens due to the light scattering caused by the non-idealities of Fabry–Perot etalons. A method for compensating this non-ideality will be discussed in detail on the next subsection.

4.4. Compensation of scattering non-idealities

The optimum result obtainable when working FPEs is dependent on the light source beam and the generic homogeneity and smoothness of the fabricated structure. This type of device is fabricated by stack-like thin-film deposition techniques inducing even more stray-light in the FPE environment due to the interface surfaces' roughness caused by the fabrication processes. The contact interfaces between layers are critical in quantifying the light scattering phenomenon that decreases the efficiency in the spectral selectivity expected for these resonant cavities. The non-idealities of this kind of FPEs are responsible for the inherent noise this device presents. This noise is independent from the etalon's thickness and it was noticed that several fabricated devices with different widths present similar noise. Therefore, an improvement of the device's spectral selectivity is obtained by doing the following procedure: first, it is necessary to add an identical passive structure but fabricated to transmit through the etalon a wavelength ten times thinner than the one filtered by the active FPE.

Due to the thin-film deposition process, the non-perfectly matching interfaces of different materials inherently present non-parallelism and surface roughness, detailed in Fig. 6(a). These plasmonic waveguides are the critical part of the FPE to be improved because they better represent the non-idealities of the fabricated device. Nevertheless, it is possible to reduce the overall roughness of the silver surface by applying a pretreatment with a SnCl_2 solution and low iodination temperature [44]. This is very important to do in the silver plasmonic waveguide because it is where the light enters the etalon and the scattering starts immediately after the first contact of the light with the optical cavity. In Fig. 10 is demonstrated how the light interacts inside the cavities with different thicknesses, and the corresponding optical output, caused mainly by two reasons. One is related to the way light travels through different mediums. As light crosses the different layers that compose the FPE, the aforementioned issues induce diffuse reflection. For the visible range, when the free-space incident light reaches the SiO_2 filtering cavity, it will shorten the wavelengths by the medium's refractive index. The other source for noise in the optical filter is caused by the

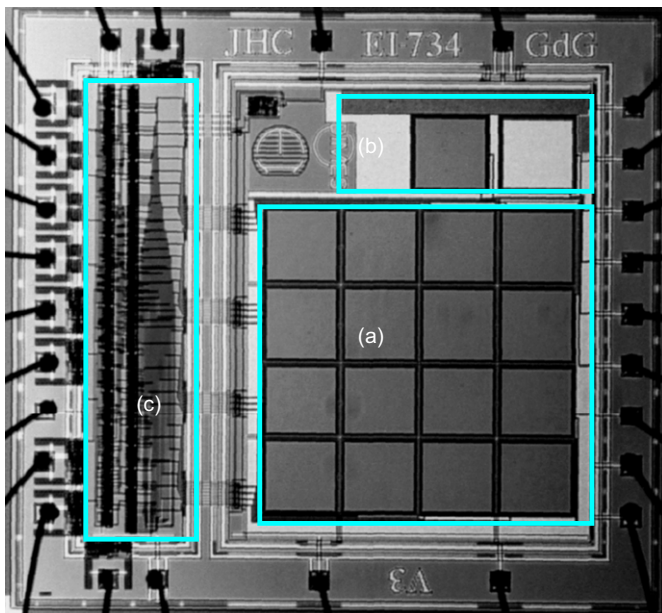


Fig. 9. Photograph of a prototype of an array-type microspectrometer composed by 16 channels, each one with a CMOS photodiode with a Fabry–Perot etalon mounted on top. Three main subsystem blocks can be identified in the photograph: (a) array of 16 Fabry–Perot mounted above 16 photodiodes, (b) dark current reduction, and (c) electronics for readout and signal processing (analog-to-digital conversion and amplification) and a serial bus for communicating with external devices [39].

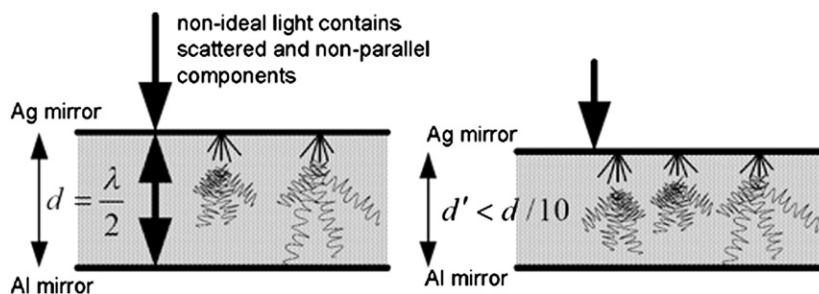


Fig. 10. The optical noise inside a Fabry–Perot etalon, where d [m] is the thickness for resonance to occur for a given wavelength λ [m], and d' [m] is at least ten times thinner than d .

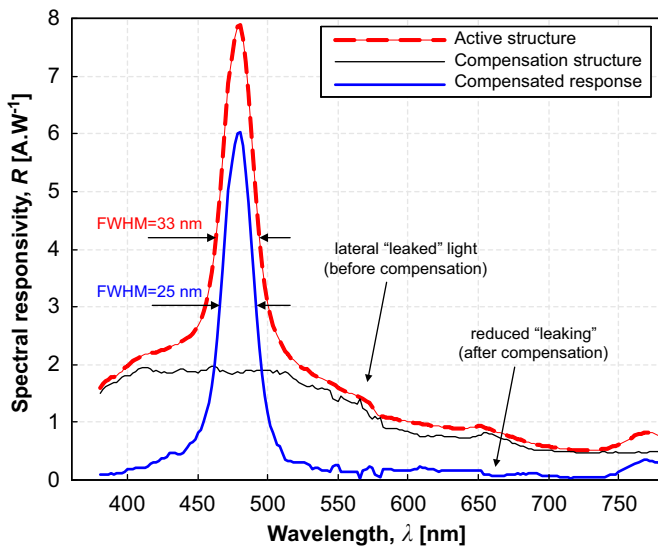


Fig. 11. Mean values of measured spectral responsivities (dashed line) for 300 nm thick FPEs and noise (thinner line) for 30 nm thick compensation FPEs. The “clean” compensated output signal after noise subtraction is also presented (thickest line). It can be observed that the mean FWHM centered at 480 nm was improved by 8 nm (e.g., from 33 nm to 25 nm).

light source’s components that are not perpendicular to the filter’s plane, which ideally should be. The non-normal components of the light, with unknown angles of incidence, induce multiple reflections inside the cavity [45]. In controlled environments, a collimator is used to minimize the stray light by narrowing the beam, therefore, the presented compensation cavity overcomes these limitations. For the visible wavelengths, the different roughness for each layer are responsible for scattering the light noticeably, visible wavelengths, the different roughness for each layer are responsible for scattering the light noticeably, hence prejudicing the FPE’s ability to distinguish a narrow tuned wavelength.

The proposed solution is a ten fold reduction in the thickness of the resonant cavity. Apart from that, this structure is exactly the same as the active FPE. The Ag/SiO₂ interface presents roughness caused by the fabrication processes, which is responsible for the light scattered into plasmonic modes in that region and, ultimately, also for the 8 nm FWHM width improvement. By using such a compensation structure with the only purpose of quantifying the noise and subtract it from the measured signal of the FPE, a reduction of the transmitted spectral band around the resonance wavelength is achieved. This is possible because the fabricated FPEs have similar background noise. Fig. 11 shows the mean values of spectral responsivities [mA/W] measured for all active FPEs and the noise compensation FPEs with thicknesses with 300 nm and 30 nm, respectively. The improved output signal obtained after the subtraction is also represented in Fig. 11. Moreover, Fig. 11 also shows that the FWHM, before and after compensation, is improved by 8 nm hence increasing considerably the device’s spectral selectivity. Furthermore, when operating in the visible part of the spectrum, the new passive FPE does not present any new resonance peaks at shorter wavelengths. Therefore, there are not undesirable consequences in adopting such a structure to measure the non-resonant effects and use them for signal compensation purposes.

5. Conclusions

This paper made a review of microspectrometers in silicon for the industry. The technical issues and challenges concerning their

fabrication were also presented, as well as the limitations imposed by their intrinsic dimensions. A compensation technique for minimizing the effect of the scattered light was also presented in this paper. By fabricating a compensating structure producing a background noise similar to the active FPE, the otherwise unwanted signal is then subtracted resulting in a better output signal than without the compensation FPE. The compensation etalon also results in a considerable improvement in the device’s spectral selectivity by reducing the FWHM from 33 nm to 25 nm. This solution was applied to a set of FPEs for a wavelength inside the visible range (e.g., $\lambda_0=480$ nm) and resulted in a FWHM improvement in the order of 24%. Adding more etalons will cover the entire 380–780 nm wavelengths. The array-type microspectrometer that was presented as case study can be used with success in the industry for doing. To finish, it must be noted that microspectrometers in silicon offer the opportunity to integrate the spectrometer, the readout and signal processing subsystems in the same die in order to provide a genuine microdevice with low-cost.

References

- [1] Jia S, Ding G, Zhao X, Yang C. Novel optic-fiber switches based on the wobble-type MEMS electromagnetic microactuator. *Optics & Laser Technology* 2007;39(2):353–8.
- [2] Li Y, Chen D, Yang C. Sub-microns period grating couplers fabricated by silicon mold. *Optics & Laser Technology* November 2001;33(8):623–6.
- [3] Feng L, Sihai C, Huan L, Yifan Z, Jianjun L, Yiqing G. Fabrication and characterization of polydimethylsiloxane concave microlens array. *Optics & Laser Technology* 2012;44(4):1054–9.
- [4] Shalaby MM, Abdelmoneum MA, Saitou K. Design of spring coupling for high-Q high-Frequency MEMS filters for wireless applications. *IEEE Transactions on Industrial Electronics* 2009;56(4):1022–30.
- [5] Liao S-D, Tsai J-C. The evolution of MEMS displays. *IEEE Transactions on Industrial Electronics* 2009;56(4):1057–65.
- [6] Jang B, Hassibi A. Biosensor systems in standard CMOS processes: fact or fiction? *IEEE Transactions on Industrial Electronics* 2009;56(4):979–85.
- [7] Li L, Uttamchandani D. Flip-chip distributed MEMS transmission lines (DMTLs) for biosensing applications. *IEEE Transactions on Industrial Electronics* 2009;56(4):986–90.
- [8] Lin Y-T, Lin Y-S, Chen C-H, Chen HC, Yang Y-C, Lu S-S. A 0.5 V biomedical system-on-a-chip for intra-body communication system. *IEEE Transactions on Industrial Electronics* 2011;58(2):690–9.
- [9] Kuo S-K, Chen S-L, Lin C-T. Design and development of RFID label for steel coil. *IEEE Transactions on Industrial Electronics* 2010;57(6):2180–6.
- [10] Alahmad MA, Hess HL. Evaluation and analysis of a new solid-state rechargeable microscale lithium battery. *IEEE Transactions on Industrial Electronics* 2008;55(9):3391–401.
- [11] Enriquez DAC, Cruz AR, Giraldo MTMR. Hybrid FBG–LPG sensor for surrounding refractive index and temperature simultaneous discrimination. *Optics & Laser Technology* 2012;44(4):981–6.
- [12] Ospina J, Canuto E, Molano Jimenez A, Acuña-Bravo W. Multilayer control of an optical reference cavity for space applications. *IEEE Transactions on Industrial Electronics* 2010;57(7):2507–18.
- [13] Grossman BG, Boonsopa S, Sokol M. Lead-insensitive fiber optic pH sensor and performance under bending. *Optics & Laser Technology* 2005;37(3):199–209.
- [14] Bifano T. MEMS deformable mirrors. *Nature Photonics* 2011;5:21–3.
- [15] Kong S-H, Wijngaards DDL, Wolffenbuttel RF. Infrared micro-spectrometer based on a diffraction grating. *Sensors and Actuators A: Elsevier Science* 2001;92:88–95.
- [16] Sakudoa A, Suganumaa Y, Kobayashia T, Onoderac T, Ikuta K. Near-infrared spectroscopy: promising diagnostic tool for viral infections. *Biochemical and Biophysical Research Communications: Elsevier Science* 2006;341:279–84.
- [17] Huang H, Yu H, Xu H, Ying Y. Near infrared spectroscopy for on/in-line monitoring of quality in foods and beverages: a review. *Journal of Food Engineering: Elsevier Science* 2008;87:303–13.
- [18] Moffat AC, Assi S, Watt RA. Identifying counterfeit medicines using near infrared spectroscopy. *Journal of Near Infrared Spectroscopy* 2010;18:1–15.
- [19] Reeves JB, McCarty GW, Reeves VB. Mid-infrared diffuse reflectance spectroscopy for the quantitative analysis of agricultural soils. *Journal of Agricultural and Food Chemistry* 2001;49(2):766–72.
- [20] Safar M, Bertrand D, Robert P, Devalued MF, Genot C. Characterization of edible oils, butters and margarines by Fourier transform infrared spectroscopy with attenuated total reflectance. *Journal of American Oil Chemists Society* 1994;71(4):371–7.
- [21] Bartick EG. Applications of Vibrational Spectroscopy in Criminal Forensic Analysis. *Handbook of Vibrational Spectroscopy*; 2006.

- [22] Fernandes AV, Cardoso VF, Rocha JG, Minas G. Smart-optical detector CMOS array for biochemical parameters analysis in physiological fluids. *IEEE Transactions on Industrial Electronics* 2008;55(9):3192–200.
- [23] de Hoog J, Osán J, Szalóki I, Eyckmans K, Worobiec A, Ro C-U, Van Grieken R. Thin-windows electron probe X-ray micro-analysis of individual atmospheric particles above the North Sea. *Atmospheric Environment* 2005;39:3231–42.
- [24] de Graaf G, der Vlist W, Wolffenbuttel RF. Design and fabrication steps for a MEMS-based infrared spectrometer using evanescent wave sensing. *Sensors and Actuators A: Elsevier Science* 2008;142:211–6.
- [25] Wolffenbuttel RF. State-of-the-art in integrated optical microspectrometers. *IEEE Transactions on Instrumentation and Measurement* 2004;53(1):197–201.
- [26] Wolffenbuttel RF. MEMS-based optical mini and microspectrometers for the visible and infrared spectral range. *Journal of Micromechanics and Microengineering: Institute of Physics (IOP)* 2005;15:S145–52.
- [27] Emadi A, Wu H, Grabarnik S, de Graaf G, Hedsten K, Enoksson P, Correia JH, Wolffenbuttel RF. Fabrication and characterization of IC-compatible linear variable optical filters with application in a micro-spectrometer. *Journal Sensors and Actuators A: Elsevier Science* 2010;162:400–5.
- [28] Sailaja S, Arora V, Kumbhare SR, Joshi RA, Naik PA, Gupta PD. Transmission grating spectrograph with on-line recording of XUV soft X-ray spectra from laser produced plasmas. *Optics & Laser Technology* 2006;38(1):46–50.
- [29] Liu J, Gao H, Zhou J, Liu D. The design of a polarizing beam splitter made from a dielectric rectangular-groove grating. *Optics & Laser Technology* 2009;41(5):622–626.
- [30] Kloos G. Design of a Michelson interferometer for the measurement of electrostrictive strains. *Optics & Laser Technology* 1996;28(6):481–4.
- [31] Srivastava A, Gupta MM, Medhekar S. Signal amplification based on the local nonlinear Mach-Zehnder interferometer. *Optics & Laser Technology* 2012;44(2):492–496.
- [32] Papadopoulos G, Zoiros KE. On the design of semiconductor optical amplifier-assisted Sagnac interferometer with full data dual output switching capability. *Optics & Laser Technology* 2011;43(3):697–710.
- [33] Wu Z, X G. Transmission of a gaussian beam after incidenting nonnormally on a Fabry-Perot etalon: a nonresonant case. *Optics & Laser Technology* 2003;35(2):123–6.
- [34] Kong S-H, Wolffenbuttel RF. Spectral performance of a micromachined infrared spectrum analyzer in silicon. *IEEE Transactions on Instrumentation and Measurement* 2005;54(1):264–7.
- [35] Grabarnik S, Emadi A, Wu H, de Graaf G, Vdovin G, Wolffenbuttel RF. Fabrication of an imaging diffraction grating for use in a MEMS-based optical microspectrograph. *Journal of Micromechanics and Microengineering* 2008;18(064006):1–6.
- [36] Chien-I Lin Thomas K. Gaylor, loss measurement of plasmonic modes in planar metal-insulator-metal waveguides by an attenuated total reflection method. *Optics Letters* 2010;35(22):3814–6.
- [37] Hass G. Filmed surfaces for reflecting optics. *Journal of Optical Society of America* 1955;45(11):945–53.
- [38] Bartek M, Correia J, Wolffenbuttel RF. Silver-based reflective coatings for micromachined optical filters. *Journal of Micromechanics and Microengineering: Institute of Physics (IOP)* 1999;9:162–5.
- [39] Correia JH, de Graaf G, Bartek M, Wolffenbuttel RF. A CMOS optical microspectrometer with light-to-frequency converter, bus interface and stray-light compensation. *IEEE Transactions Instrumentation & Measurement* 2001;50(6):1530–1537.
- [40] Emadi A, Wu H, Grabarnik S, de Graaf G, Hedsten K, Enoksson P, Correia JH, Wolffenbuttel RF. Fabrication and characterization of IC-compatible linear variable optical filters with application in a micro-spectrometer. *Journal Sensors and Actuators A* 2010;162:400–5.
- [41] Chang, C-P, Huang, R-S, A 16-channel array-type microspectrometer using integrated Fabry-Perot etalons and lateral PIN photodetectors, in *Proc. of IEEE Sensors 2003 (Second IEEE International Conference On Sensors)*, pp.675–678, 2003.
- [42] Rossberg D. Optical properties of the integrated infrared sensor. *Journal Sensors and Actuators A: Elsevier Science* 1996;54:793–7.
- [43] Ribeiro E, Malczyk A, Carvalho S, Rebouta L, Fernandes JV, Alves E, Miranda AS. Effects of ion bombardment on properties of d.c. sputtered superhard (Ti, Si, Al)N nanocomposite coatings. *Surface Coating Technology* 2002;515:151–2.
- [44] Sui K-R, Shi Y-W, Tang X-L, Zhu X-S, Iwai K, Miyagi M. Optical properties of Ag/Ag infrared hollow fiber in the visible wavelength region. *Optics Letters* 2008;33:318–20.
- [45] Morichetti F, Canciamilla A, Melloni A. Statistics of backscattering in optical waveguides. *Optics Letters* 2010;35:1777–9.

Application of Fiber Bragg Gratings to Wearable Garments

João Paulo Carmo, *Member, IEEE*, Alexandre Manuel Ferreira da Silva, *Student Member, IEEE*, Rui Pedro Rocha, and José Higinio Correia, *Member, IEEE*

Abstract—This paper presents a photonic system based on Fiber Bragg Gratings (FBGs) for application to wearable garments. The objective is spanning the FBGs over the whole area of the garments for acting as sensing elements. The FBGs are embedded on a polychloroethanediyl (polyvinyl chloride, commonly abbreviated as PVC) carrier in order to increase their sensitivity to strains and for improving the simultaneous acquisition of respiratory and cardiac frequencies with only one FBG sensor. The global structure comprising FBGs and carrier allow high strain cycles and at the same time present linear behavior with the temperature, $17 \text{ pm} \cdot ^\circ\text{C}^{-1}$. The measurements show a stable structure for temperatures up to 100°C . This brings excellent perspectives for measuring the temperature with high accuracy and range. A set of tests were done by subjecting the FBG/carrier structure (with FBG stretched and no curves) to strains up to 1.2 mm, and it was also observed a linear behaviour: e.g., displacements of $0.8 \text{ pm} \cdot \mu\text{m}^{-1}$. Behind its sensing enhancement operation, the carrier makes easy to mount the sensing structures.

Index Terms—Fiber Bragg grating (FBG), noninvasive monitoring, optical fiber sensors, wearable devices.

I. INTRODUCTION

IT IS NOT anymore strange the link between textiles and electronics, where the combination of electronics and textiles into a single structure in order to obtain electronic textiles or e-textiles [1]. In this context, this paper presents a photonic system based on Fiber Bragg Grating (FBG) for integration in garments used on environments infested with high-intensity radiation or subjected to high-magnetic fields. Solutions supported in photonic systems are good ways due to its robustness and resilience when subjected to the former conditions [2]. Optical fibers are good ways for achieving such measurement goal [3]. The first set of tries to integrate optical fibers on textiles was done in the Georgia Tech's wearable motherboard (GTWM, also known as smart shirt), where the objective of the fibers was in the bullet wounds detection for soldiers acting on war scenarios [4]. The previous works integrating FBGs into textiles pushed this concept further,

by presenting continuous monitoring systems for healthcare monitoring applications. The work developed by Jonckheere *et al.* [5], [6] is one of the first known approaches integrating FBGs in textiles and enables the measurement of respiratory movements under magnetic resonance imaging environments. A detailed comparison between three methods (all integrating fibers into textiles, e.g., macrobending sensors, FBG sensors, and time reflectometry sensors) for measuring the elongation of the abdominal circumference during breathing movements is analyzed by Grillet *et al.* [7]. The photonic system presented in this paper presents a complete monitoring system based on a single FBG concept for sensing both the respiratory and the cardiac frequency, as well as the environment temperature.

II. FBG-BASED PHOTONIC SYSTEM

A. FBG Sensors

FBG sensors can find wide applications on telecommunication and sensing systems. In fact, the FBGs are suitable sensing elements for doing physical measurements where a kind of displacement is available. Examples of such applications are found in the literature include the measurements of strain [8], tilt rotation by an angle [9], temperature [10] humidity [11], and magnetic fields [12]. FBGs are periodic changes in the refraction index of the fiber core made by adequately exposing the fiber to intense ultraviolet (UV) light. The resonance behavior depends on grating pitch and on their axial variation because the resonance behavior strictly follows external actions in the exact proportion as the silica matrix surrounding the gratings. The ultimate effect of the resonances is the reflection by successive and coherent scatterings from the index modulation of a narrowband of the incident optical field injected into the fiber. In a FBG, the strongest interaction or mode-coupling responsible for the reflected light occurs at a well-known wavelength, λ_B [nm], also known as Bragg wavelength. The Bragg's spectral component depends directly on the grating period of the FBG, Λ [nm], on the modal index, n_{eff} , also known as effective refractive index of the FBG, and is given by [13]

$$\lambda_B = 2n_{eff}\Lambda. \quad (1)$$

The shift in the wavelength, $\Delta\lambda_B$ [nm], with respect to the cross-sensitivity with the temperature and the axial strain change, ΔT [K] and $\Delta\varepsilon$, respectively, is given by [13], [14]

$$\frac{\Delta\lambda_B}{\lambda_B} = (1 - \rho_\varepsilon)\Delta\varepsilon + (\alpha + \xi)\Delta T \quad (2)$$

where ρ_ε is the photo-elastic coefficient of the fiber, α is the thermal expansion coefficient of the fiber material, and ξ is the thermo-optic coefficient of the fiber material. For a 1550 nm

Manuscript received June 28th, 2011; revised May 18, 2011; accepted June 28, 2011. Date of publication July 05, 2011; date of current version December 01, 2011. This work was supported by the Foundation for Science and Technology FCT/MIT-PT/EDAM-SI/0025/2008 project. The associate editor coordinating the review of this paper and approving it for publication was Prof. Ignacio Matias.

The authors are with the Department of Industrial Electronics, University of Minho, Campus Azurém, 4800-058 Guimarães, Portugal (e-mail: jcaro@dei.uminho.pt; id1894@alunos.uminho.pt; rrocha@dei.uminho.pt; higinio.correia@dei.uminho.pt).

Color versions of one or more of the figures in this paper are available online at <http://ieeexplore.ieee.org>.

Digital Object Identifier 10.1109/JSEN.2011.2161281

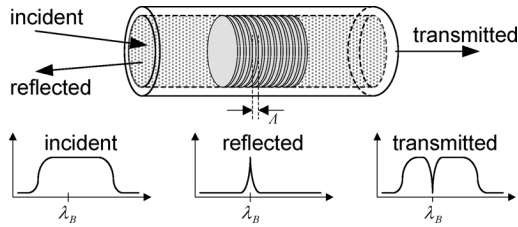


Fig. 1. Illustration of working principle of FBGs.

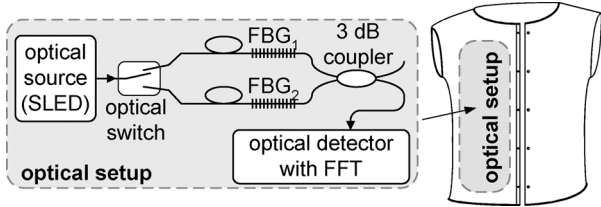


Fig. 2. The block diagram of the complete monitoring system comprising two channels tuned to a single- λ by way of a single FBG.

FBG inscribed into a silica fiber, the wavelength sensitivities with respect to changes in the temperature and in the axial strain are of $\approx 13 \text{ pm} \cdot ^\circ\text{C}^{-1}$ and $\approx 1 \text{ pm} \cdot \mu\text{E}^{-1}$, respectively [13]. It must be noted that for only-strain measuring, the temperature-offset compensation is mandatory to do.

Fig. 1 illustrates the FBG structure which is written on an optical fiber. This figure also illustrates that the injection of a broadband- λ pulse on the FBG results in a reflected beam located around the Bragg wavelength, λ_B [15]. It is possible to determine the exact strain by measuring the reflected spectra and/or the shifting produced in the Bragg wavelength [14]. Since the transmitted beam is the complementary of the reflected one, it is also possible to measure the exact strain [16]. The next section will be discussed the reasons for selecting this interrogation method.

B. FBG Interrogation System

In the system presented in this paper, a single FBG was used for simultaneously sensing the respiratory and cardiac frequencies, as well as the environment temperature. As illustrated in the Fig. 2, both FBG_1 and FBG_2 are tuned for the same wavelength, λ [nm], and demultiplexed with the help of a MEMS optical switch.

The proposed system is composed by three main subsystems: optical source (e.g., SLED), all-optical interrogation system (e.g., 2×2 fiber coupler, optical switch and the optical fibers), and the optical detector (with spectral analysis feature).

The optical source is a DL-CS5107A series SLED (Superluminescent LED) operating in a true inherent superluminescent mode in order to generate a broadband light-beam and is fabricated by DenseLight Semiconductors Company [17]. This light source can generate a broadband light beam (in [1530, 1570] nm range) with a maximal power of 8 mW.

The used FBGs were produced by the FiberSensing Company [18]. The selected length for the gratings was 8 mm and the resonance wavelength was tuned for 1541 nm, which corresponds to a refraction index modulation period of the core in the half-micrometer range ($\approx 0.52 \mu\text{m}$) based on the effective refractive index of 1.47.

TABLE I
THE USED COMPONENTS IN THE PHOTONIC SYSTEM

Component	Weight	Size dimensions	Power consumption
Optical source (SLED)		$40 \times 30 \times 9 \text{ mm}^3$	875 mW
2×2 coupler		$66 \text{ mm} \times \phi 3.8 \text{ mm}$	
1×2 optical switch	94 g	$40 \times 50 \times 15 \text{ mm}^3$	
FBGs+connectors			
Optical detector	150 g	$70 \times 46 \times 18 \text{ mm}^3$	150 mW

The optical switch model EK703-FC from Thorlabs GmbH [19] was selected for demultiplexing two optical fiber Bragg gratings. This component is a MEMS 1×2 fiber optical switch for use in the [1520, 1610] nm wavelength range, which contains an electronic system that controls a MEMS-actuated mirror for selecting the FBG to measure. This optical switch presents other characteristics that make it suitable for the proposed measuring application, e.g., low insertion loss (at 1550 nm) of 0.7 dB, high crosstalk rejection of 50 dB, and capability to handle high optical powers (up to 300 mW). Also, it is not necessary to use an optical isolator after the optical source due to the high return loss of 65 dB. The optical switch contains a digital input for selecting the output channel. Since the voltage of this signal can change between 0 and 5 V, the switch can be controlled by a microcontroller.

The 10202A-50 single-mode 2×2 fiber-optic coupler with a split ratio of 50/50 [%] from Thorlabs GmbH [19] was selected in order to combine the readings from the two optical fibers with FBGs. The most used method to get the readings from FBGs is by reflection and not by transmission. However, the reflection method implies the use of more complex solutions. The first one requires the use of an optical circulator for separating the incident and the reflected beams from the respective ports and a bidirectional switch. The second most complex solution do not require the use of an optical circulator but instead needs three fiber-optic couplers to provide the readings to the optical detector (one for each fiber between the FBG and the respective output port of the switch, and a third to combine the two reverse outputs of the previous two couplers). As illustrated in Fig. 2, it is possible to combine the two optical fibers with FBGs by using only one single optical fiber coupler and thus, achieving a cheaper and simpler solution.

Finally, the optical detector is an I-MON 80D interrogation monitor from Ibsen Photonics [20] which is especially suitable for real-time spectrum monitoring of signals acquired from FBG sensors. The operating temperature range of $0^\circ\text{C} - 70^\circ\text{C}$, the $70 \times 46 \times 18 \text{ mm}^3$ dimensions, and the low weight of 150 g makes this optical detector appropriated for integration in wearables uses in extreme harsh environments.

Table I shows the weight, size and power consumptions of the individual components. The shaded cells refer to blocks with negligible weight when compared with most bulk blocks (e.g., the optical switch and detector). The measurements were done using the SLED as optical source, which requires a source with a regulated voltage of 2.5 V and a power of 875 mW. Since it only needs a broadband pulse (with respect to the wavelengths), the LED model LED1550E from Thorlabs with a spectral FWHM of 100 nm (wide enough) applies very well due to its low-power consumption of only 2 mW [19]. This is especially important for

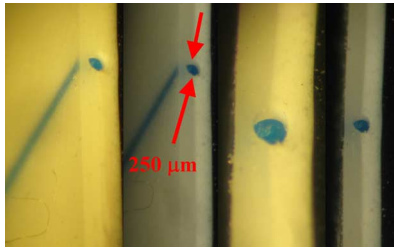


Fig. 3. A set of four photographs showing cross-section views of the layers configuration of a carrier prototype and the respective supported FBG.

the proposed portable application where it is provided a smaller power source composed by three class AA batteries each one with a voltage of 1.5 V (the same used for powering the micro-controller that controls the whole system).

C. FBG Carrier

A task to select a carrier material was done in order to increase the sensitivity of the FBG sensors to strains and at the same time for improving the adhesion. There are a lot of candidate materials for carrier usage; however, the one to be selected must also present an acceptable quality/price ratio for enabling its adoption by the industry. All of the former goals could only be achieved by using one of the three following thermoplastic polymers: the polyurethane (PUR) [21], the polyolefin (TPO) [22] and the polychloroethanediyl (polyvinyl chloride, or simply PVC) [23]. The polyurethane constitutes the option with best global performances. First, this material feels like real-leather, and second, it presents a very long durability and a high performance with regard to the flexibility. However, despite its advantages, the polyurethane is one of the most expensive flexible polymeric materials. Polyolefin can be a suitable alternative for the polyurethane by constituting a much lower price, but its flexibility and elastic limit are poorer than the case of polyurethane. Thus, in this sequence of ideas, the polychloroethanediyl was the selected material for use as FBG carrier due to its excellent performance/cost ratio and easy to manipulate during the manufacturing process. The polychloroethanediyl presents many other advantages when compared with its direct competitors, such as low production cost making this material highly competitive, high resistance to aging, high versatility, and simplicity of maintenance.

Fig. 3 shows the cross sections of the layers configuration of the carrier used for supporting the FBGs (a set of four photographs was taken under different directions and illuminations, in order to better illustrate the FBG sensor and the different layers of the carrier). The first layer of polychloroethanediyl (or external layer) is used to provide protection to the FBGs against external factors from the environment (e.g., mechanical chocks, scratches, corrosive atmospheres, among others). This is the visible layer after placing the carrier and it is about $200 \mu\text{m}$ -thick, which enables this layer to recover its initial shape after being easily bent. The optical fibers are flexible, can be easily bent and tend to recover their initial shape without breaking (when subjected to reasonable deformations, inside the safety limits). This means that a second layer (the middle layer) is needed to bond the FBGs to the carriers. The minimum thickness of this layer must be at least $300 \mu\text{m}$ in order to ensure

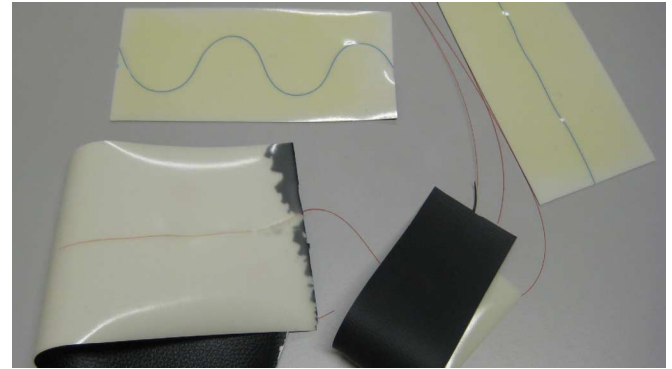


Fig. 4. A photograph of some functional prototypes with FBG sensors already embedded on the respective carriers.

the full wrap of a fiber with a diameter of $250 \mu\text{m}$. Finally, a third layer of polychloroethanediyl (or the inner layer due to obvious reasons) is the interface between the carrier and the wearable. The thickness of the inner layer is of major interest because it must provide a good transmission (enabling a good sensitivity) of cardio-respiratory stimulus and the environment temperature into the respective FBGs. Because the thickness of the inner layer constitutes a compromise between these physical measures, the most suitable thickness has been selected to be $400 \mu\text{m}$. Fig. 4 shows some functional prototypes with FBG sensors already embedded on the respective carriers. Hydrogen loaded standard telecommunication fiber (Corning SMF28e+) was used for writing the gratings in these prototypes. Only the prototype with the optical fiber describing an undulated path is useful for sensing applications because it avoids early fiber breakage due to elongation. Thus, when compared with straight FBGs, the undulated FBGs allow for the successfully measuring of high strains. Further details about the embedding of FBGs into the PVC carriers can be obtained from the work done by Silva *et al.* [24].

III. EXPERIMENTAL RESULTS AND DISCUSSION

A. FBG Displacement

A *Instron*[®] 4302 testing machine was used to evaluate the response of the FBG sensors before doing their integration into the carriers. In this sequence, an additional test was done by applying a continuous displacement at a constant increment of $16 \mu\text{m} \cdot \text{s}^{-1}$ and measuring the wavelength deviation. The graph of Fig. 5 reveals that the FBG sensors present a linear behavior for elongations above 0.6%. The elongation range was limited to 1.6% in order to avoid breaking the fiber.

B. Respiratory and Cardiac Frequencies

The temporal strain variations of FBGs can be used to measure the respiratory and the cardiac frequencies as it is the case of previous works [25]. However, contrary to such a work, one of the innovations presented in this paper is the possibility offered to measure the respiratory and the cardiac frequencies with a single FBG sensor (since the two frequency regions do not overlap). In this context, the positioning of the FBG sensor is crucial in order to maximize the transmission of cardiac motions into the fiber. The secret relies in the carrier's shape, where its

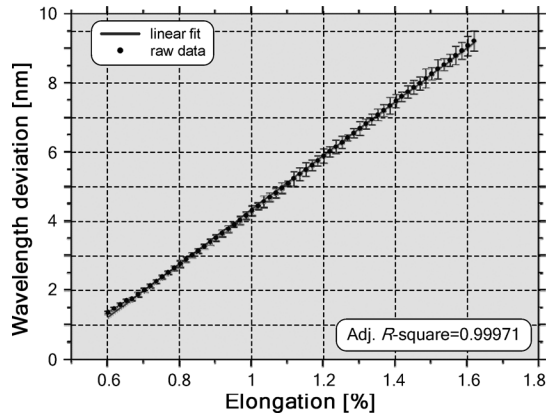


Fig. 5. The wavelength response to applied displacement.

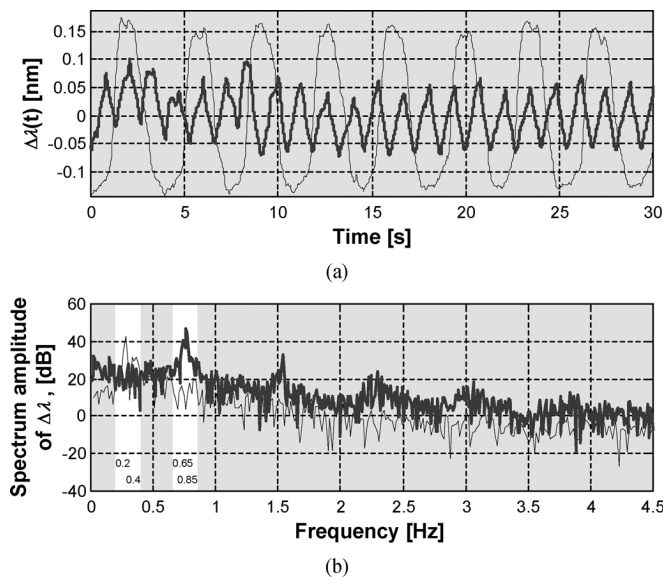


Fig. 6. Sensor response to a normal breath (raw data): (a) representation on time and (b) frequency domains.

structure must present enough area to cover a great portion of the chest and thus, in order to be capable for transmitting the chest movements due to the heart and respiration. For this purpose, it is expected that a wide rectangular structure to be more sensitive than a thin strap around the chest, because this enables the effect on the foil's corner to be sensed by the FBG sensor.

A set of tests were done with a group of 12 healthy subjects between 20 and 30 years old in order to evaluate the possibility to measure the heart and respiratory frequencies. Fig. 6(a) shows the wavelength shift, $\Delta\lambda(t)$ [nm], sensor response to a normal (thinner line) and to a fast (thicker line) breath (raw data), where the external interferences do not appear to degrade the quality of the acquired signal – it must be noted that the wavelength shift is measured in relation to the wavelength, λ_0 [nm], of the strain-less situation, thus the (1) is $\lambda_B = \lambda_0 + \Delta\lambda(t)$. The explanation for the observed small perturbations is mainly due to the transition between the inhale and the exhale stages. Fig. 6(b) shows the corresponding frequency spectrums, which reveals main frequency peaks between 0.2 and 0.4 Hz for normal breath and between 0.65 and 0.85 Hz for fast breath. An implementation in the digital domain makes easy the task to shift the central

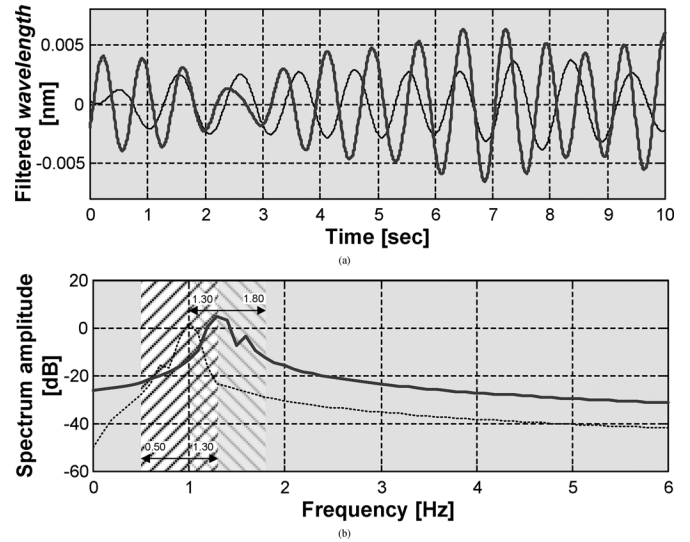


Fig. 7. (a) Developed sensing structure response with cardiac filtering stage and (b) respective frequency spectrums.

frequency of the filter and, consequently, retrieving the respiratory frequency.

The cardiac frequency can be obtained from the acquired FBG raw signal by applying a filtering. This task is relatively easy to do because the used optical detector allows the possibility to make fast Fourier transform (FFT) analysis and data logging. The acquired signals can be further processed by the analysis software, especially developed for this effect in the LabView graphical language. A bandpass filter for the [0.2, 0.4] Hz frequency range allows the measurement of the respiratory component, while a second bandpass filter with a passband in the range [0.5, 1.3] Hz can get the cardiac frequency. This second bandpass filter was used to discriminate the frequency set of interest around 1 Hz, by cutting the respiratory components below 0.5 Hz and the high frequencies (e.g., the high-frequency noise) above 1.3 Hz. Both passbands were implemented in the digital domain using the bilinear technique with the sampling frequency, f_s [Hz], of 36 Hz for approximating their analog transfer function [26]. This performs well in situations of normal heart beats (the thinner line in Fig. 7), however, for higher cardiac frequencies this frequency range cannot be enough for subjects under effort doing high exercise. The thicker line plotted in Fig. 7 refers to a signal that was acquired under a condition of high cardiac frequency. Shifting the passband of the filter on range [0.5, 1.3] Hz to [1.0, 1.8] Hz as postprocessing technique will make possible yet to still retrieve the cardiac component. Once again, this is not a problem because the filter is implemented in the digital domain, thus the coefficients can be updated in order to reflect the new transfer function.

Fig. 8(a) shows the respiratory signal after doing the bandpass filtering on the raw data acquired with the FBG sensor. The cardiac frequencies in Fig. 8(b) and (c) were, respectively, obtained by doing a second bandpass filtering on the raw data acquired with the FBG sensor and with the help of a Zephyr commercial sensor. The purpose of this last signal was validating the cardiac frequency acquired with FBG sensors and as it can be seen,

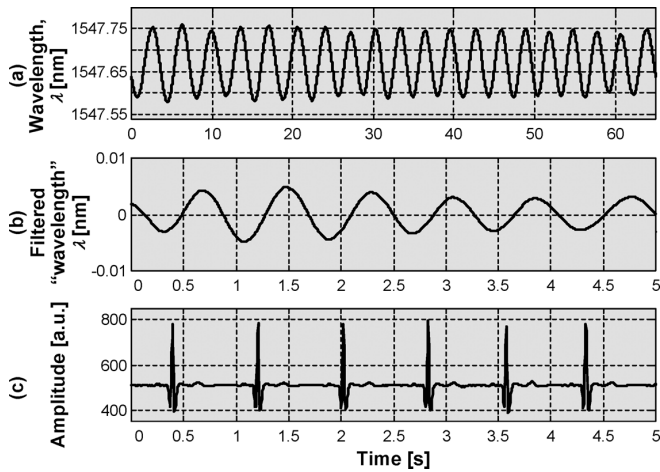


Fig. 8. Filtered signals: (a) the respiratory and (b) the cardiac frequency. (c) A cardiac frequency acquired with help of a Zephyr commercial sensor.

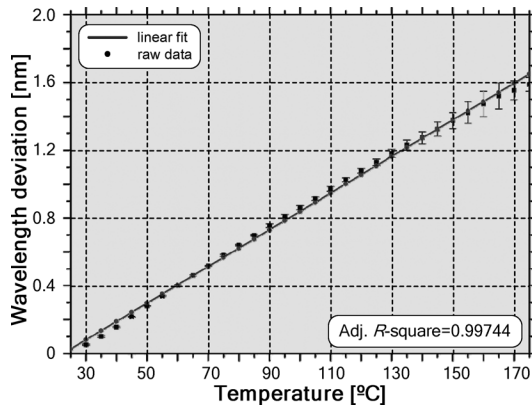


Fig. 9. The shift in the wavelength with reaction to temperature changes.

it exist a good agreement between the two waves. The vertical axis of Fig. 8(b) is expressed in terms of the wavelength (filtered “wavelength”) because it was obtained by filtering the raw data (whose values are instantaneous wavelengths).

C. Environmental Temperature

Since two single- λ FBGs can be combined with the help of the optical switch, the proposed photonic system contains an additional optical fiber sensor for sensing the environment temperature. In this sequence, the next step was the determination of the sensor performance when subjected to temperature changes. The thermal characterization was done by placing the FBG sensor of interest over a hot plate. The source of heat was programmed to provide temperatures up to 175 °C at a rate of 1 °C for each 3 s. The FBG wavelength shift was recorded with the hot plate being heated. Fig. 9 shows the measured values, where it can be observed that the obtained data tends to present a linear behavior. The FBG sensor reacted to temperature changes at a rate of 0.1 nm per 1 °C. The FBG sensor is not embedded into the carrier and kept floating with respect to the places where strains can happen due to the chest movements, in order to avoid the occurrence of cross-couples between the cardio-respiratory and the temperature components. Moreover, it is also important to have this FBG sensor fixed into a rigid support for avoiding

coupling of undesirable strains resulted from the respiratory, cardiac and voluntary movements. This allows the measuring of the temperature in an independent way, when both the magnitudes of the respiratory and cardiac frequencies as well as the temperature vary simultaneously.

IV. CONCLUSION

This paper presented a photonic system based on FBGs suitable for using in extreme harsh environments, as it is the case of fire scenarios where the temperatures are high. The novelty of the proposed solution over others available is the possibility to measure both the respiratory and the cardiac frequencies with a single FBG sensor. Moreover, the use of a digitally controlled optical switch allows the measurement of the environment temperature with a second FBG tuned at the same wavelength used for measuring the cardiac/respiratory frequencies. The interrogation system uses all-photonic components for doing the acquisition and is not restricted for the proposed functions. In fact, its scalability allows the inclusion of a larger number of FBGs. The polychloroethanediyl (PVC) material was used in the FBG carrier for increasing the sensitivity of the FBG responsible for measuring the cardiac/respiratory frequencies.

ACKNOWLEDGMENT

The authors want to acknowledgment that the integration of the FBGs into the carriers was done by TMG-Automotive (a company of the Textile Group, *Têxtil Manuel Gonçalves SA*) and the fabrication of FBG sensors was done by the FiberSensing Company SA.

REFERENCES

- [1] D. Marculescu, R. Marculescu, S. Park, and S. Jyaraman, “Ready to ware,” *IEEE Spectrum*, vol. 40, no. 10, pp. 28–32, Oct. 2003.
- [2] P. Biswas, S. Bandyopadhyay, K. Kesavan, S. Parivallal, B. A. Sundaram, K. Ravisankar, and K. Dasgupta, “Investigation on packages of fiber Bragg grating for use as embeddable strain sensor in concrete structure,” *Sens. Actuators A: Elsevier Science Direct*, vol. 157, pp. 77–83, 2010.
- [3] A. Augousti, F. Maletras, and J. Mason, “Evaluation of cardiac monitoring using fiber optic plethysmography,” *Ann. Biomed. Eng.*, vol. 34, pp. 416–425, 2006.
- [4] “The Georgia Tech wearable motherboard: The intelligent garment for the 21st century,” 1998.
- [5] J. D. Jonckheere, F. Narbonneau, M. Jeanne, D. Kinet, J. Witt, K. Krebber, B. Paquet, A. Depre, and R. Logier, “OFSETH: Smart medical textile for continuous monitoring of respiratory motions under magnetic resonance imaging,” in *Proc. 31st Annu. Int. Conf. IEEE Eng. Med. Biol. Soc.*, Minneapolis, MN, Sep. 2–6, 2009, pp. 1473–1476.
- [6] J. D. Jonckheere 1, F. Narbonneau, D. Kinet, J. Zinke, B. Paquet, A. Depré, M. Jeanne 1, and R. Logier, “Optical fibre sensors embedded into technical textile for a continuous monitoring of patients under magnetic resonance imaging,” in *Proc. 30th Annu. Int. Conf. IEEE Eng. Med. Biol. Soc.*, Vancouver, BC, Canada, Aug. 20–24, 2008, pp. 1473–1476.
- [7] A. Guillet, D. Kinet, J. Witt, M. Schukar, K. Krebber, F. Pirote, and A. Depre, “Optical fiber sensors embedded into medical textiles for healthcare monitoring,” *IEEE Sensors J.*, vol. 8, no. 7, pp. 1215–1222, Jul. 2008.
- [8] S. K. T. Grattan, S. E. Taylor, T. Sun, P. A. M. Basheer, and K. T. V. Grattan, “In-situ cross-calibration of in-fiber bragg grating and electrical resistance strain gauges for structural monitoring using an extensometer,” *IEEE Sensors J.*, vol. 9, no. 11, pp. 1355–1360, Nov. 2009.
- [9] F. Xie, Z. Chen, and J. Ren, “Stabilisation of an optical fiber Michelson interferometer measurement system using a simple feedback circuit,” *Measurement: Elsevier Science Direct*, vol. 42, pp. 1335–1340, 2009.
- [10] H. Bao, X. Dong, C. Zhao, L.-Y. Shao, C. C. Chan, and P. Shum, “Temperature-insensitive FBG tilt sensor with a large measurement range,” *Opt. Commun.*, vol. 283, pp. 968–970, 2010.

- [11] T. L. Yeo, T. Sun, K. T. V. Grattan, D. Parry, R. Lade, and B. D. Powell, "Polymer-coated fiber Bragg grating for relative humidity sensing," *IEEE Sensors J.*, vol. 5, no. 5, pp. 1082–1089, Oct. 2005.
- [12] P. Orr and P. Niewczas, "An optical fiber system design enabling simultaneous point measurement of magnetic field strength and temperature using low-birefringence FBGs," *Sens. Actuators A: Elsevier Science Direct*, vol. 163, pp. 68–74, 2010.
- [13] C.-L. Wei, C.-C. Lai, S.-Y. Liu, W. H. Chung, T. K. Ho, S. L. Ho, A. McCusker, J. Kam, and K. Y. Lee, "A fiber bragg grating sensor system for train axle counting," *IEEE Sensors J.*, vol. 10, no. 12, pp. 1905–1912, Dec. 2010.
- [14] J. Liu, C. Schmidt-Hattenberger, and G. Borm, "Dynamic strain measurement with a fiber Bragg grating sensor system," *Measurement: Elsevier Science Direct*, vol. 32, no. 2, pp. 151–161, Sep. 2002.
- [15] D. Gurkan, D. Starodubov, and X. Yuan, "Monitoring of the heartbeat sounds using an optical fiber Bragg grating sensor," in *Proc. 4th IEEE Conf. Sensors*, Irvine, CA, Oct. 30–Nov. 3 2005, pp. 306–309.
- [16] T. Erdogan, "Fiber grating spectra," *IEEE J. Lightw. Technol.*, vol. 15, no. 8, pp. 1277–1294, Aug. 1997.
- [17] Denselight Semiconductors. [Online]. Available: <http://www.denselight.com>
- [18] FiberSensing. [Online]. Available: <http://www.fibersensing.com>
- [19] Thorlabs GmbH, Germany. [Online]. Available: <http://www.thorlabs.de>
- [20] Ibsen photonics. [Online]. Available: <http://www.ibsen.dk/>
- [21] R. B. Seymour and G. B. Kauffman, "Polyurethanes: A class of modern versatile materials," *J. Chem. Education*, vol. 69, pp. 909–910, 1992.
- [22] L. S. Lim, T. Harada, M. A. Hillmyer, and F. S. Bates, "High strength polyolefin block copolymers," *Macromolecules*, vol. 37, pp. 5847–5850, 2004.
- [23] Y. Saeki and T. Emura, "Technical progresses for PVC production," *Progress in Polymer Science: Elsevier Science Direct*, vol. 27, pp. 2055–2131, 2002.
- [24] A. Silva, F. Gonçalves, P. Mendes, and J. H. Correia, "PVC formulation study for the manufacturing of a skin smart structure based in optical fiber elements," *J. Polymers Adv. Technol.*, pp. 1–8, Dec. 2010.
- [25] G. Wehrle, P. Nohama, H. J. Kalinowski, P. I. Torres, and L. C. G. Valente, "A fibre optic Bragg grating strain sensor for monitoring ventilatory movements," *Meas. Sci. Technol.*, vol. 12, pp. 805–809, 2001.
- [26] R. A. Losada and V. Pellissier, "Designing IIR filters with a given 3 dB point," *IEEE Signal Process. Mag.*, vol. 22, no. 4, pp. 95–98, Jul. 2005.



João Paulo Carmo (S'02–M'08) was born in Maia, Portugal, in 1970. He graduated in 1993 and received the M.Sc. degree in 2002, both in electrical engineering from the University of Porto, Porto, Portugal, and the Ph.D. degree in industrial electronics from the University of Minho, Guimarães, Portugal, in 2007. the Ph.D. thesis was on RF transceivers for integration in microsystems to be used in wireless sensors network applications.

Since 2008, he has been a Principal Researcher at the Algoritmi Center, University of Minho.

He is involved in the research on micro/nanofabrication technologies for mixed-mode/RF systems, solid-state integrated sensors, microactuators and micro/nanodevices for use in wireless and biomedical applications. He is also involved with the supervision of Ph.D. students from the MIT-Portugal program.

Dr. Carmo is a Member of the IEEE Industrial Electronics Society.



Alexandre Ferreira da Silva (S'10) graduated in 2007 in biomedical engineering (Integrated Masters) with specialization in medical electronics from the University of Minho, Braga, Portugal. Currently, he is working towards the Ph.D. degree at the Leaders for Technical Industries, University of Minho with the MIT-Portugal Program in the engineering design and advanced manufacturing focus-area.

Between 2006 to 2007, he spent six months at RWTH Aachen University, Germany, studying alternative sputtering processes in order to evaluate their performance and justify their utilization on electrodes production. In 2009, he performed an industrial internship at TMG Automotive for four months. In the same year, he was also a Visiting Student for four months at MIT's Materials Systems Laboratory.



Rui Pedro Rocha graduated with a Degree in industrial electronics and computers engineering from the University of Minho, Minho, Portugal, in 2006 and received the M.Sc. degree working on dynamic simulation of the microchip encapsulation from the University of Minho in 2008. Presently, he is enrolled in the Doctoral Program at the Leaders for Technical Industries, MIT-Portugal in the engineering design and advanced manufacturing focus area. His Ph.D. thesis is dealing with the development of smart optical microsystems with sensing and actuating capabilities.

He spent six months in the Micro and Nanotechnology Centre, University of Oulu, Finland, working on the development of novel fabrication methods for nanoscale photonics and microelectronics components. During the past years, he did research in micromachining and microfabrication technology mainly in thermoelectric energy scavenging microsystems and solid-state, thin-film, rechargeable Li-ion batteries.



José Higinio Correia (S'96–M'00) graduated with a Degree in physical engineering from the University of Coimbra, Coimbra, Portugal, in 1990. He received the Ph.D. degree from the Laboratory for Electronic Instrumentation, Delft University of Technology, Delft, The Netherlands, in 1999, working in the field of microsystems for optical spectral analysis.

Presently, he is a Full Professor with the Department of Industrial Electronics, University of Minho, Portugal. His professional interests are in micromachining and microfabrication technology for mixed-mode systems, solid-state integrated sensors, microactuators and microsystems.

Prof. Correia was the General-Chairman of Eurosensors 2003 and MME 2007, Guimarães, Portugal. He is a Member of the IEEE Industrial Electronics Society.